This is to certify that the
dissertation entitled

A Low-Power Radar Imaging System

presented by

Gregory Louis Charvat

has been accepted towards fulfillment
of the requirements for the

Ph.D. degree in Electrical and Computer Engineering

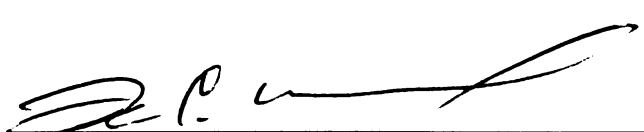

Major Professor's Signature

24 August 2007

Date

DATE DUE	DATE DUE	DATE DUE
DEC 0 9 2011	1	

A Low-Power Radar Imaging System

By

Gregory Louis Charvat

A DISSERTATION

Submitted to
Michigan State University
in partial fulfillment of the requirements
for the degree of

DOCTOR OF PHILOSOPHY

Electrical and Computer Engineering

2007

ABSTRACT

A Low-Power Radar Imaging System

By

Gregory Louis Charvat

A near real-time radar-based imaging system is developed in this dissertation. This system uses the combination of a spatially diverse antenna array, a high sensitivity range-gated frequency-modulated continuous wave (FMCW) radar system, and an airborne synthetic aperture radar (SAR) imaging algorithm to produce near real-time high resolution imagery of what is behind a dielectric wall. This system is capable of detecting and providing accurate imagery of target scenes made up of objects as small as 6 inch tall metallic rods and cylinders behind a 4 inch thick dielectric slab. A study is conducted of through-dielectric slab imaging by the development of a 2D model of a dielectric slab and cylinder. The SAR imaging algorithm is developed and tested on this model for a variety of simulated imaging scenarios and the results are then used to develop an unusually high sensitivity range-gated FMCW radar architecture. An S-band rail SAR imaging system is developed using this architecture and used to image through two different dielectric slabs as well as free-space. All results are in agreement with the simulations. It is found that free-space target scenes could be imaged using low transmit power, as low as 5 picowatts. From this result it was decided to develop an X-band front end which mounts directly on to the S-band rail SAR so that objects as small as groups of pushpins and aircraft models in free-space could be imaged. These results are compared to previous X-band direct conversion FMCW rail SAR work. It was found that groups of pushpins and models could be imaged at transmit powers as low as 10 nanowatts. A spatially diverse S-band antenna array will be shown to be developed for use with the S-band

radar; thereby providing the ability for near real-time SAR imaging of objects behind dielectric slabs with the same performance characteristics of the S-band rail SAR. The research presented in this dissertation will show that near real-time radar imaging through lossy-dielectric slabs is accomplished when using a highly sensitive radar system located at a stand-off range from the slab using a free-space SAR imaging algorithm.

For my parents, Dave and Rita Charvat

ACKNOWLEDGMENTS

I would like to acknowledge my parents Dave and Rita Charvat, who encouraged me in my interest of electronics at an early age. I would like to acknowledge my grandparents, Bud and Jane Charvat and Girard and Therese Nefcy (now deceased) for their thoughts and support.

I would like to thank my Junior High School shop teacher Kerry Pytel, who taught me that large projects are feasible if I put my mind to it. I would like to acknowledge the Amateur Radio community and my parents for suggesting it to me. Without this interest I would not have been able to gain an intuitive understanding of RF design principles at an early age. I credit Ardis Herrold for introducing me to research in general by sponsoring me as a competitor in the International Science and Engineering Fair in High School. And my friend Dr. Daniel Fleisch, who hired me as an intern at Aeroflex Lintek in Powell Ohio when I was a Junior in High School. It was from Dan that I realized the Ph.D. was the career path for me.

I acknowledge Dr. Charles MacCluer who helped me to acquire my first independent study at Michigan State University, which began my working relationship with the Electrical and Computer Engineering Department.

A special thanks to Dr. Chris Coleman who introduced me to the Electromagnetics Group and encouraged the EM group to hire me as a graduate research assistant. Chris was also responsible for introducing me to the field of SAR imaging and has continued to help me with this over the years.

Most importantly I would like to acknowledge my advisor, Dr. Leo Kempel. Thank

you for all of your help and support on this research and other projects that we developed over the years. I would like to thank Dr. Kempel, Dr. Ed Rothwell, and Dr. Shanker Balasubramaniam for introducing me to the study of electromagnetic theory and causing me to become genuinely interested.

I acknowledge Dr. Eric Mokole, head of the Surveillance Technology Branch, Radar Division, at the Naval Research Laboratory in Washington D.C. for initiating the working relationship and providing the funding for this research effort.

I would like to thank the Dow Chemical Company for sponsoring my graduate assistantship for no fewer than two years and introducing me to the patent process. I would like acknowledge the Air Force Research Laboratory, who has also been an important sponsor of my work.

I would like to acknowledge the Michigan State University Electromagnetics Research Group for providing outstanding facilities, equipment, and assistance on all of the projects that I have developed at MSU. It has been an honor to work with so many talented people, many of whom will be lifetime friends.

TABLE OF CONTENTS

LIST OF TABLES

LIST OF FIGURES

KEY TO SYMBOLS AND ABBREVIATIONS

BFO: Beat Frequency Oscillator

BPF: Band Pass Filter

CW: Continuous Wave

DIO: Digital I/O

DFT: Discrete Fourier Transform

FM: Frequency Modulated

FMCW: Frequency Modulated Continuous Wave

HPF: High Pass Filter

IDFT: Inverse Discrete Fourier Transform

I/O: Input/Output

IF: Intermediate Frequency

IFP: Image Formation Processor

LO: Local Oscillator

LPF: Low Pass Filter

LSB: Least Significant Bit

LNA: Low Noise Amplifier

MDS: Minimum Detectable Signal

PEC: Perfect Electric Conductor

RF: Radio Frequency

RCS: Radar Cross Section

RMA: Range Migration Algorithm

SAR: Synthetic Aperture Radar

TEM: Transverse Electromagnetic

VCO: Voltage Controlled Oscillator

CHAPTER 1

INTRODUCTION AND BACKGROUND

A near real-time through-dielectric slab imaging system is developed in this dissertation. This system uses the combination of a high speed antenna array, a high sensitivity range-gated FMCW radar system, and an airborne synthetic aperture radar (SAR) imaging algorithm to produce near real-time high resolution imagery of what is behind a dielectric slab. This system is capable of detecting and providing accurate imagery of target scenes made up of objects as small as 6 inch tall rods and small cylinders behind a 4 inch thick lossy dielectric slab at a stand-off range of 20 to 30 feet.

A number of research topics are developed in order to accomplish this. In Chapter 2 the Range Migration SAR algorithm is developed and tested on simulated point scatterers. In Chapters 3 through 5, a 2D through-lossy-dielectric slab SAR imaging model is developed which simulates a cylinder on the opposite side of a lossy dielectric slab. The SAR algorithm is tested on this model, with various wall thicknesses, cylinder diameters, and cylinder locations. These results are explored in detail in Chapter 6. Based on this analysis an unusually sensitive range-gated FMCW radar system architecture is developed in Chapter 7. Using this radar architecture, an S-band rail SAR imaging system is developed in Chapter 8. In Chapter 9, through-lossy-dielectric slab and free space imagery are then acquired using the S-band rail SAR, where target scenes made up of objects as small as bolts and soda cans are imaged. Results were found to be in agreement with the theoretical model. One of the more interesting results from this chapter was the fact that the rail SAR was capable of imaging free space targets using extremely low amounts of transmit power, down to 5 picowatts. Due to this result, in Chapter 10 it was decided to develop an X-band front

end based on the high sensitivity range-gated FMCW radar architecture, and image target scenes made up of small objects such as pushpins to compare this to previous work in [60]. It was found that the high sensitivity radar architecture operating at X-band was in agreement with previous results, and that the new system is capable of imaging targets as small as pushpins by using only 10 nanowatts of transmit power. Due to the results of the S-band rail SAR, it was decided to develop a high speed array to image through-dielectric slabs in near real-time. The development of this array, with free space and through-lossy-dielectric slab imaging results is presented in Chapter 11. It was found that the array imaging results were in agreement with the theoretical model. Future work and conclusions are discussed in Chapter 12.

1.1 Previous work in through-lossy-dielectric slab imaging radar system design

The research area of through-dielectric slab imaging is very diverse. Numerous approaches have been considered such as the use of millimeter wave radiometers [1], [2], [3]. Others are using UWB impulse radar at X-band to image through-dielectric slabs [4], [5], [6]. Still yet another approach is to use random noise radar [7]. Some researchers choose to focus on algorithm development, and use a vector network analyzer (VNA) as the radar sensor with bi-static transmit and receive antennas mounted on an XY scanner directly up against the lossy dielectric slab [8]. One of the most impressive systems for imaging through a dielectric slab is in [9], which is a 2.2 meter long 4 element bi-static antenna array connected to a 450 MHz to 2 GHz stepped frequency CW radar transmitting 50 milliwatts of power. This same system was then modified to operate as a distributed network for imaging through-dielectric slabs in [10]. Another interesting approach is the use of a 900 MHz through-dielectric slab doppler radar [11], designed operate as a through slab motion detector. A two receiver channel 2.4 GHz CW radar was developed as a doppler direction-of-arrival

system for tracking indoor movers in [14]. This machine tracks targets behind dielectric slabs by the doppler shift of their motion. Research has been conducted on a robot mounted pulsed-doppler radar motion sensing and ranging system operating at 5.8 GHz [12], [13], designed to maneuver around a building and detect motion and range through-dielectric slabs and map out locations of that motion. The Electromagnetics Research Group at Michigan State University has a history of imaging targets through thin lossy dielectric slabs with UWB impulse radar [15].

The majority of current through-lossy-dielectric slab research has been focused on UWB impulse radar operating in the 1 to 3 GHz frequency range [16], [17], [18], [19], [20] and [21]. UWB impulse radar technology is promising because the reflection off of the dielectric slab can be time gated (or range-gated) out of the data, protecting data acquisition equipment from being saturated and allowing for maximum system dynamic range to be applied to the range bins behind the dielectric slab. UWB impulse radar by itself is not very sensitive, and requires the use of coherent integration to achieve useful signal to noise ratios when attempting to image objects behind dielectric slabs. It is for this reason that there has been much effort in the area of optimizing coherent integration methods so that more coherent integration occurs at range bins behind the slab causing a reduction in CPU cycles when processing [22].

Other radar systems for imaging through-dielectric slabs exist that are not presented in publication. These can be found by conducting a simple internet search. These will not be cited in this dissertation for archival purposes.

The radar systems developed for through-lossy-dielectric slab imaging in this dissertation are different from the majority of previous work in that they are not UWB impulse radar systems, CW doppler, stepped frequency, or pulsed doppler. The through-dielectric imaging systems developed in this dissertation are FMCW, using a modified FMCW radar architecture that allows for hardware range gating without the use of time domain solid state switches or an increased IF bandwidth. The

approach taken here is to develop the most sensitive, greatest dynamic range radar which is fast and range-gated. It will be shown that a high sensitivity range-gated FMCW radar architecture is developed which achieves this goal.

1.2 Previous work in through-lossy-dielectric slab imaging algorithms

There are a number of interesting through-lossy-dielectric slab algorithms that have been developed, such as Space Time Focusing, tested on a 3D ray tracing model of a 5 story building in [28]. In this work 3D positions of simulated targets were located using an array of numerous radar sensors placed around the theoretical building. A number of microwave tomography and inverse scattering methods have been used to image cylinders behind lossy-dielectric slabs [29], [30], [31], [32], and dielectric barrier surfaces behind lossy-dielectric slabs [33]. Most of the through-lossy-dielectric slab radar systems that have been developed use some sort of beam forming algorithm [16], [17]. Much of the focus of beam forming algorithm research has been to develop methods to counter the effects of the dielectric slab on a radar system with antennas placed directly on the slab [23], [24], [25], [26], [27]. The effects of Snell's law severely affect the beam forming algorithms by changing the phase centers of the array elements of these radar systems. This dissertation is different than this previous work in that the radar systems developed here are designed to be placed at stand-off ranges of 20 to 30 feet or greater from the dielectric slab. It will be shown that placing the radar systems at this stand-off range does not require special treatment or de-convolution of the dielectric slab in order to process accurate radar imagery.

The through-dielectric slab imaging radar systems presented in this dissertation will use SAR imaging algorithms such as those in [34], [35], [36], rather than beam-forming techniques used in most other through-slab work. More specifically, the radar systems presented in this dissertation use the Range Migration Algorithm, which is an airborne SAR imaging algorithm from [37]. SAR imaging is a specific type of

beamforming, and the RMA is one of the more advanced SAR algorithms in use presently.

1.3 Previous work in through-dielectric slab theoretical imaging models

In the research field of through-dielectric imaging numerous approaches have been developed to model a lossy dielectric slab in a through-dielectric slab imaging scenario. These include the use of finite difference time domain (FDTD) [38], [41], geometric optics (GO) [39] [40], modeling the slab as a transmission line [4], and the use of electric field integral equation (EFIE) solved using the method of moments (MoM) for a lossy current sheet which simulates the wall of a wood packaging crate [15].

Some general purpose dielectric models were considered for this research for use in modeling the dielectric slab. One approach considered was the use of the EFIE and MoM to model a dielectric slab, by developing a thick version of the models in [42], [43] and [44] for modeling arbitrarily shaped dielectric cylinders. Some unpublished work was conducted. The integral equation solution to planar dielectrics [45] (similar to the work done by [46], and [46]) was considered for some time, and resulted in the publication of [48]. The Universal Theory Diffraction (UTD) was also explored for modeling a dielectric [49].

Based on the geometry of the problem it was decided use the plane wave approximation to model the dielectric slab. Wave matrix theory from [63] is used to model the slab. The solution to a 2D PEC cylinder from [61] is used to model a cylinder behind the slab.

1.4 Previous work in FMCW radar design

For decades FMCW radar has been used primarily for aircraft radio altimeters where the FMCW chirp would range the distance from aircraft to ground [50], [51], [52]. It was not until the late 1980's and early 90's that advancements in low cost high speed

signal processors allowed for the application of FMCW to more sophisticated applications, where the video signal of the FMCW radar could be digitized and analyzed using Fourier analysis on a single chip digital signal processor (DSP) [53]. These more advanced signal processing techniques have led to the use of FMCW radar systems in many applications such as rail SAR imaging [60] and automotive obstacle avoidance [55], [56], [57]. Previous FMCW rail SAR imaging systems such as [60] use a direct conversion FMCW radar architecture. The FMCW radar systems developed in this dissertation are different from most previous work in that they use a hardware range-gate without electronic high speed RF switches. This unusual range-gate provides for a high sensitivity receiver without the use of coherent integration or reduction of chirp rate. This modified FMCW radar architecture will be referred to as high sensitivity range-gated FMCW.

Imagery from both a direct conversion X-band FMCW rail SAR imaging system in [60] and an X-band rail SAR utilizing the high sensitivity range-gated FMCW radar architecture developed in this dissertation will be presented for comparison purposes. This will show that the high sensitivity range-gated FMCW radar architecture is of superior performance compared to direct conversion FMCW radar systems.

1.5 Previous work in spatially diverse antenna array design

The array developed for this dissertation is a large switched antenna array, where various combinations of transmit and receive elements are switched on to the transmitter and receiver to provide spatially diverse radar data for the imaging algorithm. Many of the previous through-dielectric slab UWB impulse radar systems [4], [5], [6], [16], [17], [18], [19], [20] and [21], use some type of switched antenna array. In this setup the transmitter or receiver are switched onto different transmit and receive elements, acquiring data across different combinations of elements. This multi-static data acquisition approach allows for the development of spatially diverse radar data,

facilitating the use of various radar imaging algorithms and beam forming using the unique advantages of UWB impulse radar used on an antenna array [54]. These arrays were developed to be very small, designed to be portable or hand held. The array developed in this dissertation is different in that it is significantly larger than the hand held systems. This array was developed to be 88 inches long, because of this, it produces higher cross range resolution than most existing systems using UWB impulse or even that of other FMCW radar devices used in switched antenna arrays [55], [56], [57].

1.6 Discussion of research to be presented

The research that will be presented in this dissertation will show that through-dielectric slab radar imaging is entirely feasible by combining the use of airborne SAR imaging algorithms, an unusualy high sensitivity range-gated FMCW radar design, and a large high speed array to produce near real-time radar imagery of what is behind an unknown lossy dielectric slab.

CHAPTER 2

SYNTHETIC APERTURE RADAR

Synthetic Aperture Radar (SAR) is often used as an airborne imaging sensor [58] producing nearly photographic radar imagery of a target scene. SAR Imaging can also be done on a small scale as was shown in [59]. In the laboratory environment, extremely high resolution SAR imagery can be achieved on a small scale using a wide bandwidth radar system mounted on a precision linear rail [60]. In this dissertation, a small rail SAR much like [60] will be developed to SAR image through a dielectric slab. The small aperture data collection geometry used in this dissertation for both simulated and measured data is shown in Section 2.1. The Range Migration Algorithm (RMA) is the SAR imaging algorithm that will be used for all radar imaging in this dissertation. This algorithm is discussed in Section 2.2. The RMA will be tested and proven to be effective for imaging simulated SAR data of ideal point scatterers in Section 2.3.

2.1 Data collection geometry

The rail SAR imaging geometry used for both theoretical and measured data is shown in Figure 2.1. In this data collection geometry a small radar device is mounted on an 8 ft long automated linear rail. The radar has a small wide beamwidth horn antenna that is directed out towards an unknown target scene parallel to the rail. The radar begins its journey at the end of the rail near the drive motor. The drive motor moves the radar to a location, stops, then the radar acquires a range profile. After the range profile is complete the drive motor moves the radar to the next known location and the radar acquires another range profile. This process is repeated at regular intervals along the rail until the radar device reaches the end of the rail. The range profiles

over each rail position produce a 2D data matrix in the form of

$$s\big(x_n, \omega(t)\big),$$

where $s\big(x_n, \omega(t)\big)$ is the 2D frequency domain range profile data matrix, x_n is the nth cross range position of the radar on the automated rail, and

$$\omega(t) = 2\pi\left(c_r t + f_c - \frac{BW}{2}\right) \tag{2.1}$$

is the instantaneous radial frequency of the received chirp waveform. In this c_r is the chirp rate of the linear frequency modulated (FM) chirped radar system, f_c is the radar center frequency, and BW is the chirp bandwidth. The SAR rail length is L, where in the case for all simulations and some measurements $L = 8$ ft, and the aperture spacing is $\Delta x = 2$ inches between range profiles across the rail.

It is important to note that a linear FM radar system exactly like [60] will be assumed for all cases, both theoretical and experimental. As such, the instantaneous received frequency of the radar system is a function of chirp rate and time. The chirp rate for a linear FM radar system is

$$c_r = \frac{BW}{T}, \tag{2.2}$$

where T is the chirp length and $BW = f_{stop} - f_{start}$ is the transmit bandwidth from the transmit start frequency to the transmit stop frequency in Hz. In the example presented in this chapter $T = 10$ milliseconds. Thus, the chirp rate for all theoretical and some experimental data is $c_r = 214.3$ GHz/second, where the radar system is assumed to operate at S-band occupying the frequency range of $f_{stop} = 4.069$ GHz and $f_{start} = 1.926$ GHz.

2.2 The Range Migration Algorithm (RMA)

The data matrix $s(x_n, \omega(t))$ is processed by a SAR imaging algorithm to produce an image matrix $S(X, Y)$, which is the resulting SAR image of the target scene of interest. One of the more popular SAR imaging algorithms is known as the RMA. The RMA for this dissertation was developed directly from [37]. The RMA follows these four processing steps:

1. Cross range discrete Fourier transform (DFT).
2. Matched filter.
3. Stolt interpolation.
4. Inverse discrete Fourier transform (IDFT) into resulting image.

The details of each of these processing steps will be discussed in this section by example. A single point scatterer is defined and a SAR data matrix is calculated in Section 2.2.1. The cross range DFT step will be described in Section 2.2.2. The matched filter process will be described in Section 2.2.3. Section 2.2.4 will describe how the Stolt interpolation is used for proper frequency domain data formatting. Section 2.2.5 will describe how to produce an image from the Stolt interpolated data using the IDFT.

2.2.1 Simulation of a single point scatterer

Using the data collection geometry in Section 2.1 the approximation for a single point scatterer located located at (x_t, y_t) with a reflection magnitude of a_t creates the SAR data matrix

$$s(x_n, \omega(t)) = a_t e^{-j2\frac{\omega(t)}{c}\sqrt{(x_n - x_t)^2 + y_t^2}}. \tag{2.3}$$

Where c is the speed of light approximately $3 \cdot 10^8$ m/second. Without loss of generality let $a_t = 1$. Locating the point scatter at $x_t = 0$ feet cross range from rail

center (where $x = 0$ is the center of the rail) and $y_t = -10$ feet downrange produces a simulated SAR data matrix. Using these values, this was calculated using the MATLAB program in Appendix A, where the real value of the SAR data matrix points are shown in Figure 2.2, and the phase of the SAR data matrix points is shown in Figure 2.3. The downrange DFT of the SAR data matrix is shown in Figure 2.4. This plot shows the wave-front curvature of the single point scatterer, which is in an arc because the range to target varies over the aperture length L.

2.2.2 Cross range Fourier transform

The first step in the RMA is to calculate the DFT along the cross range axis of the SAR data matrix $s\big(x_n, \omega(t)\big)$ resulting in a wave number domain data matrix $s\big(k_x, \omega(t)\big)$. In addition to the DFT, the simple substitution is made: $k_r = \omega(t)/c$. This results in the SAR data matrix $s(k_x, k_r)$. Using the MATLAB programs in Appendix B and Appendix C, the magnitude after the cross range DFT is shown in Figure 2.5 and the phase after the cross range DFT is shown in Figure 2.6.

2.2.3 Matched filter

A 2D matched filter is then applied to the $s(k_x, k_r)$ matrix. The equation for the matched filter used in the RMA is

$$s_{mf}(k_x, k_r) = e^{jR_S\sqrt{k_r^2 - k_x^2}}, \tag{2.4}$$

where R_S is the downrange distance to scene center. In this example $R_S = 0$, however in practice using a rail SAR imaging system or a spatially diverse antenna array, R_S is equal to the range to calibration target, shifting the scene center to a downrange line located at distance R_S from the rail. Multiplying equation 2.4 by $s\big(k_x, k_r\big)$ results in

$$s_{matched}(k_x, k_r) = s_{mf}(k_x, k_r) \cdot s\big(k_x, k_r\big). \tag{2.5}$$

Using the MATLAB programs in Appendix B and Appendix C, the resulting phase of $s_{matched}(k_x, k_r)$ is plotted in Figure 2.7 and the resulting downrange DFT magnitude is plotted in Figure 2.8.

2.2.4 Stolt interpolation

The Stolt interpolation transforms the 2D SAR data after the matched filter $s_{matched}(k_x, k_r)$ from the radar transmitted chirp k_r domain to the the spatial wave number domain k_y. The relationship between k_y, k_r, and k_x is given by

$$k_y = \sqrt{k_r^2 - k_x^2}. \tag{2.6}$$

A 1D interpolation must be conducted across all the downrange wave numbers k_r to map them onto k_y thus resulting in the Stolt interpolated matrix $s_{st}(k_x, k_y)$. Using the MATLAB programs in Appendix B and Appendix C, the resulting phase after the Stolt interpolation is shown in Figure 2.9.

2.2.5 Inverse Fourier transform in to image domain

In order to convert the Stolt interpolated matrix $s_{st}(k_x, K_y)$ into image domain $S(X, Y)$, a subsection of the curved Stolt interpolated data shown in Figure 2.9 must be taken such that the resulting subsection is completely filled with data. The resulting subsection of the data is shown in Figure 2.10.

The resulting SAR image data matrix $S(X, Y)$ is the 2D IDFT of the subsection of Stolt interpolated data. Using the MATLAB programs in Appendix B and Appendix C, the resulting SAR image of the point scatterer is shown in Figure 2.11.

2.3 Simulation of multiple point scatterers

Using equation 2.3 a SAR data matrix can be produced for a single point scatterer. It is often useful to simulate multiple point scatterers to test a SAR imaging algorithm.

For this reason Equation 2.3 was modified to represent N scatterers

$$s(x_n, \omega(t)) = \sum_{i=1}^{N} a_{ti} e^{-j2\omega(t)\sqrt{(x_n - x_{ti})^2 + y_{ti}^2}}. \tag{2.7}$$

Using the MATLAB program in Appendix A, three point scatterers with reflection amplitudes of $a_{t1} = a_{t2} = a_{t3} = 1$ were simulated at the following locations cross range and down range from the linear rail:

$$\begin{aligned}
(x_{t1}, y_{t1}) &= (3, -10) \quad \text{feet}, \\
(x_{t2}, y_{t2}) &= (-3, -15) \quad \text{feet}, \\
(x_{t3}, y_{t3}) &= (-2, -10) \quad \text{feet}.
\end{aligned}$$

This simulated SAR data matrix was then fed into the data conditioning MATLAB program in Appendix B and the RMA SAR imaging MATLAB program in Appendix C resulting in the SAR image shown in Figure 2.12. From this, it is clear that the RMA SAR algorithm written for this dissertation is capable of imaging a target scene.

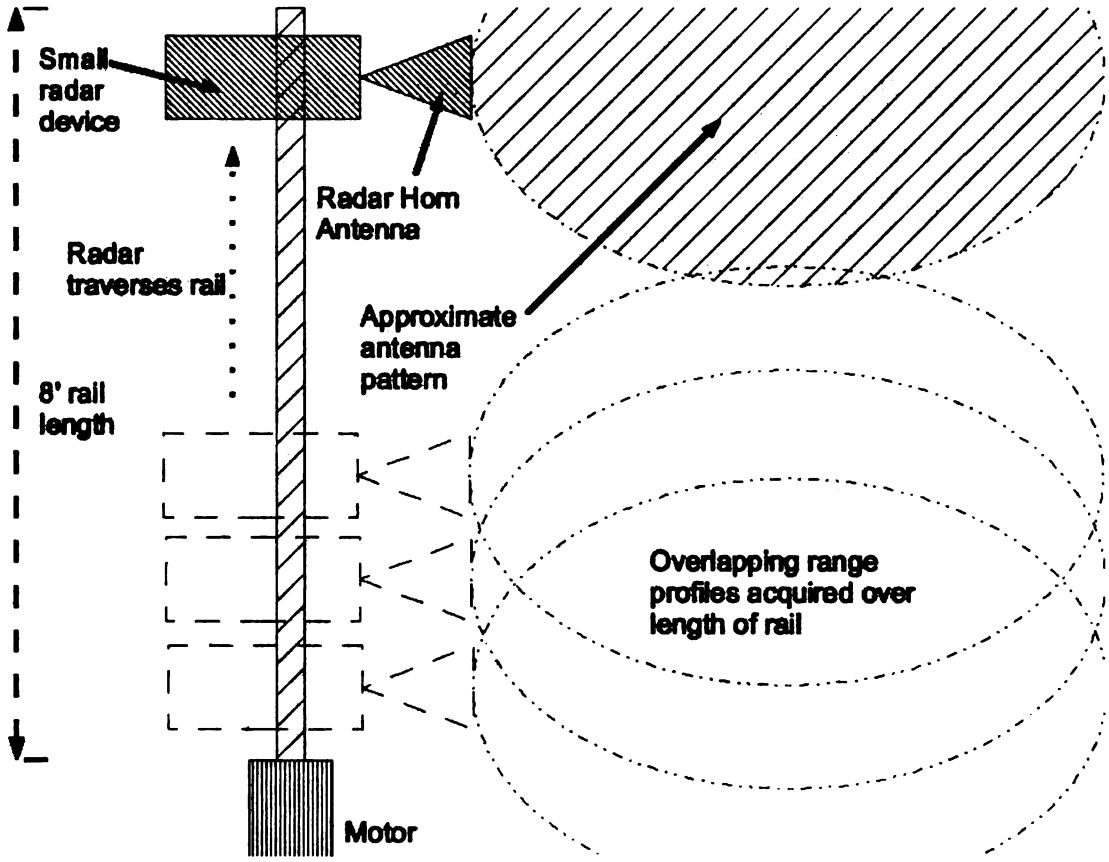

Figure 2.1. Rail SAR data collection geometry.

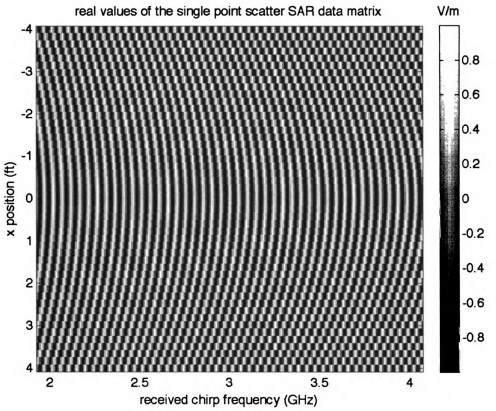

Figure 2.2. Real values of the SAR data matrix for a single point scatterer.

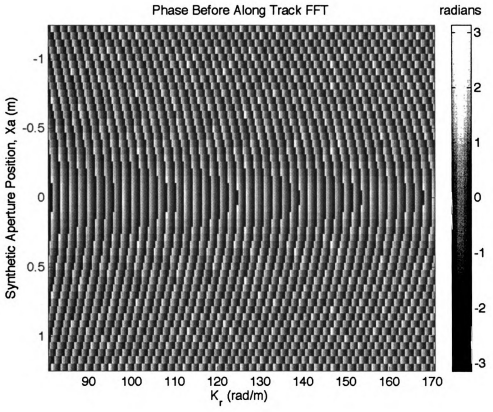

Figure 2.3. Phase of the SAR data matrix for a single point scatterer.

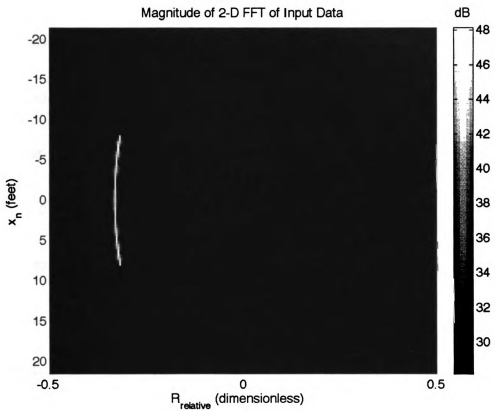

Figure 2.4. Magnitude of simulated point scatterer after downrange DFT, showing the wave-front curvature of the point scatterer.

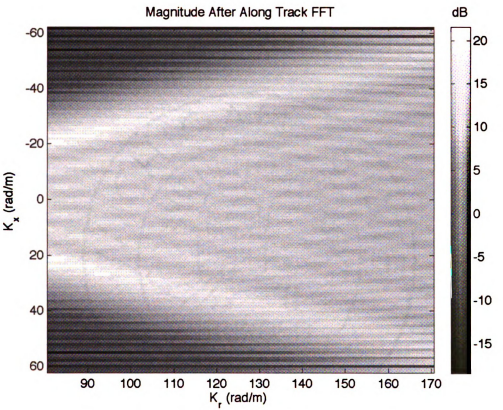

Figure 2.5. Magnitude after the cross range DFT.

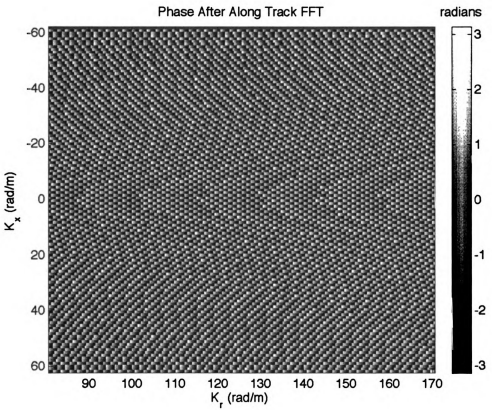

Figure 2.6. Phase after the cross range DFT.

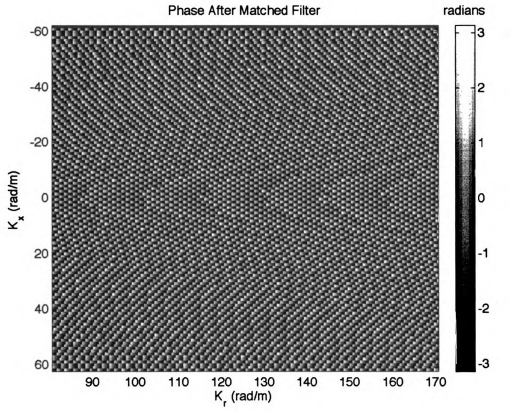

Figure 2.7. Phase after the matched filter.

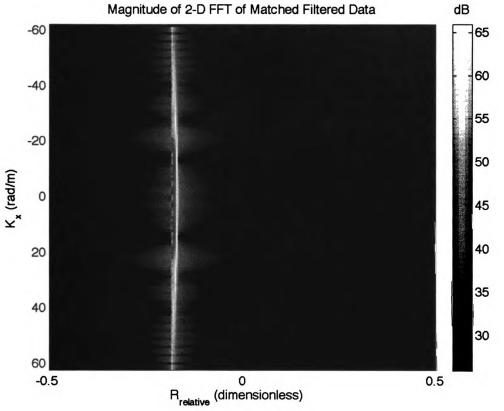

Figure 2.8. Magnitude after 2D DFT of matched filtered data.

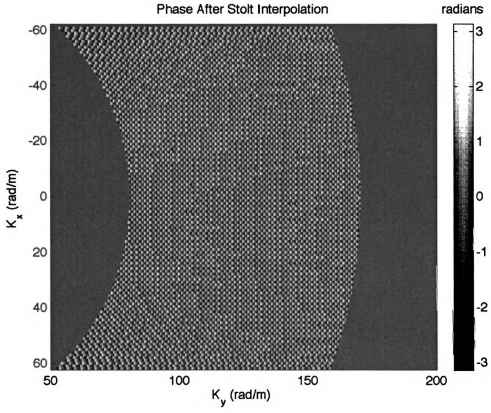

Figure 2.9. Phase after Stolt interpolation.

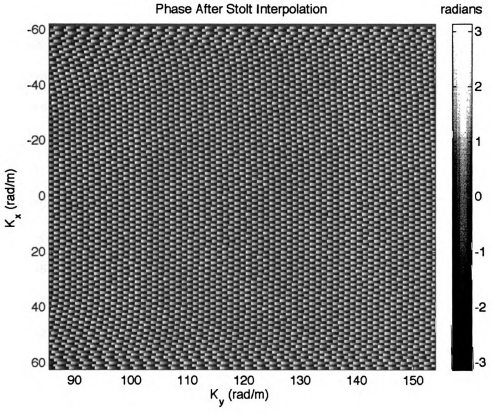

Figure 2.10. A subsection of the phase after Stolt interpolation.

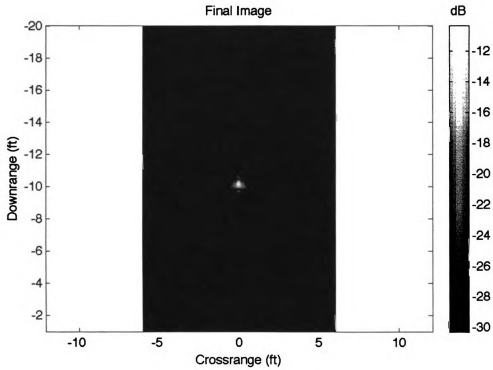

Figure 2.11. SAR image of a simulated point scatterer.

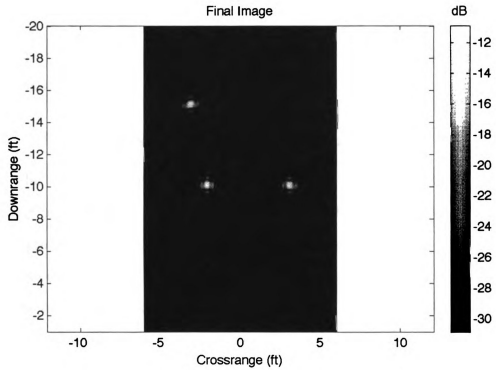

Figure 2.12. SAR image three simulated point scatterers.

CHAPTER 3

SCATTERING FROM A PERFECT ELECTRIC CONDUCTING CYLINDER

Cylinders are often used for radar system calibration and for measuring system performance. It is for this reason that a two dimensional (2D) solution based on [61] to the scattering from a perfect electric conducting (PEC) cylinder will be developed. This solution will be verified from previous results. Using the solution developed in this chapter a set of simulated SAR data will be created. The SAR imaging algorithm from Chapter 2 will then be used to image this simulated cylinder.

3.1 TM^z scattering solution to a 2D PEC cylinder

The radar system that will be used for acquiring experimental data will be using vertically polarized transmit and receive antennas. The radar will be located many wavelengths away from the target scene. It is for these reasons the plane wave approximation will be used for this solution to the scattering of a 2D PEC cylinder. Since the radar polarization is vertical the plane wave polarization that will be used for this solution is TM^z.

The geometry for a TM^z plane wave incident on a 2D PEC cylinder is shown in Figure 3.1, where a is the radius of the 2D infinite cylinder centered along the $\hat{z}$ axis. The incident TM^z plane wave is traveling towards the cylinder from the $y = -\infty$ direction towards $x = 0$, where the electric and magnetic field components are transverse to the $\hat{x}$ direction of propagation. The incident electric field $\overrightarrow{E}^i$ is polarized parallel to the $\hat{z}$ axis and the incident magnetic field $\overrightarrow{H}^i$ vector is parallel to the $-\hat{y}$ axis.

For a TM^z incident plane wave, we can represent the incident electric field as

$$\vec{E}^i = \hat{z}E_o e^{-jk_o x}, \tag{3.1}$$

where E_o is the magnitude of the incident electric field. Applying the cartesian to cylindrical coordinate transformation $x = \rho\cos\phi$, where ρ is the radius and ϕ is the angle with respect to the x-axis in cylindrical coordinates, Equation 3.1 can be re-written as

$$\vec{E}^i = \hat{z}E_o e^{-jk_o\rho\cos\phi}. \tag{3.2}$$

Using the cylindrical wave transformation from [61] this can be re-written as

$$e^{-jk\rho\cos\phi} = \sum_{n=-\infty}^{\infty} j^{-n}J_n(k\rho)e^{jn\phi}. \tag{3.3}$$

Applying this result to Equation 3.2 results in

$$\vec{E}^i = \hat{z}E_o \sum_{n=-\infty}^{\infty} j^{-n}J_n(k_o\rho)e^{jn\phi}. \tag{3.4}$$

Applying Euler's formula to the above results in

$$\vec{E}^i = \hat{z}E_o \sum_{n=-\infty}^{\infty} \left[j^{-n}J_n(k_o\rho)\cos n\phi + j\cdot j^{-n}J_n(k_o\rho)\sin n\phi\right]. \tag{3.5}$$

The second term in the above equation goes to zero because inside of the summation term

$$\sin(-n) + \sin(n) = 0.$$

Applying this to Equation 3.5 results in

$$\vec{E}^i = \hat{z}E_o \sum_{n=-\infty}^{\infty} j^{-n} J_n(k_o\rho)\cos n\phi. \tag{3.6}$$

Equation 3.6 is symmetric about the $n = 0$ term of the summation. For this reason symmetry can be used to reduce the summation from $-\infty$ to ∞ to 0 to ∞. In addition, the simplification $j^{-n} = (-j)^n$ may be used. Applying both of these to Equation 3.6 results in the simplified incident electric field equation

$$\vec{E}^i = \hat{z}E_o \sum_{n=0}^{\infty} (-j)^n \varepsilon_n J_n(k_o\rho)\cos n\phi, \tag{3.7}$$

where

$$\varepsilon_n = \begin{cases} 1 & \text{for } n = 0 \\ 2 & \text{for } n \neq 0 \end{cases}.$$

The total electric field around the cylinder shown in Figure 3.1 is defined as

$$\vec{E}^{tot} = \vec{E}^i + \vec{E}^s, \tag{3.8}$$

where $\vec{E}^s$ is the scattered electric field from the cylinder. $\vec{E}^s$ travels outward away from the cylinder and is represented by the cylindrical traveling wave equations from [61], thus the solution to the scattered field $\vec{E}^s$ has the form

$$\vec{E}^s = \hat{z}E_o \sum_{n=-\infty}^{\infty} c_n H_n^{(2)}(k_o\rho), \tag{3.9}$$

where the unknown amplitude coefficients c_n must be solved in order to find the solution to the scattered field $\vec{E}^s$.

Applying boundary conditions to the surface of the cylinder at $\rho = a$ and for $0 \leq \phi \leq 2\pi$ as shown in Figure 3.2, the total electric field becomes zero at the

cylinder surface and Equation 3.8 can be re-written as

$$0 = \vec{E}^i + \vec{E}^s. \tag{3.10}$$

Substituting the incident field Equation 3.4 and the scattered field Equation 3.9 into Equation 3.10, the above equation becomes

$$0 = \hat{z}E_o \sum_{n=-\infty}^{\infty} j^{-n} J_n(k_o a) e^{jn\phi} + \hat{z}E_o \sum_{n=-\infty}^{\infty} c_n H_n^{(2)}(k_o a). \tag{3.11}$$

Combining the summation terms and suppressing both $\hat{z}$ and E_o, the expression becomes

$$0 = \sum_{n=-\infty}^{\infty} \left[j^{-n} J_n(k_o a) e^{jn\phi} + c_n H_n^{(2)}(k_o a) \right]. \tag{3.12}$$

The expression within the summation is zero for all n to enforce the boundary conditions on the surface of the cylinder, therefore the above equation can be simplified further by considering 3.12 on a mode-by-mode basis

$$0 = j^{-n} J_n(k_o a) e^{jn\phi} + c_n H_n^{(2)}(k_o a). \tag{3.13}$$

Finally, the solution for c_n is

$$c_n = \frac{-(j)^{-n} J_n(k_o a) e^{jn\phi}}{H_n^{(2)}(k_o a)}. \tag{3.14}$$

Substituting Equation 3.14 into Equation 3.9 results in the scattered field solution to the 2D PEC cylinder

$$\vec{E}^s = \hat{z}E_o \sum_{n=-\infty}^{\infty} H_n^{(2)}(k_o \rho) \frac{-(j)^{-n} J_n(k_o a)}{H_n^{(2)}(k_o a)} e^{jn\phi}. \tag{3.15}$$

Applying Euler's equation, the scattered field becomes

$$\vec{E}^s = \hat{z}E_o \sum_{n=-\infty}^{\infty} H_n^{(2)}(k_o\rho)\frac{-(j)^{-n}J_n(k_oa)}{H_n^{(2)}(k_oa)}\left[\cos n\phi + j\sin n\phi\right]. \tag{3.16}$$

The sine term of the above equation vanishes because inside of the summation

$$\sin(-n) + \sin(n) = 0,$$

and thus Equation 3.16 can be written

$$\vec{E}^s = \hat{z}E_o \sum_{n=-\infty}^{\infty} H_n^{(2)}(k_o\rho)\frac{-(j)^{-n}J_n(k_oa)}{H_n^{(2)}(k_oa)}\cos n\phi. \tag{3.17}$$

Equation 3.17 is symmetric about the $n = 0$ term of the summation, thus symmetry can be used to reduce the summation from $-\infty$ to ∞ to 0 to ∞. Furthermore, the substitution $j^{-n} = (-j)^n$ can be made. Applying both of these to Equation 3.17 leaves the simplified scattered electric field equation

$$\vec{E}^s = -\hat{z}E_o \sum_{n=0}^{\infty} (-j)^n \varepsilon_n \frac{J_n(k_oa)}{H_n^{(2)}(k_oa)} H_n^{(2)}(k_o\rho)\cos n\phi, \tag{3.18}$$

where

$$\varepsilon_n = \begin{cases} 1 & \text{for } n = 0 \\ 2 & \text{for } n \neq 0 \end{cases}.$$

3.2 Echo width of a 2D PEC cylinder

In this section the 2D radar cross section, known as echo width, of the cylinder will be calculated in order to verify the results from Section 3.1 with the results in [61]. This verification will show that the 2D cylinder model is valid to be used in the theoretical development shown later in this dissertation.

The echo width equation from [61] is defined as

$$\sigma_{2D} = \lim_{\rho \to \infty} \left[2\pi\rho \frac{|\vec{E}^s|^2}{|\vec{E}^i|^2} \right]. \tag{3.19}$$

In the eventual theoretical imaging geometry and experimental setup the PEC cylinder target will be located approximately 20 feet or greater from the rail SAR imaging system. It was for this reason that rather than taking the limit as $\rho \to \infty$, it was decided to let $\rho = 20$ feet and modify Equation 3.19 to

$$\sigma_{2D} \approx \left[2\pi\rho \frac{|\vec{E}^s|^2}{|\vec{E}^i|^2} \right]_{\rho=20 \text{ ft}}. \tag{3.20}$$

Substituting the incident field Equation 3.7 and the scattered field solution Equation 3.18 into Equation 3.20 letting the frequency be 2 GHz (the low end of the approximately 2 GHz to 4 GHz radar transmit chirp) and the radius of the PEC cylinder $a = 0.6\lambda$ a MATLAB program was written (see Appendix D) to calculate and plot the echo width of a 2D PEC cylinder with TM^z plane wave incidence. The resulting echo width shown in Figure 3.3 matches the results shown in [61], therefore this 2D PEC cylinder model for plane wave TM^z incidence is valid for use in the theoretical developement shown throughout this dissertation.

3.3 Range profiles of a 2D PEC cylinder

Using Equation 3.18, a MATLAB program was written (see Appendix D) to simulate a 2 GHz to 4 GHz chirped radar system measuring the range profile of a cylinder located 30 feet downrange for various cylinder radii values a. The IDFT was taken of the time harmonic scattered field solution over 256 frequency data points between 2 GHz and 4 GHz. Theses range profile results are summarized in Table 3.1.

From these results it is clear that 2D PEC cylinders of various radii can be sim-

ulated downrange from a chirped radar system. Due to this result it is now possible to simulate a SAR image of a 2D PEC cylinder.

3.4 SAR image of a the 2D PEC cylinder model

Using the 2D cylinder model developed in this chapter a SAR data set was simulated using the geometry shown in Figure 2.1 and using the MATLAB program in Appendix E for a cylinder of radius $a = 3$ inches located 30 ft downrange from the center of the rail. The simulated data set was then fed into the MATLAB data conditioning program in Appendix B and processed by the MATLAB coded RMA SAR imaging algorithm in Appendix C. The resulting SAR image is shown in Figure 3.8. A second SAR image of a cylinder with a radius of $a = 6$ inches located 30 ft downrange from center rail is shown in Figure 3.9. From these results it is clear that a 2D PEC cylinder can be modeled effectively and a simulated SAR image produced from the model.

Table 3.1. Summary of range profile results.

cylinder radius	range profile in dB	real data range profile
$a = 23.62$ inch	Figure Figure 3.4	Figure Figure 3.5
$a = 1.96$ inch	Figure Figure 3.6	Figure Figure 3.7

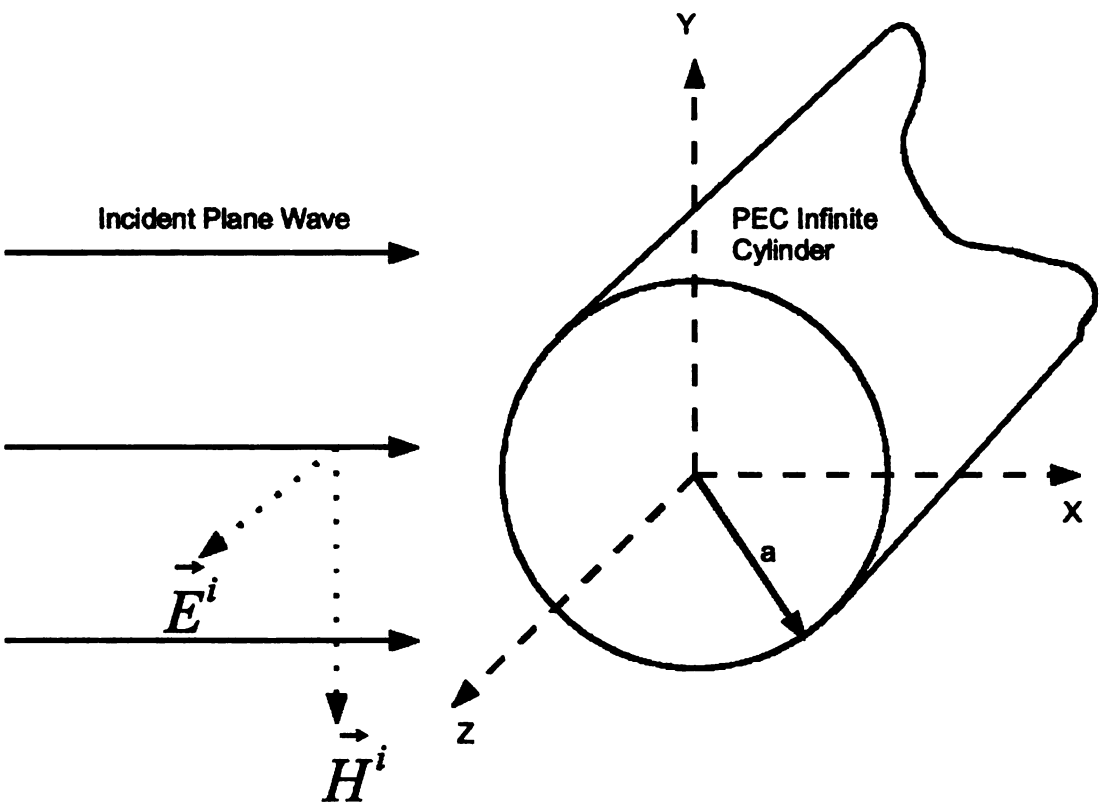

Figure 3.1. TM^z incident plane wave on the PEC cylinder geometry.

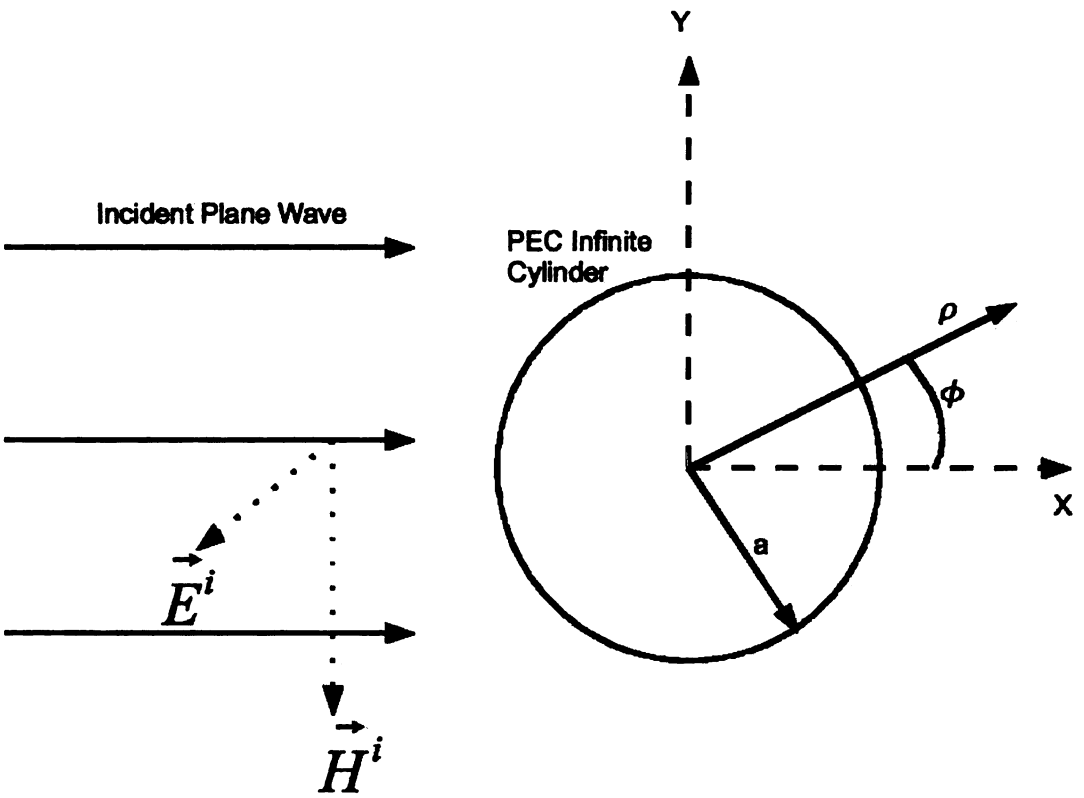

Figure 3.2. 2D TM^z incident plane wave on the PEC cylinder geometry.

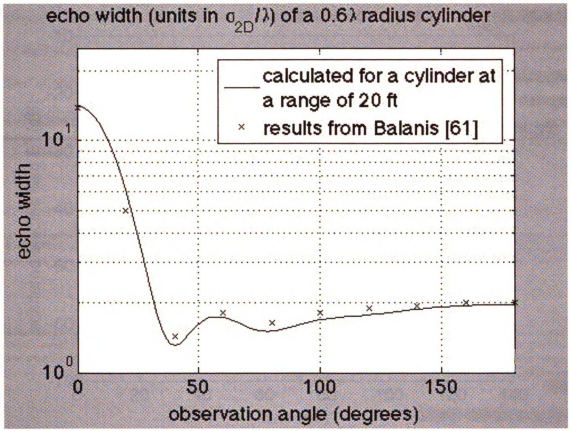

Figure 3.3. Bistatic echo width of a 2D PEC cylinder with TM^z plane wave incident electric field observed at a distance of 20 ft from the cylinder.

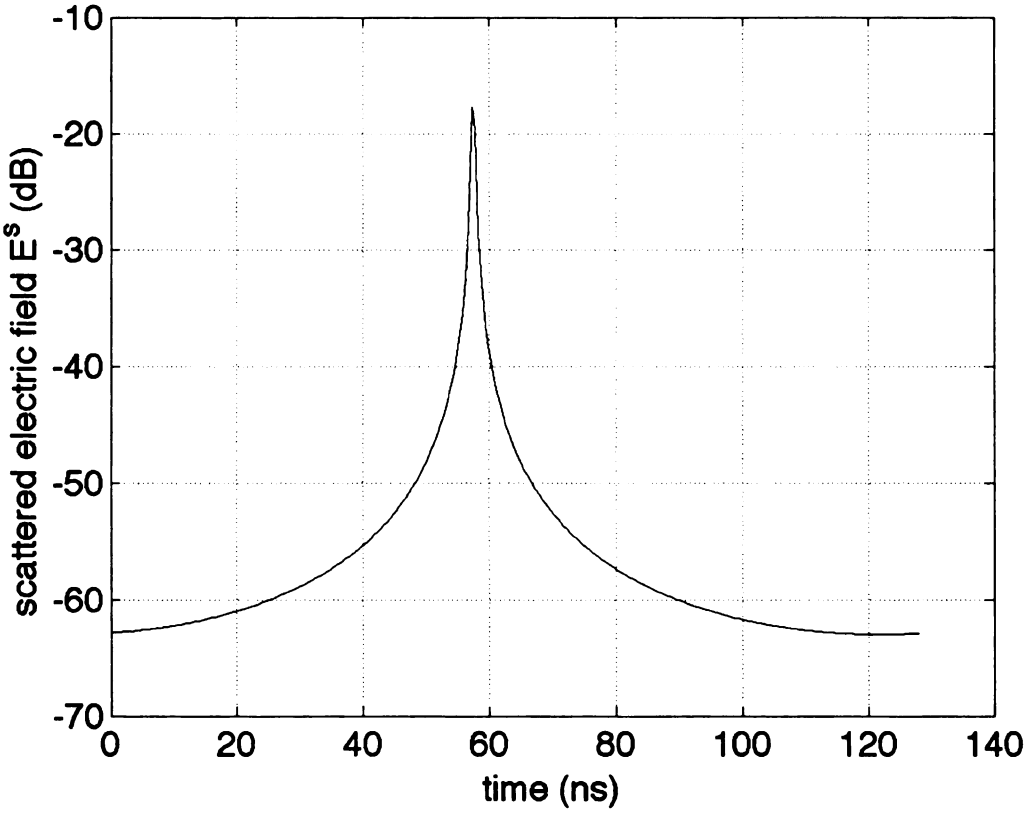

Figure 3.4. Range profile of a 23.62 inch radius cylinder with TM^z plane wave incidence, showing the downrange time delay of the front face of the cylinder.

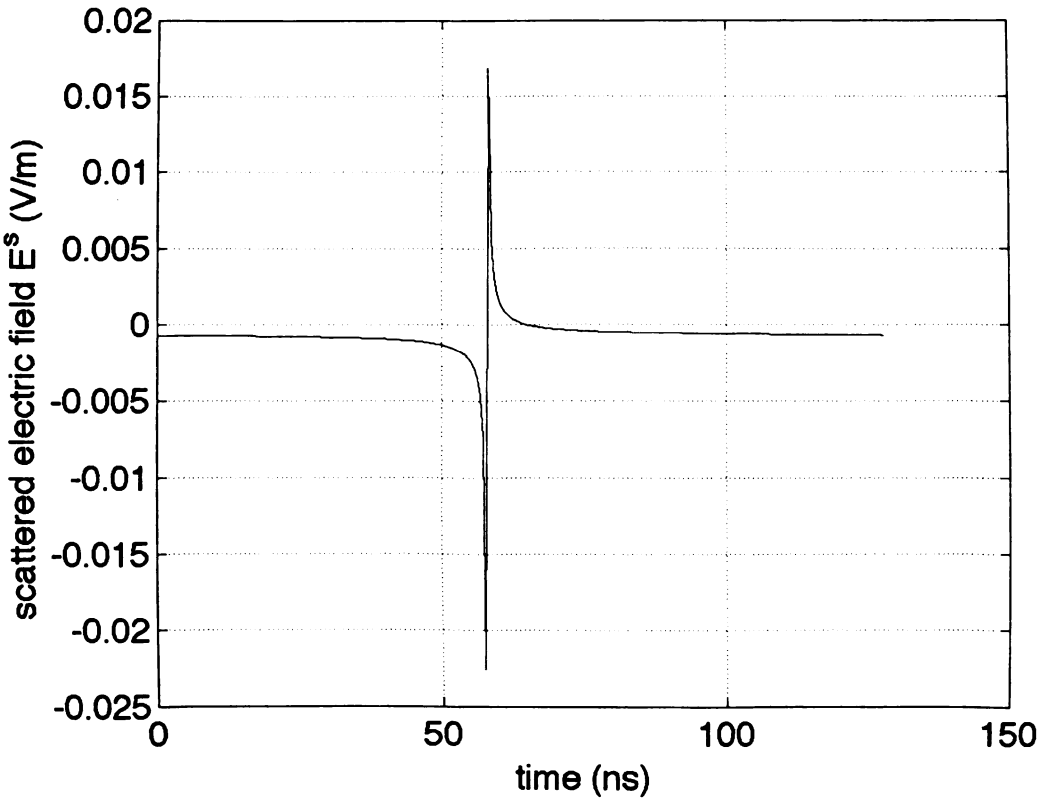

Figure 3.5. Real value of the range profile of a 23.62 inch radius cylinder with TM^z plane wave incidence.

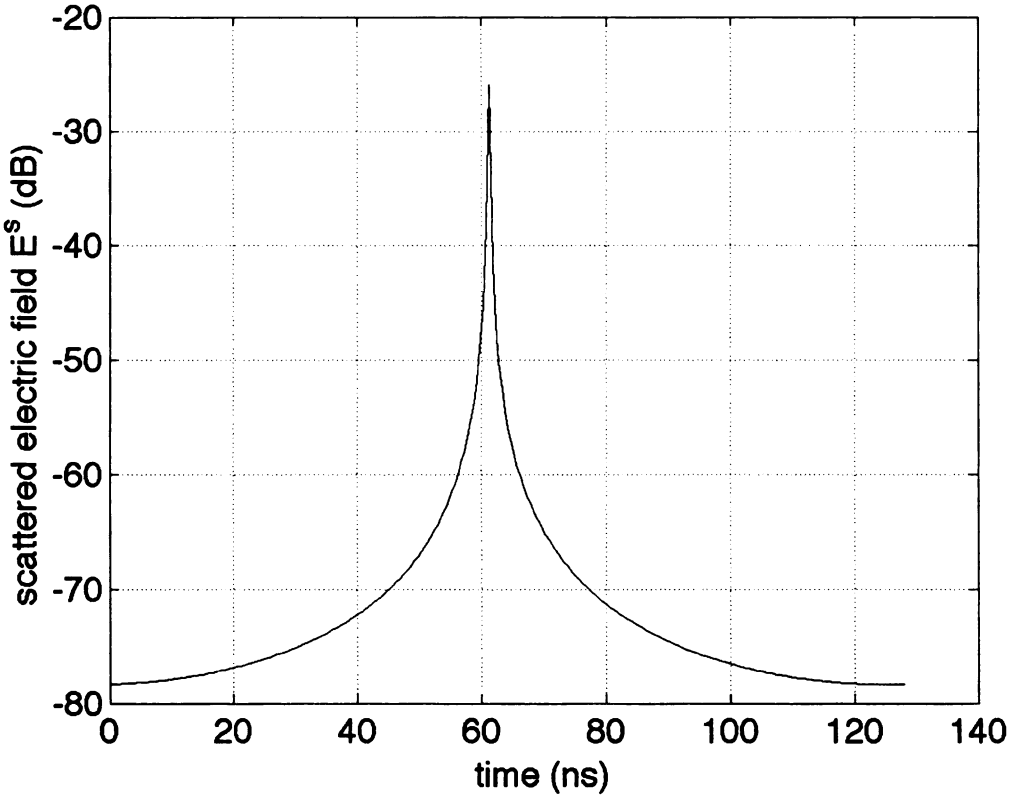

Figure 3.6. Range profile of a 1.96 inch radius cylinder with TM^z plane wave incidence, showing the downrange time delay of the front face of the cylinder.

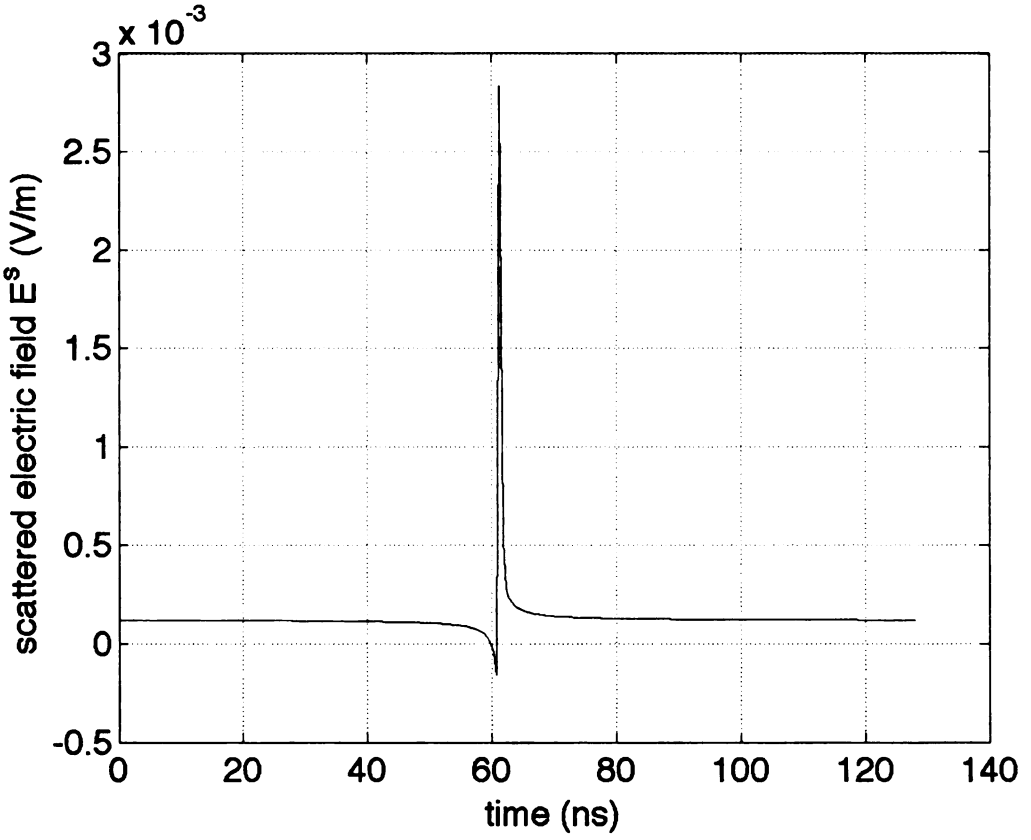

Figure 3.7. Real value of the range profile of a 1.96 inch radius cylinder with TM^z plane wave incidence.

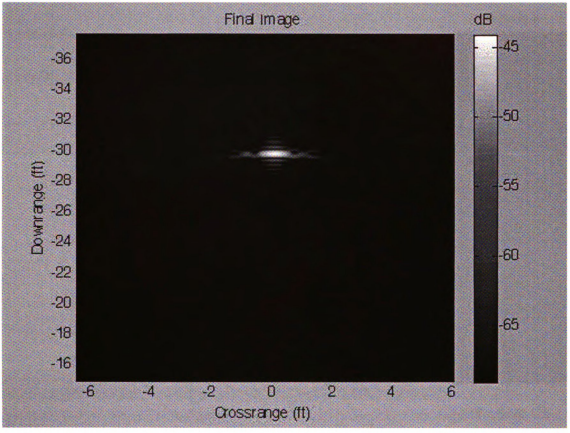

Figure 3.8. SAR image of the 2D cylinder model with a radius of $a = 3$ inches, located 30 ft downrange.

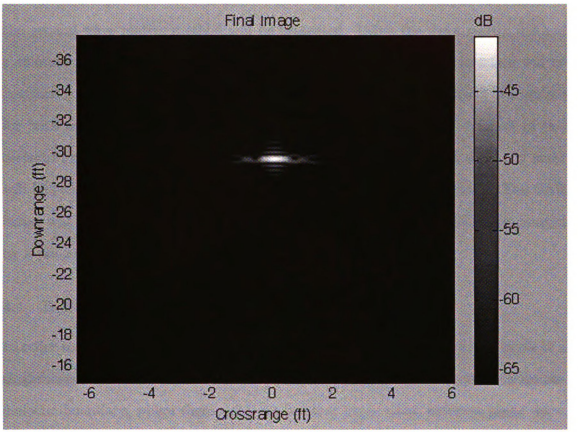

Figure 3.9. SAR image of the 2D cylinder model with a radius of $a = 6$ inches, located 30 ft downrange.

CHAPTER 4

A DIELECTRIC SHEET MODEL USING WAVE MATRICES

A dielectric sheet model of a lossy-dielectric slab will be developed in this chapter using wave matrix theory from [63]. In order to develop this model, reflection and transmission of plane waves at a dielectric boundary will first be discussed. From this the general wave matrix method will be presented. Using the wave matrix method a solution to the reflection and transmission of an air-dielectric-air interface will be developed. With this model, simulated 2 GHz to 4 GHz range profiles will be acquired for both normal and oblique incidences. Finally, a simulated SAR data set of this dielectric model will be acquired. A SAR image of the simulated dielectric sheet will be created using the SAR imaging algorithm developed in Chapter 2. This SAR image will provide reference data for a lossy-dielectric slab of equal thickness imaged by a rail SAR imaging system.

4.1 Reflection and transmission at a dielectric boundary

In order to properly examine reflection and transmission coefficients an example of a single layer air-dielectric problem will be explored. In this problem there is an air-dielecric boundary, where there exists an incident plane wave, reflected plane wave, and transmitted plane wave as shown in Figure 4.1. It is important to note that the radar system that will be used later in this dissertation for measured results uses vertically polarized antennas. For this reason it was decided that all solutions in this chapter will be for TM^z plane waves. For convenience the model will be developed for normal incidence and then modified for oblique incidence.

4.1.1 Incident, reflected and transmitted electric fields

For a TM^z incident plane wave traveling along the $\hat{x}$ direction the incident electric field is

$$\vec{E}^i = \hat{z}E_O e^{-jk_O x}, \tag{4.1}$$

where E_O is the magnitude of the incident electric field and the free space wave number is

$$k_O = \omega\sqrt{\mu_O \epsilon_O}. \tag{4.2}$$

In this, $\omega = 2\pi f$, f is the frequency of interest, μ_O is the free-space permeability and ϵ_O is the free-space permittivity. For a TM^z plane wave reflected from the interface, the electric field is

$$\vec{E}^r = \hat{z}E_r e^{jk_O x}, \tag{4.3}$$

where E_r is the magnitude of the reflected electric field. For a TM^z plane wave transmitted into the dielectric, the electric field is

$$\vec{E}^T = \hat{z}E_T e^{-jkx}, \tag{4.4}$$

where E_T is the magnitude of the transmitted electric field. The wave number inside of the dielectric is

$$k = \omega\sqrt{\mu_O\left(\epsilon_O\epsilon_r + \frac{\sigma}{j\omega}\right)}, \tag{4.5}$$

where ϵ_r is the relative complex permittivity and σ is the dielectric conductivity in units of mho/m which accounts for the loss of the dielectric material.

4.1.2 Incident, reflected and transmitted magnetic fields

The time harmonic version of Faraday's law from Maxwell's equations relating the electric field to the magnetic field is written as

$$\nabla \times \vec{E} = -j\omega\mu_O \vec{H}. \tag{4.6}$$

Applying Equation 4.6 to the incident electric field Equation 4.1 results in the incident magnetic field

$$\vec{H}^i = -\hat{y}\frac{k_O}{\omega\mu_O} E_O e^{-jk_O x}. \tag{4.7}$$

Substituting $k_O = \omega\sqrt{\mu_O \epsilon_O}$ into the above equation results in

$$\vec{H}^i = -\hat{y}\frac{\omega\sqrt{\mu_O \epsilon_O}}{\omega\mu_O} E_O e^{-jk_O x}. \tag{4.8}$$

Letting ω cancel out and simplifying further the incident magnetic field is

$$\vec{H}^i = -\hat{y}\sqrt{\frac{\epsilon_O}{\mu_O}} E_O e^{-jk_O x}. \tag{4.9}$$

At this point is is important to note that the impedance of free-space is defined as

$$Z_O = \sqrt{\frac{\mu_O}{\epsilon_O}} \tag{4.10}$$

and the admittance of free-space is the reciprocal of the impedance

$$Y_O = \frac{1}{Z_O} = \sqrt{\frac{\epsilon_O}{\mu_O}}. \tag{4.11}$$

Thus, applying Equation 4.11 to Equation 4.9 results in the equation for the incident magnetic field

$$\vec{H}^i = -\hat{y} Y_O E_O e^{-jk_O x}. \tag{4.12}$$

Applying Faraday's law Equation 4.6 to the reflected electric field Equation 4.3 results in the reflected magnetic field

$$\vec{H}^r = \hat{y}\frac{k_o}{\omega\mu_o}E_r e^{jk_o x}. \tag{4.13}$$

Substituting the free-space wave number equation $k_o = \omega\sqrt{\mu_o\epsilon_o}$ into the above equation results in

$$\vec{H}^r = \hat{y}\frac{\omega\sqrt{\mu_o\epsilon_o}}{\omega\mu_o}E_r e^{jk_o x}. \tag{4.14}$$

Letting ω cancel out and simplifying further

$$\vec{H}^r = \hat{y}\sqrt{\frac{\epsilon_o}{\mu_o}}E_r e^{jk_o x}. \tag{4.15}$$

Applying the free-space admittance Equation 4.11 to the above results in the equation for the reflected magnetic field

$$\vec{H}^r = \hat{y}Y_o E_r e^{jk_o x}. \tag{4.16}$$

Applying Faraday's law Equation 4.6 to the transmitted electric field Equation 4.4 results in the transmitted magnetic field into the dielectric medium

$$\vec{H}^T = -\hat{y}\frac{k}{\omega\mu_o}E_T e^{-jkx}. \tag{4.17}$$

Substituting the dielectric wave number k Equation 4.5 into the above results in the transmitted field within the medium

$$\vec{H}^T = -\hat{y}\frac{\omega\sqrt{\mu_o\left(\epsilon_o\epsilon_r + \frac{\sigma}{j\omega}\right)}}{\omega\mu_o}E_T e^{-jkx}. \tag{4.18}$$

Letting ω cancel out and simplifying further

$$\vec{H}^T = -\hat{y}\sqrt{\frac{\left(\epsilon_o\epsilon_r + \frac{\sigma}{j\omega}\right)}{\mu_o}}E_T e^{-jkx}. \tag{4.19}$$

At this point is is important to note that the TEM wave impedance of the dielectric is defined as

$$Z = \sqrt{\frac{\mu_o}{\left(\epsilon_o\epsilon_r + \frac{\sigma}{j\omega}\right)}} \tag{4.20}$$

and the admittance of the dielectric is the reciprocal of the impedance

$$Y = \frac{1}{Z} = \sqrt{\frac{\left(\epsilon_o\epsilon_r + \frac{\sigma}{j\omega}\right)}{\mu_o}}. \tag{4.21}$$

Applying the dielectric admittance Equation 4.21 to the Equation 4.19 results in the equation for the transmitted magnetic field

$$\vec{H}^T = -\hat{y}Y E_T e^{-jkx}. \tag{4.22}$$

4.1.3 Boundary conditions at an air-dielectric interface

Applying the boundary condition at the discontinuity interface in Figure 4.1 at the plane $x = 0$ results in the total electric field equation

$$\left[\vec{E}^i + \vec{E}^r\right]_{x=0} = \left[\vec{E}^T\right]_{x=0} \tag{4.23}$$

and the total magnetic field equation

$$\left[\vec{H}^i + \vec{H}^r\right]_{x=0} = \left[\vec{H}^T\right]_{x=0}. \tag{4.24}$$

Substituting the incident, reflected and transmitted electric field Equations 4.1,

4.3 and 4.4 into the above Equation 4.23 results in

$$\left[\hat{z}E_o e^{-jk_o x} + \hat{z}E_r e^{jk_o x}\right]_{x=0} = \left[\hat{z}E_T e^{-jkx}\right]_{x=0}. \tag{4.25}$$

Substituting $x = 0$ and letting $\hat{z}$ drop out results in the boundary equation

$$E_o + E_r = E_T. \tag{4.26}$$

Considering the total magnetic field Equation 4.24 and substituting in the incident, reflected and transmitted magnetic field Equations 4.12, 4.16 and 4.22 results in the following

$$\left[-\hat{y}Y_o E_o e^{-jk_o x} + \hat{y}Y_o E_r e^{jk_o x}\right]_{x=0} = \left[-\hat{y}Y E_T e^{-jkx}\right]_{x=0}. \tag{4.27}$$

Substituting $x = 0$, letting $\hat{y}$ and -1 drop out results in

$$Y_o E_o - Y_o E_r = Y E_T. \tag{4.28}$$

The dielectric admittance Y in Equation 4.21 gives

$$Y = \sqrt{\frac{\left(\epsilon_o \epsilon_r + \frac{\sigma}{j\omega}\right)}{\mu_o}} = \sqrt{\frac{\epsilon_o}{\mu_o}}\sqrt{\epsilon_r + \frac{\sigma}{j\omega\epsilon_o}}. \tag{4.29}$$

Substituting the free-space admittance Y_o Equation 4.11 into the above results in a slightly different form for the free-space admittance equation

$$Y = Y_o\sqrt{\epsilon_r + \frac{\sigma}{j\omega\epsilon_o}}. \tag{4.30}$$

Applying the above equation to Equation 4.28 results in

$$Y_O E_O - Y_O E_r = Y_O \sqrt{\epsilon_r + \frac{\sigma}{j\omega\epsilon_O}} E_T. \tag{4.31}$$

Canceling out the Y_O terms and collecting terms on the left results in the boundary equation

$$E_O - E_r - \sqrt{\epsilon_r + \frac{\sigma}{j\omega\epsilon_O}} E_T = 0. \tag{4.32}$$

4.1.4 Transmission and reflection coefficients

By definition (as was indicated in [63]) the reflection coefficient R_i is the ratio of reflected to incident electric field amplitudes at the interface plane $x = 0$, shown in Figure 4.1,

$$R_i = \frac{E_r}{E_O}. \tag{4.33}$$

In the case of an air-dielectric boundary, R_1 is the reflection coefficient for a wave incident from region 1 onto region 2 (as shown in Figure 4.1) which provides the following relation

$$E_r = R_1 E_O. \tag{4.34}$$

By definition (as was indicated in [63]), the transmission coefficient T_{ij} is the ratio of transmitted to incident electric field amplitudes at the interface plane $x = 0$, shown in Figure 4.1,

$$T_{ij} = \frac{E_T}{E_O}. \tag{4.35}$$

In the case of an air-dielecric boundary, T_{12} is the transmission from region 1 to region 2 (as shown in Figure 4.1) which provides the following relation

$$T_{12} E_O = E_T. \tag{4.36}$$

Substituting the reflection coefficient Equation 4.34 and the transmission coefficient Equation 4.36 into the boundary Equation 4.26 results in

$$E_o + R_1 E_o = T_{12} E_o.$$

Dividing both sides by E_o results in the equation relating T_{12} and R_1

$$1 + R_1 = T_{12}. \tag{4.37}$$

Substituting the reflection coefficient Equation 4.34 and the transmission coefficient Equation 4.36 into the boundary Equation 4.32 results in

$$E_o - R_1 E_o - \sqrt{\epsilon_r + \frac{\sigma}{j\omega\epsilon_o}} T_{12} E_o = 0.$$

Again dividing both sides by E_o results in a second equation relating T_{12} and R_1:

$$1 - R_1 = \sqrt{\epsilon_r + \frac{\sigma}{j\omega\epsilon_o}} T_{12}. \tag{4.38}$$

Equations 4.37 and 4.38 are a set of two equations and two unknowns. Solving these equations for the reflection coefficient R_1 results in

$$R_1 = \frac{1 - \sqrt{\epsilon_r + \frac{\sigma}{j\omega\epsilon_o}}}{1 + \sqrt{\epsilon_r + \frac{\sigma}{j\omega\epsilon_o}}} \tag{4.39}$$

and solving Equations 4.37 and 4.38 for the transmission coefficient T_{12} results in

$$T_{12} = \frac{2}{1 + \sqrt{\epsilon_r + \frac{\sigma}{j\omega\epsilon_o}}}. \tag{4.40}$$

The reflection coefficient Equation 4.39 can be written in terms of dielectric ad-

mittances in each medium

$$R_1 = \frac{1-\sqrt{\epsilon_r + \frac{\sigma}{j\omega\epsilon_o}}}{1+\sqrt{\epsilon_r + \frac{\sigma}{j\omega\epsilon_o}}} = \frac{1-\sqrt{\epsilon_r + \frac{\sigma}{j\omega\epsilon_o}}}{1+\sqrt{\epsilon_r + \frac{\sigma}{j\omega\epsilon_o}}} \cdot \frac{Y_o}{Y_o} = \frac{Y_o - Y_o\sqrt{\epsilon_r + \frac{\sigma}{j\omega\epsilon_o}}}{Y_o + Y_o\sqrt{\epsilon_r + \frac{\sigma}{j\omega\epsilon_o}}}.$$

Substituting the dielectric admittance Equation 4.30 into the above results in the reflection coefficient R_1 in terms of dielectric admittances

$$R_1 = \frac{Y_o - Y}{Y_o + Y}. \tag{4.41}$$

The reflection coefficient Equation 4.41 can also be written in terms of dielectric impedances in each medium

$$R_1 = \frac{Y_o - Y}{Y_o + Y} = \frac{\frac{1}{Z_o} - \frac{1}{Z}}{\frac{1}{Z_o} + \frac{1}{Z}} \cdot \frac{Z_o}{Z_o} = \frac{\frac{Z_o}{Z_o} - \frac{Z_o}{Z}}{\frac{Z_o}{Z_o} + \frac{Z_o}{Z}} = \frac{1 - \frac{Z_o}{Z}}{1 + \frac{Z_o}{Z}} \cdot \frac{Z}{Z},$$

which results in a simplified reflection coefficient R_1 in terms of dielectric impedances

$$R_1 = \frac{Z - Z_o}{Z + Z_o}. \tag{4.42}$$

The transmission coefficient Equation 4.40 can be written in terms of dielectric admittances in each medium

$$T_{12} = \frac{2}{1+\sqrt{\epsilon_r + \frac{\sigma}{j\omega\epsilon_o}}} = \frac{2}{1+\sqrt{\epsilon_r + \frac{\sigma}{j\omega\epsilon_o}}} \cdot \frac{Y_o}{Y_o} = \frac{2Y_o}{Y_o + Y_o\sqrt{\epsilon_r + \frac{\sigma}{j\omega\epsilon_o}}}.$$

Substituting the dielectric admittance Equation 4.30 into the above results in

$$T_{12} = \frac{2Y_o}{Y_o + Y}. \tag{4.43}$$

The transmission coefficient Equation 4.43 can also be written in terms of dielectric

impedances in each medium

$$T_{12} = \frac{2Y_O}{Y_O + Y} = \frac{\frac{2}{Z_O}}{\frac{1}{Z_O} + \frac{1}{Z}} \cdot \frac{Z_O}{Z_O} = \frac{2}{1 + \frac{Z_O}{Z}} \cdot \frac{Z}{Z},$$

which results in a simplified transmission coefficient T_{12} in terms of dielectric impedances

$$T_{12} = \frac{2Z}{Z + Z_O}. \tag{4.44}$$

If the geometry shown in Figure 4.1 were reversed and the incident electric field wave was traveling from region 2 to region 1 then the reflection coefficient would be found by simply swapping the admittance terms Y and Y_O in Equation 4.41 thus giving us

$$R_2 = \frac{Y - Y_O}{Y + Y_O}. \tag{4.45}$$

In a similar fashion, the admittance terms Y and Y_O in Equation 4.43 can be swapped to find the transmission coefficient for a wave traveling from region 2 to region 1

$$T_{21} = \frac{2Y}{Y + Y_O}. \tag{4.46}$$

4.2 Wave matrices

Looking again at the air-dielectric boundary problem solved in Section 4.1 and shown in Figure 4.1, let a TM^z plane wave of amplitude c_1 be incident from region 1 to region 2. At the same time, another TM^z plane wave is incident from region 2 to region 1 with an amplitude of b_2. This is a different approach for the same problem solved in Section 4.1. The geometry for this approach is shown in Figure 4.2.

The total reflected field in region 1 has the value b_1 and is due to the transmitted field from region 2 to region 1 represented by $T_{21}b_2$. Coefficient b_1 is also due to the incident plane wave in region 1 of amplitude c_1 reflecting off of the boundary at

$x = 0$ which is represented by $R_1 c_1$. The resulting reflected field amplitude equation becomes

$$b_1 = R_1 c_1 + T_{21} b_2. \tag{4.47}$$

The total reflected field in region 2 has the value c_2 and is due to the transmitted field from region 1 to region 2 represented by $T_{12} c_1$. Coefficient c_2 is also due to the incident plane wave in region 2 of amplitude b_1 reflecting off of the boundary at $x = 0$ which is represented by $R_2 b_2$. The resulting reflected field amplitude equation becomes

$$c_2 = R_2 b_2 + T_{21} b_2. \tag{4.48}$$

Rearranging the variables in Equations 4.48 and 4.47 results in

$$c_1 = \frac{c_2}{T_{12}} - \frac{R_2 b_2}{T_{12}} \tag{4.49}$$

and

$$b_1 = \left(T_{21} - \frac{R_1 R_2}{T_{12}}\right) b_2 + \frac{R_1}{T_{12}} c_2. \tag{4.50}$$

Equations 4.49 and 4.50 can be re-written in matrix form

$$\begin{bmatrix} c_1 \\ b_1 \end{bmatrix} = \frac{1}{T_{12}} \begin{bmatrix} 1 & -R_2 \\ R_1 & T_{12}T_{21} - R_1 R_2 \end{bmatrix} \begin{bmatrix} c_2 \\ b_2 \end{bmatrix} = \begin{bmatrix} A_{11} & A_{12} \\ A_{21} & A_{22} \end{bmatrix} \begin{bmatrix} c_2 \\ b_2 \end{bmatrix}, \tag{4.51}$$

where the values of matrix $[A]$ are simply

$$A_{11} = \frac{1}{T_{12}}, \tag{4.52}$$

$$A_{12} = \frac{-R_2}{T_{12}}, \tag{4.53}$$

$$A_{21} = \frac{R_1}{T_{12}} \tag{4.54}$$

and

$$A_{22} = \frac{T_{12}T_{21} - R_1R_2}{T_{12}}. \tag{4.55}$$

The reflection coefficient R_1 from region 1 to region 2 is the negative of the reflection R_2 coefficient from region 2 to 1 as shown by Equations 4.41 and 4.45, thus

$$R_1 = \frac{Y_o - Y}{Y_o + Y} = -1 \cdot R_2 = -1 \cdot \frac{Y - Y_o}{Y + Y_o} = \frac{Y_o - Y}{Y_o + Y}.$$

From this R_1 is related to R_2 where

$$R_1 = -R_2. \tag{4.56}$$

Looking at the A_{12} Equation 4.53 and applying the above relation results in

$$A_{12} = \frac{-R_2}{T_{12}} = \frac{R_1}{T_{12}}. \tag{4.57}$$

Similar to the T_{12} Equation 4.37 for transmission from region 1 to region 2, the opposite is true when transmission from region 2 to 1 occurs, where the equation for T_{21} becomes

$$T_{21} = 1 + R_2. \tag{4.58}$$

Applying the above result Equation 4.37 and Equation 4.56 to the A_{22} Equation 4.55 results in the simplification

$$A_{22} = \frac{T_{12}T_{21} - R_1R_2}{T_{12}} = \frac{(1 + R_1)(1 + R_2) - R_1R_2}{T_{12}} = \frac{(1 + R_1)(1 - R_1) + R_1^2}{T_{12}},$$

that is,

$$A_{22} = \frac{1}{T_{12}}. \tag{4.59}$$

Placing A_{ij} Equations 4.52, 4.57, 4.54, and 4.59 back into the matrix $[A]$ results in

$$\begin{bmatrix} c_1 \\ b_1 \end{bmatrix} = \frac{1}{T_{12}} \begin{bmatrix} 1 & R_1 \\ R_1 & 1 \end{bmatrix} \begin{bmatrix} c_2 \\ b_2 \end{bmatrix}. \tag{4.60}$$

Looking at the geometry in Figure 4.2, an incident plane wave traveling from region 1 to region 2 has an amplitude of c_1 at the interface $x = 0$. Similarly, a plane wave being reflected from region 2 into region 1, or due to the transmission from region 2 to region 1, has an amplitude of b_1 at the interface $x = 0$. At some location inside of region 2 at $x = x_1$ the plane wave amplitudes of the incident and reflected waves are phase shifted, where c_2 and b_2 represent the phase shifted amplitudes of the incident and reflected waves shifted to a new terminal plane at $x = x_1$

$$c_2 = c_1 e^{-jkx_1}$$

and

$$b_2 = b_1 e^{jkx_1}.$$

Solving the above for c_1 and b_1 yields the terminal shifted wave amplitudes

$$c_1 = c_2 e^{jkx_1} \tag{4.61}$$

and

$$b_1 = b_2 e^{-jkx_1}. \tag{4.62}$$

By definition [63] the electrical length is the phase difference between a wave traveling from one location to another in a dielectric medium (free space or otherwise). Electrical length θ is linear in this case (however there are other cases where it is not, and these will not be covered here) and is defined as the wave number times the

linear distance between the two locations in the dielectric medium. For the case of normal incidence according to the geometry in Figure 4.2, the electrical length is

$$\theta = kx. \tag{4.63}$$

Substituting the electrical length $\theta_1 = kx_1$ into the terminal shifted wave amplitude Equations 4.61 and 4.62 results in

$$c_1 = c_2 e^{j\theta 1} \tag{4.64}$$

and

$$b_1 = b_2 e^{-j\theta 1}. \tag{4.65}$$

Placing the above equations in to matrix form results in

$$\begin{bmatrix} c_1 \\ b_1 \end{bmatrix} = \begin{bmatrix} e^{j\theta 1} & 0 \\ 0 & e^{-j\theta 1} \end{bmatrix} \begin{bmatrix} c_2 \\ b_2 \end{bmatrix}. \tag{4.66}$$

The above matrix provides the complex amplitude of the traveling waves incident and reflected at a terminal shifted plane. Such a terminal shifted pair of forward and reflected wave amplitudes could be used to be incident on another boundary located at $x = x_1$. This phase shifted terminal plane concept is shown in Figure 4.3, and can be used to add a second dielectric layer (or many more layers) to the two region dielectric boundary problem shown in Figure 4.2 by multiplying the matrix Equation 4.60 and the matrix Equation 4.66 resulting in the following matrix

$$\begin{bmatrix} c_1 \\ b_1 \end{bmatrix} = \frac{1}{T_1} \begin{bmatrix} 1 & R_1 \\ R1 & 1 \end{bmatrix} \begin{bmatrix} e^{j\theta 1} & 0 \\ 0 & e^{-j\theta 1} \end{bmatrix} \begin{bmatrix} c_2 \\ b_2 \end{bmatrix}. \tag{4.67}$$

Notice the change in notation, where the transmission coefficient from region 1 to region 2 has become $T_{12} = T_1$. From now on this notation will be used for the transmission coefficients to more conveniently show the general case for the wave matrix solution of multiple dielectric layers.

Multiplying out the above matrix Equation 4.67 results in

$$\begin{bmatrix} c_1 \\ b_1 \end{bmatrix} = \frac{1}{T_1} \begin{bmatrix} e^{j\theta_1} & R_1 e^{-j\theta_1} \\ R_1 e^{j\theta_1} & e^{-j\theta_1} \end{bmatrix} \begin{bmatrix} c_2 \\ b_2 \end{bmatrix}, \tag{4.68}$$

which is the solution to the incident and reflected wave amplitudes at some depth in region 2. Using this concept of phase shifted terminal planes it is now possible to provide a general wave matrix solution for an n-layered material composed of n number of dielectric layers of a finite thickness. Where the finite thickness is represented by the electrical length θ_i. The general wave matrix solution is

$$\begin{bmatrix} c_1 \\ b_1 \end{bmatrix} = \prod_{i=1}^{n} \frac{1}{T_i} \begin{bmatrix} e^{j\theta_i} & R_i e^{-j\theta_i} \\ R_i e^{j\theta_i} & e^{-j\theta_i} \end{bmatrix} \begin{bmatrix} c_{n+1} \\ b_{n+1} \end{bmatrix}. \tag{4.69}$$

4.3 A dielectric sheet model based on wave matrices

In this section a model of a lossy-dielectric slab will be developed. Using the wave matrix theory developed in Section 4.2 an air-dielectric-air layered planar dielectric solution is developed. This solution is fed a set of frequency dependent dielectric property data from a set of lossy-dielectric model data from [64] so that the dielectric model has practical lossy-dielectric slab properties. This lossy-dielectric slab model is essential for analysis of the through-dielectric radar imaging problem. In the next chapter this model will be combined with the cylinder model from Chapter 3 to produce simulated SAR imagery of a cylinder behind a lossy-dielectric slab. The eventual simulation of a cylinder behind a lossy-dielectric slab will provide essential

information for developing radar system specifications and understanding imaging limitations.

In order to use the wave matrix theory developed in Section 4.2, the incident field and transmitted field impedances must be found for oblique incidence on a three layered problem, where the dielectric layers are air-dielectric-air as shown in Figure 4.4. Using these impedances, it is a matter of substitution to apply the wave matrix method to find the solution to the air-dielecric-air problem.

Looking at the geometry for an oblique incidence in Figure 4.4, the intrinsic impedance of the dielectric layer is η, and the intrinsic impedance of free space is η_o, where

$$\eta_o = \sqrt{\frac{\mu_o}{\epsilon_o}} \tag{4.70}$$

and

$$\eta = \sqrt{\frac{\mu}{\epsilon_o \epsilon r + \frac{\sigma}{j\omega}}} = \frac{\eta_o}{\sqrt{\epsilon r + \frac{\sigma}{j\omega\epsilon_o}}}. \tag{4.71}$$

It is important to note that at normal incidence the dielectric impedance as defined in Equation 4.20 equals the intrinsic impedance of the dielectric layer η. Also at normal incidence the impedance of free space as defined in Equation 4.10 equals the intrinsic impedance of free space η_o. However, in this section the air-dielecric-air wave matrix problem will be solved for an oblique incidence where this is not the case. An oblique incidence causes changes in the effective dielectric impedance with respect to the plane wave direction.

Looking at Figure 4.4, a TM^z plane wave is incident on the dielectric layer at an incident angle of ϕ_i and represented by the incident electric field Equation 4.1 (rewritten here for convenience)

$$\vec{E}^i = \hat{z} E_o e^{-jk_o x}.$$

Since the incident plane wave is at an angle ϕ_i with respect to the $\hat{x}$ direction of propagation, the dielectric can be thought of as rotated by angle ϕ_i with respect to the xy plane. This is a rotated coordinate system, where the incident plane wave in the xy axis is rotated onto the dielectric axis $x'y'$ using the standard coordinate rotation matrix [65], where the xyz coordinates as a function of $x'y'z'$ are

$$\begin{aligned} z &= z', \\ x &= x' \cos\phi_i - y' \sin\phi_i, \\ y &= x' \sin\phi_i + y' \cos\phi_i. \end{aligned} \tag{4.72}$$

Substituting Equation 4.72 into the incident electric field Equation 4.1 results in

$$\overrightarrow{E}^i = \hat{z'} E_o e^{-jk_o(x' \cos\phi_i - y' \sin\phi_i)}. \tag{4.73}$$

Applying the time harmonic version of Faraday's law from Maxwell's equations, Equation 4.6, with respect to the rotated coordinate axis $x'y'z'$ to the above Equation 4.73 results in the incident magnetic field

$$\begin{aligned} \overrightarrow{H^i} = -\hat{x'} \sqrt{\frac{\epsilon_o}{\mu_o}} \sin\phi_i E_o e^{-jk_o(x' \cos\phi_i - y' \sin\phi_i)} \\ - \hat{y'} \sqrt{\frac{\epsilon_o}{\mu_o}} \cos\phi_i E_o e^{-jk_o(x' \cos\phi_i - y' \sin\phi_i)}. \end{aligned} \tag{4.74}$$

And from Equation 4.70

$$\frac{1}{\eta_o} = \sqrt{\frac{\epsilon_o}{\mu_o}}.$$

Substituting this into the above Equation 4.74 results in the incident magnetic field

equation in coordinate rotated space

$$\overrightarrow{H^i} = -\hat{x'}\frac{1}{\eta_o}\sin\phi_i E_o e^{-jk_o(x'\cos\phi_i - y'\sin\phi_i)} - \hat{y'}\frac{1}{\eta_o}\cos\phi_i E_o e^{-jk_o(x'\cos\phi_i - y'\sin\phi_i)}. \quad (4.75)$$

Dividing the incident electric field in the $\hat{z'}$ direction (Equation 4.73) by the incident magnetic field (Equation 4.75) in the $\hat{y'}$ direction results in the impedance of the incident wave traveling in the rotated $\hat{x'}$ direction (normal to the surface of the dielectric)

$$Z_1 = \frac{-E^i_{z'}}{H^i_{y'}} = \eta_o \sec\phi_i. \quad (4.76)$$

Due to Snell's law of refraction, the direction of propagation for the transmitted electromagnetic fields is refracted towards the normal vector $\hat{n}$ in Figure 4.4 by an angle ϕ_r inside of the dielectric region [61], [63]. For this reason the transmitted electric field must be represented in terms of ϕ_r. Applying the coordinate rotation matrix Equation 4.72 with respect to ϕ_r to the transmitted field Equation 4.4 results in

$$\overrightarrow{E^T} = \hat{z'}E_T e^{-jk(x'\cos\phi_r - y'\sin\phi_r)}. \quad (4.77)$$

Applying the time harmonic version of Faraday's law from Maxwell's equations, Equation 4.6, with respect to the rotated coordinate axis $x'y'z'$ to the above Equation 4.77 results in the transmitted magnetic field

$$\overrightarrow{H^T} = -\hat{x'}\sqrt{\frac{\epsilon_o\epsilon_r + \frac{\sigma}{j\omega}}{\mu_o}}\sin\phi_r E_T e^{-jk(x'\cos\phi_r - y'\sin\phi_r)} - \hat{y'}\sqrt{\frac{\epsilon_o\epsilon_r + \frac{\sigma}{j\omega}}{\mu_o}}\cos\phi_r E_T e^{-jk(x'\cos\phi_r - y'\sin\phi_r)}. \quad (4.78)$$

From Equation 4.71

$$\frac{1}{\eta} = \sqrt{\frac{\epsilon_o \epsilon_r + \frac{\sigma}{j\omega}}{\mu_o}}.$$

Substituting this into the above Equation 4.78 results in the incident magnetic field equation in coordinate rotated space

$$\overrightarrow{H^T} = -\hat{x'}\frac{1}{\eta}\sin\phi_r E_T e^{-jk(x'\cos\phi_r - y'\sin\phi_r)} - \hat{y'}\frac{1}{\eta}\cos\phi_r E_T e^{-jk(x'\cos\phi_r - y'\sin\phi_r)}. \quad (4.79)$$

Dividing the transmitted electric field in the $\hat{z'}$ direction (Equation 4.77) by the transmitted magnetic field (Equation 4.79) in the $\hat{y'}$ direction results in the impedance of the transmitted wave traveling in the rotated $\hat{x'}$ direction (normal to the surface of the dielectric) inside of the dielectric

$$Z_2 = \frac{-E^T_{z'}}{H^T_{y'}} = \eta \sec\phi_r. \quad (4.80)$$

It is useful to normalize the impedances of the incident and transmitted waves with respect to the impedance of the incident wave in free space. For the incident field in free space the normalized impedance is simply 1, where

$$1 = \frac{Z_1}{Z_1}. \quad (4.81)$$

For the transmitted field in the dielectric the normalized impedance becomes

$$Z = \frac{Z_2}{Z_1} = \frac{\eta \sec\phi_r}{\eta_o \sec\phi_i} = \frac{\frac{\eta_o}{\sqrt{\epsilon_r + \frac{\sigma}{j\omega\epsilon_o}}}\sec\phi_r}{\eta_o \sec\phi_i}.$$

Simplifying the above results in the normalized dielectric impedance with respect to

incidence angle ϕ_i and angle of refraction ϕ_r

$$Z = \frac{\cos\phi_i}{\sqrt{\epsilon_r + \frac{\sigma}{j\omega\epsilon_o}} cos\phi_r}. \tag{4.82}$$

The above equation for normalized impedance is difficult to use in practice because it is a function of both incidence angle ϕ_i and angle of refraction ϕ_r. Snell's law must be applied in this case in order to simplify the equation and make it a function of ϕ_i and the dielectric properties only. The equation for Snell's law [61] relates angle ϕ_i to ϕ_r as follows

$$k_o \sin\phi_i = k \sin\phi_r. \tag{4.83}$$

Solving for the angle of refraction ϕ_r yields

$$\phi_r = \sin^{-1}\left(\frac{\sin\phi_i}{\sqrt{\epsilon_r + \frac{\sigma}{j\omega\epsilon_o}}}\right). \tag{4.84}$$

Apply this result by evaluating the $\cos\phi_r$ term in the denominator of Equation 4.82

$$\cos\phi_r = \cos\left[\sin^{-1}\left(\frac{\sin\phi_i}{\sqrt{\epsilon_r + \frac{\sigma}{j\omega\epsilon_o}}}\right)\right].$$

Applying the trigonometric identity $\cos(\sin^{-1} x) = \sqrt{1-x^2}$ results in

$$\cos\phi_r = \sqrt{1 - \frac{\sin^2\phi_i}{\epsilon_r + \frac{\sigma}{j\omega\epsilon_o}}} = \frac{\sqrt{(\epsilon_r + \frac{\sigma}{j\omega\epsilon_o}) - \sin^2\phi_i}}{\sqrt{\epsilon_r + \frac{\sigma}{j\omega\epsilon_o}}}.$$

Substituting the above result for $\cos\phi_r$ in to Equation 4.82 results in the normalized impedance of the dielectric with a plane wave incident at an angle of ϕ_i

$$Z = \frac{\cos\phi_i}{\sqrt{(\epsilon_r + \frac{\sigma}{j\omega\epsilon_o}) - \sin^2\phi_i}}. \tag{4.85}$$

The normalized impedance reflection coefficient for an incident plane wave traveling from free-space in to the dielectric is

$$R_1 = \frac{Z-1}{Z+1}. \tag{4.86}$$

The normalized impedance reflection coefficient for an incident plane wave traveling from the dielectric to free-space is

$$R_2 = \frac{1-Z}{Z+1}. \tag{4.87}$$

The transmission coefficient for an incident plane wave traveling from free-space in to the dielectric is

$$T_1 = 1 + R_1. \tag{4.88}$$

The transmission coefficient for a plane wave traveling out from inside of the dielectric to free-space is

$$T_2 = 1 + R_2. \tag{4.89}$$

Applying the above reflection and transmission coefficients in Equations 4.86 through 4.89 for the air-dielectric-air problem to the general form of the wave matrix solution Equation 4.69 in Section 4.2 results in the following wave matrix solution:

$$\begin{bmatrix} c_1 \\ b_1 \end{bmatrix} = \frac{1}{T_1 T_2} \begin{bmatrix} e^{j\theta_i} & R_1 e^{-j\theta_i} \\ R_1 e^{j\theta_i} & e^{-j\theta_i} \end{bmatrix} \begin{bmatrix} 1 & R_2 \\ R_2 & 1 \end{bmatrix} \begin{bmatrix} c_3 \\ b_3 \end{bmatrix}, \tag{4.90}$$

where the electrical length for a dielectric with a thickness d for an oblique incidence angle ϕ_i is

$$\theta = k_O d \sqrt{(\epsilon_r + \frac{\sigma}{j\omega\epsilon_O}) - \sin^2 \phi_i}\ . \tag{4.91}$$

Using the wave matrix Equation 4.90, a theoretical radar target can be located on

the opposite side of the dielectric slab by simply solving for c_3 and b_1. In Equation 4.90, b_3 is a function of radar target function Γ where

$$b_3 = \Gamma c_3. \tag{4.92}$$

The use of this technique will be shown in the next chapter, however it is important to mention it here in order to explain why Equation 4.90 is being solved for both c_3 and b_1.

Solving Equation 4.90 for c_3 and b_1 results in the solution to an air-dielecric-air interface for an oblique incidence angle:

$$c_3 = \frac{c_1 T_1 T_2}{e^{j\theta} + R_1 R_2 e^{-j\theta} + \Gamma\left(R_2 e^{j\theta} + R_1 e^{-j\theta}\right)} \tag{4.93}$$

$$b_1 = \frac{c_3}{T_1 T_2}\left[R_1 e^{j\theta} + R_2 e^{-j\theta} + \Gamma\left(R_1 R_2 e^{j\theta} + e^{-j\theta}\right)\right]. \tag{4.94}$$

4.4 Simulated range profiles of the dielectric sheet model

In this section practical lossy-dielectric properties will be fed into the dielectric model developed in Section 4.3. This will result in a theoretical model of a lossy-dielectric slab of finite thickness. Range profiles will then be taken of this dielectric slab model. These simulated range profiles will provide insight into what radar returns are expected from a lossy-dielectric slab standing by itself. Two range profiles will be taken, one at normal incidence and the other at an oblique incidence. The range profile geometry is shown in Figure 4.6. In both cases (normal and oblique incidences), the radar is 20 ft from the surface of the slab.

The simulated range profile data set is calculated by solving Equations 4.92 through 4.94 for b_1. The parameters and specifications used to simulate these range profiles of the dielectric slab are shown in Table 4.1.

The incident plane wave is TM^z and for this reason the wave amplitude coefficient at the dielectric boundary c_1 is

$$c_1 = E_o e^{-jk_o r_1}. \tag{4.95}$$

The received scattered field is simply a plane wave traveling back from the dielectric surface to the radar receiver (the theoretical radar system in this case is assumed to be mono-static), and thus the received scattered field equation is

$$E_s = b_1 e^{-jk_o r_1}. \tag{4.96}$$

The IDFT is taken of E_s, and the resulting time domain range profile is shown. All of these calculations were done using the MATLAB program shown in Appendix F.

The resulting range profile for a normally incident $\phi_i = 0$ plane wave is shown in Figure 4.7. Looking at this result it is clear that the strongest reflection was due to the surface of the dielectric, which is 20 ft downrange from the radar system. It is also interesting to note the second, but barely noticeable, reflection from the back side of the dielectric is shown in Figure 4.7 to be the smaller reflection just to the right of the large surface reflection.

The resulting range profile for an oblique incident $\phi_i = \frac{\pi}{6}$ plane wave is shown in Figure 4.8. The results for this range profile are nearly identical to that of Figure 4.7. Looking at Figure 4.8 it is clear that the strongest reflection was due to the surface of the dielectric, and the second much smaller reflection from the back side of the dielectric.

From the these theoretical range profile results presented, it is clear that the dielectric model is functioning properly for both normal and oblique incident waves. Based on these results it is now possible to simulate a SAR image of the dielectric to

see what a concrete slab might look like when imaged by an 8 foot linear rail SAR imaging system.

4.5 Simulated SAR image of the dielectric slab model

In this section simulated SAR imagery is created of the dielectric sheet model developed in this chapter. This is done by acquiring 48 evenly spaced range profiles across an 8 foot long simulated linear rail placed in front of a lossy-dielectric slab at a range of 20 feet.

The imaging geometry here is somewhat complicated. Looking at Figure 4.9 it is assumed that some unknown radar target is located at a distance d_3 downrange from the rail and exactly at the rail center $L/2$. In the next chapter a cylinder will be placed at this location, for now however, there will be nothing located at this position making the radar target function $\Gamma = 0$. It is important to image the target scene as if there were a target there behind the slab. This is done for comparison purposes. In the next chapter the target scene with a target behind the slab can be compared to the results in this chapter for a target scene without a target behind the slab using the exact same imaging geometry which facilitates the use of coherent background subtraction in the simulated data.

In Figure 4.9 the radar travels down the linear rail of length L, acquiring range profiles at evenly spaced increments located at rail positions $x(n)$. The incident angle ϕ_i is dependent upon the radar position on the rail $x(n)$ and the location of the unknown radar target relative to the rail. From this, the $x(n)$ dependent incident angle function $\phi_i(n)$ is

$$\phi_i(n) = \cos^{-1}\left[\frac{d_3}{\sqrt{\left(\frac{-L}{2} + x(n)\right)^2 + \left(r_1(n) + r_2(n)\right)^2}}\right], \tag{4.97}$$

where $r_1(n)$ is the distance from the radar itself to the dielectric slab

$$r_1(n) = \frac{d_1}{\cos\phi_i(n)}, \tag{4.98}$$

and $r_3(n)$ is the distance from the opposite side of the slab to the unknown target location

$$r_3(n) = \frac{d_3 - d_1 - d}{\cos\phi_i(n)}. \tag{4.99}$$

Where d is the thickness of the dielectric slab and d_1 is the distance from the linear rail to the surface of the dielectric slab. From these equations an $x(n)$ dependent incident field amplitude can be derived

$$c_1(n) = E_o e^{-jk_o r_1(n)}. \tag{4.100}$$

The $x(n)$ dependent scattered field equation is

$$E_s(n) = b_1(n) e^{-jk_o r_1(n)}, \tag{4.101}$$

where $b_1(n)$ is dependent upon the $x(n)$ dependent impedance equation

$$Z(n) = \frac{\cos\phi_i(n)}{\sqrt{(\epsilon_r + \frac{\sigma}{j\omega\epsilon_o}) - \sin^2\phi_i(n)}}. \tag{4.102}$$

The $x(n)$ dependent reflection and transmission coefficients are

$$R_1(n) = \frac{Z(n) - 1}{Z(n) + 1}, \tag{4.103}$$

$$R_2(n) = \frac{1 - Z(n)}{Z(n) + 1}, \tag{4.104}$$

$$T_1(n) = 1 + R_1(n) \tag{4.105}$$

and

$$T_2(n) = 1 + R_2(n). \tag{4.106}$$

Using the above equations, the $x(n)$ dependent amplitude coefficients become

$$c_3(n) = \frac{c_1(n)T_1(n)T_2(n)}{e^{j\theta(n)} + R_1(n)R_2(n)e^{-j\theta(n)} + \Gamma\big(R_2(n)e^{j\theta(n)} + R_1(n)e^{-j\theta(n)}\big)} \tag{4.107}$$

and

$$b_1(n) = \frac{c_3(n)}{T_1(n)T_2(n)}\Big[R_1(n)e^{j\theta(n)} + R_2(n)e^{-j\theta(n)} + \Gamma\Big(R_1(n)R_2(n)e^{j\theta(n)} + e^{-j\theta(n)}\Big)\Big]. \tag{4.108}$$

Where the $x(n)$ dependent electrical length $\theta(n)$ is

$$\theta(n) = k_o d\sqrt{\big(\epsilon_r + \frac{\sigma}{j\omega\epsilon_o}\big) - \sin^2\phi_i(n)}. \tag{4.109}$$

In addition, the radar target function Γ relates $b_3(n)$ to $c_3(n)$ by the equation

$$b_3(n) = \Gamma c_3(n). \tag{4.110}$$

In this case $\Gamma = 0$.

Using the model derived shown in Equations 4.97 through 4.110, a simulated SAR image data set was calculated using the parameters shown in Table 4.2.

The MATLAB program used to calculate the SAR data set is shown in Appendix G. Where, first the MATLAB program in Appendix G was run, after which the data conditioning MATLAB program in Appendix B was run followed by the RMA SAR imaging algorithm MATLAB program in Appendix C.

Figure 4.10 shows the theoretical image of a 4 inch thick lossy-dielectric slab,

Table 4.1. Parameters and specifications used for simulating range profiles of the dielectric slab.

The radar target function $\Gamma = 0$
Permittivity of the slab $\epsilon_r = 5$ based on [64]
Conductivity σ is a function of frequency based on [64] (see Figure 4.5)
Incident angle $\phi_i = 0$ for normal, $\phi_i = \frac{\pi}{6}$ for oblique
Thickness of dielectric $d = 3.94$ inches
Distance from radar to slab face $r_1 = 20$ ft
Chirp frequency: 2 GHz to 4 GHz in 256 steps
Incident wave amplitude $E_o = 1$

Table 4.2. A simulated SAR image of the dielectric slab was calculated using these parameters and specifications.

Permittivity of the slab $\epsilon_r = 5$ based on [64]
Conductivity σ is a function of frequency based on [64] (see Figure 4.5)
Distance from rail to front of dielectric $d_1 = 20$ ft
Distance from rail to unknown target center $d_3 = 30$ ft
The unknown radar target function $\Gamma = 0$
Linear rail length $L = 8$ ft
Number of evenly space range profiles across rail length: 44
Chirp frequency: 2 GHz to 4 GHz in 256 steps
Incident wave amplitude $E_o = 1$

where $d = 4$ inches. It is clear from this image that both the front and back sides of the slab show up in the image. However, the back of the slab is greatly attenuated due to the conductivity loss of the lossy-dielectric slab model.

These results show that it is possible to simulate a SAR image of a dielectric slab. The next logical step is to image both a dielectric slab and a radar target on the opposite side of the slab. This will be done in the next chapter with interesting results to follow.

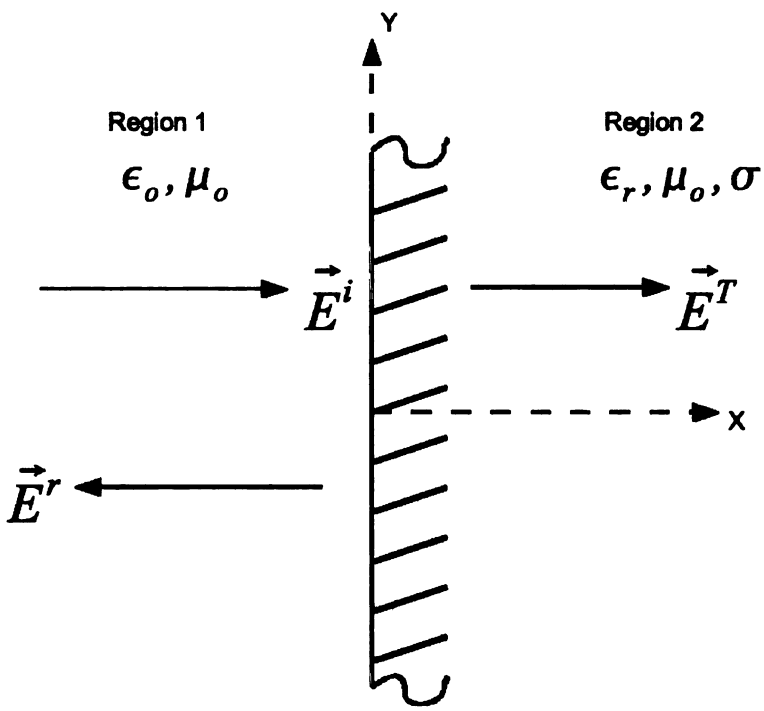

Figure 4.1. Incident, reflected and transmitted fields from an air-dielectric interface.

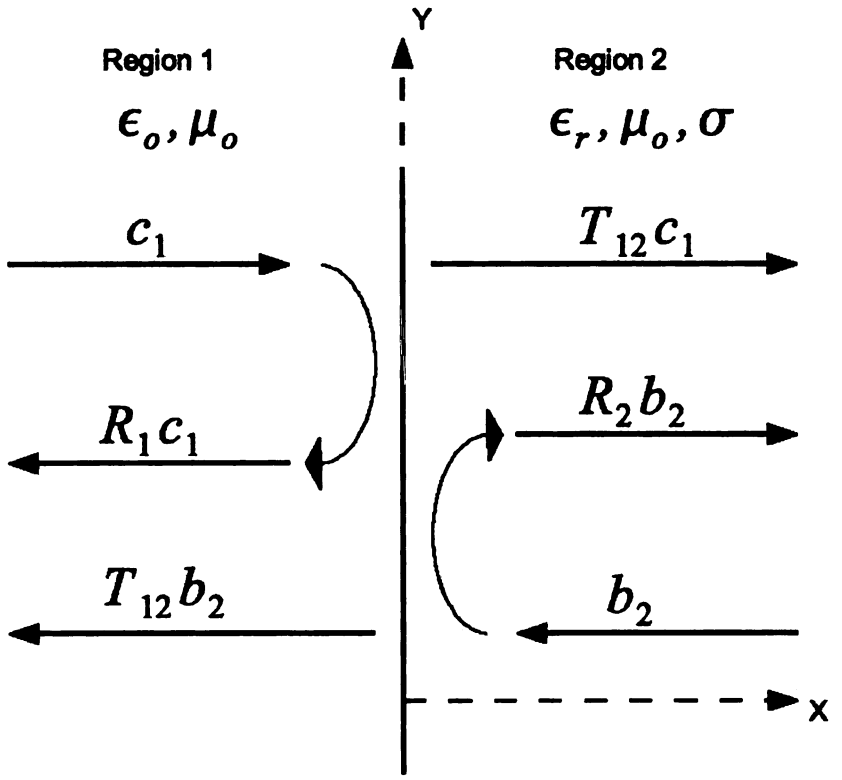

Figure 4.2. Incident, reflected and transmitted fields from an air-dielectric interface represented by wave amplitude coefficients.

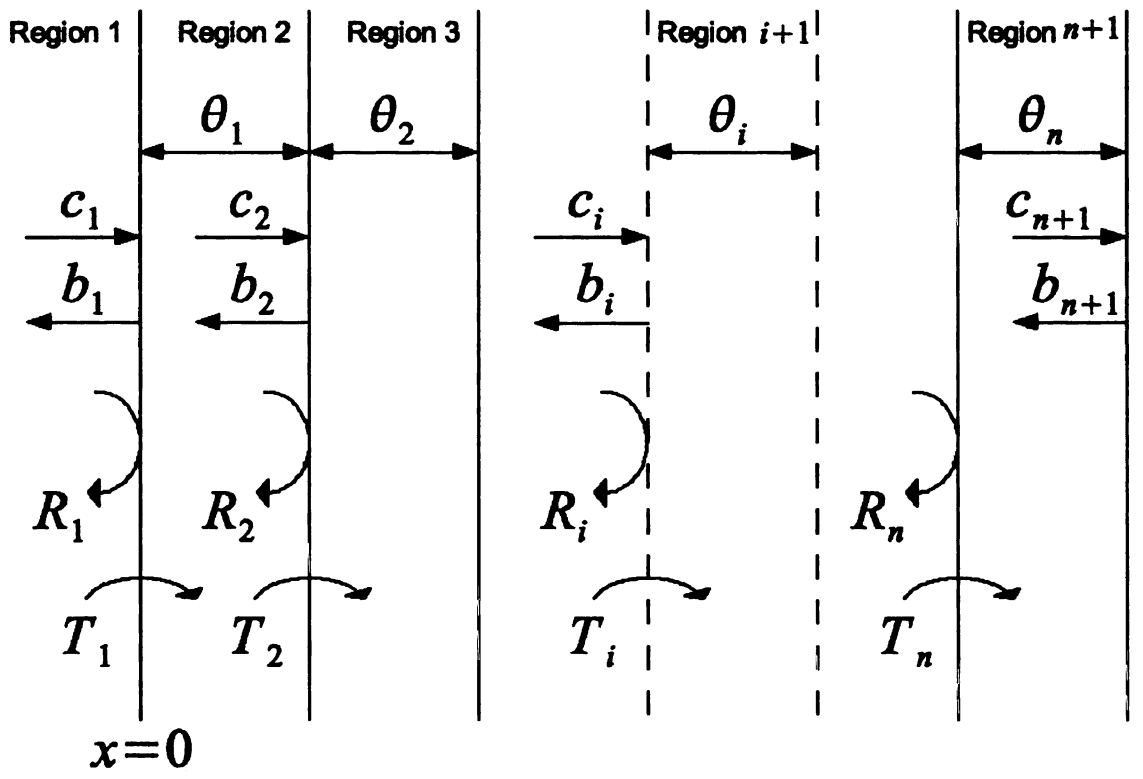

Figure 4.3. The wave matrix geometry for multiple dielectric layers.

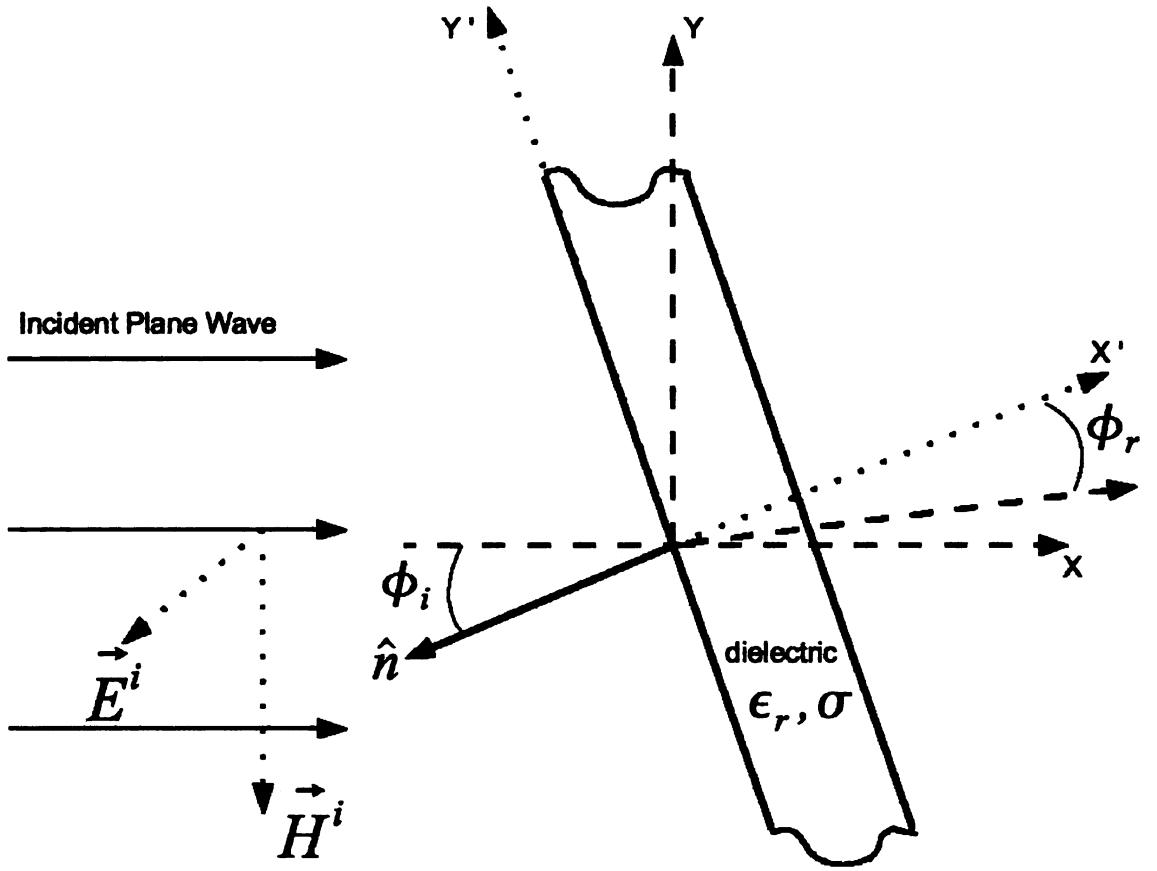

Figure 4.4. The air-dielectric-air geometry for oblique plane wave incidence.

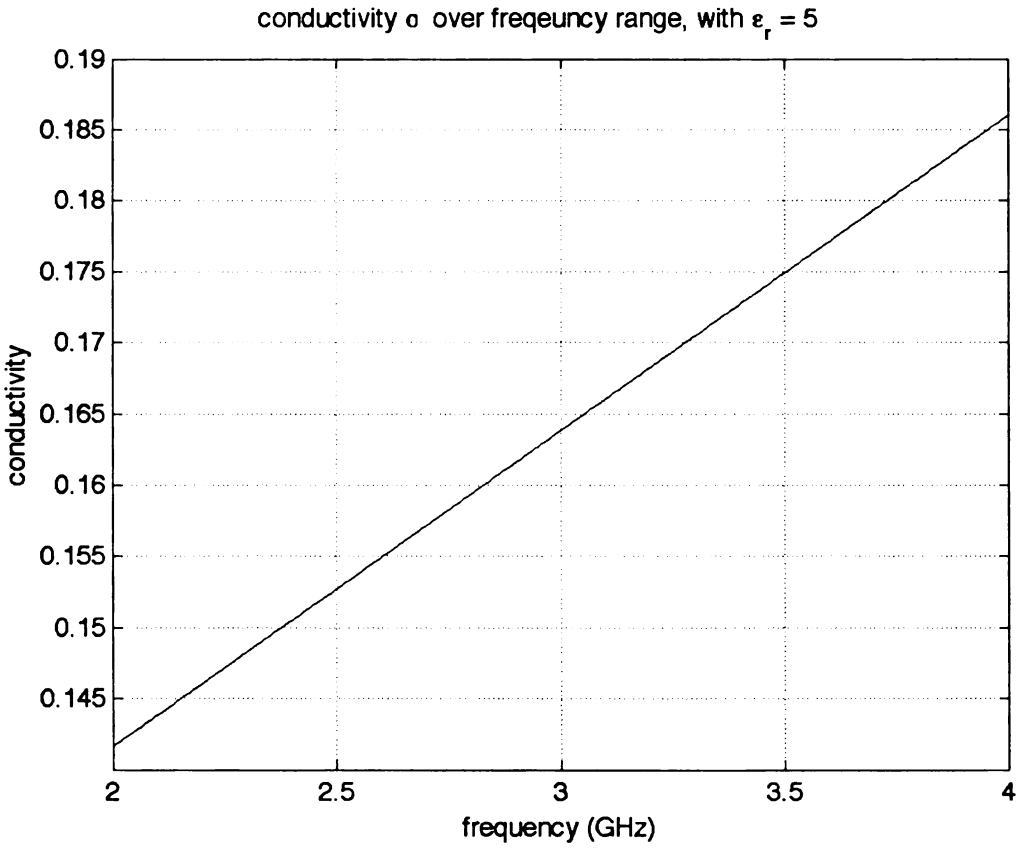

Figure 4.5. Conductivity of the lossy-dielectric slab model, where $\epsilon_r = 5$.

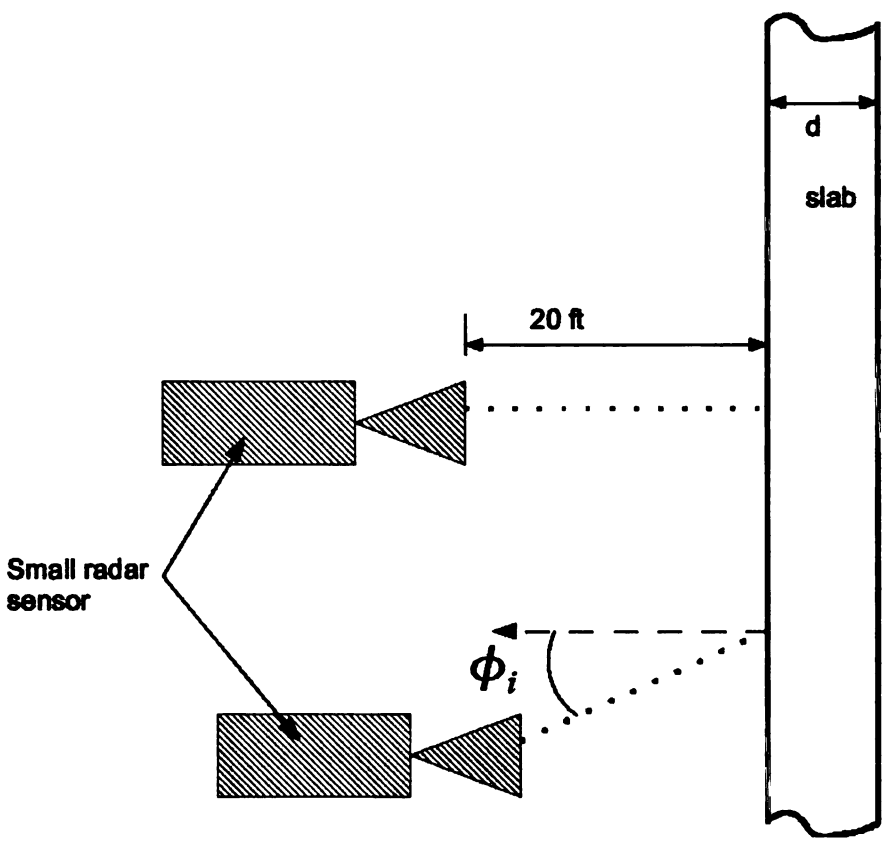

Figure 4.6. Geometry for simulated range profile data of a lossy-dielectric slab.

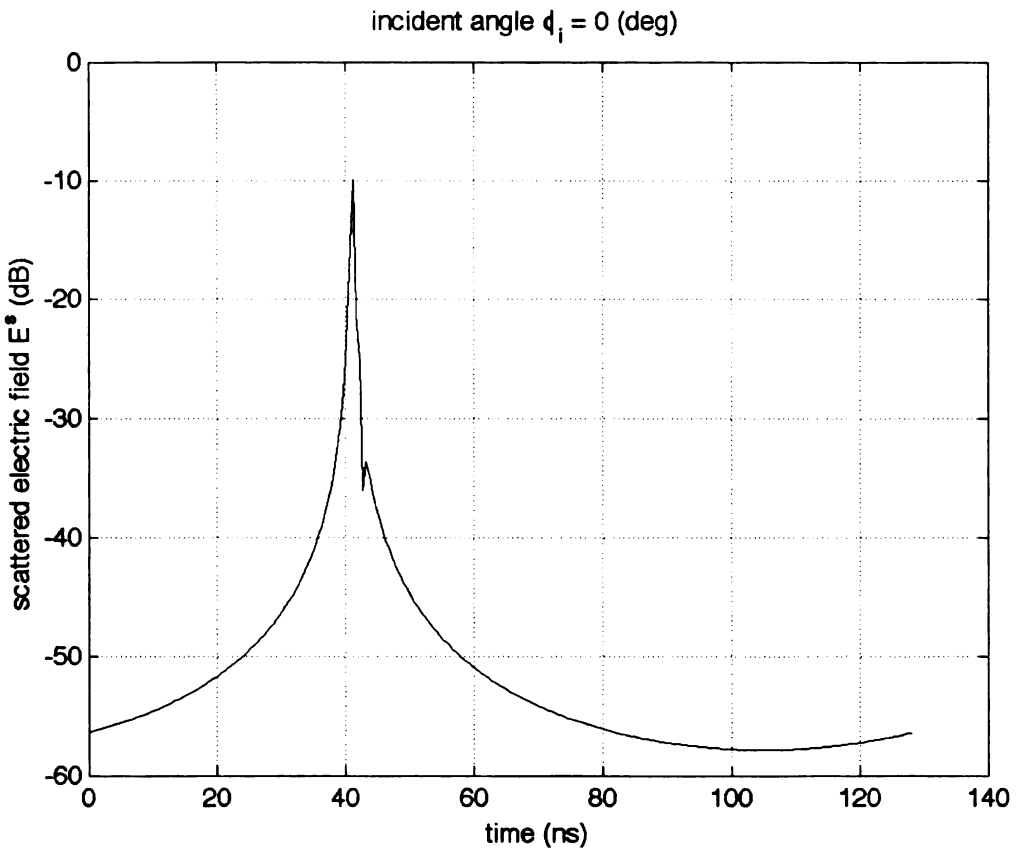

Figure 4.7. Range profile of a 3.94 inch thick simulated slab at incidence angle $\phi_i = 0$.

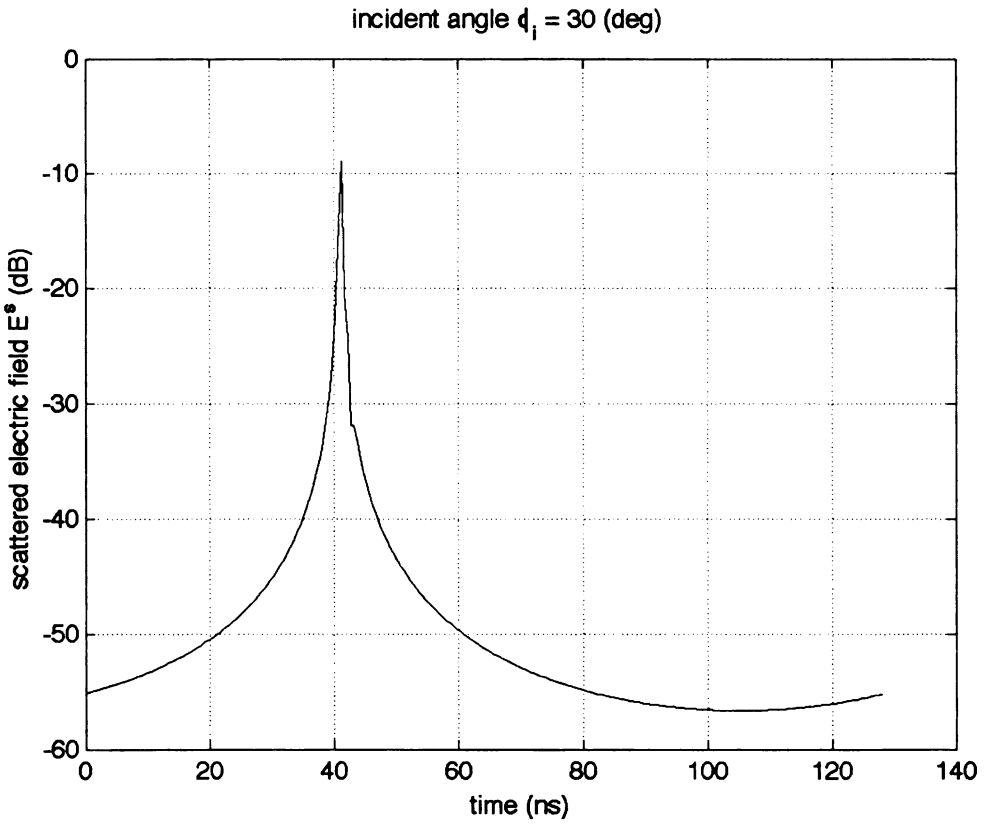

Figure 4.8. Range profile of a 3.94 inch thick simulated slab at incidence angle $\phi_i = \frac{\pi}{6}$.

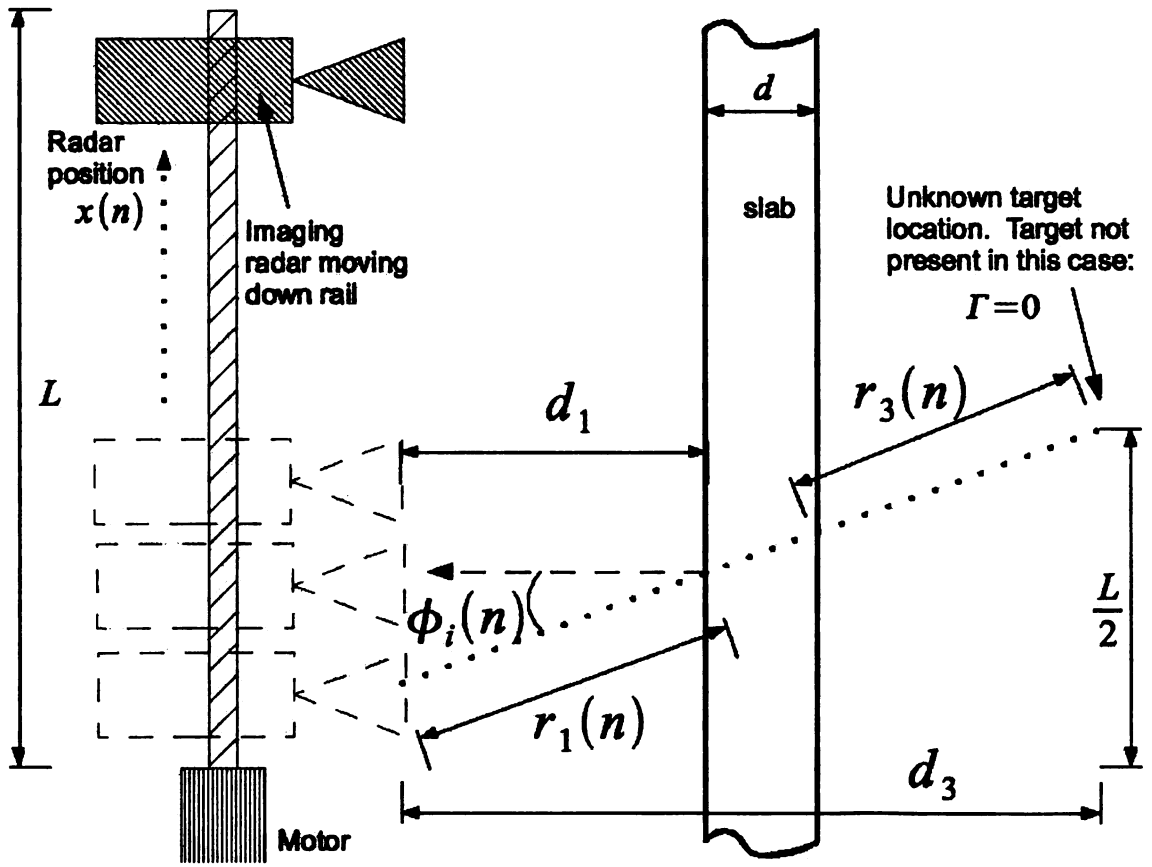

Figure 4.9. Simulated SAR imaging geometry of slab only.

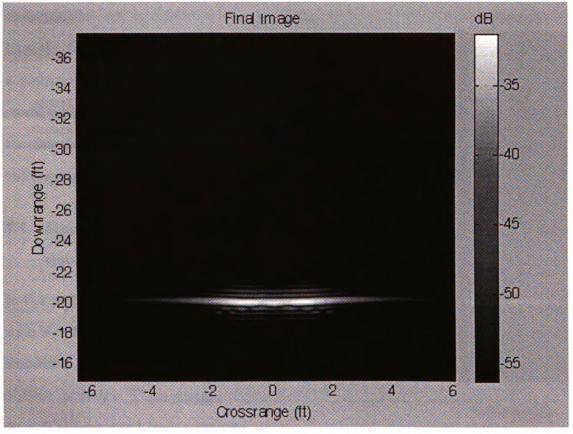

Figure 4.10. SAR image of a 4 inch thick lossy-dielectric slab model.

CHAPTER 5

SIMULATION OF A THROUGH-DIELECTRIC SLAB RADAR IMAGE

Combining the dielectric model developed in Chapter 4 with the 2D PEC cylinder model developed in Chapter 3 a complete model of a 2D PEC cylinder behind a dielectric slab will be developed in this chapter. The dielectric slab in this case will have the electromagnetic properties found in [64]. Range profiles of a cylinder behind a dielectric slab will first be discussed in Section 5.1. In Section 5.2 a complete model with a 2D PEC cylinder located behind a dielectric slab will be developed and simulated SAR imagery will be presented. These results will be used to determine radar system specifications and design architecture in later chapters.

5.1 Simulated range profiles of a 2D PEC cylinder behind a dielectric slab

In this section the lossy-dielectric slab model developed in Chapter 4 will be combined with the 2D PEC cylinder model developed in Chapter 3 and tested by acquiring simulated range profiles of the cylinder behind the slab at normal incidence and oblique incidence. These simulated range profiles will provide insight into what radar returns are expected from a cylinder behind a lossy-dielectric slab.

The geometry is shown in Figure 5.1 where a dielectric slab is placed between a radar system and a PEC cylinder. The radar system is located 20 ft from the front of the slab and the cylinder is located 10 ft from the back side of the slab. The thickness of the slab is d. Simulated range profiles using this geometry are acquired for both normal and oblique incidences.

The simulated range profile data is calculated by solving Equations 4.92 through 4.94 for b_1, where the radar target function Γ is that of a 2D PEC cylinder which was

solved in Chapter 3. Phase shifting the terminal plane of the cylinder some distance r_3 from the terminal plane of the dielectric slab

$$E_{shifted} = e^{-j2k_o r_3}$$

and multiplying this phase shifted plane by the solution to the 2D PEC cylinder Equation 3.18 (ignoring the vector direction since all solutions here are TM^z) results in the radar target function for a 2D PEC cylinder

$$\Gamma = -e^{-j2k_o r_3} \sum_{n=0}^{\infty} (-j)^n \varepsilon_n \frac{J_n(k_o a)}{H_n^{(2)}(k_o a)} H_n^{(2)}(k_o \rho) \cos n\phi, \tag{5.1}$$

where

$$\varepsilon_n = \begin{cases} 1 & \text{for } n = 0 \\ 2 & \text{for } n \neq 0 \end{cases}$$

and the bi-static observation angle $\phi = -\pi$.

The incident plane wave is TM^z and thus the wave amplitude coefficient at the dielectric boundary c_1 is

$$c_1 = E_o e^{-jk_o r_1} \tag{5.2}$$

where r_1 is the distance from the radar system to the surface of the dielectric wall.

The received scattered field is a plane wave traveling back from the dielectric surface to the radar receiver (the theoretical radar system in this case is assumed to be mono-static), and thus the received scattered field equation is

$$E_s = b_1 e^{-jk_o r_1}. \tag{5.3}$$

The IDFT is taken of E_S for a number of test frequencies which emulate a FMCW radar transmit chirp. Parameters used to simulate range profiles for normal and

oblique incidence is shown in Table 5.1.

A MATLAB program was written to simulate the range profiles of a cylinder behind a dielectric slab and is shown for reference in Appendix H. All results presented here were calculated using this program.

The resulting range profile for a normally incident $\phi_i = 0$ plane wave is shown in Figure 5.2. The location of the front of the slab is clearly indicated at approximately 40 nS. The location of the front of the cylinder is also clearly shown at approximately 60 nS. The cylinder is approximately 32 dB below the initial reflection off of the front of the slab. This result is of particular interest in determining radar dynamic range, transmit power and sensitivity requirements.

The resulting range profile for an oblique incident $\phi_i = 7.6^{\circ}$ plane wave is shown in Figure 5.3. The results for this range profile are nearly identical to that of Figure 5.2. Looking at Figure 5.3 the front of the dielectric slab shows up where expected at approximately 40 nS. The cylinder reflection is also clearly indicated at approximately 60 nS. The cylinder reflection is 32 dB below the initial reflection from the surface of the slab.

Based on these theoretical results it is clear that a minimum of 32 dB of dynamic range will be required to see such a cylinder behind a 3.94 inch thick lossy dielectric slab. These simulated results are interesting because it would not be difficult to replicate in a laboratory setting using a tall metal pipe in place of the 2D cylinder.

5.2 Simulation of a through-dielectric slab radar image

In this section simulated SAR imagery of a 2D PEC cylinder placed behind a lossy-dielectric slab will be developed. Using the same procedure as was shown in Section 4.5, a 2 GHZ to 4 GHz chirped radar system is simulated. This radar system acquires 48 evenly spaced range profiles across an 8 foot long simulated linear rail placed in front of the dielectric slab. A 2D PEC cylinder is placed behind the lossy-dielectric

slab at some distance.

The imaging geometry here is similar to what was used in Section 4.5. Looking at Figure 5.4 a 2D PEC cylinder of radius a is located at a distance d_3 downrange from the rail and exactly at the rail center $\frac{L}{2}$. The 2D PEC cylinder has a radar target function Γ. The radar travels down the linear rail of length L acquiring range profiles at evenly spaced increments located at rail positions $x(n)$. The incident angle ϕ_i is dependent upon the radar position on the rail $x(n)$ and the location of the unknown radar target relative to the rail. And from this the $x(n)$ dependent incident angle function $\phi_i(n)$ is re-written here from Section 4.5 for convenience

$$\phi_i(n) = \cos^{-1}\left[\frac{d_3}{\sqrt{\left(\frac{-L}{2} + x(n)\right)^2 + (r_1(n) + r_2(n))^2}}\right], \tag{5.4}$$

where $r_1(n)$ is the distance from the radar itself to the dielectric slab

$$r_1(n) = \frac{d_1}{\cos\phi_i(n)} \tag{5.5}$$

and $r_3(n)$ is the distance from the opposite side of the slab to the unknown target location

$$r_3(n) = \frac{d_3 - d_1 - d}{\cos\phi_i(n)}. \tag{5.6}$$

Where d is the thickness of the dielectric slab and d_1 is the distance from the linear rail to the surface of the dielectric slab. From these equations the $x(n)$ dependent incident field amplitude coefficient can be derived

$$c_1(n) = E_o e^{-jk_o r_1(n)}. \tag{5.7}$$

The $x(n)$ dependent scattered field equation is

$$E_s(n) = b_1(n)e^{-jk_o r_1(n)}, \tag{5.8}$$

where $b_1(n)$ is dependent upon the $x(n)$ dependent impedance equation

$$Z(n) = \frac{\cos\phi_i(n)}{\sqrt{(\epsilon_r + \frac{\sigma}{j\omega\epsilon_o}) - \sin^2\phi_i(n)}}. \tag{5.9}$$

The $x(n)$ dependent reflection and transmission coefficients are given by

$$R_1(n) = \frac{Z(n) - 1}{Z(n) + 1}, \tag{5.10}$$

$$R_2(n) = \frac{1 - Z(n)}{Z(n) + 1}, \tag{5.11}$$

$$T_1(n) = 1 + R_1(n) \tag{5.12}$$

and

$$T_2(n) = 1 + R_2(n). \tag{5.13}$$

Using the above equations the $x(n)$ dependent amplitude coefficients become

$$c_3(n) = \frac{c_1(n)T_1(n)T_2(n)}{e^{j\theta(n)} + R_1(n)R_2(n)e^{-j\theta(n)} + \Gamma\left(R_2(n)e^{j\theta(n)} + R_1(n)e^{-j\theta(n)}\right)} \tag{5.14}$$

and

$$b_1(n) = \frac{c_3(n)}{T_1(n)T_2(n)}\Big[R_1(n)e^{j\theta(n)} + R_2(n)e^{-j\theta(n)} + \Gamma\Big(R_1(n)R_2(n)e^{j\theta(n)} + e^{-j\theta(n)}\Big)\Big]. \tag{5.15}$$

Where the $x(n)$ dependent electrical length $\theta(n)$ is given by

$$\theta(n) = k_O d\sqrt{(\epsilon_r + \frac{\sigma}{j\omega\epsilon_O}) - \sin^2\phi_i(n)}. \tag{5.16}$$

In addition, the radar target function Γ relates $b_3(n)$ to $c_3(n)$ by the equation

$$b_3(n) = \Gamma c_3(n). \tag{5.17}$$

In this case a 2D PEC cylinder is located behind the slab and has the $x(n)$ dependent radar target function (derived from Equation 5.1)

$$\Gamma(n) = -e^{-j2k_O r_3(n)} \sum_{i=0}^{\infty} (-j)^i \varepsilon_i \frac{J_i(k_O a)}{H_i^{(2)}(k_O a)} H_i^{(2)}(k_O \rho)\cos n\phi, \tag{5.18}$$

where

$$\varepsilon_n = \begin{cases} 1 & \text{for } n = 0 \\ 2 & \text{for } n \neq 0 \end{cases}.$$

Using the model derived in Equations 5.4 through 5.17 a simulated SAR image data set was calculated using the parameters shown in Table 5.2.

The MATLAB program used to calculate the SAR data set is shown in Appendix I. In this, first the MATLAB program in Appendix I was run after which the data conditioning MATLAB program in Appendix B was run followed by the RMA SAR imaging algorithm MATLAB program in Appendix C.

Two simulated SAR images were calculated using a slab thickness of $d = 4$ inches and for cylinders of radius $a = 3$ inches (see Figure 5.5) and $a = 6$ inches (see Figure 5.6).

The amplitude of the cylinder in both images is significantly less than the lossy-dielectric slab. The dynamic range required to display these image results is great (notice the amplitude scale when comparing imagery) requiring 50 to 60 dB of image

Table 5.1. The substitutions shown here were used to simulate range profiles of a cylinder behind a dielectric slab.

Range from the radar to the front of the slab $r_1 = 20$ ft
Range from back side of slab to cylinder center $r_3 = 10$ ft
Permittivity of the wall $\epsilon_r = 5$ based on [64]
Cylinder radius $a = 3$ inches
Conductivity σ is a function of frequency based on [64] (see Figure 4.5)
Incident angle $\phi_i = 0$ for normal, $\phi_i = 7.6^\circ$ for oblique
Thickness of dielectric $d = 3.94$ inches
Chirp frequency: 2 GHz to 4 GHz in 256 steps
Incident wave amplitude $E_o = 1$

Table 5.2. The substitutions shown here were used to simulate SAR image data of a cylinder behind a dielectric slab.

Permittivity of the slab $\epsilon_r = 5$ based on [64]
Conductivity σ is a function of frequency based on [64] (see Figure 4.5)
Distance from rail to front of dielectric $d_1 = 20$ ft
Distance from rail to unknown target center $d_3 = 30$ ft
The unknown radar target function $\Gamma = 0$
Linear rail length $L = 8$ ft
Number of evenly space range profiles across rail length: 48
Chirp frequency: 2 GHz to 4 GHz in 256 steps
Incident wave amplitude $E_o = 1$

dynamic range. This observation is consistent with the simulated range profiles in Section 5.1.

The simulated SAR imagery of cylinders in this section are not much different than the simulated cylinder without a slab in Section 3.4. This result is promising showing that the lossy-dielectric slab does not significantly distort the SAR image of an object behind the slab using this geometry where the rail SAR is located 20 feet away from the slab. The cylinder image is, however, greatly attenuated. These results indicate that radar sensitivity and dynamic range appear to be the greatest challenge to imaging behind a lossy-dielectric slab with the same dielectric properties from [64].

5.3 Simulation of a through-dielectric slab radar image using coherent background subtraction

Coherent background subtraction is typically used in small rail SAR systems such as the systems presented in [59] [60]. In these systems the background clutter is significant compared to the target scene. Reducing or eliminating background clutter from radar imagery is achieved by the use of background subtraction. Background subtraction works by first measuring the target scene producing data matrix $s_{back}(x_n, \omega(t))$. After this, by placing targets in the target scene and measuring again producing data matrix $s_{scene}(x_n, \omega(t))$. The resulting background-subtracted data set is the difference between the target scene with targets placed and the target scene before the targets were placed:

$$s_{targets}(x_n, \omega(t)) = s_{scene}(x_n, \omega(t)) - s_{back}(x_n, \omega(t)). \tag{5.19}$$

It is difficult to notice the location of the cylinders in the images shown in Figure 5.5 and Figure 5.6. For this reason a simulated data set using background subtraction

will be developed in this section by applying Equation 5.19, where:

$s_{back}(x_n, \omega(t))$ = dielectric slab model from Section 4.5,

$s_{scene}(x_n, \omega(t))$ = dielectric slab and cylinder model from Section 5.2.

Two simulated images were created using background subtraction with a slab of thickness $d = 4$ inches using a cylinder with a radius of $a = 3$ inches (see Figure 5.7) and $a = 6$ inches (see Figure 5.8).

In comparing the simulated imagery of cylinders in free space in Figure 3.8 and Figure 3.9 to the background subtracted cylinders behind a lossy dielectric slab in Figure 5.7 and Figure 5.8, it is interesting to note that the cylinder images look similar but the return amplitudes are 25 to 30 dB less behind a lossy dielectric slab than in free space. This is due to the attenuation inside of the slab and the boundary conditions of the slab reflecting most of the incident field. It is also interesting to note that the imagery of cylinders behind a slab are shifted slightly downrange by a few inches compared to the imagery of cylinders in free space. This is due to the round trip delay through the dielectric slab, where inside the slab the waves travel at a slower velocity causing the target location to be delayed slightly in downrange. These results will be discussed further and used to develop a set of radar system design specifications and architecture requirements in the next chapter.

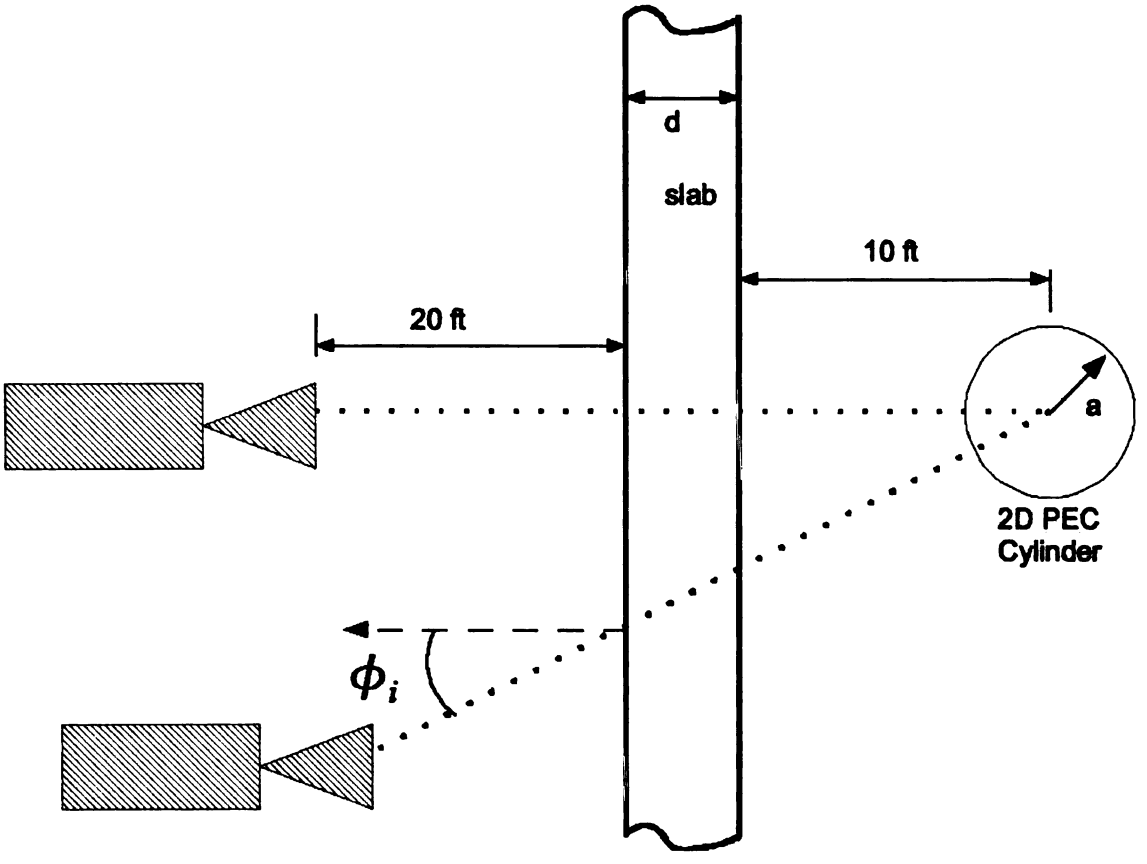

Figure 5.1. Geometry of simulated range profile data.

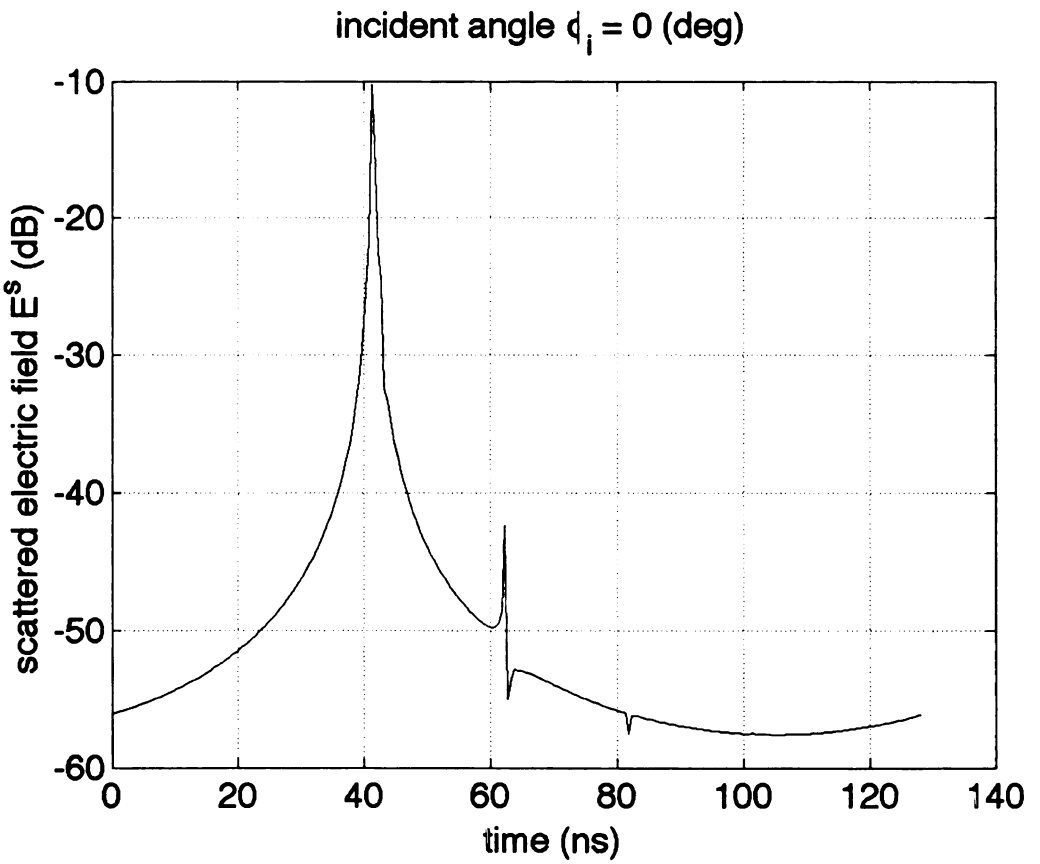

Figure 5.2. Range profile of a lossy-dielectric slab in front a 3 inch radius cylinder at normal incidence.

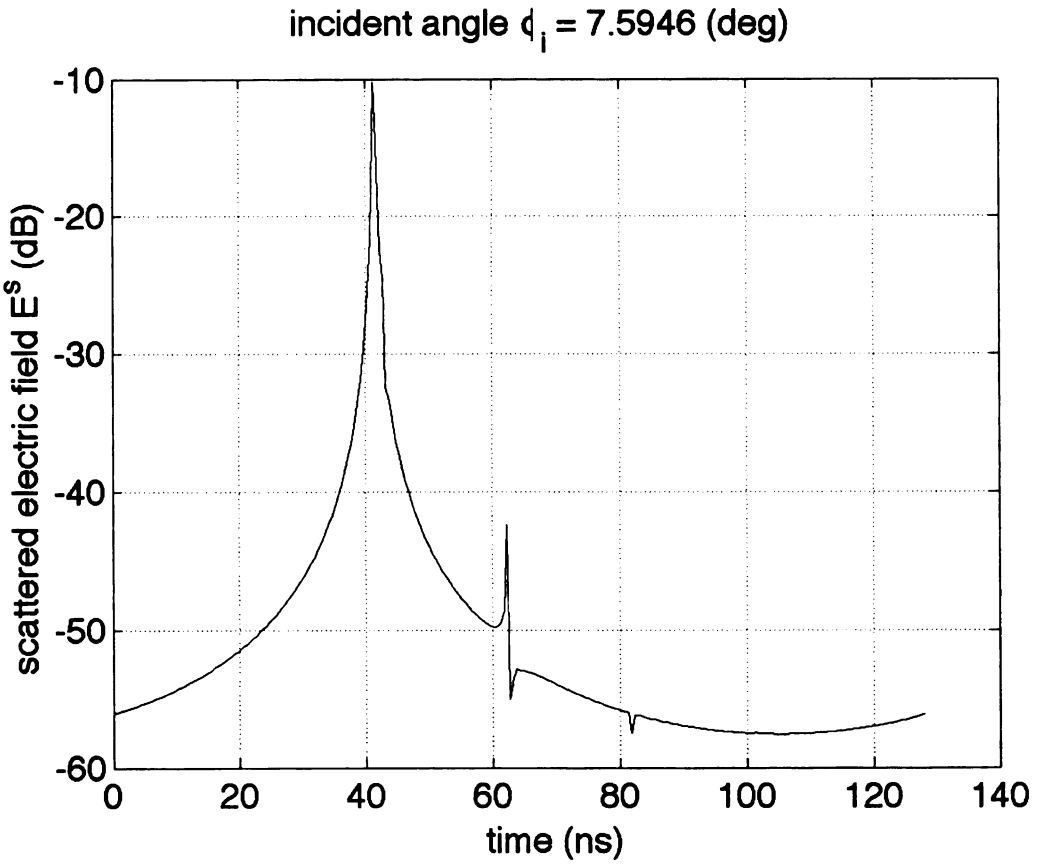

Figure 5.3. Range profile of a lossy-dielectric slab in front a 3 inch radius cylinder at an oblique incidence.

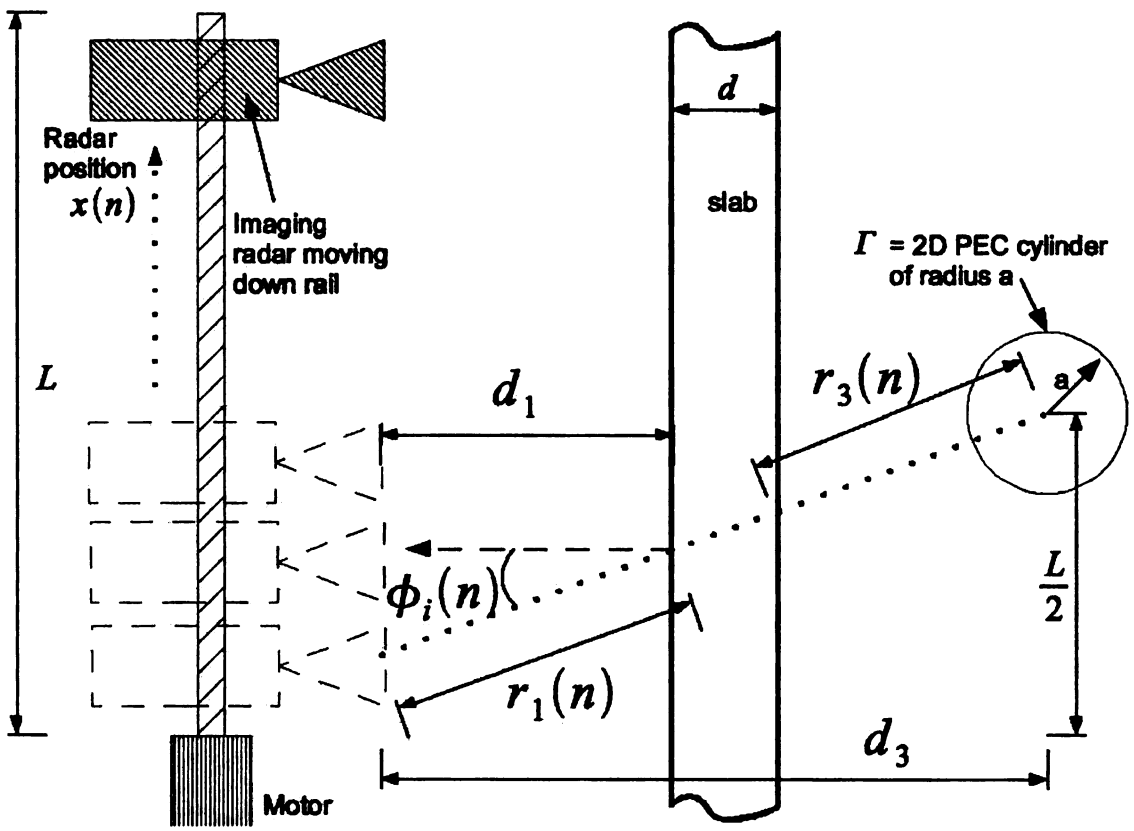

Figure 5.4. Simulated SAR imaging geometry.

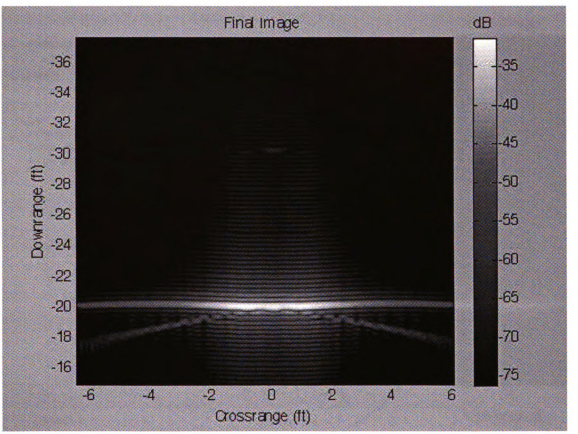

Figure 5.5. SAR image of a simulated target scene made up of a 3 inch radius cylinder target behind a 4 inch thick lossy-dielectric slab.

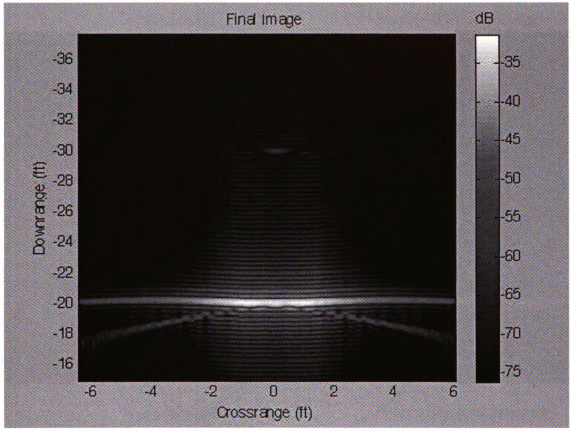

Figure 5.6. SAR image of a simulated target scene made up of a 6 inch radius cylinder target behind a 4 inch thick lossy-dielectric slab.

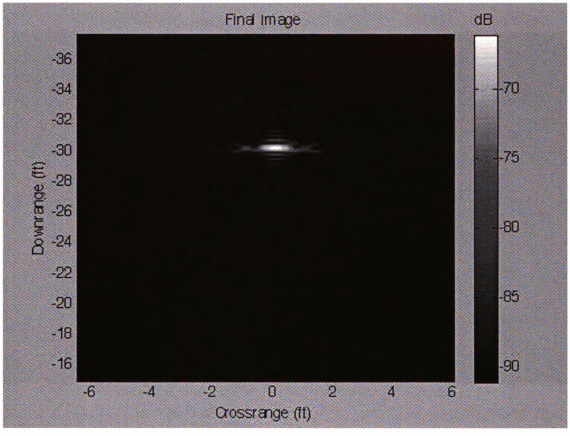

Figure 5.7. SAR image of a simulated target scene made up of a 3 inch radius cylinder target behind a 4 inch thick lossy-dielectric slab using background subtraction.

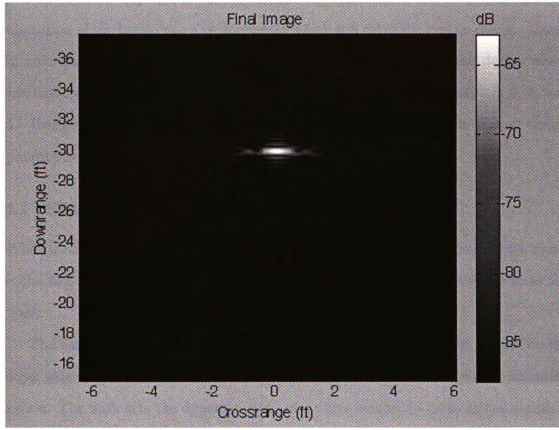

Figure 5.8. SAR image of a simulated target scene made up of a 6 inch radius cylinder target behind a 4 inch thick lossy-dielectric slab using background subtraction.

CHAPTER 6

RADAR SYSTEM DESIGN REQUIREMENTS AND THEORETICAL ANALYSIS

A theoretical model provides insight into the numerous practical design challenges present when developing a measurement system. This chapter was written as a general discussion of the basic design requirements which will drive the system designs shown in later chapters. In this chapter theory meets the reality of system design where simulated radar data is produced using the models developed in Chapters 3, 4, and 5. Using this simulated data some general design guidlines and an overall design philosophy will be developed.

6.1 Flash and through-lossy-dielectric slab attenuation

When measuring a target behind a dielectric slab the strongest scattered return signal is the slab itself. The strong scattered signal from the slab will be referred to as the 'flash.'

The flash is the single greatest technical challenge when measuring targets on the other side of a dielectric slab. The flash saturates radar receivers, causing desensitization. The flash sets the dynamic range of a radar system by peaking the digitizer, causing the least significant bits (LSB's) of the digitizer to be above the level of the scattered returns from the targets behind the slab.

In order to examine the flash more closely the model in Section 5.1 was utilized where the distance from the radar to the slab is 20 feet, slab thickness is $d = 4$ inches and the distance from the radar to the 2D PEC cylinder is 30 feet. Using this theoretical setup the effects of flash are shown in Figure 6.1 (b) for a cylinder of $a = 3$ inches in radius and Figure 6.2 (b) for a cylinder of $a = 6$ inches in radius. For comparative purposes the simulated range profile model of a 2D cylinder in free

space developed in Section 3.3 is shown in Figure 6.1 (a) for a cylinder of radius $a = 3$ and Figure 6.2 (a) for a cylinder of radius $a = 6$ inches. Looking at these figures, the flash from the lossy dielectric slab is significantly greater than the cylinder behind the slab. The slab is the target located at approximately 40 nS down range and the cylinder is the target located at approximately 60 nS downrange.

Targets behind a lossy-dielectric slab scatter significantly less energy back to the radar system compared to the same targets in free space. This is because a large amount of attenuation occurs when a pulse emitted from a radar transmitter travels through a slab. This loss is also due to the radar transmitter signal reflecting off of the air-slab boundary. This attenuation is upwards of 10 dB for a 4 inch thick lossy-dielectric slab and much greater attenuation occurs for thicker lossy-dielectric slabs. What is left of the transmitted signal on the other side of the slab travels towards the target then scatters off the target. The scattered signal then has to pass back through the slab experiencing further attenuation (another 10 dB or so) due to the loss tangent of the lossy slab material and reflection off of the air-slab boundary. This results in a reduction of the scattered return magnitude of the target compared to the same target in free space, typically 15 dB to 30 dB lower. Through-lossy-dielectric slab attenuation is evident in the case of a 4 inch thick slab shown in Figure 6.1 and Figure 6.2, where in both cases the return amplitude of the cylinder behind the slab is approximately 15 dB lower than the same cylinder in free space. For a 12 inch thick lossy-dielectric slab the scattered signal from the cylinder is attenuated significantly to the point of being undetectable using the theoretical model developed in Section 5.1, this is shown in Figure 6.4.

The flash and the through slab attenuation severely impede system performance. The flash limits dynamic range, the through slab attenuation places targets below the receiver noise floor and limits receiver sensitivity.

6.2 The necessity of a range gate

There is one sure way to get rid of the flash, that is with the use of a time domain rang-gate. A time domain range-gate will switch on the radar receiver at just the right time so that it is receiving the scattered signals from the targets behind the slab and not the flash from the slab. If a time domain range-gate were used on the theoretical range profiles shown in Figure 6.1 (b), Figure 6.2 (b) and Figure 6.4 (b) then there would be no flash at 40 nS down range.

With the flash eliminated a radar system could use its full dynamic range to acquire data on the targets located behind the slab increasing sensitivity of the resulting measurement. A time domain range gate is a necessity for through-lossy-dielectric slab radar imaging.

6.3 In-line attenuator approximation

Through-slab attenuation limits receiver sensitivity. One way to look at targets on the other side of a lossy-dielectric slab is to ignore the flash using a time domain range-gate, and focus on the through-slab attenuation. It will be shown in this section that the distortion effects on a target placed on the other side of a lossy-dielectric slab are minimal. This is due to the lossy properties of the dielectric. If the flash can be ignored then the through slab imaging problem simply becomes an issue of receiver sensitivity, where what amounts to an in-line attenuator is placed between the transmit and receive paths of the scattered radar signals.

6.3.1 Comparison of through-lossy-dielectric slab and free-space range profile results

When looking at the simulated results for a lossy-dielectric slab in Figure 6.1 (b) and Figure 6.2 (b) it is observed that the scattered magnitude of the cylinder behind a slab is simply attenuated, shifted downrange by a few nano-seconds, but not distorted.

This is due to the fact that the dielectric slab is lossy with a frequency dependent conductivity plotted in Figure 4.5. There is little to no distortion in the range profile of a cylinder located behind this dielectric slab.

6.3.2 Lack of multi-bounce in simulated range profile results

If the conductivity were set to $\sigma = 0$, then using the model developed in Section 5.1 the range profile of a lossless dielectric slab with thickness $d = 4$ inches, distance from radar to wall of 20 feet, distance from radar to cylinder 30 feet, is shown in Figure 6.3. Scattering from the front and back of the slab can be seen in these results at approximately 40 nS down range. The scattering from the lossless slab shows up as a double-bounce in time domain. Similarly, scattering from the cylinder located at approximately 60 nS downrange also shows up as a double bounce.

Increasing the slab thickness to $d = 12$ inches, making the conductivity $\sigma = 0$ and using the model developed in Section 5.1, the range profile of a $a = 3$ inch radius cylinder behind a lossless 12 inch thick dielectric slab is shown in Figure 6.5. It is clear from these results that the double bounce starting at 40 nS down range is the front and back of the slab and the double bounce starting at approximately 65 nS is the cylinder causing multiple echos due to the scattered fields traveling in and out of the dielectric.

6.3.3 Comparison of lossly and lossless dielectric range profiles

In summary; if a dielectric slab were lossless then the range profile results would be extremely distorted with a double-bounce for the slab and each target in the scene. This was shown in Figure 6.3 and Figure 6.5. As it turns out the dielectric of interest from [64] is a very lossy material and so the range profile of this dielectric slab is much less full of distortion as shown in Figure 6.1 and Figure 6.2. This is because the lossy properties of the dielectric cause attenuation to signals that bounce more than once through the slab. Based on these results it appears that signal attenuation due to

the radar signals traveling through a lossy slab, not distortion due to the lossy slab, is the limiting factor to detecting a cylinder located behind a lossy-dielectric slab.

6.3.4 In-line attenuator approximation applied to theoretical range profile results

Based on the results presented in this section there is very little distortion affecting the range profile of a cylinder behind a lossy-dielectric slab. For this reason the dielectric slab can be approximated as simply an attenuator in-line with the target scene. This in-line attenuator approximation is accurate only if a time domain range-gate is utilized (which eliminates the flash from the slab) in the radar system design. The in-line attenuator approximation is shown in Figure 6.16, where for a $d = 4$ inch thick slab there is 7.5 dB of attenuation from the transmitted signal to the target scene and 7.5 dB of additional attenuation due to the scattered target scene back through the slab to the radar receiver.

6.4 Using the RMA for through-dielectric slab imaging

It will be shown in this section that free-space SAR imaging algorithms or other free-space radar algorithms are accurate when radar imaging through a finite thickness lossy-dielectric slab at stand-off ranges of 20 feet to 30 feet.

6.4.1 Comparison of simulated free-space and through-dielectric slab SAR imagery

Using the model developed in Section 5.3 and SAR processed using the RMA developed in Chapter 2 a comparison of the theoretical background subtracted SAR imagery of a cylinder behind a $d = 4$ inch thick lossy-dielectric slab to that of a cylinder in free-space based on the imaging geometry shown in Figure 5.4 is shown in Figure 6.6 for a cylinder of radius $a = 3$ inches. The same is shown in Figure 6.7 for a cylinder of radius $a = 6$ inches. In both cases the cylinder image appears to

be the same as it is in free-space except that the return amplitude of the cylinder is significantly lower by approximately 15 dB. There is little noticeable distortion in the simulated SAR image of a cylinder behind a lossy-dielectric slab, except that the cylinder image is slightly wider and shifted downrange by a small amount.

A similar result can be found when increasing the slab thickness to $d = 12$ inches and is shown in Figure 6.12. Again, there is little noticeable distortion in the theoretical SAR image of a cylinder behind a lossy-dielectric slab except that the cylinder image is noticeably wider and shifted downrange by a small amount. However, the increase width of the cylinder is not so wide that the image is severely degraded.

These results show that according to the model when imaging through a lossy-dielectric slab the free space RMA SAR imaging algorithm is effective in imaging a target scene. This is due to the fact that dielectric is lossy and the radar system is located at a stand-off range of 20 feet to 30 feet.

6.4.2 Comparison of simulated free-space and through-lossless-dielectric slab SAR imagery

The phenomena of multi-bounce shown in Section 6.3.2 occurs in simulated SAR imagery of a cylinder behind a finite thickness lossless-dielectric slab. This causes image blurring and distortion making imaging through a lossless-dielectric at a stand-off range difficult using a free space imaging algorithm such as the RMA.

Using the theoretical model developed in Section 5.3, SAR processed using the RMA developed in Chapter 2 and letting the dielectric conductivity $\sigma = 0$ for the imaging geometry shown in Figure 5.4, a simulated image of a cylinder with radius $a = 3$ through a dielectric slab of thickness $d = 4$ inches was created. The results for this are shown in Figure 6.8. It is clear from this image that multi-bounce effects of a lossless-dielectric affect the SAR image by blurring the position of the cylinder.

A similar result can be found by increasing the slab thickness to $d = 12$ inches and is shown in Figure 6.13. This image is interesting because it shows the cylinder in two

different locations down range. This result is due to the increased thickness of the dielectric and the lossless properties of the dielectric. The lossless properties of the dielectric are causing an increase in the multi-bounce effects inside of the dielectric by not attenuating the multi-bounce effects. These multi-bounce effects are showing up in the resulting simulated SAR image.

6.4.3 Simulated offset through-lossy-dielectric slab imagery

Theoretical SAR imagery of an offset PEC cylinder was created using the model developed in Section 5.3, and SAR processed using the RMA developed in Chapter 2. This model uses the offset imaging geometry shown in Figure 6.9. A simulated image of a cylinder offset in cross range (not centered with rail) with radius $a = 3$ through a lossy-dielectric slab with thickness $d = 4$ inches was created, results are shown in Figure 6.10. It is clear from this image that little noticeable image distortion is present when imaging a cylinder that is slightly offset in cross range.

Using the same imaging geometry, but changing the slab thickness to $d = 12$ inches, similar results were found and shown in Figure 6.14. Some minor differences are noticeable including some downrange target shifting and the cylinder image is slightly wider than free space. With those exceptions there is little to no noticeable image distortion is present.

6.4.4 Offset through-lossless-dielectric slab imagery

The resulting simulated SAR image becomes blurred and distorted when there is no loss in the dielectric slab imaging geometry shown in Figure 6.9. This result is shown in Figure 6.11, where a simulation of a cylinder with radius $a = 3$ is imaged behind a lossless-dielectric slab of thickness $d = 4$ inches. Multiple bounce effects occur which are similar to those found in Section 6.4.2.

A second case was tested with more dramatic effect where the lossless-dielectric was increased to $d = 12$ inches in thickness. This resulting imagery is shown in Figure

6.15.

6.4.5 Summary of using the RMA for through-dielectric slab imaging

From the results in Section 6.4.1 it is clear that the in-line attenuator approximation is effective when ranging or imaging cylinders through lossy-dielectrics at stand-off ranges. It also holds true for SAR imaging geometries where the target is slightly shifted in cross range, as was shown in Section 6.4.3.

It was also shown in Sections 6.4.2 and 6.4.4, that if dielectric slabs were lossless then the RMA would not be useful.

Based on these simulated results, imagery from a lossy dielectric slab is better than imagery from a lossless slab. These results show that free space SAR algorithms such as the RMA developed in Chapter 2 are very effective at imaging a target scene behind a finite thickness lossy-dielectric slab when the radar system is placed at a stand-off range from the slab.

6.5 Summary of the general design requirements

By analyzing results generated from the models developed in Chapters 3, 4 and 5, two major design specifications were realized in this chapter:

- Time domain range gate
- High sensitivity receiver

In addition to these specifications it has been assumed throughout this dissertation that the following system specifications will be adhered to:

- Chirped radar system, from 2 GHz to 4 GHz
- Linear rail SAR imaging geometry using an 8 foot linear rail where the range profile data is acquired once every 2 inches across the rail

In addition to these specifications it was found that the RMA free-space SAR imaging algorithm works extremely well for imaging radar scenes through a lossy-dielectric slab with a finite thickness when the radar is placed at a stand-off range.

A unique design approach will be shown in the next chapter that meets these design requirements fully. It will be shown that this system is capable of imaging through lossy-dielectric slabs and other material.

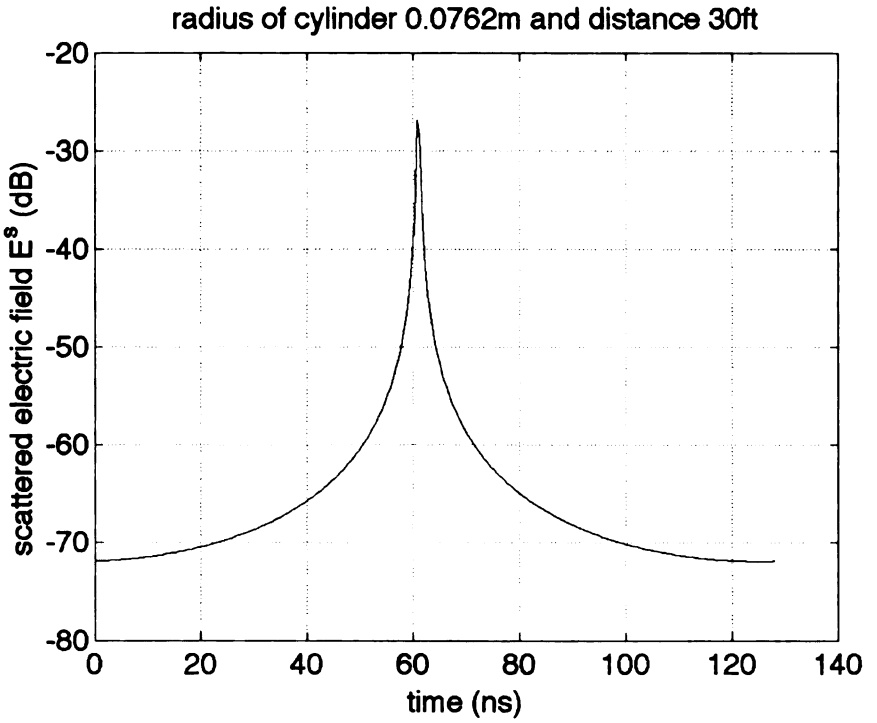

(a)

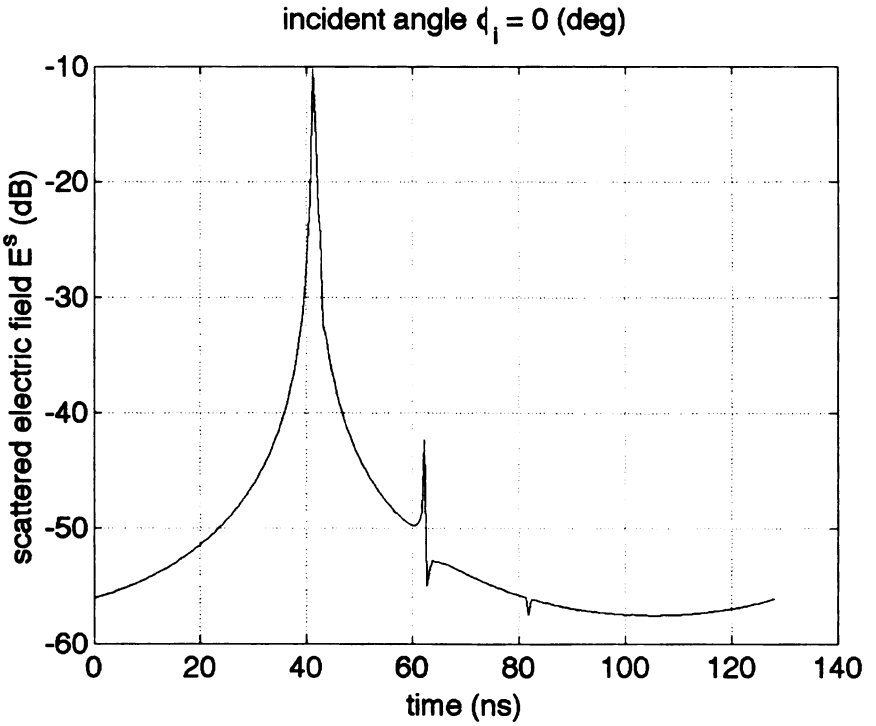

(b)

Figure 6.1. Simulated range profiles of a cylinder with radius $a = 3$ inches in free-space (a) and behind a 4 inch thick lossy-dielectric slab (b).

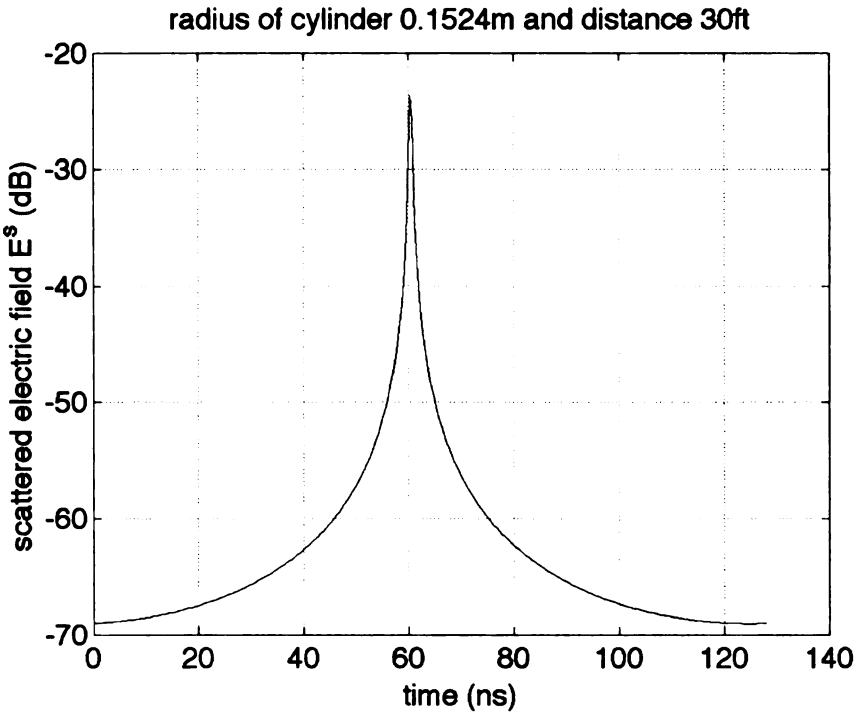

(a)

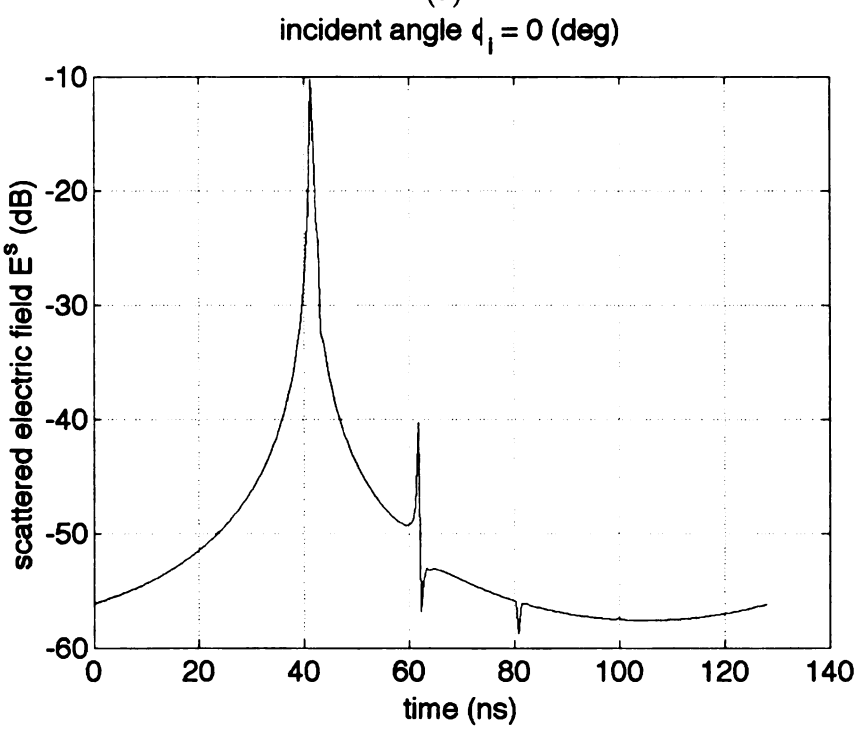

(b)

Figure 6.2. Simulated range profiles of a cylinder with radius $a = 6$ inches in free-space (a) and behind a 4 inch thick lossy-dielectric slab (b).

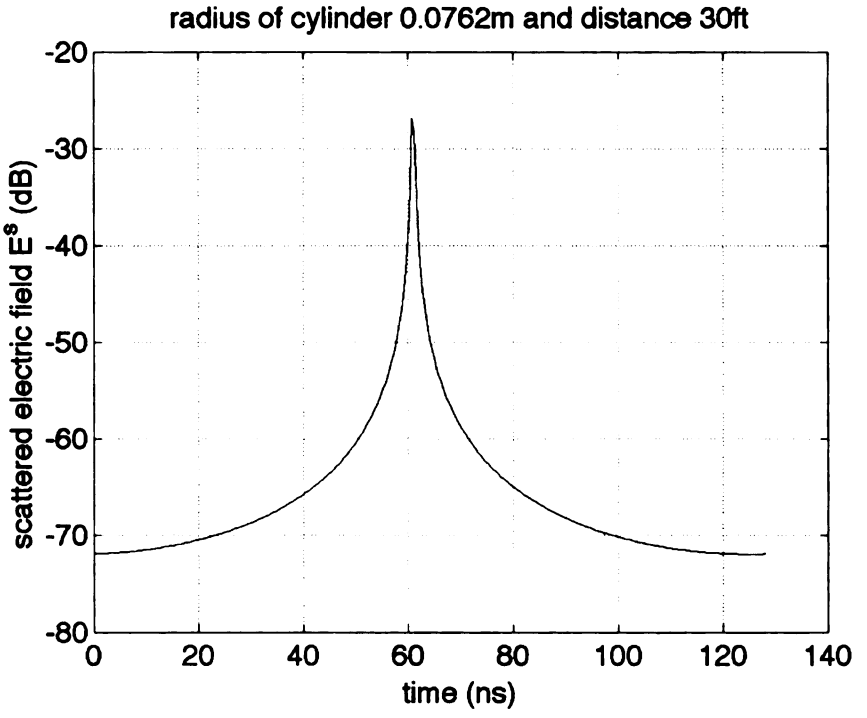

(a)

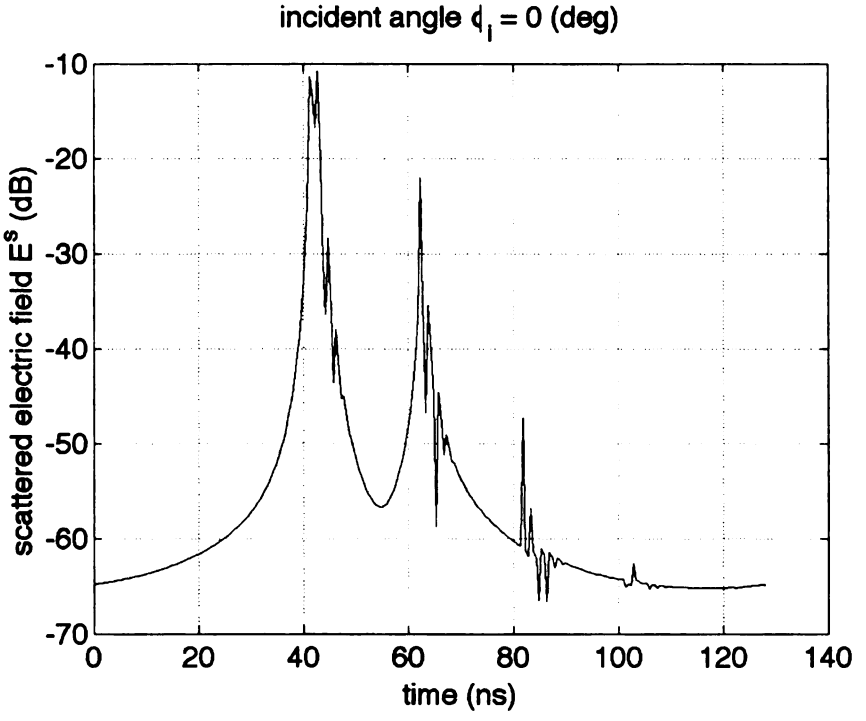

(b)

Figure 6.3. Simulated range profiles of a cylinder with radius $a = 3$ inches in free-space (a) and behind a 4 inch thick lossless-dielectric slab (b).

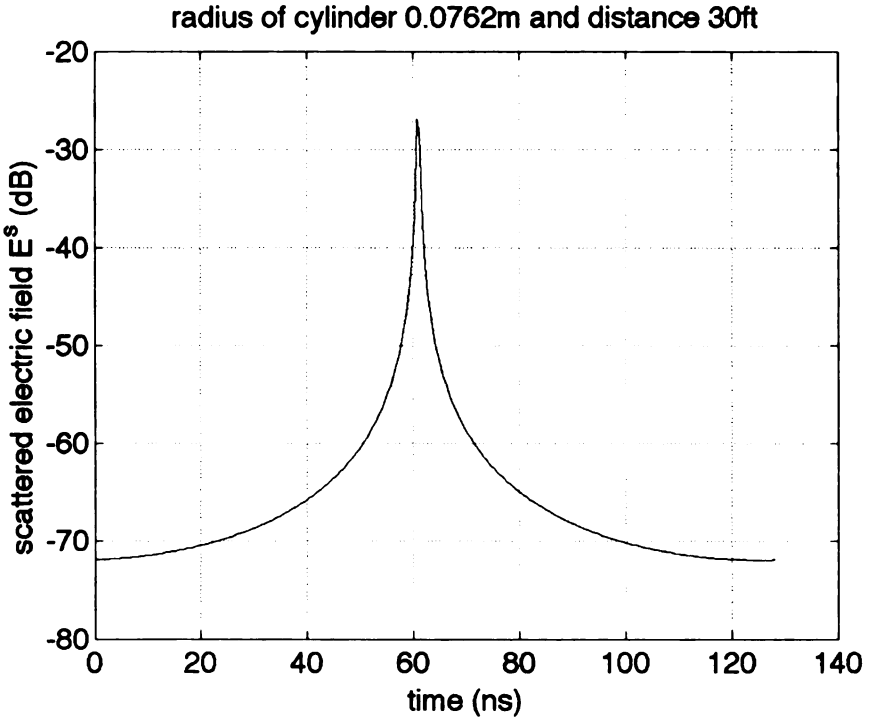

(a)

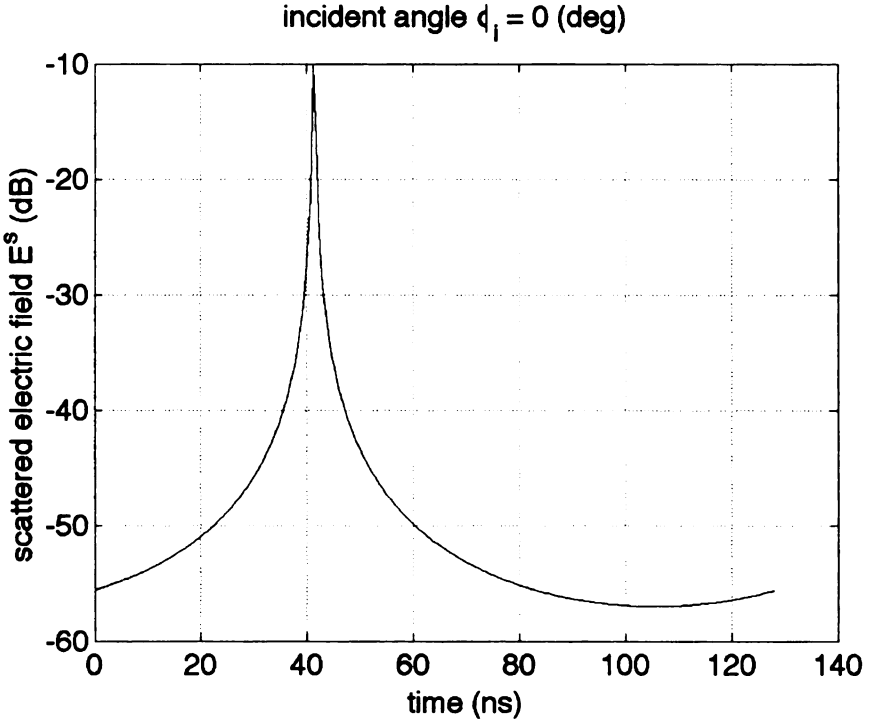

(b)

Figure 6.4. Simulated range profiles of a cylinder with radius $a = 3$ inches in free-space (a) and behind a 12 inch thick lossy-dielectric slab (b).

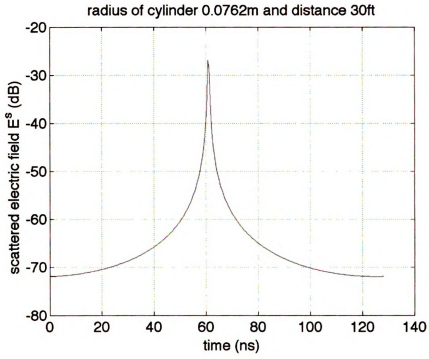

(a)

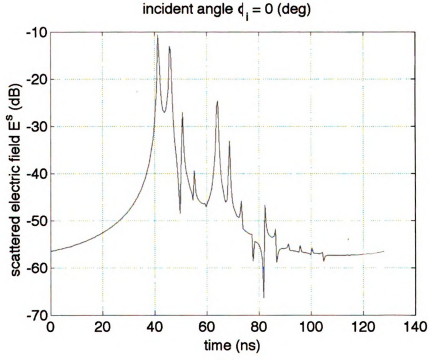

(b)

Figure 6.5. Simulated range profiles of a cylinder with radius $a = 3$ inches in free-space (a) and behind a 12 inch thick lossless-dielectric slab (b).

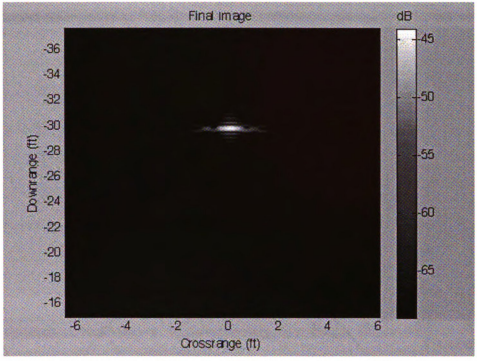

(a)

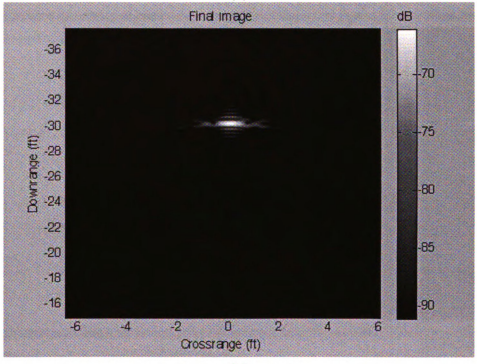

(b)

Figure 6.6. Simulated SAR imagery of a 2D cylinder with radius $a = 3$ inches in free-space (a) and behind a 4 inch thick lossy-dielectric slab using background subtraction (b).

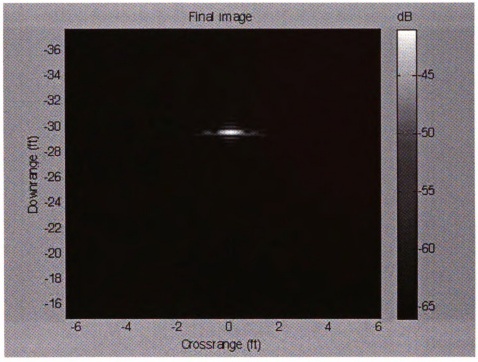

(a)

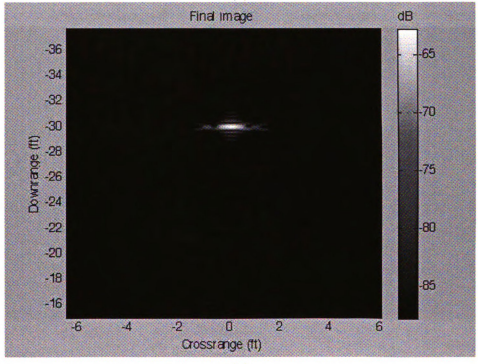

(b)

Figure 6.7. Simulated SAR imagery of a 2D cylinder with radius $a = 6$ inches in free-space (a) and behind a 4 inch thick lossy-dielectric slab using background subtraction (b).

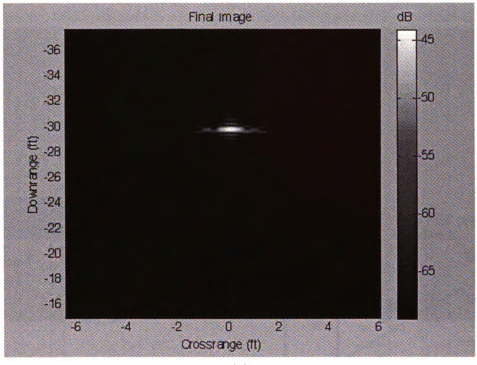

(a)

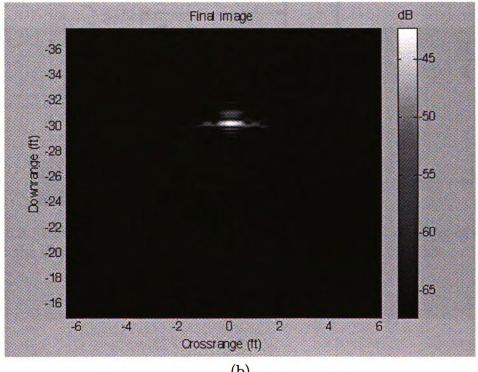

(b)

Figure 6.8. Simulated SAR imagery of a 2D cylinder with radius $a = 3$ inches in free-space (a) and behind a 4 inch thick lossless-dielectric slab using background subtraction (b).

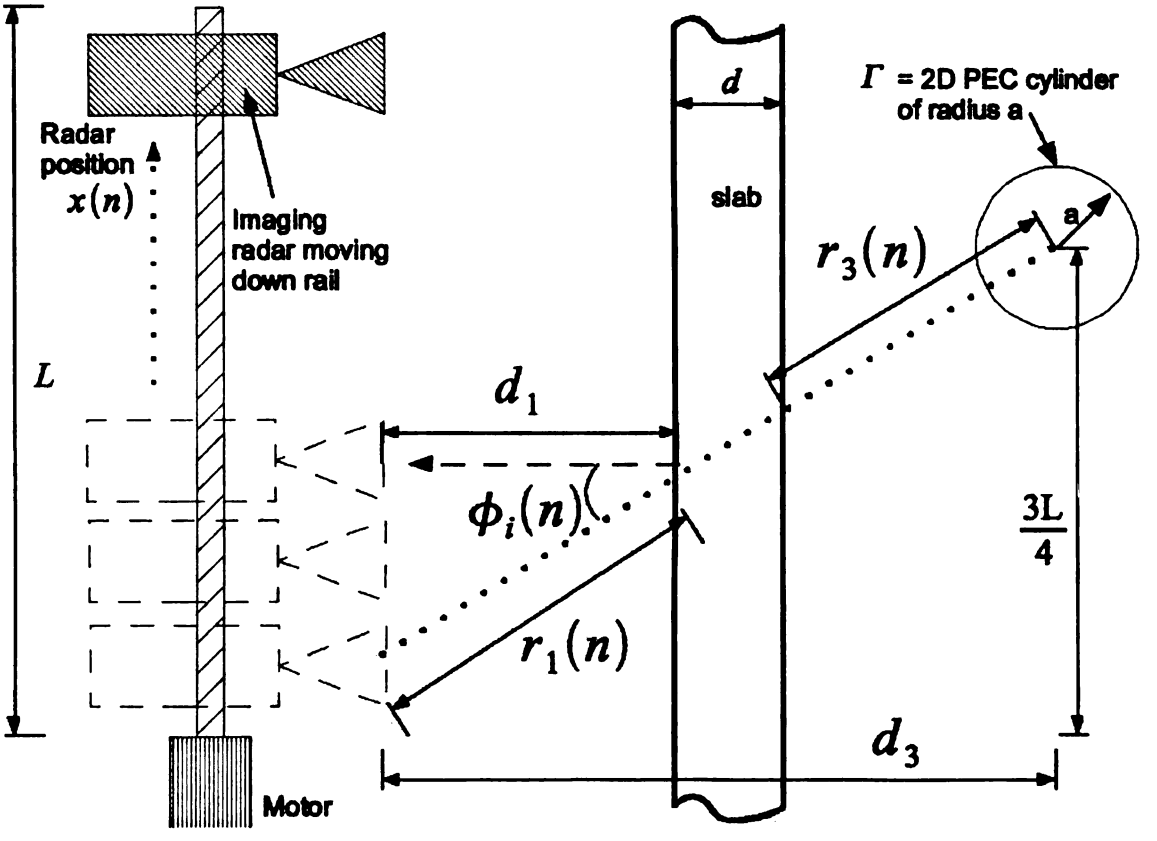

Figure 6.9. The 2D PEC cylinder is offset in cross range from the center of the rail to show the theoretical effects of an offset target behind a dielectric slab.

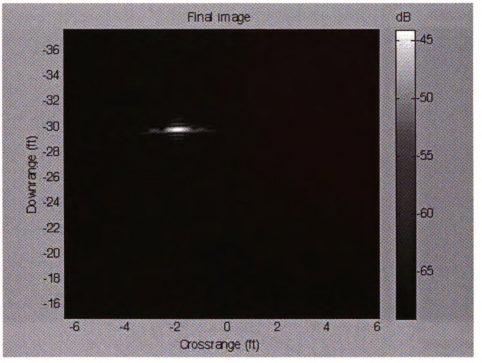

(a)

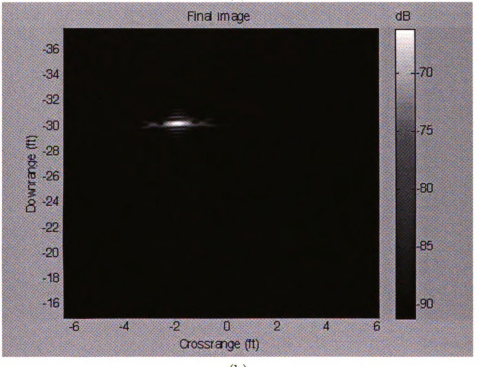

(b)

Figure 6.10. Simulated SAR imagery of a 2D cylinder offset by approximately 2 feet with radius $a = 3$ inches in free-space (a), behind a 4 inch thick lossy-dielectric slab using background subtraction (b).

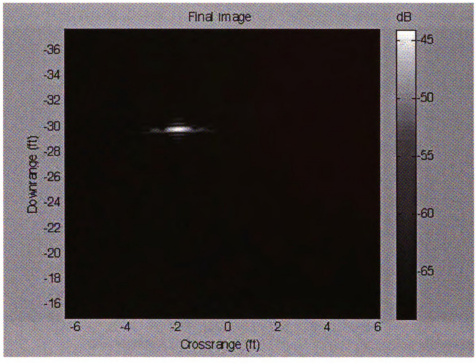

(a)

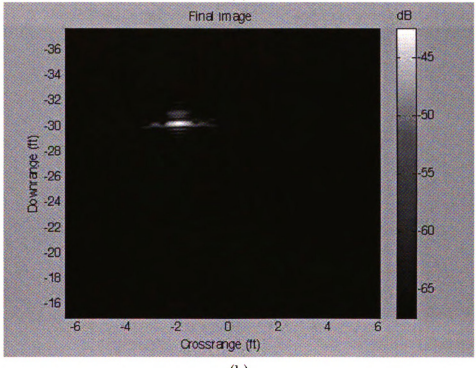

(b)

Figure 6.11. Simulated SAR imagery of a 2D cylinder offset by approximately 2 feet with radius $a = 3$ inches in free-space (a), behind a 4 inch thick lossless-dielectric slab using background subtraction (b).

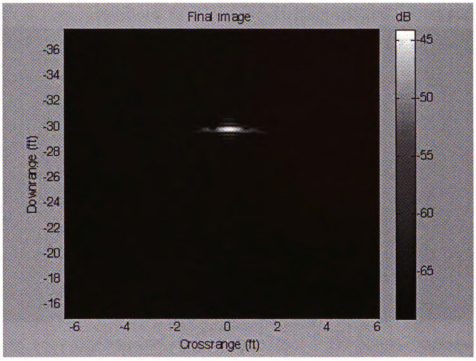

(a)

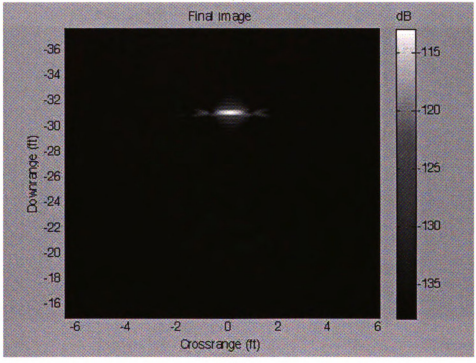

(b)

Figure 6.12. Simulated SAR imagery of a 2D cylinder with radius $a = 3$ inches in free-space (a) and behind a 12 inch thick lossy-dielectric slab using background subtraction (b).

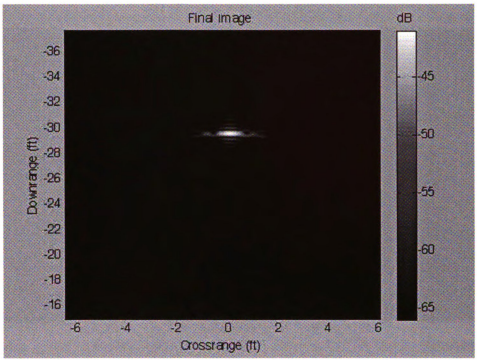

(a)

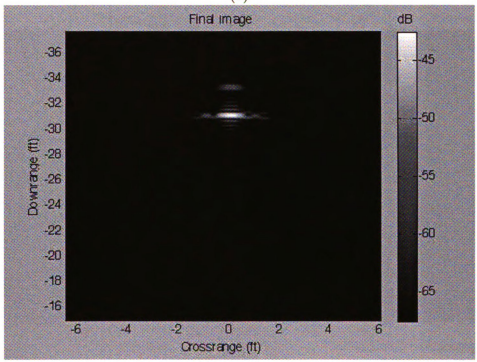

(b)

Figure 6.13. Simulated SAR imagery of a 2D cylinder with radius $a = 3$ inches in free-space (a) and behind a 12 inch thick lossless-dielectric slab using background subtraction (b).

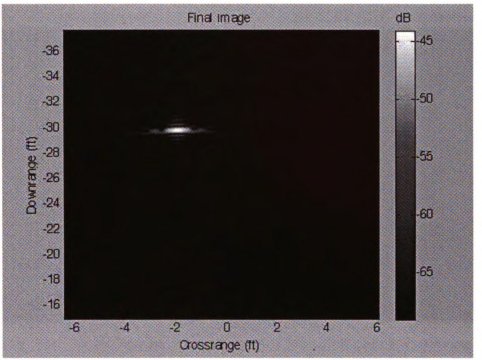

(a)

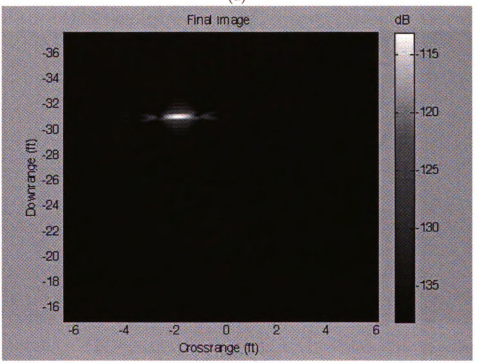

(b)

Figure 6.14. Simulated SAR imagery of a 2D cylinder offset by approximately 2 feet with radius $a = 3$ inches in free-space (a), behind a 12 inch thick lossy-dielectric slab using background subtraction (b).

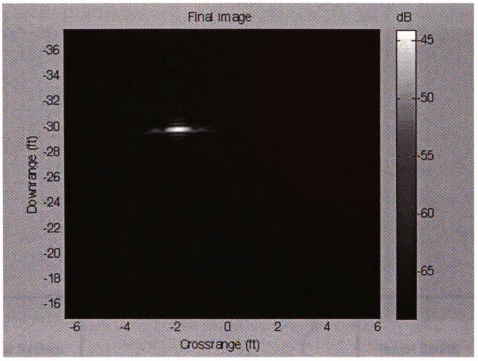

(a)

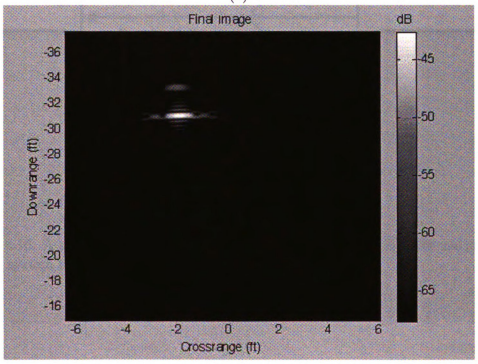

(b)

Figure 6.15. Simulated SAR imagery of a 2D cylinder offset by approximately 2 feet with radius $a = 3$ inches in free-space (a), behind a 12 inch thick lossless-dielectric slab using background subtraction (b).

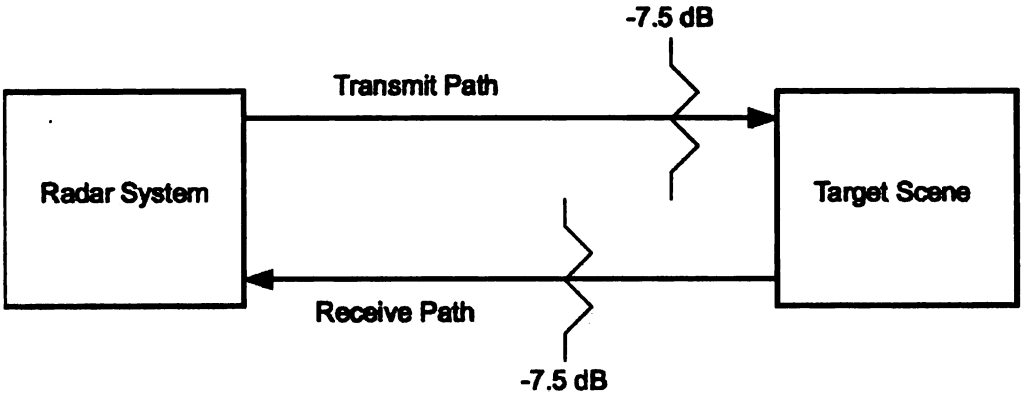

Figure 6.16. A simple attenuation model for the lossy-dielectric slab for use in determining system specifications.

CHAPTER 7

HIGH SENSITIVITY RANGE-GATED FMCW RADAR ARCHITECTURE

A radar architecture was developed which includes a range-gate to eliminate the flash off of the slab and a high sensitivity receiver to overcome through-slab attenuation. The system presented in this chapter fulfills the design specifications outlined in Chapter 6. It will be shown in this chapter that a traditional time domain range-gate reduces receiver sensitivity when it is short in time duration (as what is uniquely required for small radar imaging applications). The radar architecture developed in this chapter is unusual in that it allows for a small duration time domain range-gate while at the same time increasing receiver sensitivity.

7.1 Noise bandwidth and receiver sensitivity

According to standard receiver design theory [67] [68] the sensitivity is directly related to the IF bandwidth. The narrower the IF bandwidth the better the sensitivity. According to [67] for an ideal receiver (disregarding the effects of all the stages) the sensitivity of a SSB or CW receiver can be determined by calculating the minimum detectable signal (MDS) which is related directly to the IF bandwidth:

$$MDS_{dBm} = -174 + 10\log_{10} B_n + NF, \tag{7.1}$$

where:

B_n = noise bandwidth of the receiver (Hz), which will be assumed to be the IF bandwidth in this chapter for an ideal receiver:

-174 dBm is the available thermal noise power per Hz at room temperature of

290°K :

$NF = 3.3$dB front end noise figure for a typical Mini-Circuits broad band amplifier that might be used at the 2 GHz to 4 GHz band for through-lossy-dielectric slab imaging.

From this equation the relation is obvious; the narrower the IF bandwidth B_n the more sensitive the receiver.

7.2 Time domain range-gate and receiver sensitivity

A typical coherent time domain range-gated radar system [34] might utilize a pulsed IF radar architecture such as the one shown in Figure 7.1. Where a pulse is produced with the wave-form generator, fed into the transmit mixer MXR1. MXR1 is fed by OSC3 which is a microwave frequency oscillator operating close to the frequency of interest to make a measurement. OSC2 and OSC3 are phase locked to master clock oscillator OSC1. The output of MXR1 is fed into the transmitter which contains power amplifiers, filters, and RF switches. The output of the transmitter is fed into a duplexer which is connected to the antenna. The antenna is switched between the transmitter and receiver circuits through the duplexer. Inside the duplexer there are circulators and transmit and receive switches. The receive port of the duplexer feeds the front end receiver low noise amplifier LNA1. The output of LNA1 is fed into MXR2. MXR2 is driven by OSC3 so it is perfectly coherent with MXR1. The output of MXR2 is fed into the IF amplifier AMP1. AMP1 adds gain to the system and pushes the IF into the IF filter FL1. FL1 is a band limiting filter, the bandwidth of this filter depends on the minimum range gate that the system is designed to handle. The bandwidth of FL1 sets the equivalent noise bandwidth of the receiver following Equation 7.1. The bandwidth depends on the minimum pulse time that the radar is expected to detect. A typical specification would be $B_n = 1/T$ where $T =$ range gate

time duration in seconds. The output of FL1 is fed into a splitter which then feeds into the IQ demodulator made up of MXR3, MXR4, and fed by OSC2. The output of the IQ demodulator is baseband, DC to whatever the bandwidth of FL1 is. This signal is amplified by Video Amp 1 and Video Amp 2 then digitized. The digitizers sample at or above the minimum sampling rate of B_n for an IQ demodulator, where B_n is the IF bandwidth of the radar system. The range-gate is pulsed at a high rate. During each pulse OSC3 is tuned to a different frequency making up a range profile of frequency domain data. The radar could also span a number of frequencies during a single pulse, which would require a higher receiver equivalent noise bandwidth B_n. If 10 frequency steps were made during one pulse then the radar receiver would require a bandwidth of $B_n = 10/T$.

7.2.1 Example of a 40 nS time domain range-gate in a pulsed IF radar system ranging a target through a dielectric slab

As was shown in Chapter 6, a range-gate is necessary to image a target behind a dielectric slab. Examining the likely imaging scenario shown in Figure 7.2, where radar range to slab $d_1 = 20$ feet and the cylinder target is located $d_3 = 30$ feet from the radar, the maximum length range-gate for this geometry is less than 40 nS. Looking at this range profile example in Figure 7.3 the location of the slab, target and multipath are clearly shown. The multipath is due to the transmitted pulse bouncing off the slab, back to the radar system itself, then off the radar again and back to the slab. This multipath return would be detecting the radar equipment and anything or anyone near the radar equipment rather than targets behind the slab. Multipath is a serious problem when imaging through dielectric slabs, causing the slab to act like a mirror producing imagery of targets that appear to be behind the slab but which are actually in front of the slab inside of the desired range-gate. It is for this reason that the range-gate shown in Figure 7.3 be no greater than 40 nS long. The shorter the range-gate the less likely multi-path returned signals will be detected, the better

it is for through-slab imaging.

Since the range-gate must be $T = 40$ nS or less then the minimum IF bandwidth of a typical pulsed IF radar design for this scenario would be $B_n = 1/T = 25$ MHz. According to Equation 7.1 the ideal receiver sensitivity would be -96.7 dBm.

7.2.2 Example of a 20 nS time domain range-gate in a pulsed IF radar system ranging a target through a dielectric slab

It is likely that a through-dielectric slab imaging system would be placed 10 feet in front of a slab, or closer. Such a geometry is explored here where looking at Figure 7.2 the dielectric slab is located $d_1 = 10$ feet from the radar system and the target is located at $d_3 = 15$ feet from the radar system. A range profile result of this geometry is shown in Figure 7.4 where the reflection off of the slab is located at 20 nS, the target is located at 30 nS and the multi-path begins at 40 nS. The multi-path in this case would be the radar system itself and anything or anyone standing behind the radar system as measurements are acquired. The geometry here is tighter in spacing than the previous section. For this reason the range-gate must be shorter in duration, approximately 20 nS or less, in order to avoid detecting the slab or multi-path.

For a range-gate of $T = 20$ nS or less the minimum IF bandwidth would be $B_n = 1/T = 50$ MHz. According to Equation 7.1 the ideal receiver sensitivity would be -93.7 dBm.

7.2.3 Time domain range-gates and their limitations

Based on results in Sections 7.2.1 and 7.2.2 it was shown that short duration range-gates are required to eliminate the flash from the dielectric slab and to remove unwanted multi-path reflections. The tighter the down range image geometry the smaller the range-gate. In most through-dielectric slab imaging scenarios the down range geometry will be very close requiring the use of small duration range-gates. The smaller the range-gate the less sensitive the radar receiver. This sets a limit on radar system

performance if conventional design architecture, such as pulsed IF, or UWB impulse (where the receiver bandwidth would exceed 500 MHz) were used. However, a much less conventional method will be shown in the next section that implements a short duration range-gate while at the same time increasing, rather than decreasing, receiver sensitivity.

7.3 High sensitivity range-gated FMCW radar architecture

It will be shown in this section that a chirped radar (rather than a time domain pulsed IF system) used with some creative design could implement a short duration time domain range-gate using readily available low cost high frequency parts while at the same time increasing receiver sensitivity.

7.3.1 FMCW radar

Rather than using a time domain pulse, frequency modulated continuous wave (FMCW) radar uses a linearly modulated voltage controlled oscillator (VCO) amplified and transmitted out towards a target scene to range targets. Figure 7.5 shows a block diagram of a typical FMCW radar, such as that found in [60]. Range to target information from an FMCW radar is in the form of low frequency beat tones at or near the audio frequency range. This is accomplished by a linear ramp modulated VCO OSC1. The output of OSC1 is fed directly to the transmit antenna ANT1 and transmitted out toward a target. The chirped signal transmitted out to the target scene is represented by the equation:

$$TX(t) = \cos\left(2\pi(f_{osc} + c_r t)t\right), \tag{7.2}$$

where:

f_{osc} = start frequency of linear ramp modulated VCO and

c_r = radar chirp rate.

The transmitted signal is radiated out towards the target scene and bounces off of a target. The round trip time from the transmitter antenna ANT1 to the target, back to the receiving antenna ANT2, is t_{delay}. This time shifted delayed transmit signal $TX(t - t_{delay})$ is amplified by LNA1 and fed into the RF port of MXR1.

Some of the power from OSC1 is coupled off using CLPR1 and fed into the LO port of MXR1 making the receiver coherent with the VCO OSC1 so that $TX(t)$ is multiplied by $TX(t - t_{delay})$. This is represented by the video amplifier output equation (disregarding amplitude coefficients)

$$Video(t) = TX(t) \cdot TX(t - t_{delay}),$$

$$Video(t) = \cos\left(2\pi(f_{osc} + c_r t)t\right) \cdot \cos\left(2\pi(f_{osc} + c_r t)(t - t_{delay})\right).$$

The higher frequency term is ignored because the IF port of a practical mixer could not produce the resulting microwave frequencies. The resulting video signal is the audio frequency beat tone which is directly proportional to the chirp rate c_r and the round trip radar to target and back time delay t_{delay} plus a DC phase term:

$$Video(t) = \cos\left(2\pi f_{osc} t_{delay} + c_r t t_{delay}\right). \tag{7.3}$$

If there are a variety of targets down range then the signal $Video(t)$ will be a superposition of beat tones at various frequencies and amplitudes. All of this is digitized and fed into signal processing and data conditioning hardware.

7.3.2 High sensitivity range-gated FMCW radar system design theory

The range to target information from an FMCW radar system is in the form of low frequency beat tones. For this reason it is possible to implement a short duration range gate in an FMCW radar system by simply placing a band pass filter (BPF) on

the output of Video Ampl in Figure 7.5. However, this is difficult to implement in practice because it is extremely difficult to design effective high Q bandpass filters at base-band. Much higher performance BPF's are available in the form of widely used IF communications filters which operate at high frequencies. These filters are found in two way radios, TV sets and radio receivers. Examples of these IF filters include:

- crystal filters
- ceramic filters
- SAW filters
- mechanical filters

These communications IF filters typically operate at standard IF frequencies of 10.7 MHz, 21.4 MHz, 455 KHz, 49 MHz and etc. These communications filters are high Q, where Q is defined as [70]:

$$Q = \frac{f_C}{B}, \tag{7.4}$$

where:

f_C = center frequency of the BPF and

$B = -3$ dB bandwidth of the filter.

A typical operating frequency of a crystal filter would be $f_C = 10.7$ MHz with a bandwidth of $B = 7.5$ KHz. The resulting Q of this filter would be $Q = 1426.7$. High Q's such as this are extremely difficult to achieve with BPF designs at base-band audio frequencies. The design shown in this section uses high Q IF filters to create a short duration range gate, while at the same time, reduces receiver noise bandwidth B_n causing a dramatic increase in receiver sensitivity. With this design; the shorter duration the range gate, the more sensitive the radar receiver.

A simplified block diagram of the high sensitivity range-gated FMCW radar system is shown in Figure 7.6. In the following explanation amplitude coefficients will be ignored. OSC1 is a high frequency tunable oscillator which could be anything from a PLL synthesizer to an old vacuum tube signal generator. The frequency output of OSC1 is f_{BFO} which can be represented by the equation:

$$BFO(t) = \cos\left(2\pi f_{BFO} t\right). \tag{7.5}$$

The output of OSC1 is fed into the IF port of MXR1. The LO port of MXR1 is driven by OSC2. OSC2 is a 2 GHz to 4 GHz voltage tuned YIG oscillator (YIG oscillators are VCO's which are capable of producing highly linear voltage tuning slopes). OSC2 is FM modulated by a linear ramp input, where the output of OSC2 can be represented by the equation:

$$LO(t) = \cos\left(2\pi(2 \cdot 10^9 + c_r t)t\right). \tag{7.6}$$

OSC1 and OSC2 are mixed together in MXR1 to produce the transmit signal which is then amplified by power amplifier PA1. The output of PA1 is fed into the transmit antenna ANT1 and propagated out towards the target scene. The transmitted signal out of ANT1 is $TX(t)$, where:

$$TX(t) = LO(t) \cdot BFO(t),$$

$$TX(t) = \cos\left(2\pi(2 \cdot 10^9 + c_r t)t\right) \cdot \cos\left(2\pi f_{BFO} t\right).$$

After some simplification this becomes

$$TX(t) = \cos\left(2\pi(2 \cdot 10^9 + c_r t)t + 2\pi f_{BFO} t\right) + \cos\left(2\pi(2 \cdot 10^9 + c_r t)t - 2\pi f_{BFO} t\right). \tag{7.7}$$

The transmitted waveform $TX(t)$ is radiated out to the target scene, reflected off of a target, delayed by some round trip time t_{delay} and propagated back to the receiver antenna ANT2. The received signal at ANT2 is represented by the equation:

$$\begin{aligned} RX(t) = &\cos\left(2\pi(2 \cdot 10^9 + c_r t)(t - t_{delay}) + 2\pi f_{BFO}(t - t_{delay})\right) \\ &+ \cos\left(2\pi(2 \cdot 10^9 + c_r t)(t - t_{delay}) - 2\pi f_{BFO}(t - t_{delay})\right). \end{aligned} \tag{7.8}$$

The output of ANT2 is amplified by LNA1 and fed into MXR2. The LO port of MXR2 is fed by OSC2. The IF output of MXR2 is the product

$$IF(t) = LO(t) \cdot RX(t).$$

Evaluating this product results in

$$\begin{aligned} &IF(t) = \\ &\cos\left(2\pi(2 \cdot 10^9 + c_r t)t\right) \cdot \cos\left(2\pi(2 \cdot 10^9 + c_r t)(t - t_{delay}) + 2\pi f_{BFO}(t - t_{delay})\right) \\ &+\cos\left(2\pi(2 \cdot 10^9 + c_r t)t\right) \cdot \cos\left(2\pi(2 \cdot 10^9 + c_r t)(t - t_{delay}) - 2\pi f_{BFO}(t - t_{delay})\right). \end{aligned} \tag{7.9}$$

Multiplying out the terms in the above equation results in

$$
\begin{aligned}
&IF(t) = \\
&\cos\left(2\pi(2\cdot 10^9 + c_r t)(t - t_{delay}) + 2\pi f_{BFO}(t - t_{delay}) + 2\pi(2\cdot 10^9 + c_r t)t\right) \\
&+ \cos\left(2\pi(2\cdot 10^9 + c_r t)(t - t_{delay}) + 2\pi f_{BFO}(t - t_{delay}) - 2\pi(2\cdot 10^9 + c_r t)t\right) \\
&+ \cos\left(2\pi(2\cdot 10^9 + c_r t)(t - t_{delay}) - 2\pi f_{BFO}(t - t_{delay}) + 2\pi(2\cdot 10^9 + c_r t)t\right) \\
&+ \cos\left(2\pi(2\cdot 10^9 + c_r t)(t - t_{delay}) - 2\pi f_{BFO}(t - t_{delay}) - 2\pi(2\cdot 10^9 + c_r t)t\right).
\end{aligned}
\tag{7.10}
$$

As a practical consideration the IF port of MXR2 can not output microwave frequencies so the high frequency terms can be dropped resulting in:

$$
\begin{aligned}
&IF(t) = \\
&\cos\left(2\pi(2\cdot 10^9 + c_r t)(t - t_{delay}) + 2\pi f_{BFO}(t - t_{delay}) - 2\pi(2\cdot 10^9 + c_r t)t\right) \\
&+ \cos\left(2\pi(2\cdot 10^9 + c_r t)(t - t_{delay}) - 2\pi f_{BFO}(t - t_{delay}) - 2\pi(2\cdot 10^9 + c_r t)t\right).
\end{aligned}
\tag{7.11}
$$

Expanding out the terms inside of the cosine argument results in:

$$
\begin{aligned}
IF(t) = \cos\Big[&2\pi(2\cdot 10^9 + c_r t)t - 2\pi(2\cdot 10^9 + c_r t)t_{delay} \\
&+ 2\pi f_{BFO}(t - t_{delay}) - 2\pi(2\cdot 10^9 + c_r t)t\Big] \\
+ \cos\Big[&(2\pi(2\cdot 10^9 + c_r t)t - 2\pi(2\cdot 10^9 + c_r t)t_{delay} \\
&- 2\pi f_{BFO}(t - t_{delay}) - 2\pi(2\cdot 10^9 + c_r t)t\Big].
\end{aligned}
\tag{7.12}
$$

Letting the high frequency terms cancel out:

$$IF(t) = \cos\Big[-2\pi(2\cdot 10^9 + c_r t)t_{delay} + 2\pi f_{BFO}(t - t_{delay})\Big] + \cos\Big[-2\pi(2\cdot 10^9 + c_r t)t_{delay} - 2\pi f_{BFO}(t - t_{delay})\Big]. \quad (7.13)$$

As another practical consideration the DC blocking capacitors in the IF amplifier AMP1 will reject the DC phase terms, resulting in:

$$IF(t) = \cos\big(-2\pi c_r t t_{delay} + 2\pi f_{BFO} t\big) + \cos\big(-2\pi c_r t t_{delay} - 2\pi f_{BFO} t\big).$$

Simplifying the arguments in the cosine terms:

$$IF(t) = \cos\big(2\pi(f_{BFO} - c_r t_{delay})t\big) + \cos\big(2\pi(f_{BFO} + c_r t_{delay})t\big). \quad (7.14)$$

$IF(t)$ is fed into the high Q IF filter FL1. FL1 is a high Q communications bandpass filter. FL1 has a center frequency of f_c and a bandwidth of BW. OSC1 is set to a frequency such that $f_{BFO} \geq \frac{BW}{2} + f_c$ causing FL1 to pass only the lower sideband of $IF(t)$, thus causing the output of FL1 to be:

$$FIL(t) = \begin{cases} \cos\big(2\pi(f_{BFO} - c_r t_{delay})t\big) & \text{if } \frac{-BW}{2} + f_c < f_{BFO} - c_r t_{delay} < \frac{BW}{2} + f_c \\ 0 & \text{for all other values} \end{cases} \quad (7.15)$$

Only beat frequencies in the range of $\frac{-BW}{2} + f_c < f_{BFO} - c_r t_{delay} < \frac{BW}{2} + f_c$ are passed through IF filter FL1. Since it was shown in Section 7.3.1 that in an FMCW radar system the range to target is directly proportional to the beat frequency

$c_r t_{delay}$, then the band limited IF signal (which is is proportional to downrange target location) is effectively a hardware range-gate.

Increasing the bandwidth of FL1 increases the range-gate duration. Decreasing the bandwidth of FL1 decreases the range-gate duration. It is for this reason that the range-gate is adjustable if a number of different bandwidth filters were used switched in and out, of the IF signal chain.

If f_{BFO} were increased then the filter FL1 passes only signals that fit the equality in Equation 7.15. Since the $c_r t$ term is subtracted from f_{BFO} then the $c_r t$ term would have to be greater in size to compensate for a higher f_{BFO} frequency in order to let the IF signals pass through FL1. Thus, the filter FL1 would only pass beat tones further down range but at the same range duration in length if the frequency f_{BFO} were increased. So the range-gate is adjustable in physical downrange location (physical down range time delay).

In addition to these desirable properties the narrow bandwidth of FL1 greatly increases the receiver sensitivity according to Equation 7.1. For the pulsed IF radar discussed in Section 7.2 the shorter the range-gate the worse the receiver sensitivity became. The opposite is true for the range-gated FMCW radar architecture shown in this section because according to Equation 7.15 the narrower the IF bandwidth the shorter the range-gate. According to Equation 7.1, the narrower the IF bandwidth the more sensitive the receiver. The radar architecture presented in this section has accomplished both high sensitivity and short duration range-gating without the loss of receiver sensitivity performance. For the design presented in this section the receiver sensitivity increases the shorter the range gate becomes.

FL1 might be a filter with f_c = 10.7 MHz and BW = 7.5 KHz. According to Equation 7.1 the receiver sensitivity would be -131.9 dB, which is significantly higher than a pulsed IF radar system. At the same time, the bandwidth would allow for a range-gate duration of only 9.375 nS for a chirp rate of c_r = 800 GHz/second. This

sensitivity performance is significantly greater than a pulsed IF radar system with a 9.375 nS range-gate, which according to 7.1 would be approximately -90.4 dBm ideal.

One last step occurs in the signal chain shown in Figure 7.6 where the output of FL1 is downconverted to base band through MXR3. The LO port of MXR3 is driven by OSC1 so the output of MXR3 is fed through Video Amp1 and can be represented by the equation:

$$Video(t) = BFO(t) \cdot FIL(t).$$

Video Amp1 is an active low pass filter, rejecting the higher frequency component of the cosine multiplication, resulting in video output signal:

$$Video(t) = \begin{cases} \cos\left(2\pi c_r t_{delay} t\right) & \text{if } \frac{-BW}{2} + f_c - f_{BFO} < c_r t_{delay} < \frac{BW}{2} + f_c - f_{BFO} \\ 0 & \text{for all other values} \end{cases} . \tag{7.16}$$

The result is a range gated base-band FMCW video signal similar to (except without the DC phase term) Equation 7.3. This is identical to a traditional FMCW system discussed in Section 7.3.1 except that this signal is band limited by a high Q bandpass filter with an adjustable center frequency which effectively range-gates the video signal that is fed into the digitizer.

7.4 High sensitivity range-gated FMCW radar architecture conclusions and advantages

The high sensitivity range-gated FMCW radar architecture presented in this chapter was shown to be capable of producing a short duration range-gate while at the same time dramatically increasing receiver sensitivity compared to a pulsed IF radar system of similar range-gate duration. The range-gate in this case requires the use of low-

cost high frequency parts, many of which can easily be fabricated by hand directly from references such as [70]. Such a range-gated high sensitivity system would be inexpensive to implement and require a minimum quantity of expensive microwave components.

This architecture will be used to implement complete imaging radar systems in the next chapters. These include an S-band through-dielectric slab imaging system, an X-band free space imaging system, and a near real-time high speed spatially diverse antenna array imaging system.

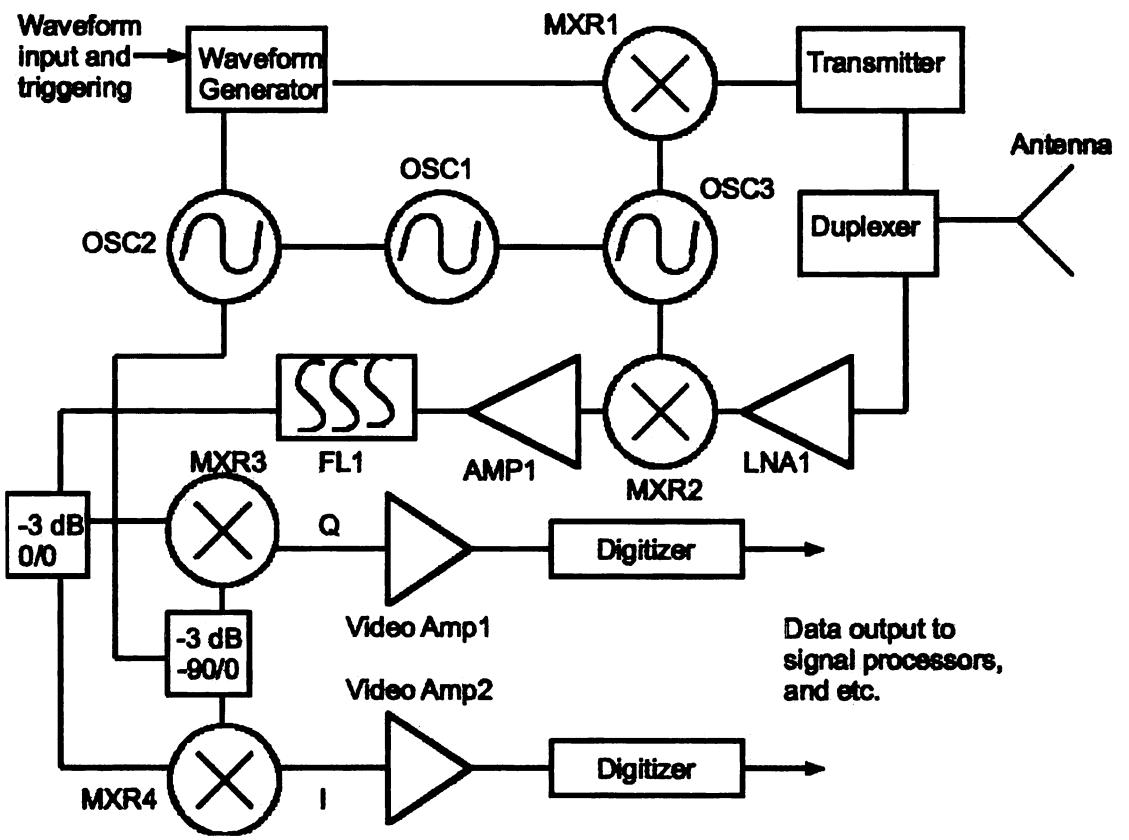

Figure 7.1. Block diagram of a typical coherent pulsed IF radar system where the IF bandwidth must be wide enough to capture the returned pulse from the target scene.

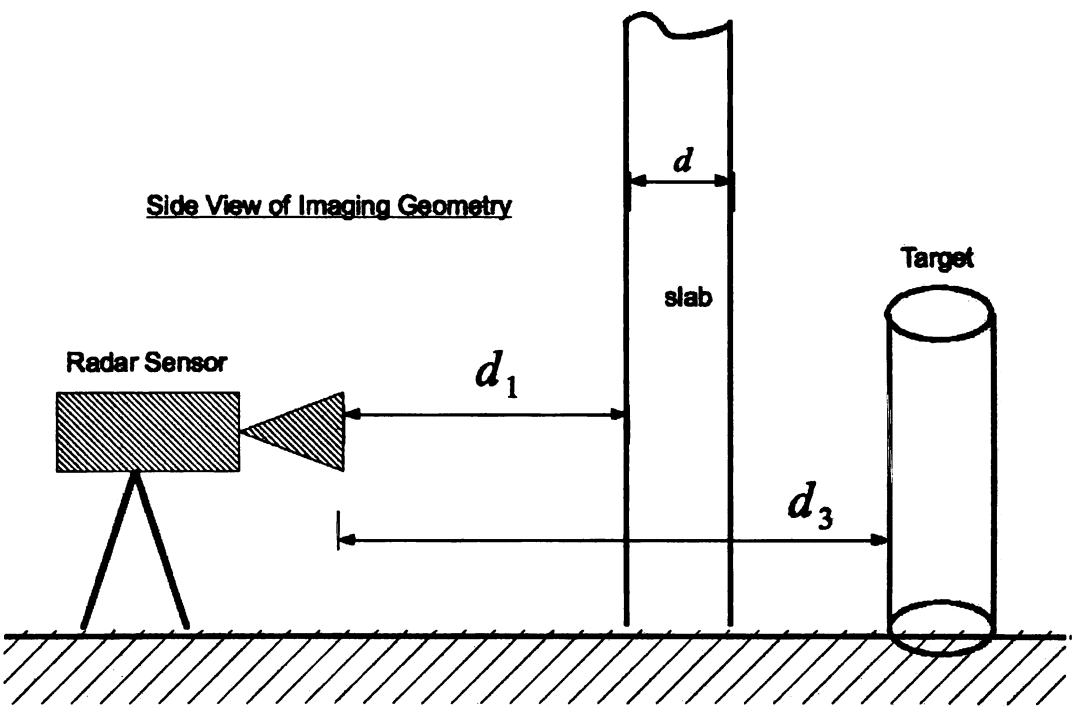

Figure 7.2. Side view of a typical through-dielectric slab imaging geometry.

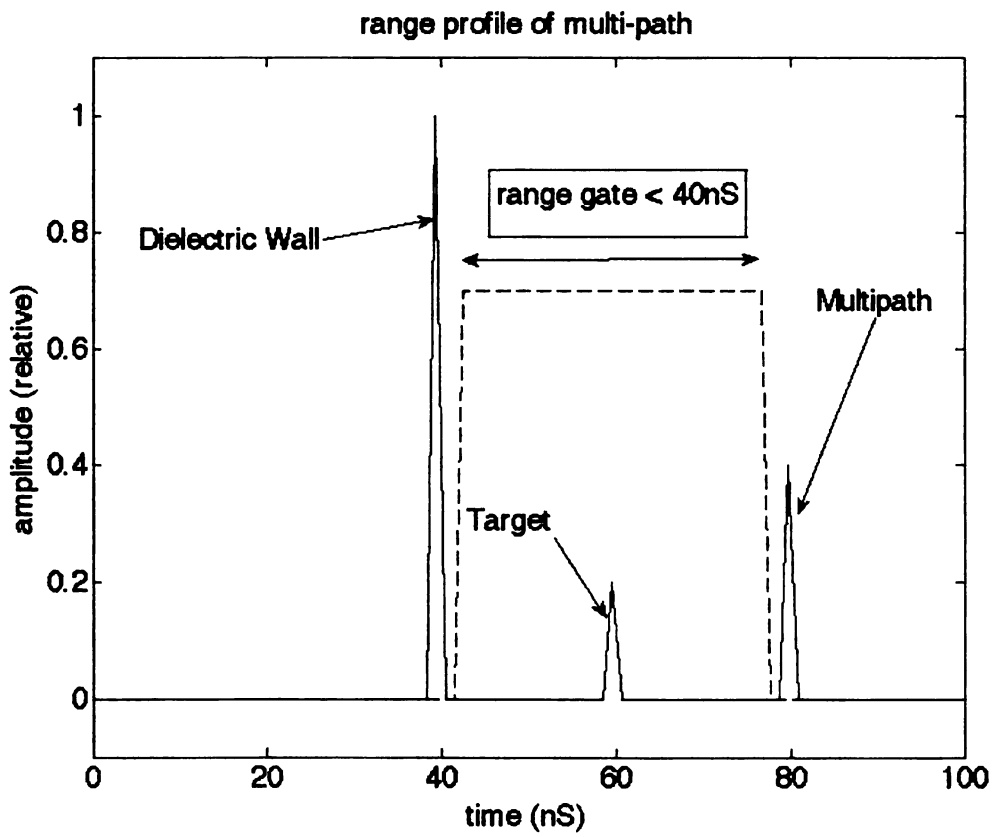

Figure 7.3. Example of a 40nS range-gate where the slab is located at $d_1 = 20$ feet down range, target is located $d_3 = 60$ nS down range and mulipath (from slab to radar and back again) is shown 80 nS down range.

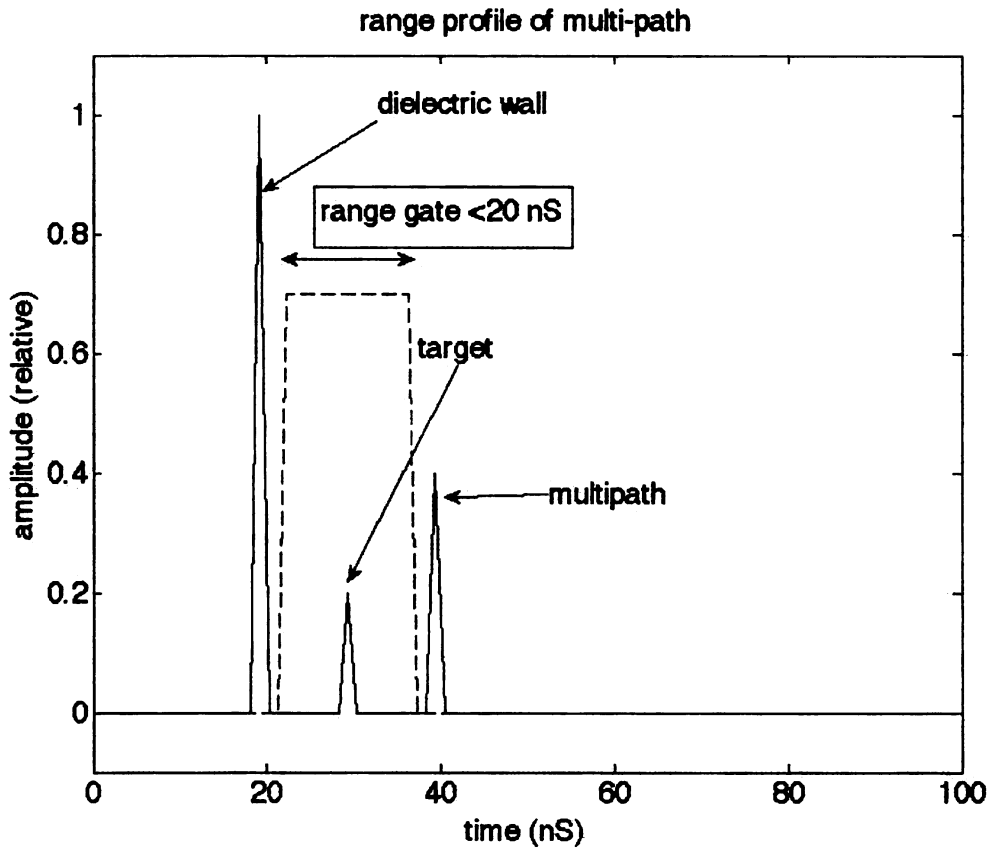

Figure 7.4. Example of a 20nS range-gate where the slab is located at $d_1 = 10$ feet down range, target is located $d_3 = 30$ nS down range and mulipath (from slab to radar and back again) is shown 40 nS down range.

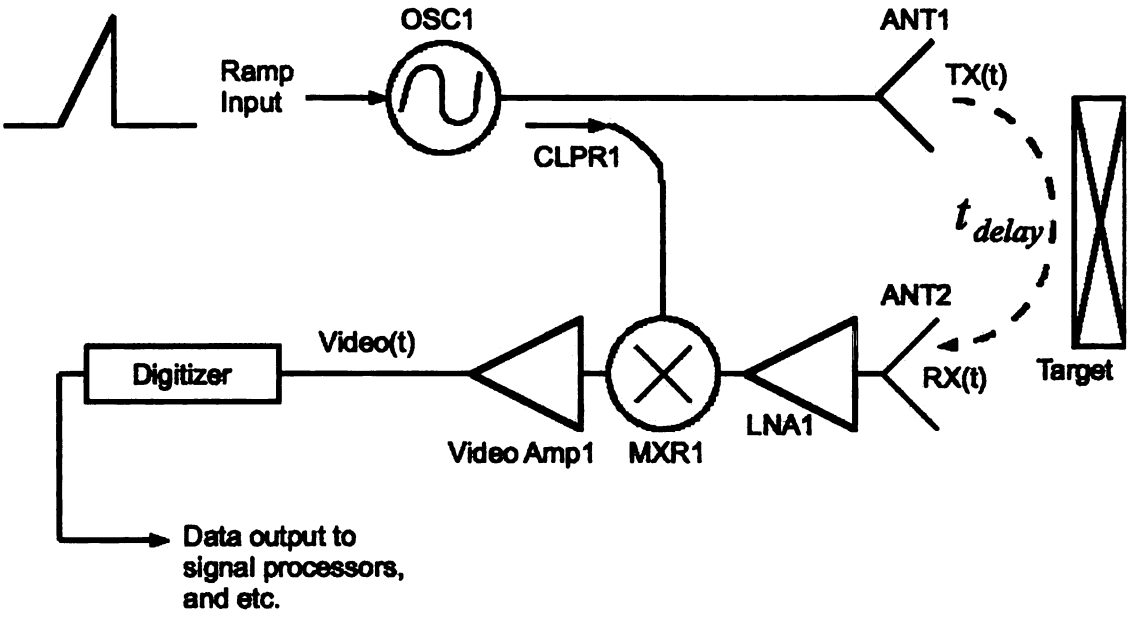

Figure 7.5. A direct conversion FMCW radar system.

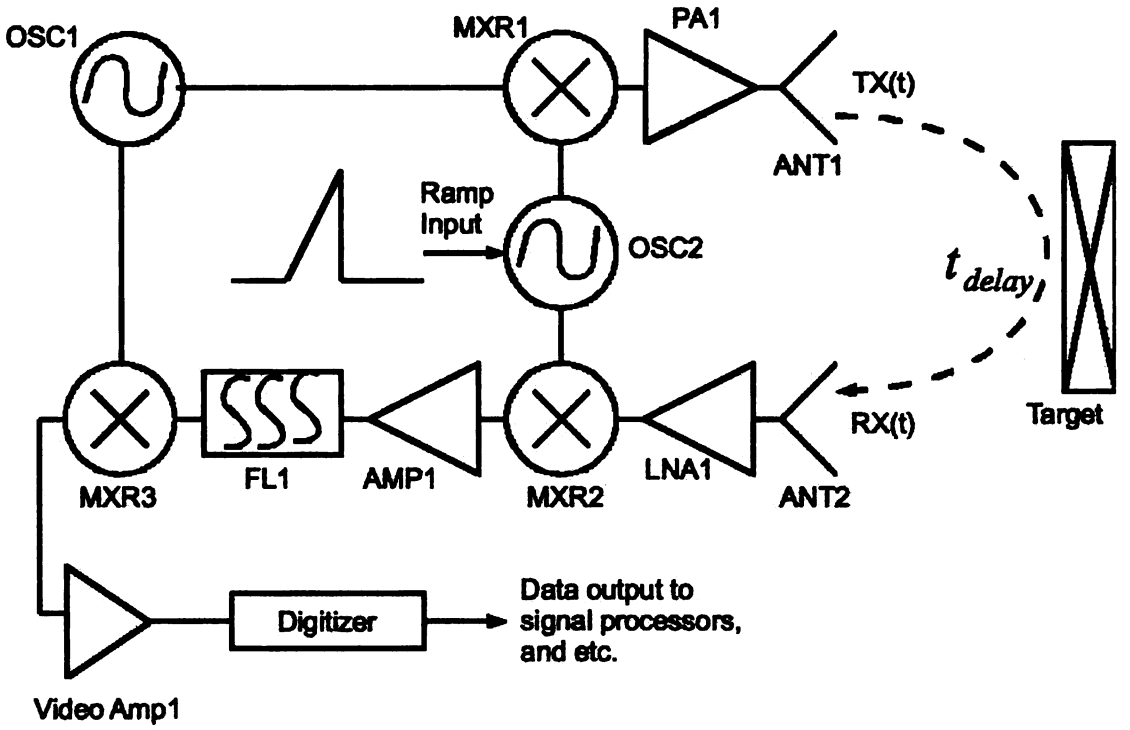

Figure 7.6. Simplified block diagram of the high sensitivity range-gated FMCW radar system.

CHAPTER 8

S-BAND THROUGH-DIELECTRIC SLAB RAIL SAR IMAGING SYSTEM

Using the high sensitivity range-gated FMCW radar architecture developed in Chapter 7, an S-band (2 GHz to 4 GHz) through-dielectric slab radar imaging system will be shown in this chapter. This radar system is a linear rail SAR much like [60] where a radar sensor is mounted on a linear rail and moved automatically down the rail acquiring range profiles of the target scene at evenly spaced increments across the rail. The imaging geometry of this type of rail SAR utilized in a through dielectric slab imaging scene is shown in Figure 5.4. All topics related to this radar system will be discussed in this chapter including theory of operation, parts lists and schematics.

It is important to note that power distribution, pin-outs and specifics of various toggle switches and indicator lamps will be omitted. Only linear power supplies were used throughout this system. The various modules use a wide variety of voltages and the details of how power was routed to the various modules will not be covered in this dissertation.

A picture of the S-band through dielectric slab rail SAR imaging system is shown in Figure 8.11. The entire system block diagram is shown in Figure 8.1, Figure 8.2, Figure 8.3, Figure 8.4, Figure 8.5 and Figure 8.6. A list of parts in these Figures is shown in Table 8.1 and Table 8.2.

8.1 Radar control and data acquisition

Looking at Figure 8.6 all radar system control is done using a PC running Labview. Software written in Labview moves the radar system down the rail one increment at a time by communicating with the Motor Controller through the RS232 port. The motor controller moves the rail. Once the move is complete the computer uses the

PCI6014 NIDAQ Card to simultaneously and coherently trigger a linear ramp using the CTR0 pin while at the same time digitizing the Video Output from the radar IF using the AI0 pin at a rate of 200 KSPS with 16 bits of resolution.

The ramp generator (schematic shown in Figure 8.10) receives an inverted pulse input from CTR0 and outputs a linear ramp which FM modulates the YIG Oscillator. The ramp generator is an adjustable Wilson current mirror [78] which drives a 0.1 uF capacitor. The current mirror is set using a 10 turn precision potentiometer which allows for the chirp rate c_r to be adjusted. An N-channel MOSFET is wired in parallel with the capacitor on the output of the current mirror. The MOSFET shorts the capacitor when CTR0 is high and presents an open-circuit to the capacitor when CTR0 is low. Thus when CTR0 is low the radar begins to chirp. A picture of the motion control, data conditioning, ramp generator and power supplies is shown in Figure 8.12.

The output of the Ramp Generator feeds the VCO control voltage input of the Yig Oscillator. The YIG Oscillator is a Weinschel Engineering 430A Sweep Oscillator with a 432A RF Unit capable of 2 GHz to 4 GHz operation. The output of the YIG Oscillator is fed into SPLTR1 in the power splitter chassis.

The Beat Frequency Oscillator (BFO) is a Hewlett Packard HP3325A Synthesizer/Function Generator set to approximately 10.7 MHz CW (frequency is changed by 10's of KHz depending on range gate location, see Section 7.3.2 for details). The BFO output is fed into the radar IF. The radar system is chirped at a chirp rate of approximately $c_r = 200 \cdot 10^9$ Hz/second with a chirp time of $T = 10$ mS allowing for a maximum detection range of approximately 150 feet for an ADC sample rate of 200 KSPS. Chirp time is variable and can be increased at the cost of reducing maximum detectable range. A picture of the BFO, Yig oscillator and the power splitter chassis is shown in Figure 8.13.

8.2 S-band transmitter signal chain

The YIG Oscillator output in Figure 8.6 is fed out to the power splitter and delay line chassis shown in Figure 8.3. The YIG Oscillator output is then fed into a -3 dB splitter SPLTR1. SPLTR1 is a Mini-Circuits ZN2PD2-50-S, 500 MHz to 5 GHz, 2-way -3 dB splitter. Half of the output is fed into the transmitter front end shown in Figure 8.4. The other half is fed through a coaxial delay line DELAY1 and out to the receiver front end Figure 8.5. The LO output to the transmitter front end from SPLTR1 is fed directly into the LO port of MXR1 on the transmitter front end. A picture of the transmitter front end is shown in Figure 8.14.

The BFO output from Figure 8.6 is fed into the BFO input in Figure 8.1 where a picture of the radar IF is shown in Figure 8.16. The BFO signal is fed through CLPR1 and into the LO port of MXR3. Some of the power from the BFO is coupled out of CLPR1, which is a Mini-Circuits ZX30-12-4, 5 MHz to 1 GHz, -12 dB directional coupler. -12 dB of the BFO is coupled off and fed out of the IF to the adjustable attenuator ATTN3 shown in Figure 8.2. ATTN3 allows for the adjustment of drive power to the transmitter front end. ATTN1, ATTN2 and ATTN3 are located on the top of the radar system so as to make easy adjustments while measuring. A picture of this setup is shown in Figure 8.17

The output of ATTN3 is fed into the IF port of MXR1 inside of the transmitter front end in Figure 8.4. MXR1 is a Mini-Circuits ZEM-4300MH, 300 MHz to 4300 MHz, Level 13 (+13 dBm LO). The LO from the YIG Oscillator is mixed with the BFO in MXR3. The output product from MXR3 is amplified by AMP1 which is a Mini-Circuits ZJL-4G, Gain=11 dB, IP1=12 dBm, NF=5.5 dB. The output of AMP1 is fed through FL2 which is a Mini-Circuits VLP-41, 4.1 GHz LPF. FL2 filters transmitter harmonics. The transmitter signal is fed out through CLPR2 then to the transmitter antenna ANT1. CLPR2 is a Midwest Microwave, 2 GHz to 4 GHz, -20

dB directional coupler. Some power is coupled off of the transmit signal for diagnostic purposes. Transmitter power is approximately 10 dBm and varies upwards of 4 dB over the bandwidth of the chirp due to the transmitter signal chain and YIG oscillator amplitude responses.

The transmit signal radiates out of ANT1 which is a vertically polarized linearly tapered slot antenna (LTSA), developed from work in [71], [72], [73], [74], [75] and [76]. Transmit signals are radiated out of ANT1 and propagate into the target scene.

8.3 S-band receiver signal chain

The transmitted signal is reflected off of the target scene and received by ANT2. ANT2 is a vertically polarized LTSA identical to the transmitter antenna ANT1. The output of ANT2 is fed into the receiver front end shown in Figure 8.5. A picture of the receiver front end is shown in Figure 8.15. The output of ANT2 is fed into FL3 which is a Mini-Circuits VHF-1200, 1200 MHz HPF. This signal is amplified by LNA1 which is a Mini-Circuits ZX60-6013E amplifier, 20 MHz to 6 GHz, Gain=14 dB, NF=3.3 dB. The output of LNA1 is filtered by FL4 which is a Mini-Circuits VHF-1200, 1200 MHz HPF. The output of FL4 is filtered by FL5 which is a Mini-Circuits VLP-41, 4.1 GHz LPF. The output of FL5 is fed into the RF port of MXR2. MXR2 is a Mini-Circuits ZEM-4300MH, 300 MHz to 4300 MHz, Level 13 (+13 dBm LO). The LO port of MXR2 is driven by the LO output of the power splitter shown in Figure 8.3. The resulting IF output from MXR2 is the de-chirped frequency domain data centered at the BFO frequency and filtered by FL1. FL1 is a Mini-Circuits SLP-10.7, 11 MHz LPF. The output of FL1 is amplified by AMP2 which is a Mini-Circuits ZFL-1000VH, Gain=20 dB, IP1=25 dBm, NF=4.5 dB.

The IF output from the receiver front end is fed into the IF shown in Figure 8.1. The receiver IF signal is filtered through the selectable crystal filter switch matrix XTAL Filter Mux2. The schematic of XTAL Filter Mux2 is shown in Figure 8.7.

This is a PiN diode selectable filter matrix with three different IF filters of center frequency f_C = 10.7 MHz and selectable bandwidths of B = 7.5 KHz, B = 15 KHz and B = 30 KHz. There is also a 'through' line which bypasses the filters. Isolation between filters is high, measured to be > 90 dB. The filter mux is capable of handling upwards of 23 dBm of power before the PiN diodes begin to distort (switch on and off causing undesirable mixer products in the IF signal chain).

The output of the XTAL Filter Mux2 is fed into FL6 which is a Mini-Circuits PLP-10.7, 11 MHz LPF. The output of XTAL Mux2 is amplified by AMP3 which is a Mini-Circuits ZKL-2R5, Gain=30 dB, IP1=15 dBm, NF=5 dB. The output of AMP3 is fed out of the IF and through the Kay Model 20 adjustable attenuator ATTN2. The output of ATTN2 is fed back into the IF and amplified by AMP5. AMP5 is a Mini-Circuits ZHL-6A, Gain=25 dB, IP1=22 dBm, NF=9.5 dB.

The output of AMP5 is fed into XTAL Filter Mux1 which is identical to XTAL Filter Mux2. The output of XTAL Mux1 is fed into the RF port of MXR3. MXR3 is a Mini-Circuits RAY-6U, Level 23 (+23 dBm LO). The schematic for MXR3 is shown in Figure 8.8. The LO port of MXR3 is fed by the BFO so as to shift the IF down to base band. The output of MXR3 is amplified by the video amplifier VideoAmp1. The schematic for VideoAmp1 is shown in Figure 8.9. VideoAmp1 is made up of an amplification stage and a 4th order active LPF optimized for uniform delay [79].

The output of the video amplifier is fed directly into the AI0 digitizer input pin on the PCI6014 data acquisition card. This digitized video data is the frequency domain range profile data which is acquired at every rail position.

ATTN1 and ATTN2 are adjusted to maximize the voltage swing on the digitizer input so as to take advantage of as much of the digitizer dynamic range as possible without saturating the receiver signal chain. Due to the high LO drive level of the front end mixer MXR2 and the IF mixer MXR3 the receiver does not saturate unless there is -5 dBm of power at the antenna terminals. The receiver sensitivity with

ATTN1 and ATTN2 set to 0 dB is approximately -131.9 dBm theoretical on the lowest bandwidth setting of $B = 7.5$ KHz according to Equation 7.1. Receiver sensitivity was measured to be < -125 dBm. The system dynamic range was measured to be > 120 dB.

8.4 Calibration and background subtraction

The radar system is calibrated before measurements are made. The calibration is done to sharpen imagery and not an exact sphere target calibration (this was due to fact that a large calibration sphere sizable enough to achieve the desired signal to noise ratio in a high clutter environment was not available in the laboratory at the time). The calibration procedure is simple. A 5 foot tall 3/4 inch diameter copper pole is used as a cal target. This cal target is used because it is easily detectable at S-band using a vertically polarized antenna system. The cal target is placed at a known location down range from the radar sensor. A range profile is taken of the pole represented by $s_{pole}(\omega(t))$. The pole is then removed and a background range profile is taken, the result is represented by $s_{calback}(\omega(t))$. The background is subtracted from the pole range profile resulting in a clean range profile of the pole only, where

$$s_{cal}(\omega(t)) = s_{pole}(\omega(t)) - s_{calback}(\omega(t)). \tag{8.1}$$

The cal data is referenced to a theoretical point scatterer which is represented by the equation

$$s_{caltheory}(\omega(t)) = e^{-j2k_r R_{pole}}, \tag{8.2}$$

where R_{pole} is the range to the cal pole and $k_r = \omega(t)/c$. The cal factor is calculated by the equation

$$s_{calfactor}(\omega(t)) = \frac{s_{caltheory}(\omega(t))}{s_{cal}(\omega(t))}. \tag{8.3}$$

This cal factor is multiplied by each range profile acquired across the rail.

Coherent background subtraction using Equation 5.19 is utilized on all measured data.

8.5 S-band SAR data processing

Data form the PC running control software in Labview is saved in the MATLAB .MAT matrix format. From this data both calibration and coherent background subtraction are implemented using the MATLAB program written and shown in Appendix J. Once the data is calibrated and backgrond subtracted the RMA SAR algorithm developed in Chapter 2 and written in MATLAB in Apprendix C is then run to produce the resulting image.

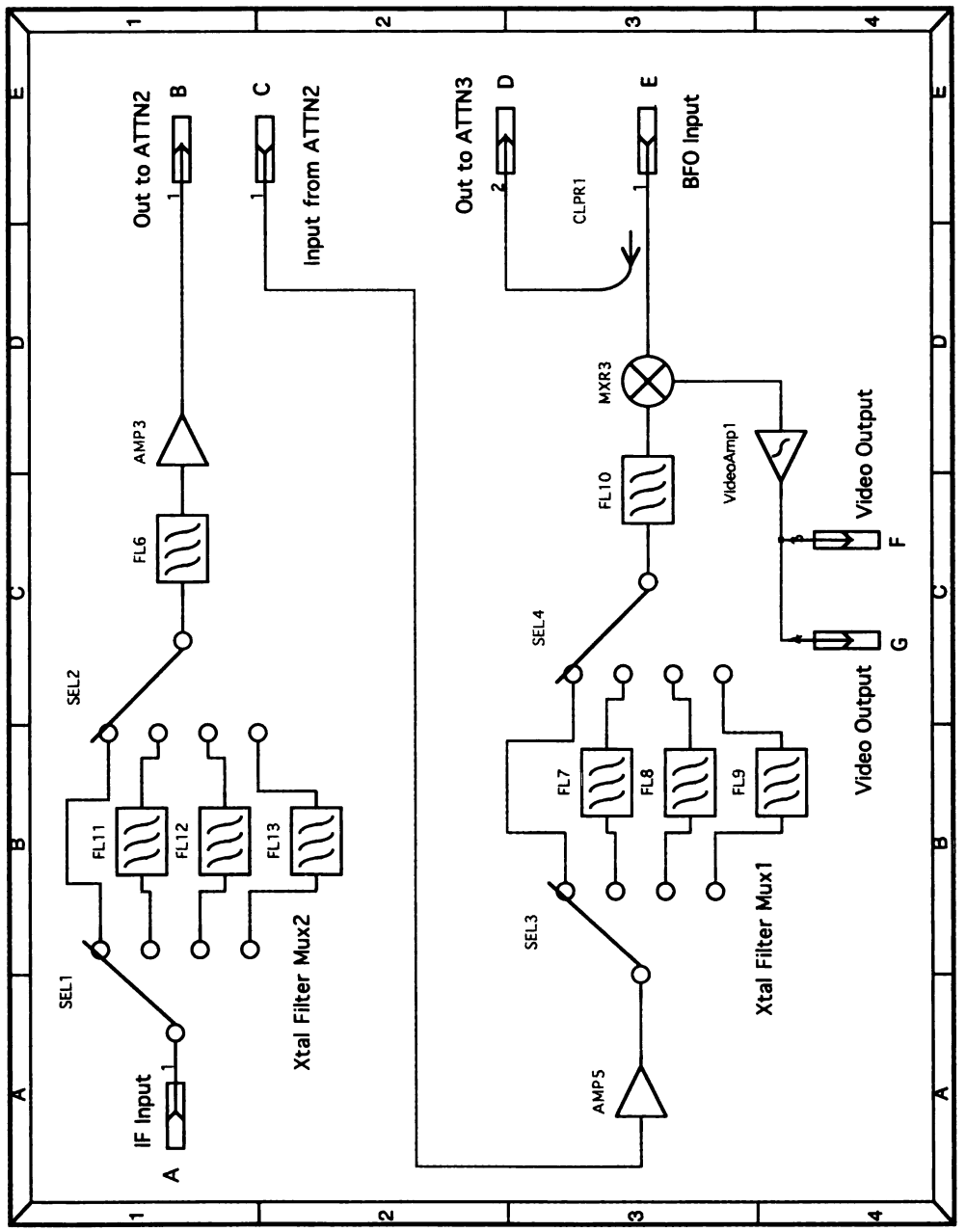

Figure 8.1. Block diagram of the IF.

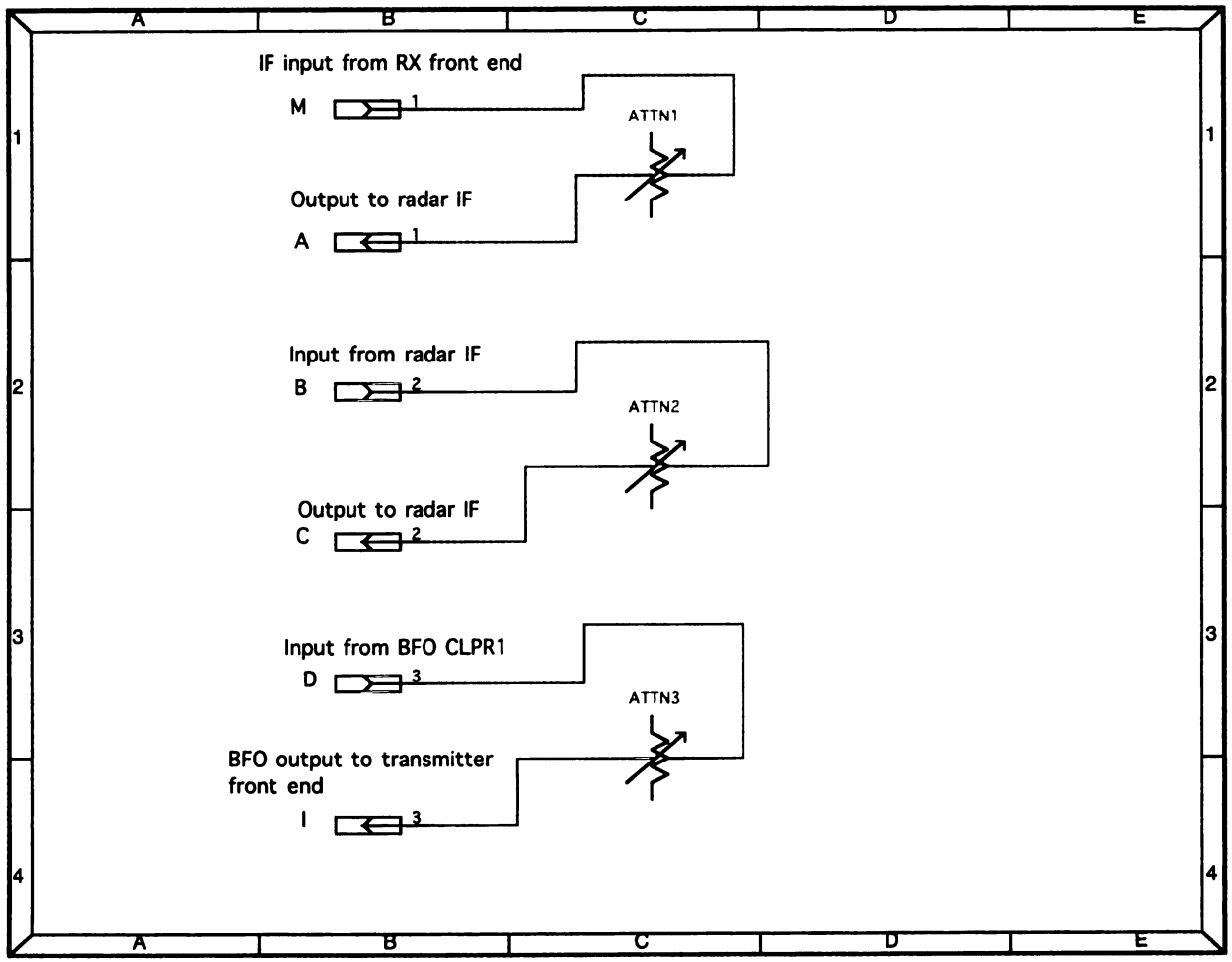

Figure 8.2. Attenuator chassis.

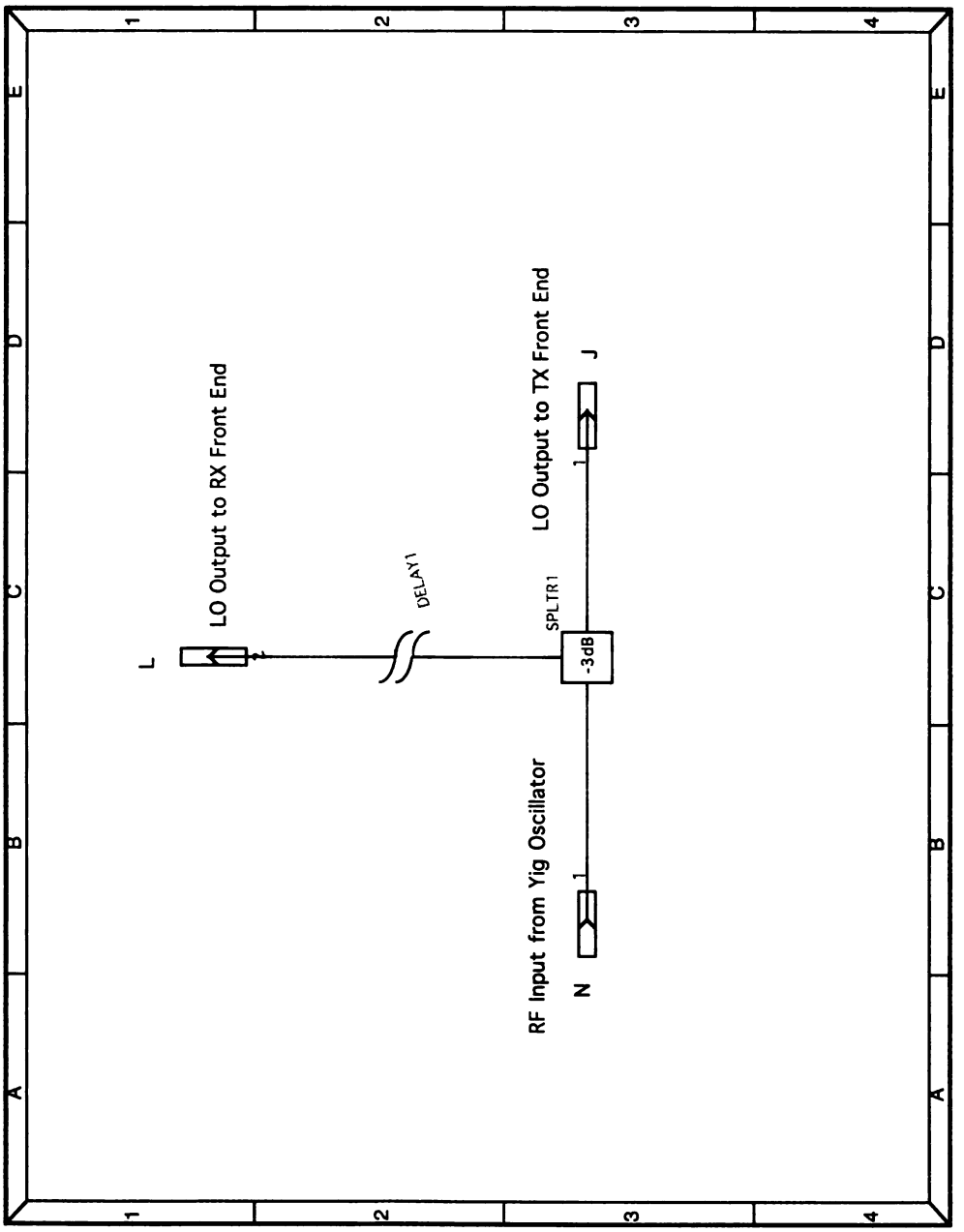

Figure 8.3. Power splitter and delay line.

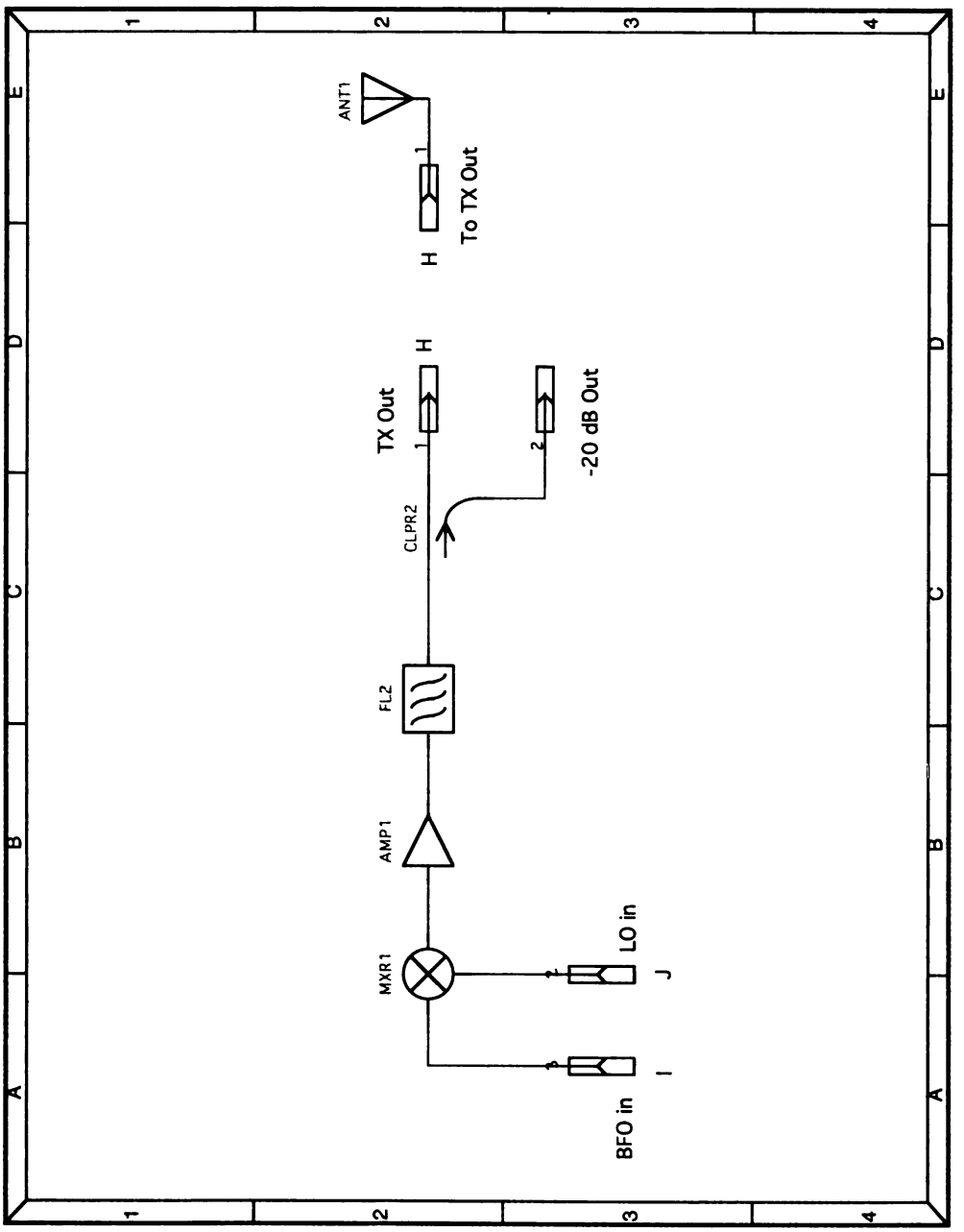

Figure 8.4. S-band transmitter front end.

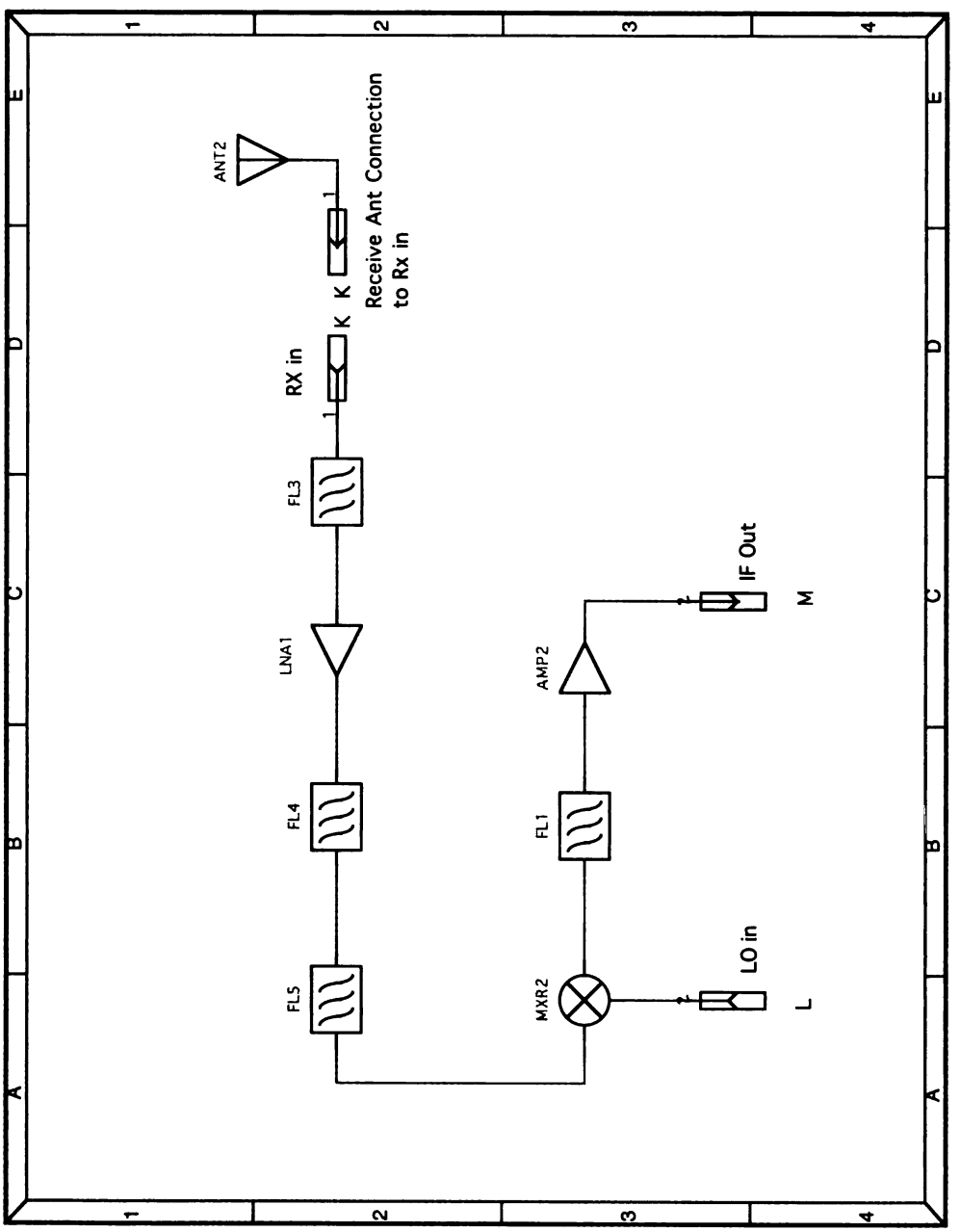

Figure 8.5. S-band receiver front end.

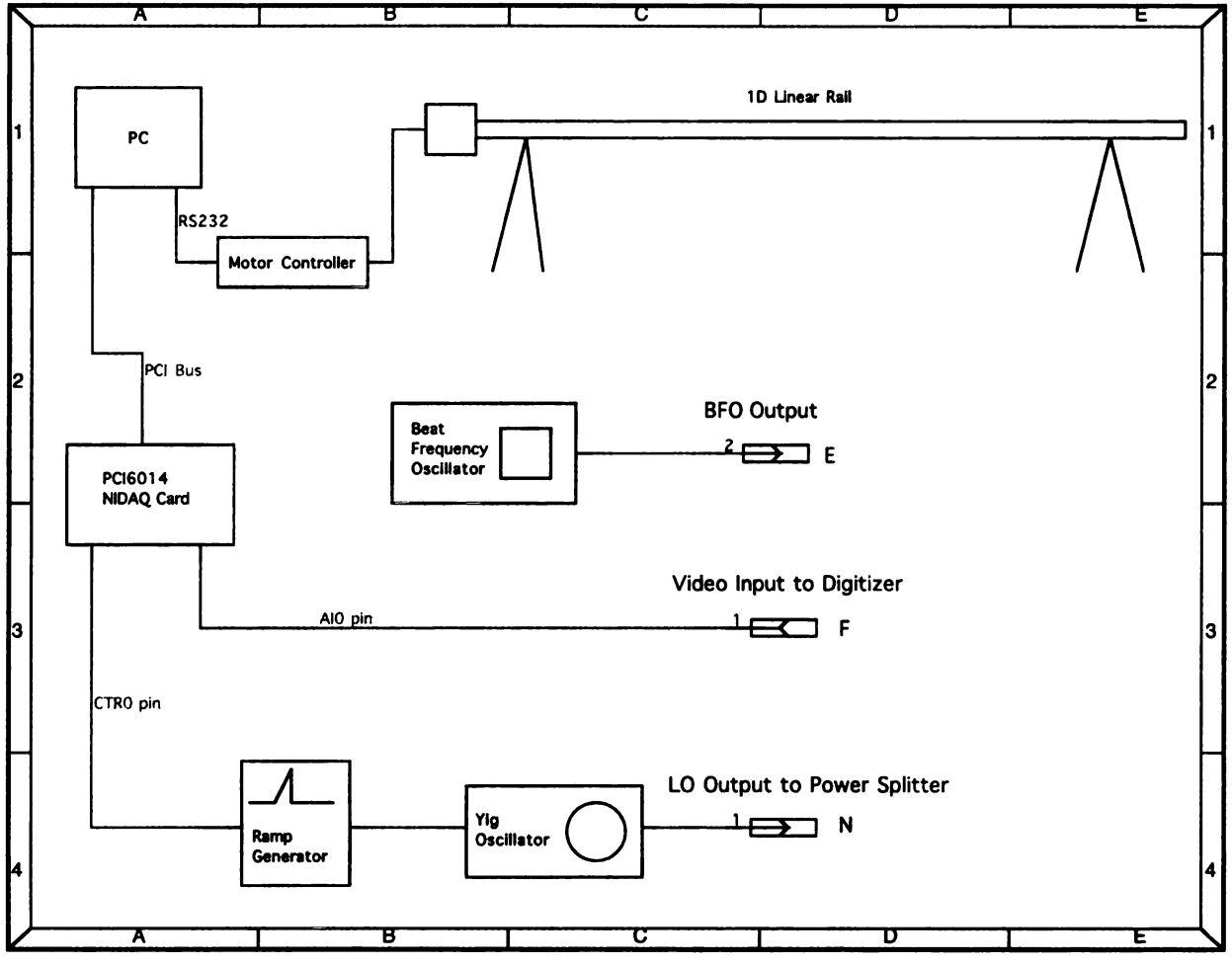

Figure 8.6. High level block diagram of the PC connected to motion control and data acquisition/triggering.

Table 8.1. S-band modular component list.

Component	Description	Figure (if applicable)
AMP1	Mini-Circuits ZJL-4G, Gain=11 dB, IP1=12 dBm, NF=5.5 dB	NA
AMP2	Mini-Circuits ZFL-1000VH, Gain=20 dB, IP1=25 dBm, NF=4.5 dB	NA
AMP3	Mini-Circuits ZKL-2R5, Gain=30 dB, IP1=15 dBm, NF=5 dB	NA
AMP5	Mini-Circuits ZHL-6A, Gain=25 dB, IP1=22 dBm, NF=9.5 dB	NA
ANT1	Linear Tapered Slot Antenna, vertically polarized [71]-[77]	NA
ANT2	Linear Tapered Slot Antenna, vertically polarized [71]-[77]	NA
ATTN1	Surplus 3 position attenuator: thru/-30 dB/load	NA
ATTN2	Kay Model 20 adjustable attenuator	NA
ATTN3	Surplus rotary attenuator	NA
Beat Frequency Oscillator	Hewlett Packard HP3325A Synthesizer/Function Generator	NA
CLPR1	MIni-Circuits ZX30-12-4, 5 MHz to 1 GHz, -12 dB directional coupler	NA
CLPR2	Midwest Microwave, 2 GHz to 4 GHz, -20 dB directional coupler	NA
Delay Line	Misc. microwave coax cables	NA
FL1	Mini-Circuits SLP-10.7, 11 MHz LPF	NA
FL2	Mini-Circuits VLP-41, 4.1 GHz LPF	NA
FL3	Mini-Circuits VHF-1200, 1200 MHz HPF	NA
FL4	Mini-Circuits VHF-1200, 1200 MHz HPF	NA
FL5	Mini-Circuits VLP-41, 4.1 GHz LPF	NA
FL6	Mini-Circuits PLP-10.7, 11 MHz LPF	Figure 8.7
FL7	ECS-10.7-7.5B, 4 pole crystal filter, $f_C = 10.7$ MHz, $B = 7.5$ KHz	Figure 8.7
FL8	ECS-10.7-15B, 4 pole crystal filter, $f_C = 10.7$ MHz, $B = 15$ KHz	Figure 8.7
FL9	ECS-10.7-30B, 4 pole crystal filter, $f_C = 10.7$ MHz, $B = 30$ KHz	Figure 8.7

Table 8.2. S-band modular component list (continued).

Component	Description	Figure (if applicable)
FL10	Mini-Circuits PLP-10.7, 11 MHz LPF	Figure 8.7
FL11	ECS-10.7-7.5B, 4 pole crystal filter, $f_C = 10.7$ MHz, $B = 7.5$ KHz	Figure 8.7
FL12	ECS-10.7-15B, 4 pole crystal filter, $f_C = 10.7$ MHz, $B = 15$ KHz	Figure 8.7
FL13	ECS-10.7-30B, 4 pole crystal filter, $f_C = 10.7$ MHz, $B = 30$ KHz	Figure 8.7
LNA1	Mini-Circuits ZX60-6013E, 20 MHz to 6 GHz, Gain=14 dB, NF=3.3 dB	NA
Motor Controller	RMV SPRT232-ST stepper motor controller	NA
MXR1	Mini-Circuits ZEM-4300MH, 300 MHz to 4300 MHz, Level 13 (+13 dBm LO)	NA
MXR2	Mini-Circuits ZEM-4300MH, 300 MHz to 4300 MHz, Level 13 (+13 dBm LO)	NA
MXR3	Mini-Circuits RAY-6U, Level 23 (+23 dBm LO)	Figure 8.8
PC	PC running Labview, all system control software was written in Labview	NA
PCI-6014	National Instruments PCI-6014 data acquisition and IO card	NA
Ramp Generator	Wilson current mirror [78] based linear ramp generator	Figure 8.10
SPLTR1	Mini-Circuits ZN2PD2-50-S, 500 MHz to 5 GHz, 2-way -3 dB splitter	NA
VideoAmp1	Active LPF, based using the MAX414 op-amp	Figure 8.9
XTAL Filter Mux1	Pin diode selectable crystal filter mux	Figure 8.7
XTAL Filter Mux2	Pin diode selectable crystal filter mux	Figure 8.7
Yig Oscillator	Weinschel Engineering 430A Sweep Oscillator and 432A RF Unit	NA

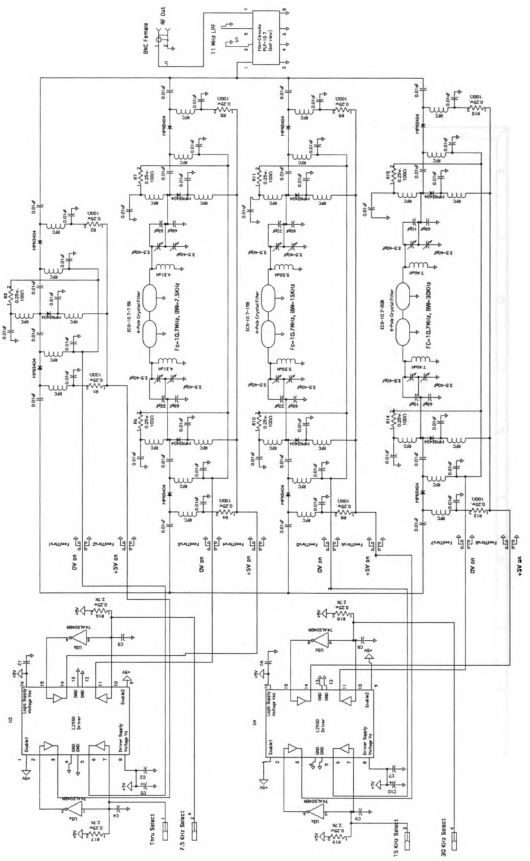

Figure 8.7. Schematic of IF filter switch matrix XTAL Filter Mux1 and XTAL Filter Mux2.

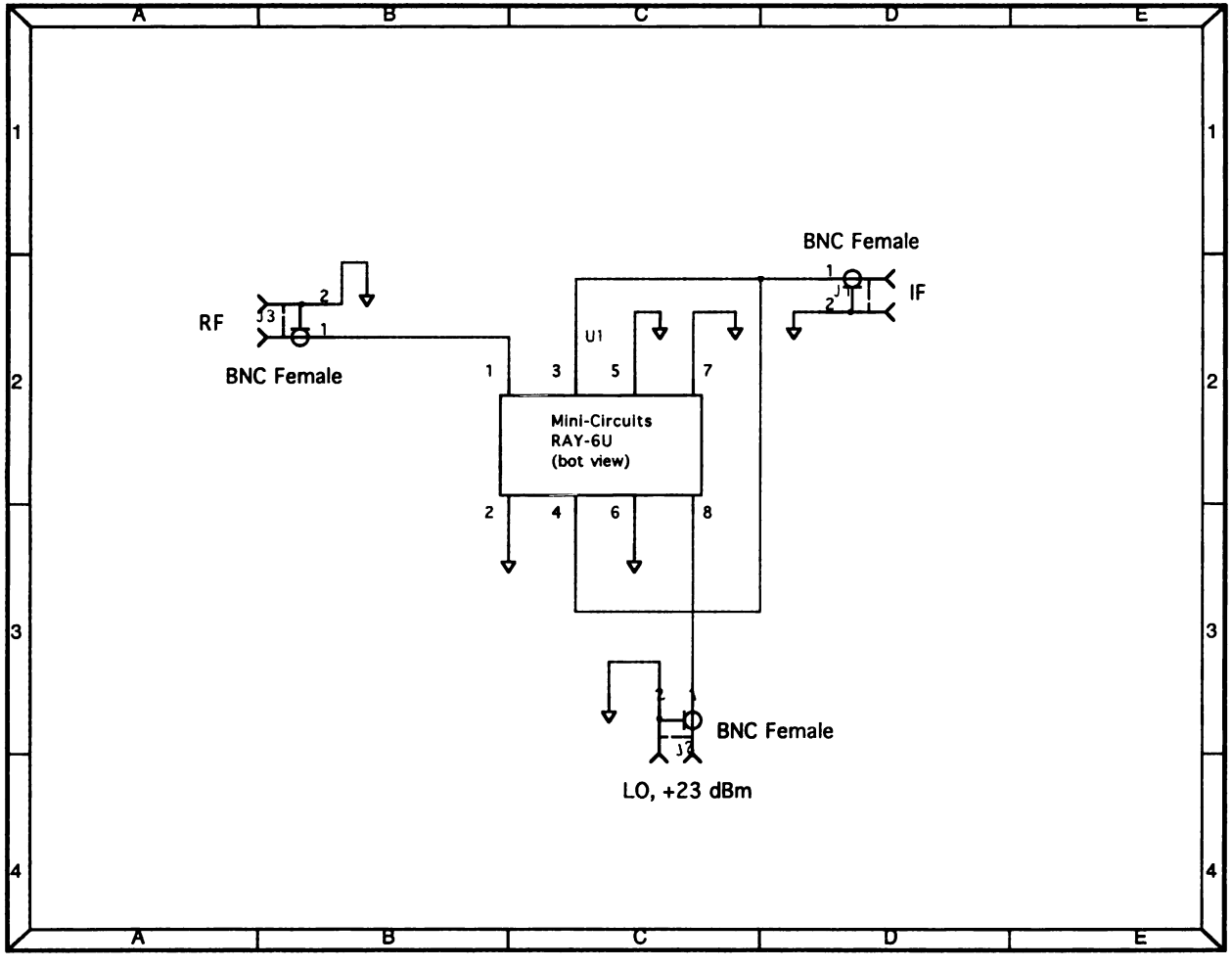

Figure 8.8. Schematic of double balanced mixer module MXR3.

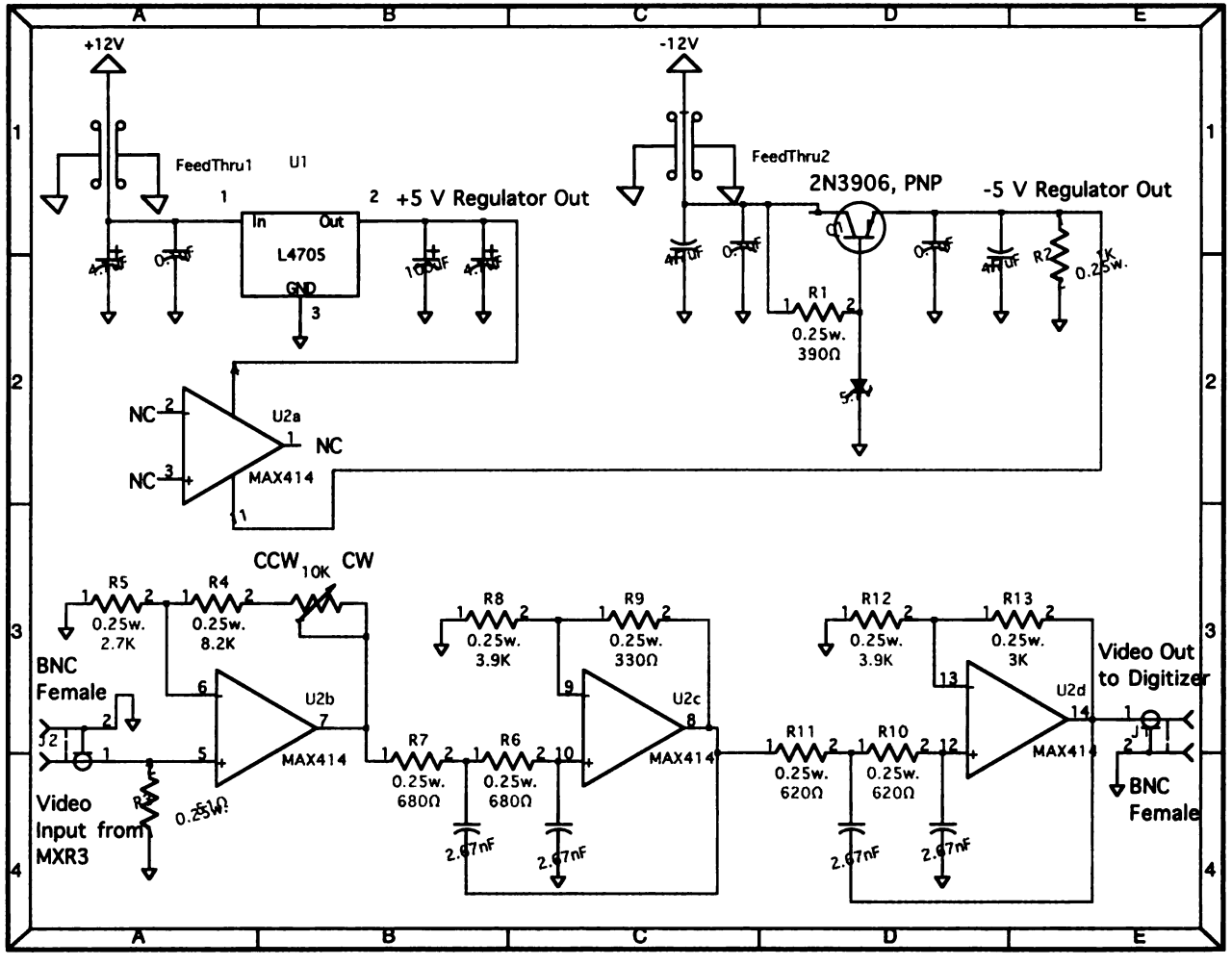

Figure 8.9. Schematic of the video amplifier VideoAmp1.

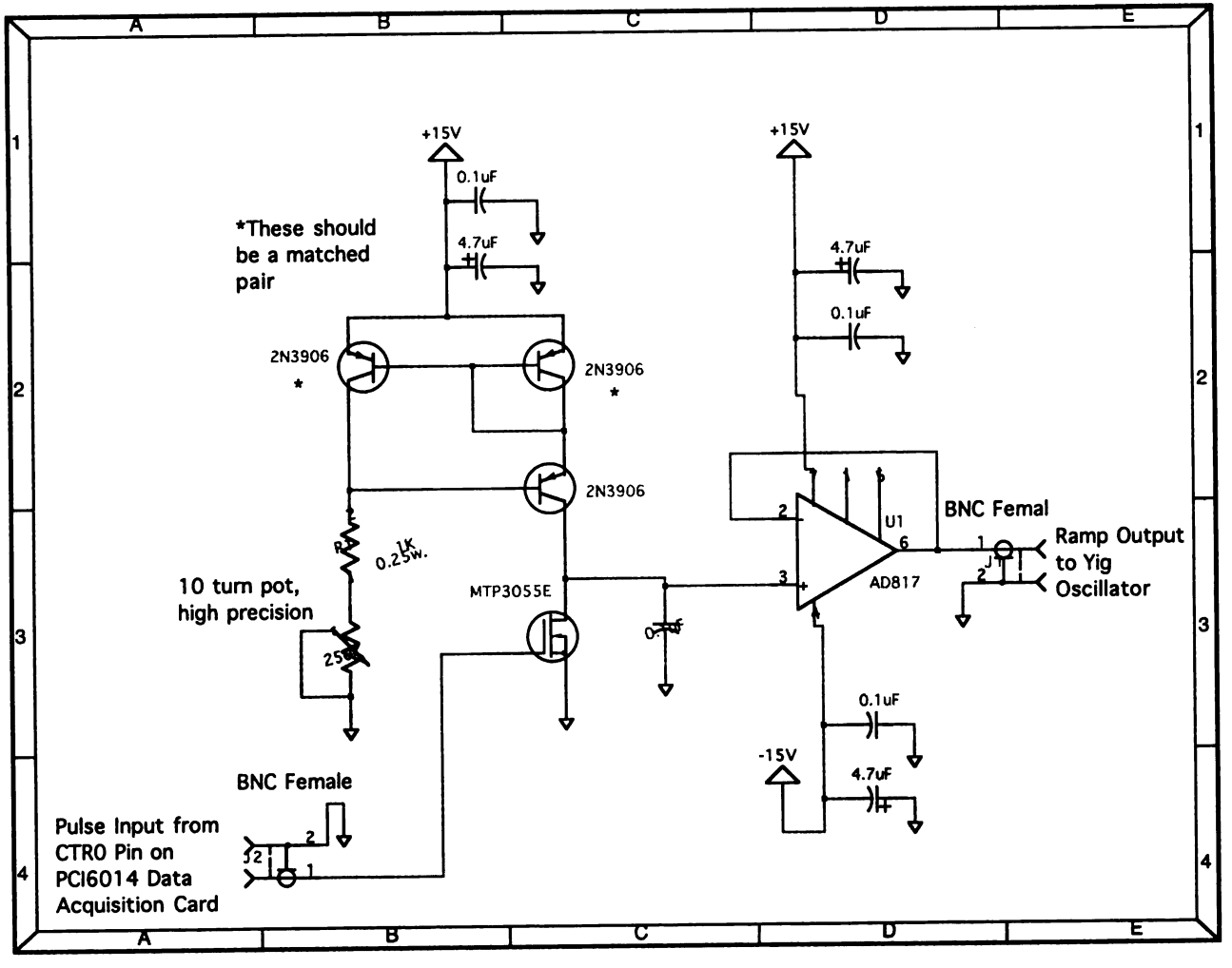

Figure 8.10. Schematic of the Ramp Generator.

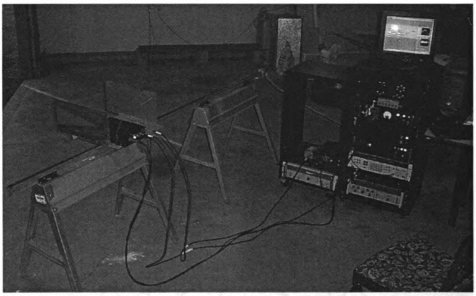

Figure 8.11. The S-band rail SAR imaging system.

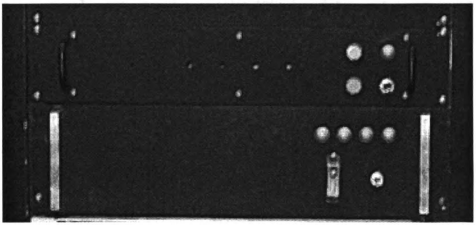

Figure 8.12. Data conditioning hardware, motion control and power supplies.

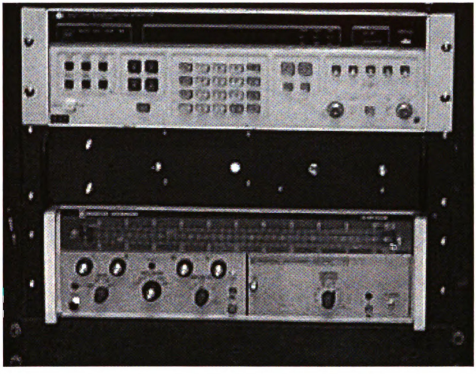

Figure 8.13. From the top down: Hewlett Packard HP3325A Synthesizer/Function Generator BFO, the power splitter chassis and the Weinschel Engineering 430A Sweep Oscillator with the 432A RF Unit.

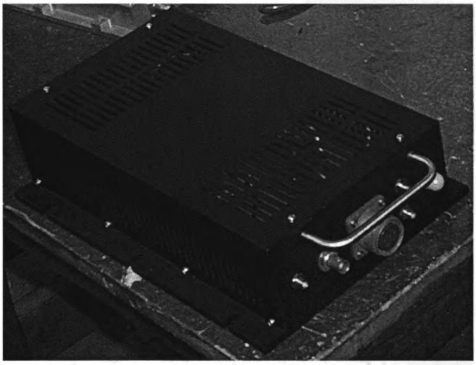

Figure 8.14. The S-band transmitter front end.

Figure 8.15. The S-band receiver front end.

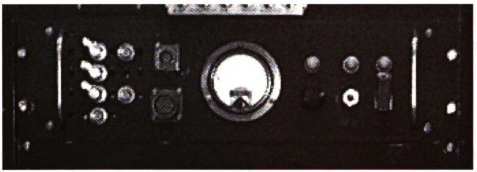

(a)

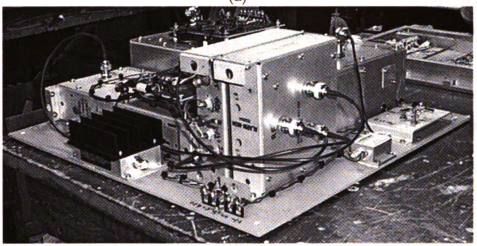

(b)

Figure 8.16. Radar IF (a), inside of the radar IF (b).

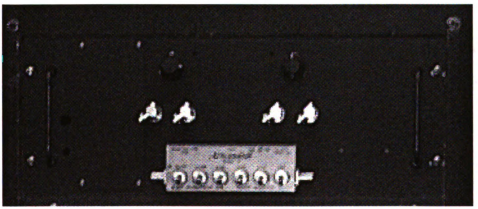

Figure 8.17. ATTN1, ATTN2 and ATTN3 mounted on the attenuator chassis.

CHAPTER 9

THROUGH-DIELECTRIC AND FREE-SPACE S-BAND RAIL SAR IMAGING RESULTS

Using the S-band rail SAR imaging system developed in Chapter 8 radar imaging through two types of lossy dielectrics and free-space will be shown in this chapter. Comparisons between simulations and measured data will be shown. Many interesting results are presented beginning with free-space imagery and low transmit power free-space imagery. Imaging through a 4 inch thick lossy-dielectric slab will be shown where image scenes made up of objects as small as 12 oz aluminum cans and 6 inch tall bolts are imaged. It will be shown that imaging similar target scenes through an unknown lossy-dielectric slab is possible.

9.1 Free-space imaging results

The rail SAR was first setup in a free-space imaging scenario where targets were placed down range from the rail and imaged in free-space without a dielectric slab in the target scene. A transmit power of approximately 10 milliwatts was used for the imagery shown in this section. Experiments were conducted to compare measured cylinder imagery to simulated. Other targets were also imaged in free space.

9.1.1 Comparison of measured and simulated free-space cylinder imagery

Simulated imagery of cylinders using the model developed in Chapter 3 are compared to measured SAR imagery of cylinders. This comparison shows that the imaging system functions properly in free-space. The geometry of this experiment is shown in Figure 9.1 where d_3 is the range from the rail SAR to the cylinder and d_4 is the cross range location of the cylinder with respect to the center of the rail.

Experimental SAR imagery of an $a = 3$ inch radius cylinder located at approxi-

mately $d_3 = 12$ feet and $d_4 = -0.5$ feet is shown in Figure 9.2b. A simulated SAR image of a 2D cylinder with the same dimensions is shown in Figure 9.2a. Measured data closely matches simulated in this case.

Experimental SAR imagery of an $a = 6$ inch radius cylinder located at approximately $d_3 = 12$ feet and $d_4 = -0.5$ feet is shown in Figure 9.3b. A simulated SAR image of a 2D cylinder with the same dimensions is shown in Figure 9.3a. Measured data closely matches simulated data in this case.

9.1.2 Free-space SAR imagery of various targets

It was shown in the previous section that measured and simulated free-space cylinder imagery is in agreement. For this reason free-space SAR imagery was acquired on a number of other other targets. A SAR image of an $a = 4.3$ inch radius sphere is shown in Figure 9.4a. Shown in Figure 9.4b is a SAR image of a group of 6 inch tall 3/8 inch diameter carriage bolts in a block 'S' pattern. A picture of carriage bolts is shown in Figure 9.5a and a picture of the block 'S' target scene is shown in Figure 9.5b.

Both target groups are relatively small at S-band and demonstrate the S-band rail SAR free-space imaging abilities.

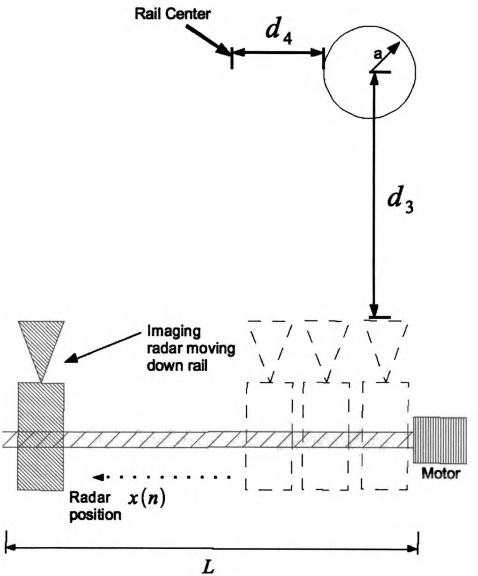

Figure 9.1. Free-space SAR imaging geometry.

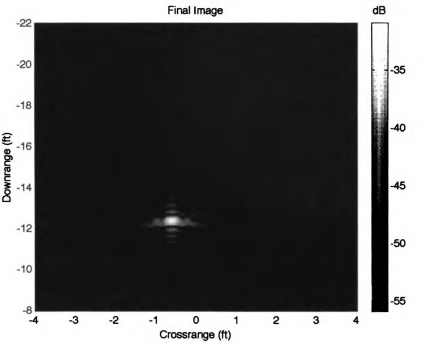

(a)

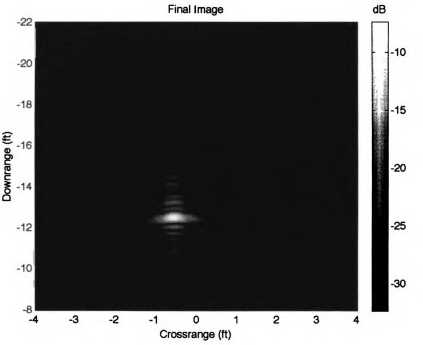

(b)

Figure 9.2. SAR imagery of an $a = 3$ inch radius cylinder in free-space; simulated (a), measured (b).

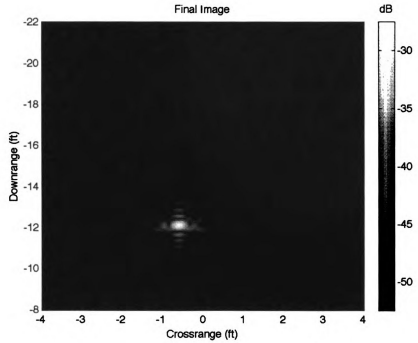

(a)

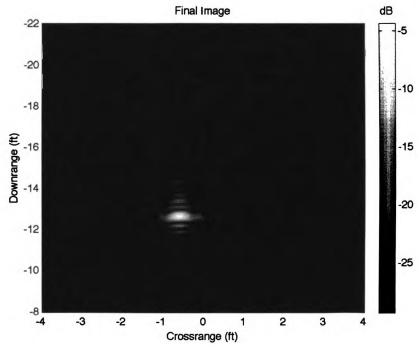

(b)

Figure 9.3. SAR imagery of an $a = 6$ inch radius cylinder in free-space; simulated (a), measured (b).

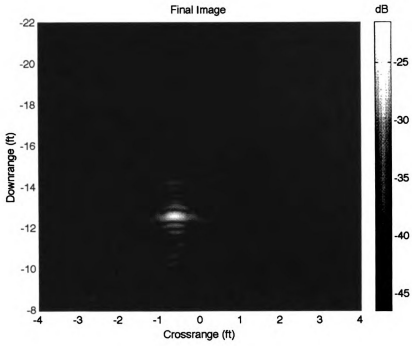

(a)

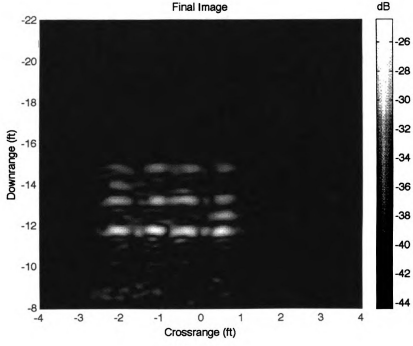

(b)

Figure 9.4. Measured free-space SAR imagery of an $a = 4.3$ inch radius sphere (a), a group of 6 inch tall 3/8 inch diameter carriage bolts in a block 'S' pattern (b).

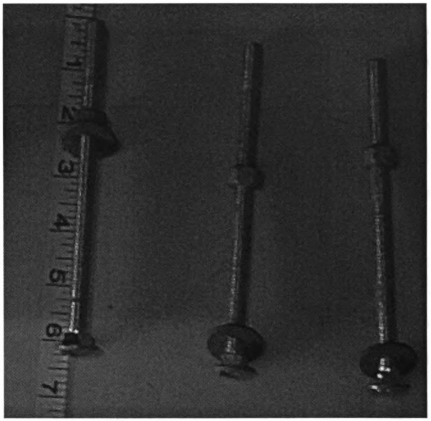

(a)

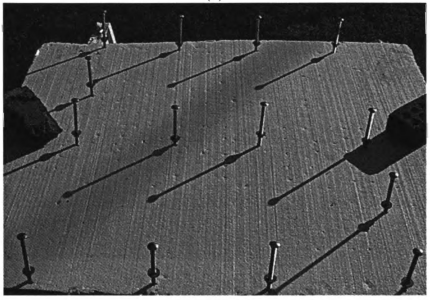

(b)

Figure 9.5. Picture of 6 inch tall 3/8 inch diameter carriage bolts (a), target scene of carriage bolts in a block 'S' pattern (b).

9.2 Low power free-space imaging results

In order to test the high sensitivity radar architecture developed in Chapter 7 it was decided to rail SAR image a number of target scenes using extremely low transmit power. In the previous section rail SAR imagery was acquired at a transmit power level of approximately 10 milliwatts. In this section rail SAR imagery is acquired using 5 picowatts to 10 nanowatts of transmit power at the antenna terminals.

9.2.1 Comparison of measured and theoretical low power free-space cylinder imagery

Using 100 picowatts of transmit power the S-band rail SAR acquired imagery of two different cylinders. This imagery is compared to simulated imagery from the cylinder model in Chapter 3 in this subsection. The imaging geometry for this experiment is shown in Figure 9.1 where both cylinders are located at approximately $d_3 = 12$ feet and $d_4 = 0.5$ feet.

Figure 9.6a shows a simulated SAR image of an $a = 3$ inch radius cylinder. Figure 9.6b shows a measured SAR image of an $a = 3$ inch radius cylinder using 100 picowatts of transmit power. Simulated and measured data are in close agreement and therefore reducing transmit power has little effect on the resulting SAR image in this case.

Figure 9.7a shows a theoretical SAR image of an $a = 6$ inch radius cylinder. Figure 9.6b shows a measured SAR image of an $a = 6$ inch radius cylinder using 100 picowatts of transmit power. Simulated and measured data are in close agreement and therefore reducing transmit power has little effect on the resulting SAR image in this case.

From these results it was shown that reducing the radar transmit power has little effect on the resulting SAR image for cylinders of radius $a = 3$ inch and $a = 6$ inch. These results also show that the free-space model is in agreement with the measurements acquired using low transmit power.

9.2.2 Low power free-space SAR imagery of various targets

In the previous section the radar system has been shown to be capable of imaging cylinders in free space with extremely low transmit power. For this reason it was decided to try imaging a variety of other target scenes using varying levels of transmit power.

Figure 9.8 shows the SAR image of an $a = 4.3$ inch radius sphere using 100 picowatts of transmit power.

A group of 6 inch tall 3/8 inch diameter carriage bolts setup in a block 'S' pattern were imaged at various low transmit powers. A picture of this target scene is shown in Figure 9.5. The bolts imaged using the full transmit power of 10 milliwatts is shown in Figure 9.4b. The same target scene of bolts imaged using a transmit power of only 10 nanowatts is shown in Figure 9.9. Little difference is noticeable between this and the full power image. The target scene of bolts imaged using a transmit power of 100 pico-watts is shown in Figure 9.10. Very little difference is noticeable between this image and the full power image. The target scene of bolts imaged using a transmit power of only 5 pico-watts is shown in Figure 9.11. The top row of bolts in this image begins to fade into the noise.

From these results it was shown that the S-band rail SAR imaging system is very sensitive when operating in free-space without a dielectric slab in the target scene.

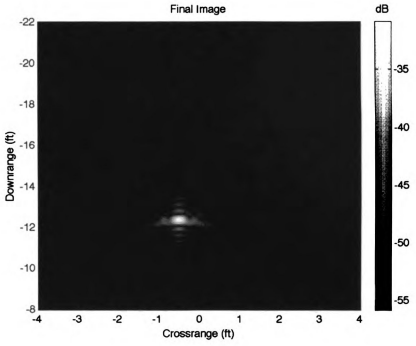

(a)

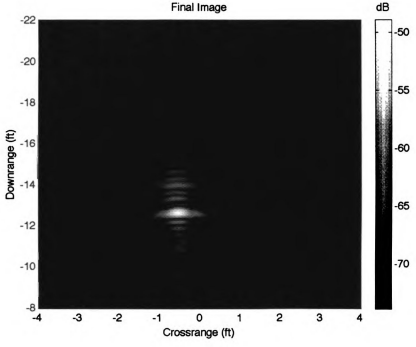

(b)

Figure 9.6. Simulated SAR image of an $a = 3$ inch radius cylinder in free-space (a), measured SAR image of an $a = 3$ inch radius cylinder using a transmit power of 100 picowatts (b).

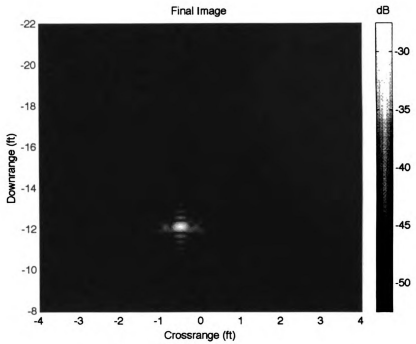

(a)

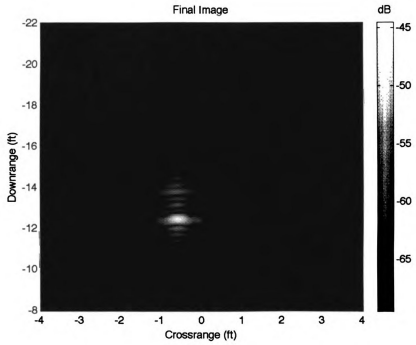

(b)

Figure 9.7. Theoretical SAR image of an $a = 6$ inch radius cylinder in free-space (a), measured SAR image of an $a = 6$ inch radius cylinder using a transmit power of 100 picowatts (b).

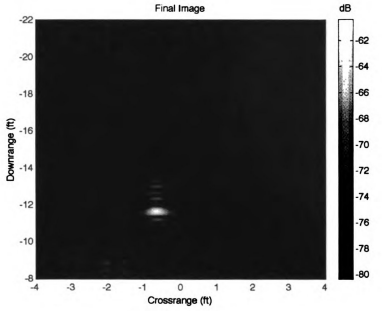

Figure 9.8. SAR image an $a = 4.3$ inch radius sphere in free-space using 100 picowatts of transmit power.

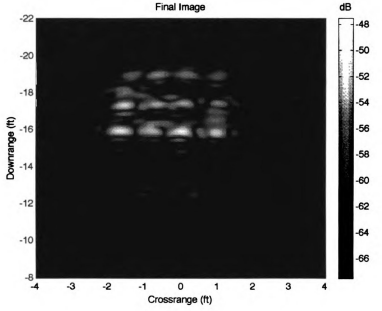

Figure 9.9. SAR image of a group of carriage bolts in free-space using 10 nanowatts of transmit power.

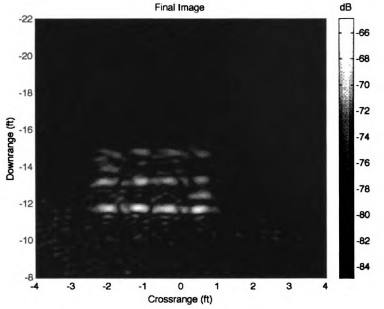

Figure 9.10. SAR image of a group of carriage bolts in free-space using 100 picowatts of transmit power.

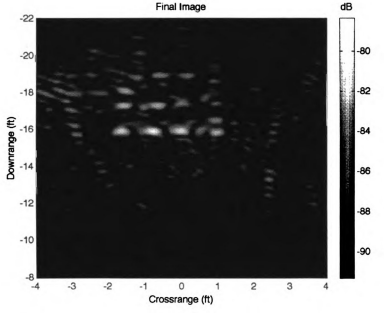

Figure 9.11. SAR image of a group of carriage bolts in free-space using 5 picowatts of transmit power.

9.3 Through-lossy-dielectric slab imaging results

Results are presented in this section of various targets which are imaged through a lossy-dielectric slab. A picture of the slab used for these measurements with a target scene of 12 oz aluminum cans behind it is shown in Figure 9.12. A picture of the imaging geometry with the S-band rail SAR in the foreground is shown in Figure 9.13. For these measurements the radar system was transmitting approximately 10 milliwatts of power at the antenna terminals and it was located approximately 29.5 feet from the slab.

9.3.1 Comparison of measured and simulated through-lossy-dielectric slab imagery of cylinders

In this subsection measured and simulated through-lossy-dielectric slab imagery of cylinders is compared. The simulated imagery was calculated from the model developed in Chapter 5. The geometry of this target scene is shown in Figure 9.14 where $d_1 = 29.5$ feet, $d_3 = 37.5$ feet and $d_4 = 1.1$ feet.

A measured through-lossy-dielectric slab image of a cylinder with a radius of $a = 3$ inches is shown in Figure 9.15b. A simulated through-lossy-dielectric slab image of a cylinder using the same dimensions is shown in Figure 9.15a. Through-slab measured imagery and theoretical imagery are in agreement. There is greater image clutter in the measured image compared to the theoretical. This is due to the high clutter environment from which the measured data was acquired where the cylinder was likely interacting with the background subtracted clutter.

A measured through-lossy-dielectric slab image of an $a = 6$ inch radius cylinder is shown in Figure 9.16b. A simulated through-lossy-dielectric slab image of a cylinder using the same dimensions is shown in Figure 9.16a. Through-slab measured and simulated imagery are in agreement. Increased image clutter is noticeable in the measured image. This is likely due to the highly cluttered laboratory environment from

which the measured data was acquired where the cylinder was probably interacting with the background subtracted clutter.

In both cases the measured results are nearly identical to the simulations. This shows that the rail SAR is effective at imaging targets on the opposite side of a lossy-dielectric slab. This also shows that the plane wave approximation used to develop the through-lossy-dielectric slab model works effectively for modeling this geometry.

9.3.2 Through-lossy-dielectric slab SAR imagery of various targets

It was decided to image a number of targets behind the lossy-dielectric slab. In these experiments the slab was located at $d_1 = 29.5$ feet from the rail SAR imaging system. For these measurements the transmitter was set to an output power level of approximately 10 milliwatts. Targets were placed at various locations behind the lossy-dielectric slab.

A sphere with a radius of $a = 4.3$ inches was imaged through the slab, results are shown in Figure 9.17. The location of the sphere is clearly shown in this image.

An image scene made up of 12 oz aluminum soft drink cans configured in a block 'S' is shown in Figure 9.12. A through slab radar image was taken of this target scene and is shown in Figure 9.18. Most of the cans are visible in this image with some fading into the background clutter.

A target scene made up of three 6 inch tall 3/8 inch diameter carriage bolts (picture of a carriage bolt is shown in Figure 9.5a) placed in a diagonal was imaged behind the slab. A radar image of this target scene is shown in Figure 9.19. The location of each of the three bolts is clearly shown in this image.

From these results it was shown that targets as small as 12 oz aluminum soft drink cans and 6 inch tall bolts can be imaged behind a 4 inch thick lossy-dielectric slab using 10 milliwatts of radar transmit power with the radar located at a stand-off range of 29.5 feet from the slab.

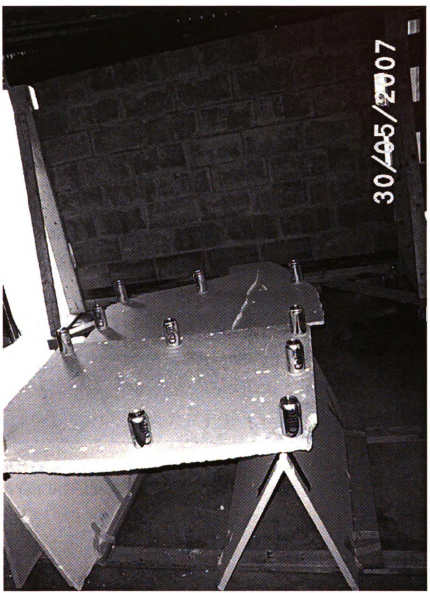

Figure 9.12. The 4 inch thick lossy-dielectric slab.

Figure 9.13. Through-lossy-dielectric slab image scene where the S-band rail SAR is located 29.5 feet from the slab.

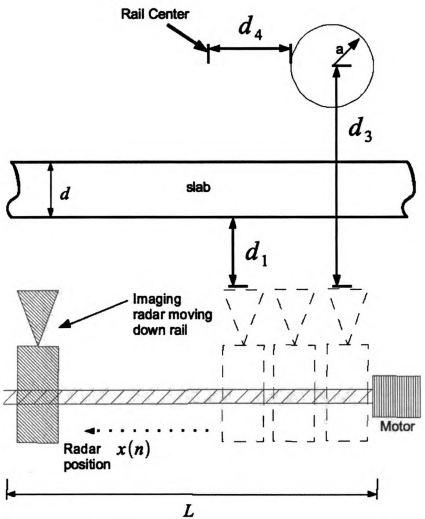

Figure 9.14. Through-slab rail SAR imaging geometry.

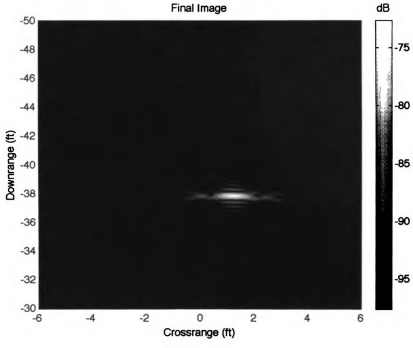

(a)

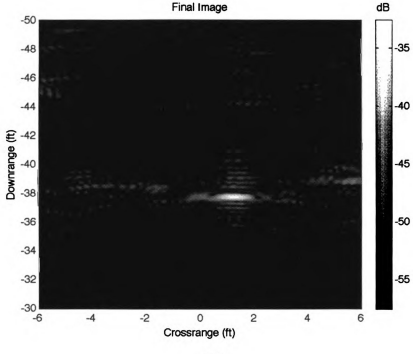

(b)

Figure 9.15. Theoretical SAR image of an $a = 3$ inch radius cylinder behind a 4 inch thick lossy-dielectric slab (a), measured SAR image of an $a = 3$ inch radius cylinder behind a 4 inch thick lossy-dielectric slab (b).

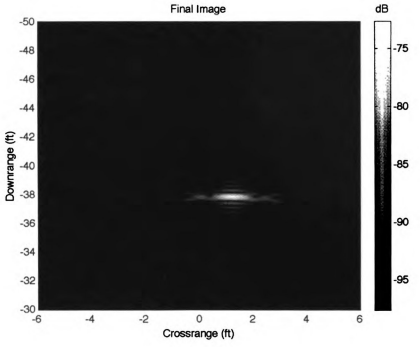

(a)

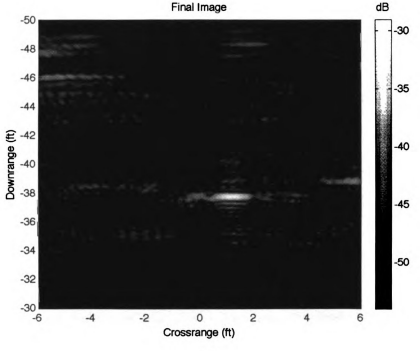

(b)

Figure 9.16. Theoretical SAR image of an $a = 6$ inch radius cylinder behind a 4 inch thick lossy-dielectric slab (a), measured SAR image of an $a = 6$ inch radius cylinder behind a 4 inch thick lossy-dielectric slab (b).

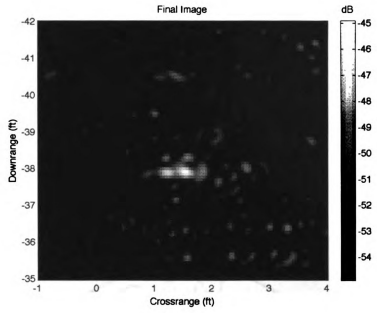

Figure 9.17. Sphere with a radius of $a = 4.3$ inches imaged behind a 4 inch thick lossy-dielectric slab.

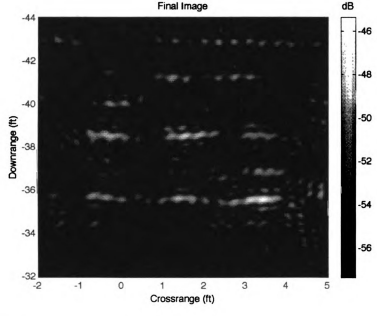

Figure 9.18. 12 oz aluminum beverage cans in a block 'S' configuration imaged behind a 4 inch thick lossy-dielectric slab.

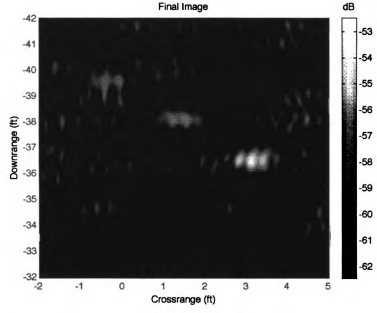

Figure 9.19. Diagonal row of three 6 inch tall 3/8 inch diameter carriage bolts imaged behind a 4 inch thick lossy-dielectric slab.

9.4 Through an unknown lossy-dielectric slab imaging results

It was shown in the previous section that the through-dielectric slab model and measurements were in agreement. It was for this reason that it was decided to test the performance of the S-band rail SAR imaging system on an unknown dielectric slab. This dielectric is not a homogeneous one and it has less loss than the lossy-dielectric slab measured in the previous section. Nothing is known about the electromagnetic properties or the physical composition of this dielectric. A picture of the unknown lossy dielectric slab used in this experiment is shown in Figure 9.20. The transmit power level in these experiments was approximately 10 milliwatts. The unknown slab was located approximately $d_1 = 10$ feet downrange from the rail SAR.

A measured radar image of a cylinder with a radius of $a = 3$ inches located behind the slab is shown in Figure 9.21. A measured radar image of a cylinder with a radius of $a = 6$ inches behind the slab is shown in Figure 9.22. For both images the position of the cylinders is clearly shown and some image distortion due to the slab is noticeable compared to the free space imagery in Figure 9.2b and Figure 9.3b.

Figure 9.23 shows the through-slab measured radar image of a sphere with a radius $a = 4.3$ inches. Noticeable distortion is present around the sphere compared to its free space image in Figure 9.4a.

A through-slab radar image of a group of 6 inch tall 3/8 inch diameter bolts in a block 'S' configuration is shown in Figure 9.24. The position of each bolt is shown however there is more clutter present compared to the free space image in Figure 9.4b.

A variety of target scenes were shown to be imaged behind the unknown lossy dielectric slab in this section. Targets as small as 6 inch tall bolts were detectable. These results show the flexibility of this radar system to image target scenes through unknown dielectric slabs.

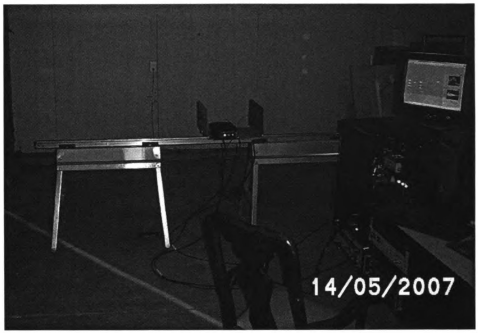

(a)

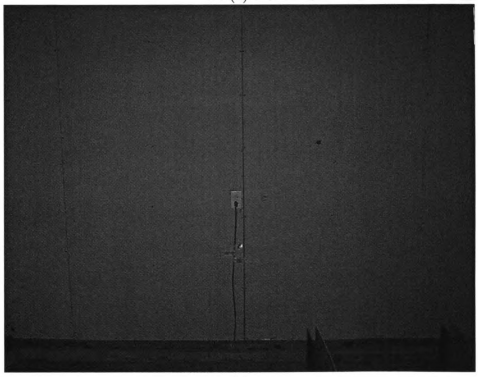

(b)

Figure 9.20. Experimental setup for imaging through an unknown lossy-dielectric slab (a), a close up view of the unknown lossy-dielectric slab (b).

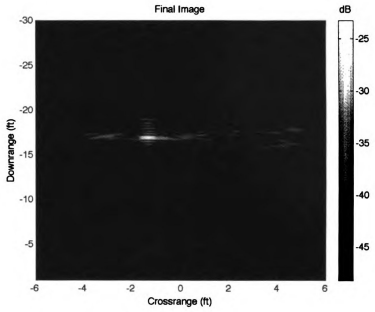

Figure 9.21. A radar image of a cylinder with a radius of $a = 3$ inches behind the unknown dielectric slab.

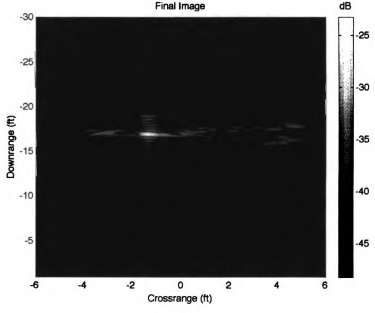

Figure 9.22. A radar image of a cylinder with a radius of $a = 6$ inches behind the unknown dielectric slab.

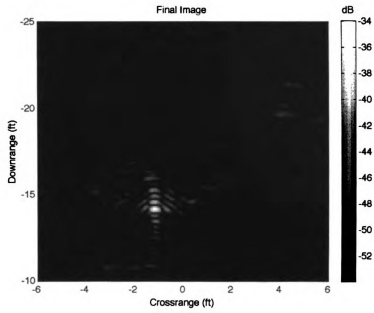

Figure 9.23. A radar image of a sphere with a radius of $a = 4.3$ inches behind the unknown dielectric slab.

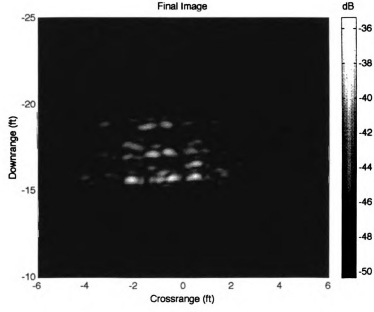

Figure 9.24. A target scene of carriage bolts in a block 'S' configuration imaged behind the unknown dielectric slab.

9.5 Low-power through an unknown lossy-dielectric slab imaging results

The radar imaging through an unknown lossy dielectric slab results from the previous section are replicated in this section using only 10 nanowatts of transmit power at the antenna terminals.

A radar image of a cylinder with a radius of $a = 3$ inches behind the unknown slab is shown in Figure 9.25. A radar image of a cylinder with a radius of $a = 6$ inches behind the uknown slab is shown in Figure 9.26. The image distortion appears to be the same except for slightly less cross range clutter compared to the full power images in Figure 9.21 and Figure 9.22. The position of the cylinders is clearly shown and some image distortion due to the slab is noticeable compared to the free-space cylinder imagery in Figure 9.2b and Figure 9.3b.

Figure 9.27 shows the radar image of a sphere with a radius of $a = 4.3$ inches behind the unknown slab. This image is similar to the full power sphere image in Figure 9.23. Noticeable distortion is present around the sphere compared to its free-space image in Figure 9.4a.

A radar image of a group of carriage bolts in a block 'S' configuration behind the unknown slab is shown in Figure 9.28. This image appears to have less clutter than the full power image in Figure 9.24. This is probably due to target interactions with the unknown slab. The location of the bolts are clearly detectable, however there is more clutter present compared to the free-space image in Figure 9.4b.

These low transmit power results were nearly identical to the full power results. This is an interesting observation and shows how effectively the S-band rail SAR can image through an unknown dielectric slab.

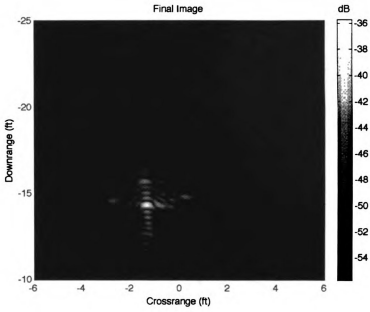

Figure 9.25. A cylinder with a radius of $a = 3$ inches radar imaged behind an unknown slab using 10 nanowatts of transmit power.

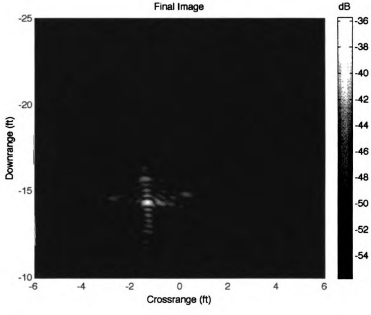

Figure 9.26. A cylinder with a radius of $a = 6$ inches radar imaged behind an unknown slab using 10 nanowatts of transmit power.

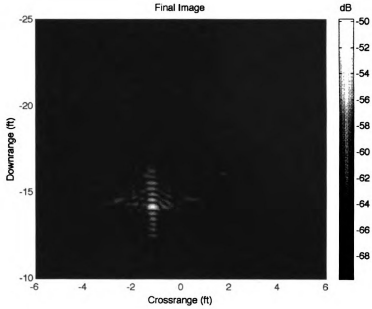

Figure 9.27. A sphere with a radius of $a = 4.3$ inches radar imaged behind an uknown slab using 10 nano-watts of transmit power.

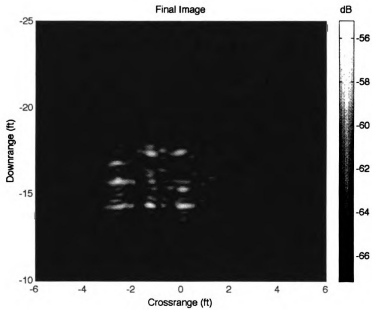

Figure 9.28. A target scene of carriage bolts in a block 'S' configuration radar imaged behind an unknown slab using 10 nanowatts of transmit power.

9.6 Discussion of S-band rail SAR imaging results

In this chapter it was shown that the high sensitivity range-gated FMCW radar architecture developed in Chapter 7 is effective operating as an S-band rail SAR in free space, through a lossy-dielectric slab and through an unknown-dielectric slab.

The theoretical model of a cylinder in free-space was shown to be accurate compared to measured data using full transmit power and low transmit power. The S-band rail SAR has proven itself to be a highly sensitive machine. It was shown in this chapter that imaging objects in free-space as small as carriage bolts using only 5 picowatts of transmit power is possible.

Imaging through a lossy-dielectric slab was achieved. The theoretical model was in agreement with measured results. The S-band rail SAR could image target scenes made up of objects as small as soda cans and carriage bolts behind a 4 inch thick lossy-dielectric slab.

Imaging through an unknown dielectric slab was shown to be possible using the S-band rail SAR. Image scenes made up of objects as small as aluminum beverage cans and 6 inch tall bolts were imaged through the unknown slab. These results were replicated using only 10 nanowatts of transmit power.

In this chapter the model was shown to agree with the measured results. The high sensitivity range-gated FMCW radar architecture was shown to be very effective in imaging through lossy-dielectric slabs and in free space. These results are encouraging and it is for this reason that the next step in through-slab radar imaging development will be to build a high speed antenna array so that near real-time radar imagery of what is behind an unknown slab can be displayed to the radar operator. This near real-time system development will be shown later in this dissertation.

CHAPTER 10

X-BAND RAIL SAR IMAGING SYSTEM

An X-band front end was developed which plugs directly into the IF and control systems of the S-band rail SAR developed in Chapter 8 changing it into an X-band rail SAR imaging system. This X-band rail SAR imaging system design was based on the high sensitivity range-gated FMCW radar architecture developed in Chapter 7. It will be shown in this chapter that the X-band rail SAR is capable of imaging target scenes made up of pushpins using only 10 nanowatts of transmit power. Imaging results from the X-band rail SAR will be compared to a direct conversion FMCW radar system from [60]. In this chapter it will be shown that the high sensitivity range-gated FMCW radar architecture is highly effective at X-band for applications such as RCS measurement.

10.1 High sensitivity range-gated FMCW X-band radar front end

A block diagram of the X-band front end is shown in Figure 10.1 and a list of all components in Table 10.1. A picture of the X-band front end is shown in Figure 10.3. The X-band front end was developed to plug into the radar IF and control assemblies from Chapter 8. This allows the X-band front end to operate according to the high sensitivity range-gated FMCW radar architecture developed in Chapter 7.

In order to operate at X-band the YIG Oscillator is modified by removing the 432A RF Unit from the Weinschel Engineering 430A Sweep Oscillator and replacing it with the 434A RF Unit which is capable of linear tuning from 7.835 GHz to 12.817 GHz. The chirp rate c_r is increased significantly when using the 434A RF Unit because the 434A RF unit covers more frequency than the S-band 432A RF Unit but the chirp time remains the same.

The power splitter chassis shown in the block diagram in Figure 8.3 is no longer

used when using the 434A RF Unit. The output of the 434A RF Unit is fed directly into the front end YIG Oscillator LO Input port shown in the X-band front end block diagram in Figure 10.1. From this the LO is fed through CLPR4 which is a Omni Spectra X-band -10 dB directional coupler. The output of CLPR4 is fed through ATTN4 and ATTN6 which are 3 dB and 6 dB attenuators. The output of ATTN6 feeds CIRC1 which is a UTE Microwave X-band isolator. The output of CIRC1 is fed into the LO port of MXR4 which is a Watkins Johnson M31A mixer. Some of the signal is coupled off of CLPR4 and fed through CIRC2 which is a UTE Microwave X-band isolator. The output of CIRC2 is fed through a coaxial delay line DELAY2. The output of DELAY2 feeds the LO port of the mixer MXR5.

The coupled BFO output from ATTN3 in Figure 8.2 feeds into the BFO In port on the X-band front end block diagram in Figure 10.1. The BFO mixes with the X-band LO and the output of MXR4 is fed into AMP6 which is a Microwave Components Corporation MH858231, Gain=25 dB, IP1=23 dBm. The output of AMP6 is fed through CIRC3 which is an X-band isolator. The output of CIRC3 is fed out of the front end assembly to either a step attenuator ATTN5 or a through line. ATTN5 is a Narda Microline Step Attenuator Model 705-69. ATTN5 is used to reduce the transmit power when acquiring low power rail SAR measurements. The output of either the through line or ATTN5 is fed through CLPR3 then to the transmitter antenna ANT3. CLPR3 is a -20 dB directional coupler. ANT3 is a Microtech 205297 X-band horn with a WR90 waveguide flange. The X-band microwave signals fed into ANT3 are radiated out towards the target scene. Some of the transmit signal is coupled off CLPR3 for diagnostic purposes.

Scattered X-band signals from the target scene are received by ANT4 which is a Microtech 205297 X-band horn with a WR90 waveguide flange. The output of ANT4 is amplified by LNA2 which is an Amplica Inc. XM553403, Gain=20dB, IP1=25 dBm. The output of LNA2 is fed into the RF port of MXR5 which is a TRW Microwave

MX18533. The IF output of MXR5 is amplified by AMP7 which is a Mini-Circuits MAR-4, Gain = 8 dB, NF=6 dB, IP1=12.5 dBm, schematic shown in Figure 10.2 . The output of AMP7 is fed into filter FL14 which is a Mini-Circuits PBP-10.7, 10.7 MHz bandpass filter, schematic also shown in Figure 10.2. The IF output of FL14 is fed out to the IF input of ATTN1 in the attenuator chassis shown in Figure 8.2.

X-band rail SAR imaging is achieved by plugging the X-band front end in to the existing S-band radar IF and mounting the X-band front end on to the linear rail. The same imaging algorithm and MATLAB codes are used for SAR imaging except that a few numbers are changed. When using the X-band front end the radar chirp rate is $c_r = 500 \cdot 10^9$ Hz/S. The transmit power is approximately 10 milliwatts and adjustable down to picowatts. The aperture spacing across the linear rail is different: the radar traverses only 90 inches (rather than 96 inches at S-band) acquiring range profile data every 1 inch (rather than every 2 inches at S-band).

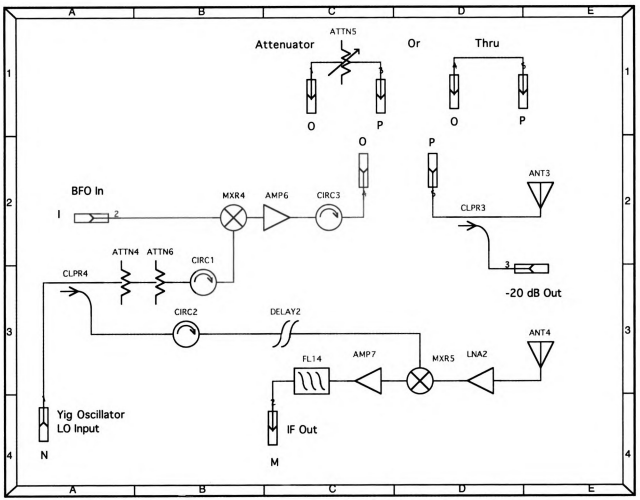

Figure 10.1. Block diagram of the X-band front end.

Table 10.1. X-band front end modular components list.

Component	Description	Figure (if applicable)
AMP6	Microwave Components Corporation MH858231, Gain=25 dB, IP1=23 dBm	NA
AMP7	Mini-Circuits MAR-4, Gain = 8, NF=6 dB, IP1=12.5 dBm	Figure 10.2
ANT3	Microtech 205297, X-band horn with WR90 waveguide flange	NA
ANT4	Microtech 205297, X-band horn with WR90 waveguide flange	NA
ATTN4	3 dB in line attenuator	NA
ATTN5	Narda Microline Step Attenuator, Model 705-69	NA
ATTN6	Midwest Microwave 6 dB in line attenuator	NA
CIRC1	UTE Microwave X-band isolator	NA
CIRC2	UTE Microwave X-band isolator	NA
CIRC3	Unknown surplus X-band isolator	NA
CLPR3	Unknown surplus X-band -20 dB directional coupler	NA
CLPR4	Omni Spectra X-band -10 dB directional coupler	NA
DELAY2	Coaxial delay line	NA
FL14	Mini-Circuits PBP-10.7, 10.7 MHz bandpass filter	Figure 10.2
LNA1	Amplica, Inc. XM553403, Gain=20dB, IP1=25 dBm	NA
MXR4	Watkins Johnson M31A	NA
MXR5	TRW Microwave MX18533	NA

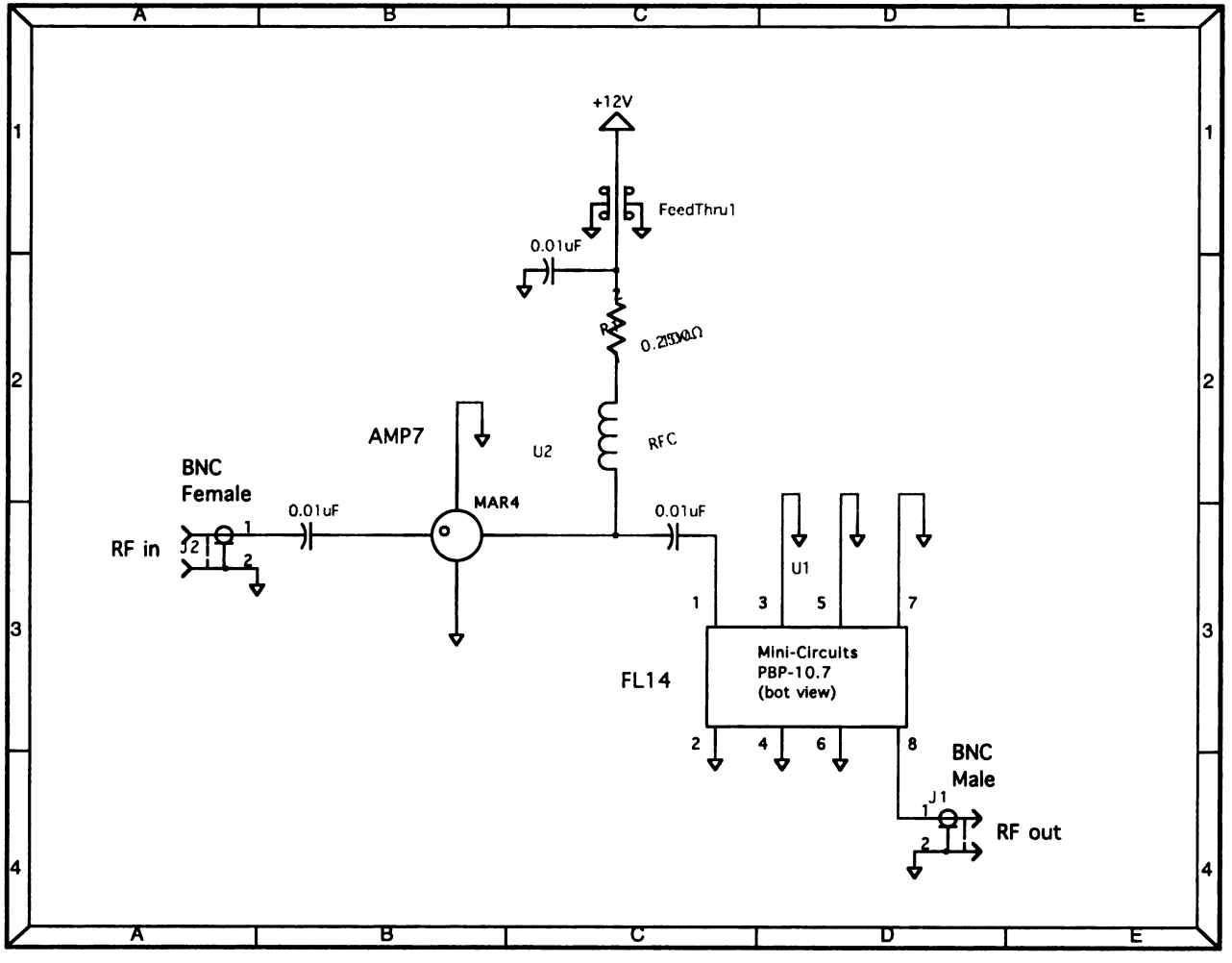

Figure 10.2. Schematic of the module that contains AMP7 and FL14.

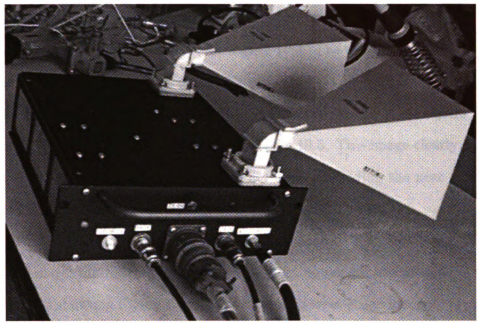

(a)

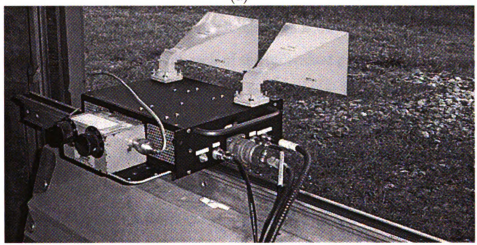

(b)

Figure 10.3. X-band front end (a), X-band front end in operation with adjustable transmit attenuator ATTN5 in line (b).

10.2 Free-space X-band imaging

A 1:32 scale model F14 and a group of pushpins were imaged using the X-band rail SAR. Approximately 10 milliwatts of transmit power was used for the measurements shown in this section. All measurements were acquired outdoors. A picture of the outdoor experimental setup is shown in Figure 10.4. The targets were placed on the styrofoam table down range in front of the rail.

A rail SAR image of a 1:32 scale model F14 aircraft coated in aluminum foil was measured. The resulting image is shown in Figure 10.5. This image clearly shows an aircraft slightly off-axis. Many details are noticeable including the nose and wings. Much of the metal surface was illuminated in this radar image.

A rail SAR image of a group of pushpins was acquired. Pushpins are the small plastic and metal thumbtacks that are used to hold up papers and posters. A picture of a pushpin is shown in Figure 10.6a. A picture of a target group made up of pushpins is shown in Figure 10.6b. A radar image of a group of pushpins was acquired and is shown in Figure 10.7. The location of all pushpins is clearly shown. Looking at this radar image it is possible to count each of the individual pushpins. Some cross range blurring on the pushpins making up the 'G' is noticeable. This was likely due to wind gusts on the day this image was acquired. Fading out is noticeable at the bottom of the '92.' This is due to the -3 dB cutoff of the range-gate which happened to be set too close to the bottom of the target scene.

A zoomed out radar image of the group of pushpins is shown in Figure 10.8. No additional downrange clutter and very little crossrange clutter is present in this image. This image demonstrates the effectiveness of the range-gate in an X-band imaging scenario.

The results shown in this section demonstrate the effectiveness of the high sensitivity range-gated FMCW architecture used for X-band high resolution SAR imaging

applications. A system such as this could be used for radar cross section measurements (RCS) or other applications requiring a sensitive radar system with a range-gate.

Figure 10.4. The X-band rail SAR and target scene.

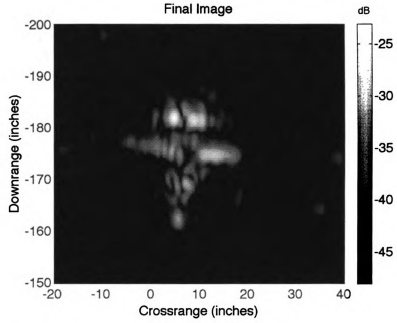

Figure 10.5. X-band rail SAR image of a 1:32 scale F14 model.

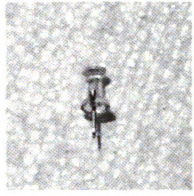

(a)

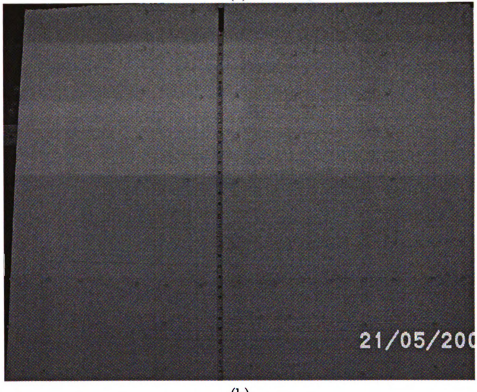

(b)

Figure 10.6. One pushpin (a), image scene of 'GO STATE' in pushpins (b).

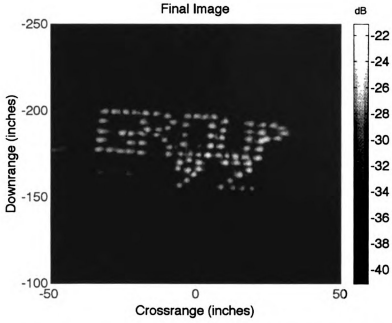

Figure 10.7. X-band rail SAR image of a group of pushpins.

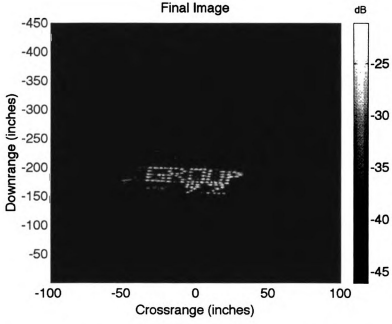

Figure 10.8. Zoomed-out X-band rail SAR image of a group of pushpins.

10.3 Low power free-space X-band imaging

In Section 9.2 it was shown that extremely low transmit power could be used to image a target scene at S-band. For this reason it was decided to place an attenuator in the transmitter signal chain of the X-band front end and image groups of pushpins using low transmit power.

An X-band rail SAR image was acquired of a group of pushpins using only 100 nanowatts of transmit power. This result is shown in Figure 10.9. This image is nearly identical to the full power image of a group of pushpins shown in Figure 10.7 (except for the text in the image). Clutter and signal-to-noise are nearly identical in both images.

An X-band rail SAR image was acquired of a group of pushpins using only 10 nanowatts of transmit power. This result is shown in Figure 10.10. The pushpins further down range in this image have faded into the noise compared to the full power image shown in Figure 10.7. All pushpins in this image are clearly visible.

An X-band rail SAR image was acquired of a group of pushpins using only 1 nanowatt of transmit power. This result is shown in Figure 10.11. Only a few pushpins on the bottom row of letters are visible. This transmit power level is too low for use in imaging small targets such as pushpins.

These low power results demonstrate the effectiveness of the high sensitivity range-gated radar architecture applied to X-band. A low power radar system such as this one could be used for RCS measurements and detection applications such as automotive radar. Based on the low-power results presented in this section a radar system using this architecture could be developed to easily meet various federal regulations for transmit power allowing for the widespread use of high performance low power radar sensors.

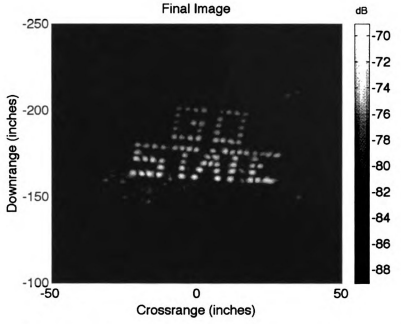

Figure 10.9. X-band rail SAR image of a group of pushpins using 100 nanowatts of transmit power.

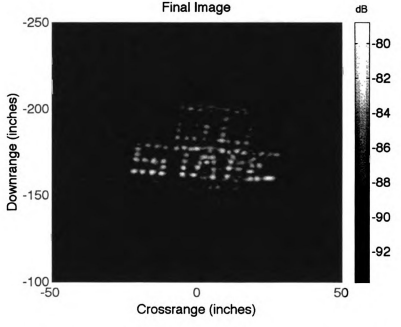

Figure 10.10. X-band rail SAR image of a group of pushpins using 10 nanowatts of transmit power.

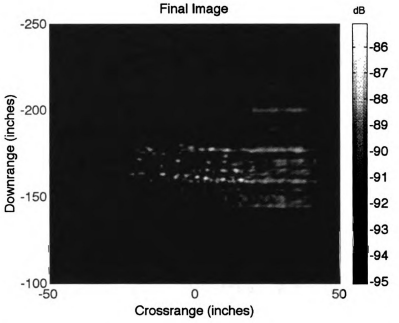

Figure 10.11. X-band rail SAR image of a group of pushpins fading into the noise using 1 nanowatt of transmit power.

10.4 Comparison of high sensitivity range-gated FMCW to a typical FMCW radar imaging system

A low cost X-band rail SAR imaging system was developed in [60] capable of imaging small objects such as scale model aircraft and pushpins. The radar system developed for [60] was a simple direct conversion FMCW system. FMCW radar architecture was discussed in Section 7.3.1. In this section imagery from the radar system developed in [60] will be compared to radar imagery produced by the X-band rail SAR developed in this chapter which is based on the high sensitivity range-gated FMCW radar architecture.

Figure 10.12 shows a radar image of a 1:32 scale model F14 aircraft from [60]. Figure 10.5 shows a radar image of the same model acquired using the X-band rail SAR. Both images are in agreement.

Figure 10.13 shows a radar image of a pushpin target scene from [60]. Figure 10.7 shows a radar image of a pushpin target scene measured using the X-band rail SAR. The image from [60] in Figure 10.13 shows more clutter and the amplitude return of the pushpins in the last few rows is shown fading into the noise.

A zoomed-out pushpin image from [60] is shown in Figure 10.14. Much clutter is present down range and some cross range. By contrast, the zoomed out image acquired by the X-band rail SAR shown in Figure 10.8 contains no noticeable downrange clutter due to the range gate and much less cross range clutter.

In this section it was shown that the high resolution range-gated FMCW radar architecture is more effective compared to direct conversion FMCW for small rail SAR applications where down range clutter must be eliminated and high sensitivity is required.

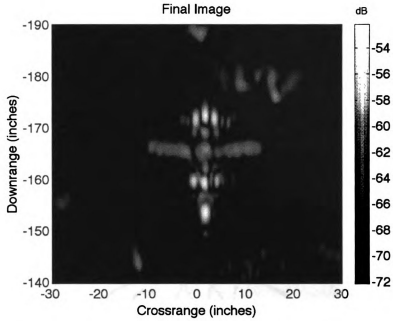

Figure 10.12. SAR image of a 1:32 scale model F14 using a direct conversion FMCW radar system.

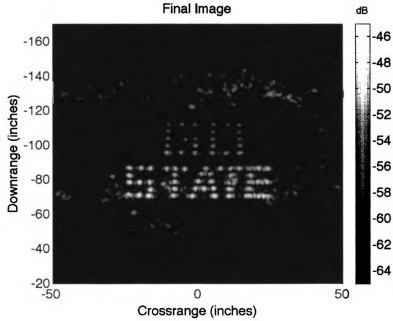

Figure 10.13. SAR image of a group of pushpins using a direct conversion FMCW radar system.

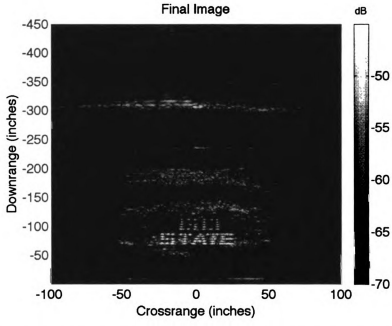

Figure 10.14. Zoomed out SAR image of a group of pushpins using a direct conversion FMCW radar system showing the presence of significant clutter outside the target scene of interest.

10.5 Discussion of X-band rail SAR imaging results

In this chapter it was shown that the high sensitivity range-gated FMCW radar architecture developed in Chapter 7 can be applied to the X-band frequency range. This application was shown to be an effective use of the high resolution range-gated FMCW radar architecture. High resolution imagery of model aircraft and groups of pushpins were acquired. Extremely low transmit power imagery of pushpin target scenes were acquired. It was shown that this X-band rail SAR imaging system is more effective than previous direct conversion FMCW radar systems [60] in reducing downrange clutter. With its simplicity of design this radar architecture could be used for RCS measurements, automotive radar, or other radar sensor applications where low transmit power, high sensitivity and range gating are attractive features on a low-budget.

CHAPTER 11

HIGH SPEED SAR IMAGING ARRAY

It takes 7 to 10 minutes to acquire data using the S-band rail SAR imaging system developed in Chapter 8. This is too slow for practical applications that might result from this research. In this chapter a near real-time proof-of-concept array based SAR imaging system is developed that meets these requirements. This system is capable of acquiring data and processing a SAR image of a target scene continuously on a computer screen with an update rate of up to 1 image every 1.9 seconds. This allows for the ability to quickly locate and track targets behind dielectric slabs.

It will also be shown in this chapter that the high sensitivity range-gated FMCW radar architecture developed in Chapter 7 is capable of operating at high speeds. The S-band radar system developed in Chapter 8 will be used as the radar sensor connected to the high speed imaging array developed in this chapter. This radar will be shown to operate at high speeds while imaging targets in free-space and through a lossy-dielectric slab in near real-time.

11.1 SAR on an array

When imaging a target scene using a rail SAR the radar sensor physically moves down a linear track acquiring range profile data at known locations (see Figure 2.1). For the case of the S-band rail SAR imaging system developed in Chapter 8 the radar sensor is mounted on an 8 foot long linear rail and it acquires a range profile once ever 2 inches. Rather than physically moving the radar down a rail it is possible to electronically switch the radar antenna (assuming a mono-static radar in this case) between 48 antenna elements which are evenly spaced every 2 inches apart. This array would be equivalent to a rail SAR acquiring data every 2 inches 48 times down an 8 foot long rail, see Figure 11.1.

The problem with this simple array is that it requires a large number of elements; 48 elements, one for every rail position. The S-band radar system developed in Chapter 8 is a bi-static radar which uses a separate transmit and receive antennas. When the transmit and receive elements are close to each other relative to the range to target scene they are equivalent to one single element at the mid-point. This is known as the phase center. The phase center is equivalent to a mono-static radar antenna at the mid-point between a closely spaced transmit and receive element as shown in Figure 11.2. In order to make the equivalent array in Figure 11.1 using a bi-static radar it would require 48 transmit antennas and 48 receive antennas for a total of 96 antennas as shown in Figure 11.3. This is a large number of antenna elements, expensive and complicated to implement. However, when using a bi-static radar, thoughtful design can utilize careful positioning of bi-static elements to maximize the number of phase centers with the fewest antenna elements possible.

A better use of transmit and receive elements is shown in Figure 11.4 where using the spacing shown and combinations of two receive elements and six transmit elements yields 12 phase centers. This is done by switching the receiver on to only one receive element at a time and by switching the transmitter on to only one transmit element at a time. By switching combinations of transmit and receive elements the number of phase centers created is maximized. The combinations are shown in Figure 11.4 by straight lines running through their corresponding receive element, transmit element, and resulting phase center. This is a much lower cost option. A large array is built for a relatively low cost in the next section by cascading a number of these together to create a 44 phase center array using only eight receive elements and 13 transmit elements.

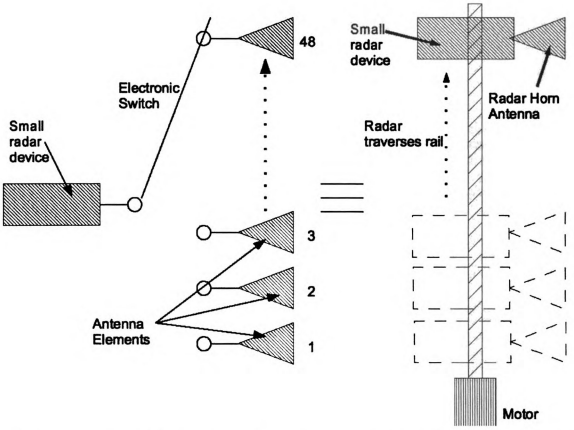

Figure 11.1. A radar device electronically switched across an array of evenly spaced antenna elements is equivalent to a rail SAR.

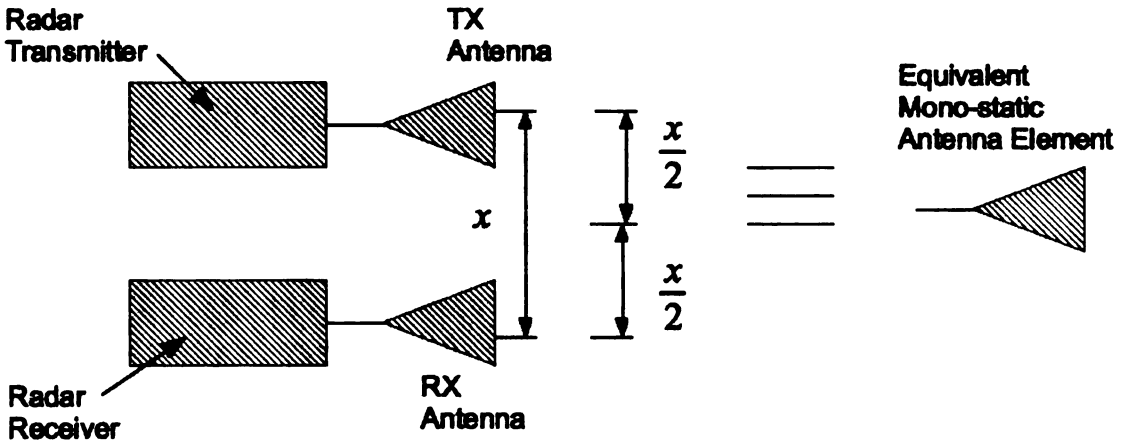

Figure 11.2. When bi-static transmit and receive elements are close together (relative to target range) spaced apart by x it is equivalent to a single mono-static element at the mid point $x/2$.

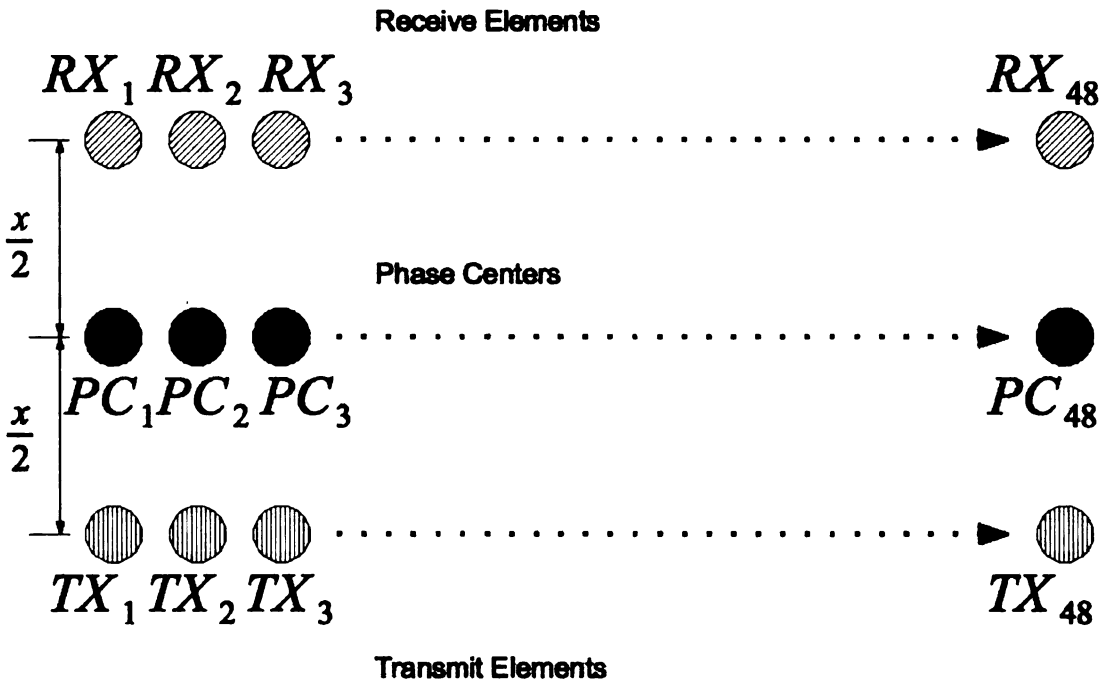

Figure 11.3. Side view of a simple bi-static antenna array using 48 transmit and 48 receive elements for a total of 96 elements.

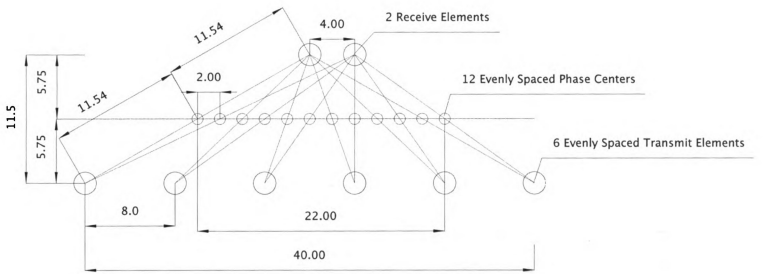

Figure 11.4. A more advanced bi-static antenna array producing 12 mono-static phase centers at the expense of only 2 receive elements and 6 transmit elements (units in inches).

11.2 Array implementation

All design details of the high speed SAR array are presented in this section. These include the array physical layout, antenna switch block diagram and the connections between the array and the existing S-band radar system developed in Chapter 8.

11.2.1 Array antenna spacing and physical layout

Using the concept developed in Section 11.1 a large array was developed by cascading several of the array sections from Figure 11.4 in series. The layout of the resulting large array is shown in Figure 11.5 and Figure 11.6. This array is effectively 88 inches long with a cross range sample spacing of 2 inches producing 44 equivalent phase centers across the aperture. All antenna combinations used to create the 44 phase centers are shown in Figure 11.5 and Figure 11.6. The physical location of each phase center is also shown in this figure.

11.2.2 Array implementation and interface

This array was designed to plug into the existing S-band radar system developed in Chapter 8. A modification was made to the system block diagram in Figure 8.6 by adding a National Instruments PCI-6509 digital I/O (DIO) card to control the antenna array. This modification is shown in Figure 11.7. A picture of this array built out of vertically polarized LTSA antenna elements is shown in Figure 11.12. The antenna element configuration is noticeable in Figure 11.12a.

All antennas in this array are identical and based on the LTSA design from [71]. These elements were produced in volume by a printed circuit board manufacturer to be identical to each other. The LTSAs are built out low cost readily available 1/16 inch thick FR-4 circuit board material with the resulting LTSA pattern etched on the surface. The LTSA layout is shown in Figure 11.10 and a picture of a completed receive LTSA with antenna feed is shown in Figure 11.11. The antenna is fed by soldering a low loss CNT100a coaxial cable to the area shown in the layout in Figure

11.10. In this the center conductor of the coaxial feed is soldered to the top copper trace and the shield is soldered to the bottom copper trace. An optimum feed point is found by sliding the coax cable back and forth down the 4 inch long slot until optimum SWR is achieved for the desired bandwidth. In the case of this LTSA design the antenna covers 1 GHz to 4 GHz with an SWR $\leq 2:1$ across the entire band. Each of the 21 LTSA antennas in the array were individually tuned using this method.

The feed lines running to the transmit LTSAs (ANT1 through ANT13) are fed directly into the switch matrix. The feed lines running from the receive LTSAs (ANT14 through ANT21) feed directly into a small pre-amplifier mounted on each of the receive LTSAs. This is shown in Figure 11.11b.

The LTSA feed lines run directly into the switch matrix box which is located on the back of the array shown in Figure 11.13. The block diagram of the switch matrix is shown in Figure 11.8 and Figure 11.9 with a parts list in Table 11.1. The switch matrix switches the S-band transmitter and receiver front ends to the correct antenna combination to create the desired phase center. The switch matrix that controls these antenna elements is made up of two different sub-switch matrices: a transmitter switch matrix with block diagram shown in Figure 11.8 and a receive switch matrix with block diagram shown in Figure 11.9.

The transmitter front end shown in Figure 8.4 feeds directly into the transmit switch matrix RF input port shown in Figure 11.8. This is fed through a -10 dB Narda directional coupler CLPR1 into SW1 which is a Mini-Circuits ZSWA-4-30DR, DC-3 GHz 4-way GaAs Switch. SW1 branches out into three other identical switches SW2, SW3 and SW4 all of which are controlled by DIO from the PCI-6509 card. Some power is coupled off CLPR1 and fed out for diagnostic purposes. The output of these switches is fed directly to all of the transmit antenna elements which make up the transmit sub-array consisting of the bottom row of LTSA's shown in Figure

11.12. All solid state switches in both switch matrices are designed to operate only up to 3 GHz however it was found through laboratory tests that these switches could operate up to 4 GHz with a 2 dB increase in insertion loss and a 5 dB reduction in port to port isolation.

The receiver front end shown in Figure 8.5 is connected directly to the receive switch matrix shown in Figure 11.9 through the RF output port. Received signals detected by the antennas and amplified by LNA1 through LNA8 are fed into SW6 and SW7 which are Mini-Circuits ZSWA-4-30DR, DC-3 GHz 4-way GaAs Switches controlled by DIO from the PCI-6509 card. The output of these switches is fed into SW5 which is a Mini-Circuits ZSDR-230, DC-3 GHz PiN Diode Switch controlled by DIO from the PCI-6509 card.

The PCI-6509 card selects the proper switch combination to turn on the correct antenna pair to make the required phase center. This is done by sending a 32 bit hexadecimal word out of the DIO ports on the PCI-6509. The pin-out of this hex word and its connection to the switches is shown in Table 11.2 and Table 11.3. Table 11.4 and Table 11.5 are look up tables which show the hex code required to turn on a given phase center number. In these tables the transmit and receive element combination for a given phase center and the hex code which is sent to the switch matrix box used to switch on this phase center is shown.

When the S-band front ends are connected to the high speed SAR array there is no reduction in receiver sensitivity due to the low-noise amplifiers mounted on the receive elements. There is a significant reduction in transmit power due to the loss through the transmitter switch matrix. This loss is around 8 to 10 dB across the 2 GHz to 4 GHz band. The result is a transmit power of about 1 to 2 milliwatts. This is an estimation since it is difficult to probe the power at the transmitter antenna feeds which are soldered directly to the coaxial feed lines. All data presented in this chapter was acquired using this reduced transmit power of about 1 or 2 milliwatts.

11.2.3 Processing and control software

Labview software was written to rapidly acquire data across the array then calculate a radar image. This software also calibrates the array and performs coherent background subtraction. The RMA SAR algorithm written in MATLAB code from Appendix C was re-written in Labview.

Background subtraction is identical to that presented in Section 5.3. The calibration procedure is much different than for the rail SAR. All phase centers must be calibrated because of the small 1 or 2 dB inconsistencies compounding throughout the signal path due to hand-soldered antenna feeds, LNA's and the switch matrix losses. The calibration is a 2-D calibration where each of the 44 phase centers is calibrated.

This array calibration is done to sharpen imagery and is not an exact sphere target calibration. This is due to the lack of an available large-enough calibration sphere. A 5 foot tall 3/4 inch diameter copper pole is used as a calibration target. The calibration target is placed at exactly 11 feet down range and centered to the middle of the array. Range profile data is acquired across the array at each of the 44 phase centers. This data is represented by $s_{pole}(x_n, \omega(t))$ where x_n is the cross range phase center position. The pole is then removed and a background 2D range profile data array is acquired. The result is represented by $s_{calback}(x_n, \omega(t))$. The background is subtracted from the pole range profile data resulting in a 2D range profile array of the pole only

$$s_{cal}(x_n, \omega(t)) = s_{pole}(x_n, \omega(t)) - s_{calback}(x_n, \omega(t)). \tag{11.1}$$

The calibration data is referenced to a theoretical point scatterer which is represented by the equation

$$s_{caltheory}(x_n, \omega(t)) = e^{-j2k_r R_{pole}}. \tag{11.2}$$

Where the R_{pole} is a 2D range to pole across the array represented by the equation

$$R_{pole} = \sqrt{x_n^2 + (11 \cdot 0.3048)^2}. \tag{11.3}$$

Where $k_r = \omega(t)/c$. The calibration factor is calculated by the equation

$$s_{calfactor}(x_n, \omega(t)) = \frac{s_{caltheory}(x_n, \omega(t))}{s_{cal}(x_n, \omega(t))}. \tag{11.4}$$

This 2D cal factor is multiplied by each 2D SAR data set acquired by the array.

The software written to run the array performs calibration then coherent background subtraction. Once this is complete the software continuously acquires data from the array, performs the RMA, displays the image and starts over again. No coherent integration is applied to the data. This system will produce one image every 1.9 seconds for a $c_r = 845.2 \cdot 10^9$ Hz/Sec or one image ever 2.8 seconds for a $c_r = 422 \cdot 10^9$ Hz/Sec.

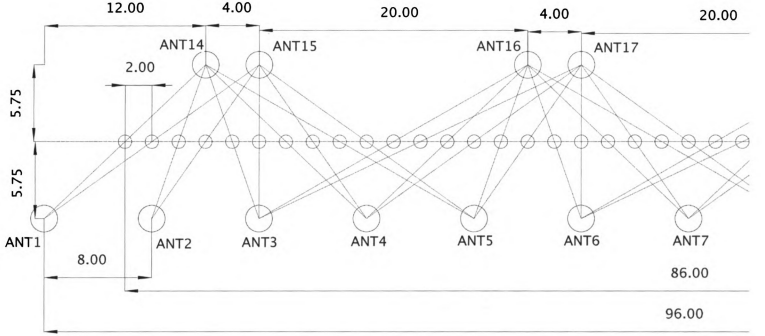

Figure 11.5. The high speed SAR imaging array physical layout (all units are in inches), antenna combinations and phase center locations (1 of 2).

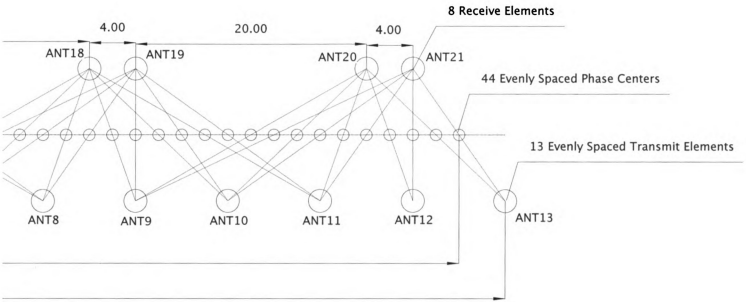

Figure 11.6. The high speed SAR imaging array physical layout (all units are in inches), antenna combinations and phase center locations (2 of 2).

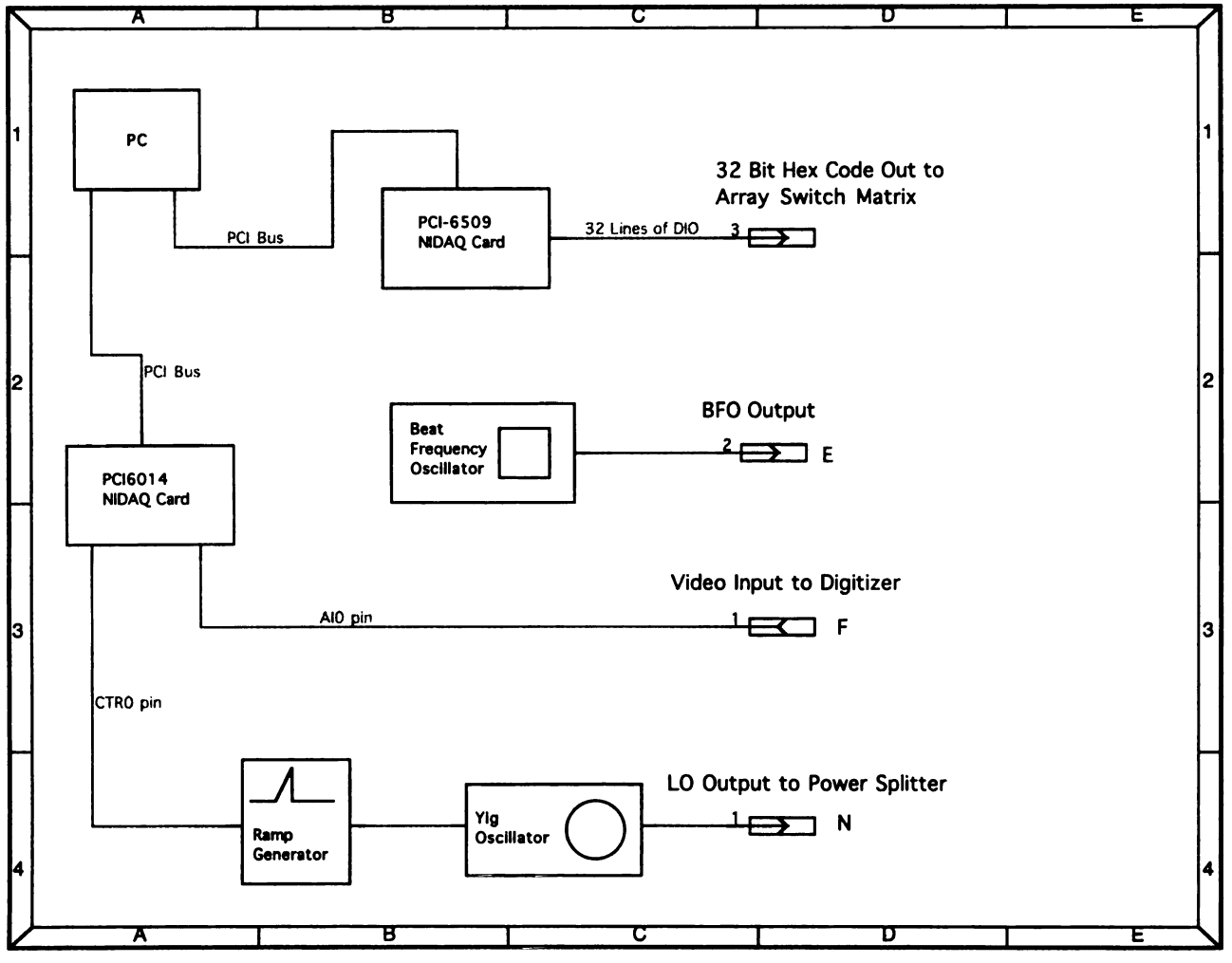

Figure 11.7. The overall radar system block diagram with modifications required to control the antenna array.

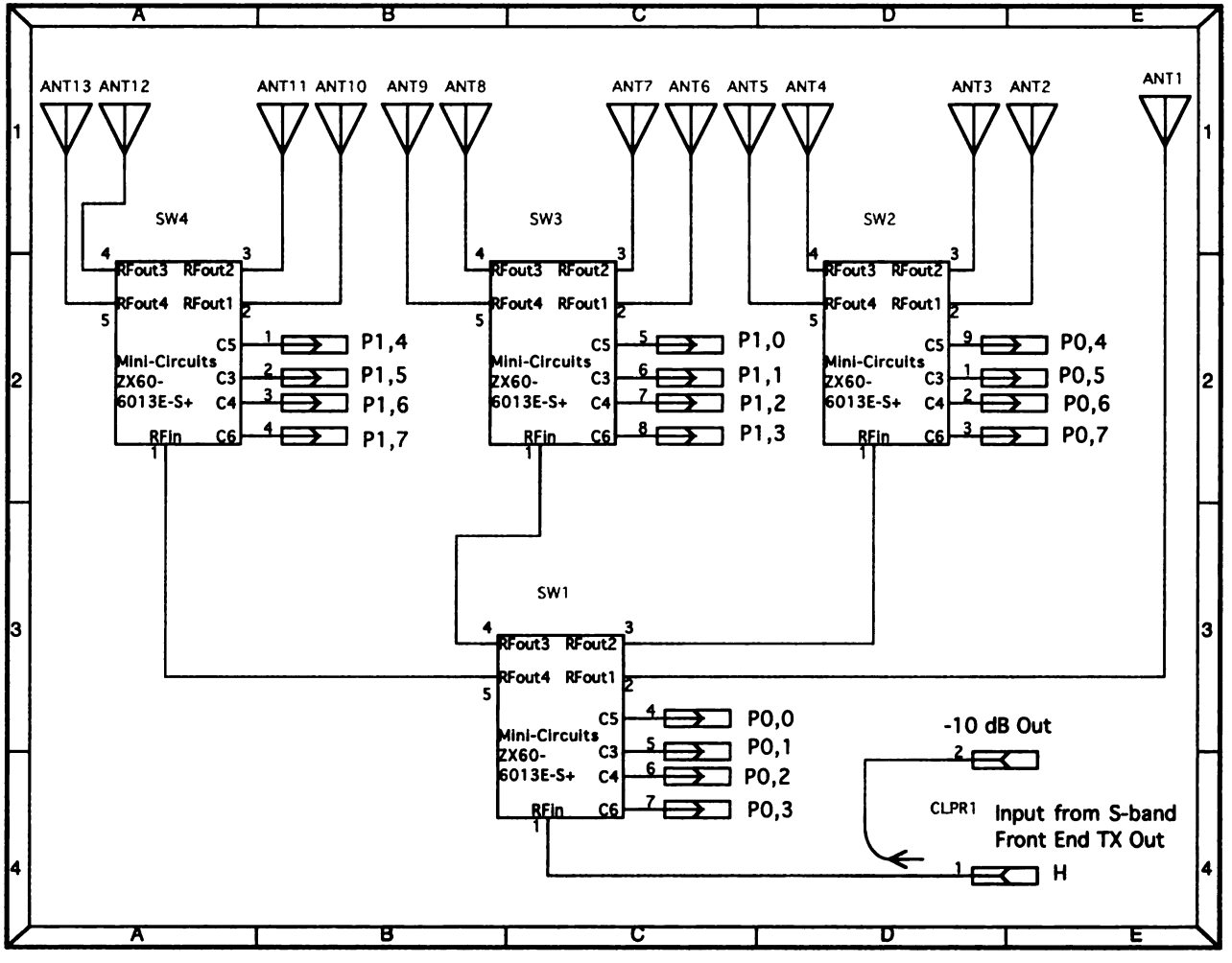

Figure 11.8. Block diagram of the transmitter switch matrix.

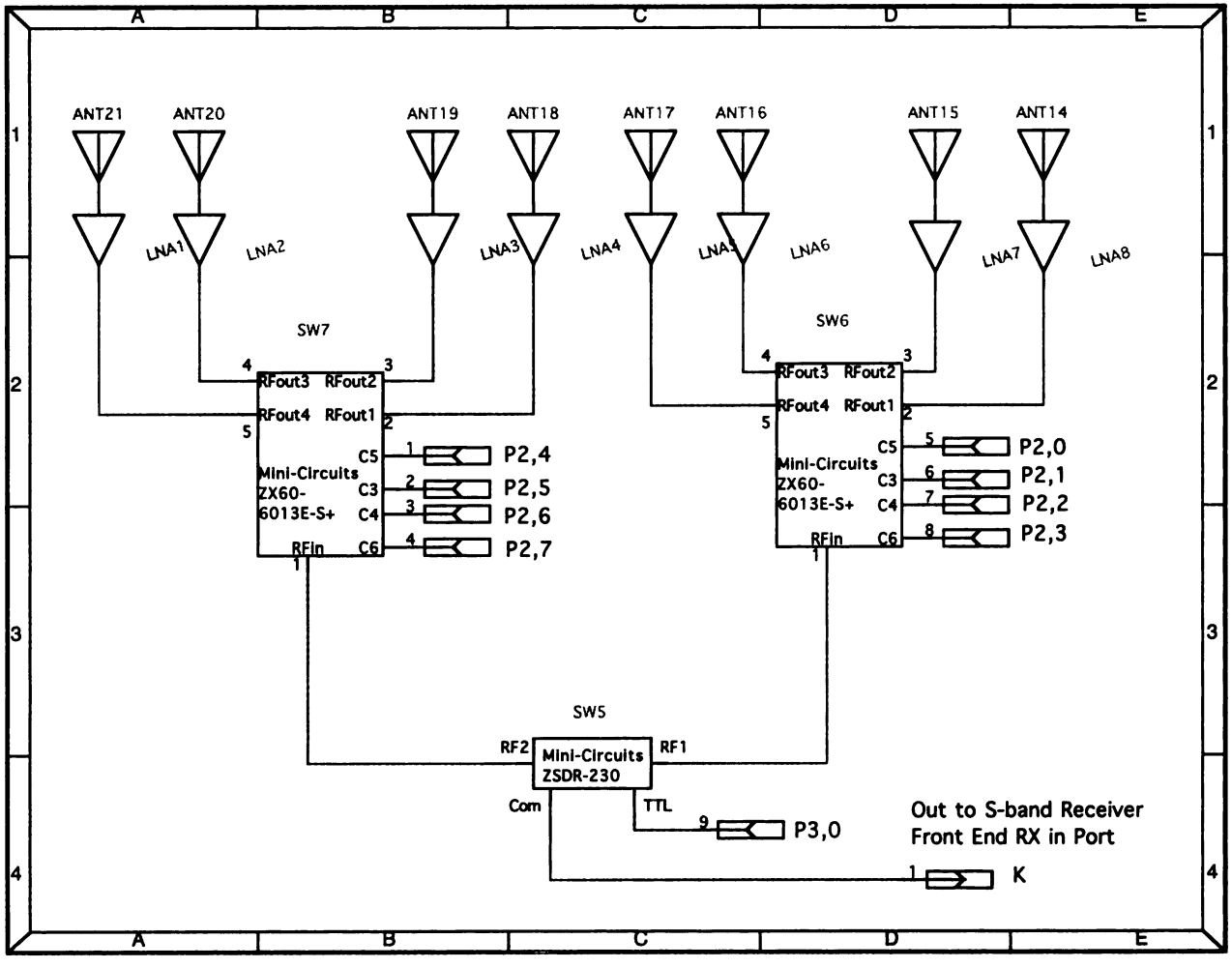

Figure 11.9. Block diagram of the receiver switch matrix.

Table 11.1. High speed SAR imaging array modular component list.

Component	Description	Figure (if applicable)
ANT1 through ANT21	LTSA built on FR4	Figure 11.10
CLPR1	Narda -10 dB Directional Coupler	NA
LNA1 through LNA8	Mini-Circuits ZX60-6013E-S+	NA
SW1 through SW4, SW6, SW7	Mini-Circuits ZSWA-4-30DR, DC-3 GHz 4-way GaAs Switch	NA
SW5	Mini-Circuits ZSDR-230, DC-3 GHz PiN Diode Switch	NA

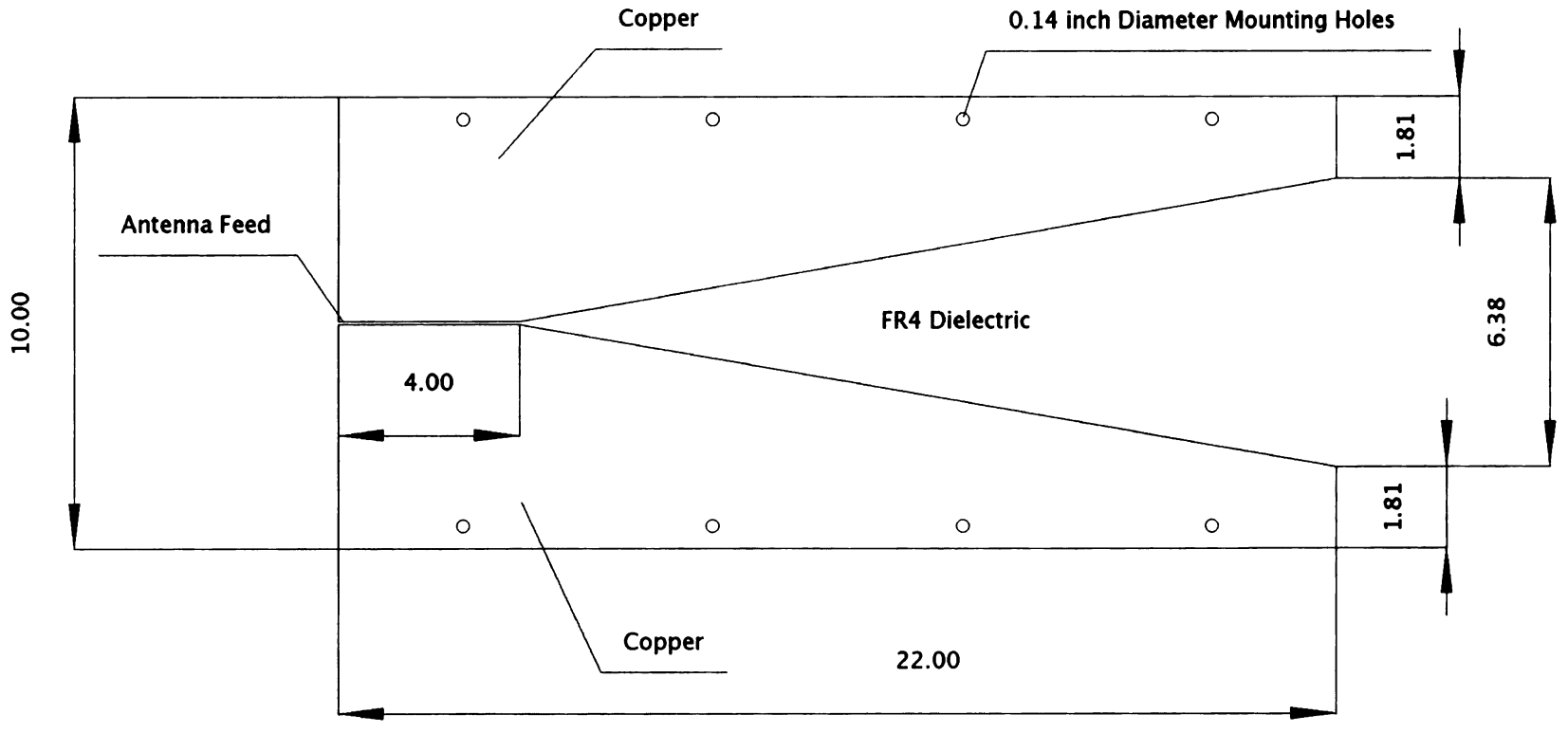

Figure 11.10. Layout of the LTSA used for both the transmit and receive elements in the high speed SAR array (units in inches).

Table 11.2. 32 bit hex word for communicating with the switch matrix (1 of 2).

Transmitter Switch Matrix															
Port 1								Port 0							
7	6	5	4	3	2	1	0	7	6	5	4	3	2	1	0
SW4				SW3				SW2				SW1			
C5	C3	C4	C6	C5	C3	C4	C6	C5	C3	C4	C6	C5	C3	C4	C6

Table 11.3. 32 bit hex word for communicating with the switch matrix (2 of 2).

Receiver Switch Matrix								
Port 3	Port 2							
0	7	6	5	4	3	2	1	0
SW5	SW7				SW6			
TTL	C5	C3	C4	C6	C5	C3	C4	C6

Table 11.4. High speed SAR array hex look-up table (1 of 2).

Phase Center	Receive Element	Transmit Element	Hex Code
1	14	1	1010001
2	15	1	1020001
3	14	2	1010012
4	15	2	1020012
5	14	3	1010022
6	15	3	1020022
7	14	4	1010042
8	15	4	1020042
9	14	5	1010082
10	15	5	1020082
11	16	3	1040022
12	17	3	1080022
13	16	4	1040042
14	17	4	1080042
15	16	5	1040082
16	17	5	1080082
17	16	6	1040104
18	17	6	1080104
19	16	7	1040204
20	17	7	1080204
21	16	8	1040404
22	17	8	1080404

Table 11.5. High speed SAR array hex look-up table continued (2 of 2).

Phase Center	Receive Element	Transmit Element	Hex Code
23	18	6	0100104
24	19	6	0200104
25	18	7	0100204
26	19	7	0200204
27	18	8	0100404
28	19	8	0200404
29	18	9	0100804
30	19	9	0200804
31	18	10	0101008
32	19	10	0201008
33	18	11	0102008
34	19	11	0202008
35	20	9	0400804
36	21	9	0800804
37	20	10	0401008
38	21	10	0801008
39	20	11	0402008
40	21	11	0802008
41	20	12	0404008
42	21	12	0804008
43	20	13	0408008
44	21	13	0808008

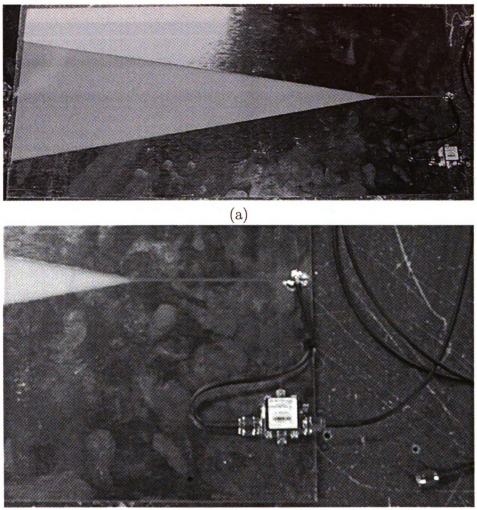

(a)

(b)

Figure 11.11. A receiver LTSA antenna element with LNA mounted on the antenna (a), close up view of LNA mounted at the end of the LTSA (b).

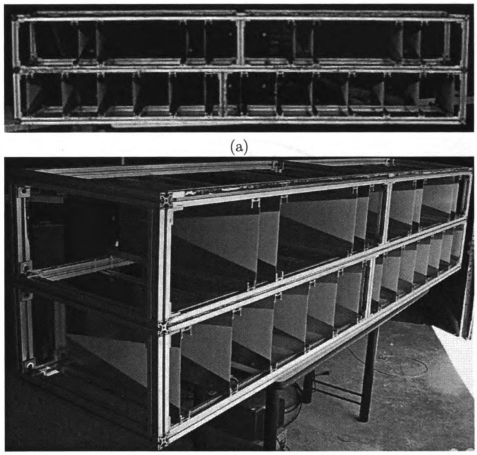

(a)

(b)

Figure 11.12. The front of the array showing the vertically polarized LTSA antennas (a), the array at an angle showing the 'V' of the LTSA elements pointing out towards the target scene (b).

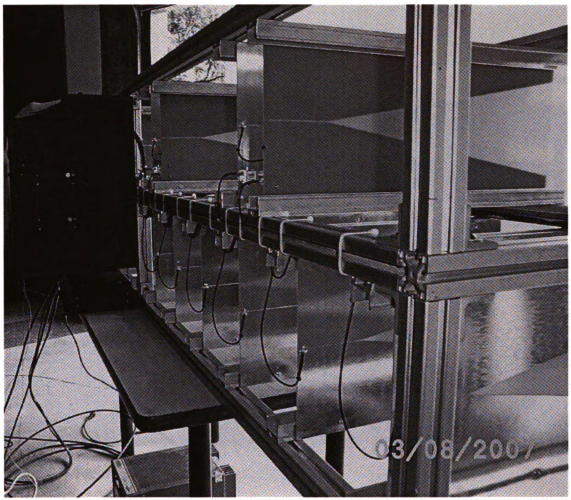

Figure 11.13. The back side of the array showing the LTSA antenna feeds running to the switch matrix box mounted on the back of the array.

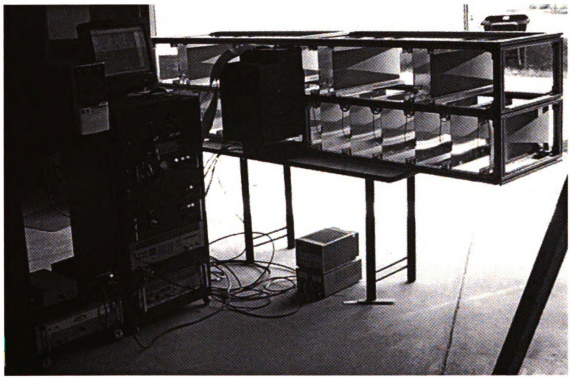

Figure 11.14. The near real-time S-band radar imaging system.

11.3 Array measured data

A number of images were acquired using the high speed SAR imaging array. The Labview software written for this system can save MATLAB .MAT matrix files of the RMA processed SAR image. The resulting imagery presented here were acquired using the high speed array and are displayed using MATLAB for convenience. The chirp rate for all measurements presented in this section is $c_r = 422 \cdot 10^9$ Hz/Sec which provided a radar image of the target scene once every 2.8 seconds. Coherent integration was not used while acquiring the data presented in this section.

11.3.1 Comparison of free-space simulations and measured data

Imagery of cylinders was acquired using the high speed SAR array. This imagery is compared to simulated imagery of cylinders using the model developed in Chapter 3.

Simulations were conducted by programming the theoretical model to the same cross range and down range sample spacing used in the high speed array imaging system. SAR imagery of cylinders was simulated by running three MATLAB programs. Simulated free-space cylinder data was calculated using the MATLAB program in Appendix E. The data conditioning program was run in Appendix B followed by the RMA imaging algorithm in Appendix C which produced the resulting simulated SAR image.

Figure 11.15a is a simulated radar image of a cylinder with radius $a = 3$ inches in free-space. Figure 11.15b is a measured radar image of a cylinder in free-space with radius $a = 3$. Both images are in agreement and the cylinder cross range and down range resolution is similar in both cases.

Figure 11.16a is a simulated radar image of a cylinder with a radius of $a = 6$ inches in free-space. Figure 11.16b is a measured radar image of a cylinder with the same radius in free-space. Both theoretical and measured images are in close agreement.

Both simulated cylinders were close to the measured cylinders. This shows that

the high speed SAR imaging array is an effective SAR imaging system.

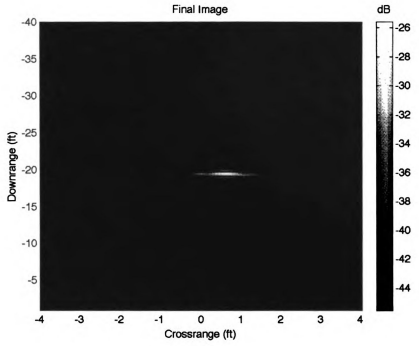

(a)

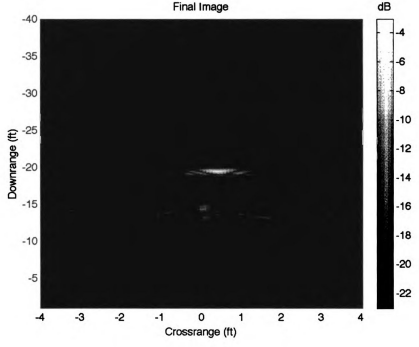

(b)

Figure 11.15. SAR imagery of a $a = 3$ inch radius cylinder in free space: simulated (a), acquired from the high speed array (b).

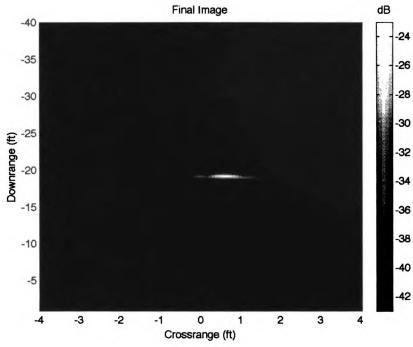

(a)

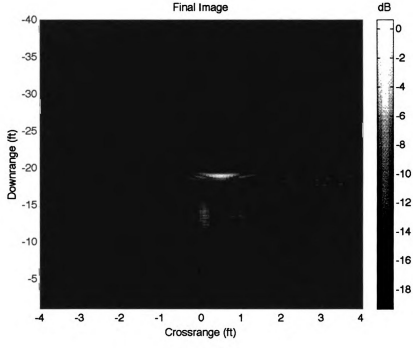

(b)

Figure 11.16. SAR imagery of a $a = 6$ inch radius cylinder in free space: simulated (a), acquired from the high speed array (b).

11.3.2 Free-space imagery

System performance was found to be close to simulation in the previous section. For this reason it was decided to image a number of other various target scenes.

Figure 11.17 is a SAR image of a sphere in free space. This is in agreement with the radar image of the same sphere acquired by the S-band rail SAR in Figure 9.4a.

Figure 11.18 is a SAR image of a carriage bolt target scene configured in a block 'S.' This is in agreement with the same target scene acquired by the S-band rail SAR in Figure 9.4b.

Figure 11.19 is a SAR image of a 12 oz aluminum beverage can. This target will be imaged behind a lossy-dielectric slab later in this chapter.

Groups of three different sized nails were imaged to determine the smallest target detectable. Figure 11.20 is a SAR image of a group of 3 inch tall nails in a block 'S' configuration. All nails are clearly visible in this image where the top row further down range is fading out. Figure 11.21 is a SAR image of a group of 2 inch tall nails in the same configuration. The location of each nail is clearly shown. Figure 11.22 is a SAR image of a group of 1.25 inch tall nails in a block 'S' configuration. The bottom two rows are clearly shown and a few of the nails at the top row are noticeable. This image shows that the array is a very sensitive high speed SAR imaging device capable of detecting and providing the location of targets as small as 1.25 inch tall nails.

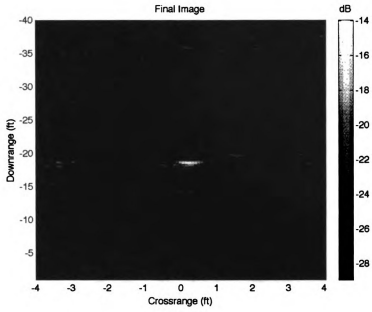

Figure 11.17. SAR image of an $a = 4.3$ inch radius sphere in free-space.

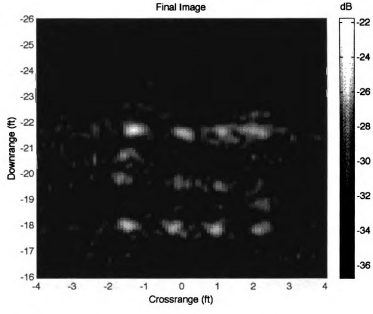

Figure 11.18. SAR image of a group of 6 inch long 3/8 inch diameter carriage bolts in free-space.

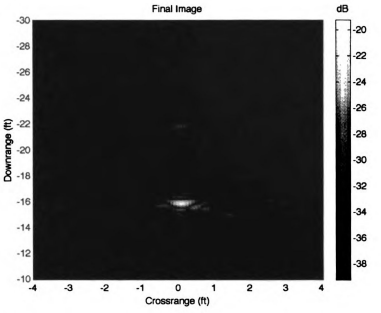

Figure 11.19. Image of a 12 oz aluminum beverage can in free-space.

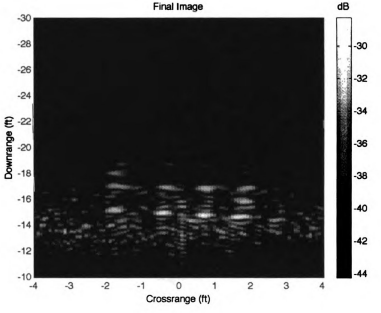

Figure 11.20. Image of a group of 3 inch tall nails in free-space.

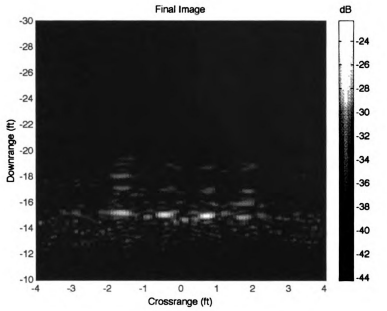

Figure 11.21. Image of a group of 2 inch tall nails in free-space.

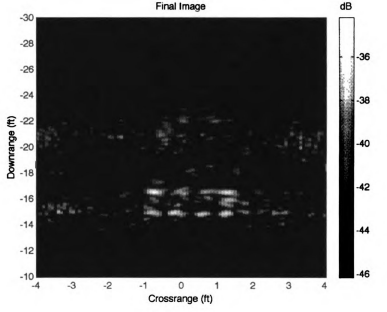

Figure 11.22. Image of a group of 1.25 inch tall nails in free-space.

11.3.3 Comparison of through-dielectric slab simulations and measured data

A comparison of measured and theoretical through-lossy-dielectric slab imagery will be shown in this section.

Measured SAR imagery were acquired by placing the high speed SAR array at a range of 20 feet from a $d = 4$ inch thick lossy-dielectric slab. Targets were placed at various ranges on the opposite side of the slab.

Simulated data of cylinders behind a lossy-dielectric slab was calculated by using background subtraction and the MATLAB programs in Appendix I and G. This simulated data was fed into the data conditioning MATLAB program in Appendix B and processed by the RMA in Appendix C resulting in the simulated SAR imagery.

Figure 11.23a shows a simulated SAR image of a cylinder with a radius of $a = 3$ inches behind a $d = 4$ inch thick lossy-dielectric slab. Figure 11.23b shows a measured SAR image of the cylinder behind a $d = 4$ inch thick lossy-dielectric slab. The measured is in agreement with the theoretical except for an increase in clutter. This may be due to the background subtraction interacting with the target.

Figure 11.24a shows a theoretical SAR image of a cylinder with a radius of $a = 6$ inches behind a $d = 4$ inch thick lossy dielectric slab. Figure 11.24b shows a measured image of the cylinder behind a $d = 4$ inch thick lossy-dielectric slab. The measured is in agreement with the theoretical with some noise and clutter present.

In both cases the measured data from the high speed SAR array was is agreement with the simulated. Increased noise is present in these images compared to the rail SAR imagery of the same targets shown in Figure 9.15b and Figure 9.16b. This may be due to the transmit loss caused by the switch matrix. The rail SAR feeds more power to the transmit antenna than the high speed SAR imaging array and this might be the reason for the differences.

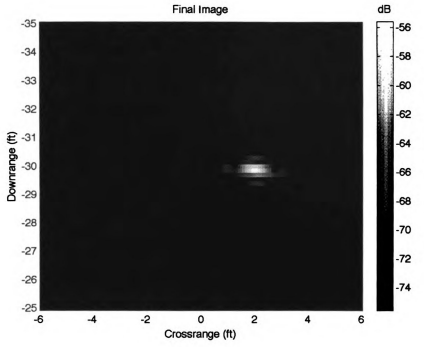

(a)

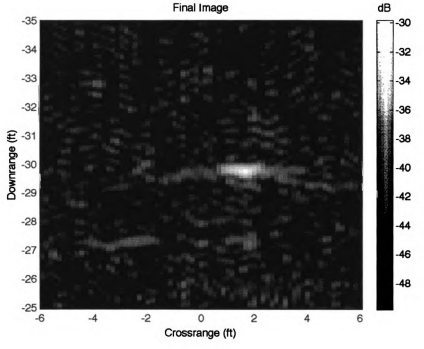

(b)

Figure 11.23. Imagery of an $a = 3$ inch radius cylinder behind a $d = 4$ inch thick lossy-dielectric slab: simulated (a), acquired from the high speed array (b).

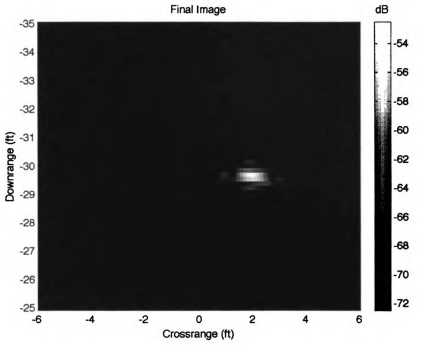

(a)

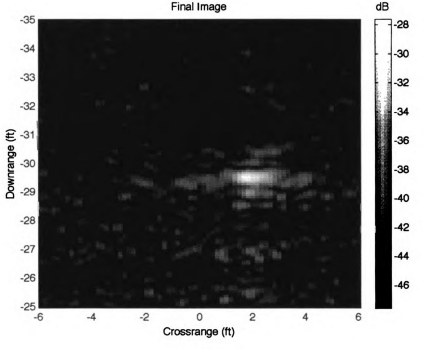

(b)

Figure 11.24. Imagery of an $a = 6$ inch radius cylinder behind a $d = 4$ inch thick lossy-dielectric slab: simulated (a), acquired from the high speed array (b).

11.3.4 Through-dielectric slab imagery

In this section through lossy-dielectric slab imagery was acquired on a number of other miscellaneous targets using the high speed array.

Figure 11.25 is a through lossy dielectric slab image of a 12 oz aluminum beverage can. The location of this can is clearly shown behind the lossy-dielectric slab.

Figure 11.26 is a through lossy-dielectric slab image of a single carriage bolt. This shows that the high speed SAR array is capable of detecting and indicating the location of small objects behind lossy-dielectric slabs.

Figure 11.27 is a through-lossy-dielectric slab image of a sphere with radius $a = 4.3$ inches. This image is close to the through slab rail SAR image of the same sphere shown in Figure 9.17.

This data shows that the high speed SAR array is capable of accurately imaging target scenes made up of small objects through a lossy-dielectric slab.

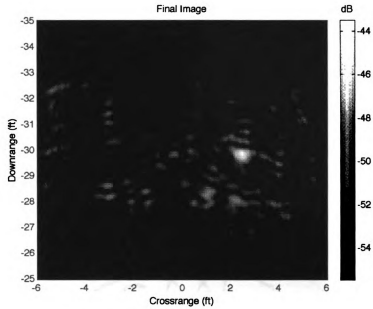

Figure 11.25. SAR image of a 12 oz aluminum beverage can through a $d = 4$ inch thick lossy-dielectric slab.

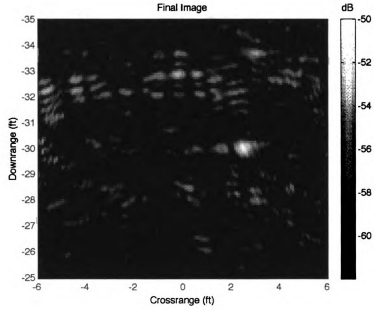

Figure 11.26. SAR image of a 6 inch tall 3/8 inch diameter carriage bolt through a $d = 4$ inch thick lossy-dielectric slab.

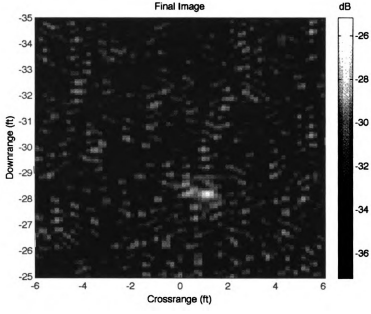

Figure 11.27. SAR image of an $a = 4.3$ inch radius sphere through a $d = 4$ inch thick lossy-dielectric slab.

11.4 Discussion of the high speed SAR imaging array

The results in this chapter prove the concept of attaching the high sensitivity range gated FMCW radar system to a high speed antenna array to create near real-time imagery of targets behind a dielectric slab. This system operates at an image re-fresh rate of one image every 1.9 seconds to 2.8 seconds (depending on chirp rate settings). This is very fast for a SAR imaging system. The concept was proven here, however, it would not be difficult to increase the imaging re-fresh rate to more than 5 or 6 images per second by upgrading to more sophisticated data acquisition hardware. A high speed real-time SAR imaging system that is capable of imaging through dielectric slabs at such a rate of speed has numerous applications.

CHAPTER 12

CONCLUSIONS AND FUTURE WORK

A near real-time through-lossy-dielectric slab radar imaging system was developed in this dissertation which is different from most previous work. It uses a modified FMCW radar design which is very sensitive, capable of range-gating and using extremely low levels of transmit power. One of the largest switched antenna arrays built for through-slab imaging was developed for this system. It operates at a stand-off range of 20 to 30 feet from the slab. This system is capable of near real-time through-slab imaging using an airborne SAR algorithm. It was shown that this radar design is flexible and can be adapted to other frequency bands such as X-band.

The entire development process was shown in this dissertation. Starting with a through-slab imaging model and ending with three functional proof-of-concept prototypes.

The model was effective at generating simulated rail SAR data of a 2D PEC cylinder placed behind a dielectric slab. Simulated and measured data were in agreement for both the rail SAR and the antenna array. Future modeling work could be to develop a periodic metal structure made up of PEC rods inside of a lossy dielectric slab. This might also lead to the modeling of multiple layers of lossy-dielectric slabs.

One unexpected result from this research was the ability for both the S-band and X-band radar systems to image small targets using extremely low transmit power. Future work with low power radar imaging has many applications including automotive radar, marine and aviation navigational radar and unmanned ground vehicle radar. This equipment could use nano-watts or pico-watts of transmit power to avoid obstacles or image unknown terrain at a short distance. These systems would not be difficult to implement. Some possible future work might be to simply plug the X-band

front end directly into a consumer X-band marine radar to see how far the radar could range targets using a PPI scope with only 10 mili-watts of transmit power.

The near real-time imaging system has numerous applications including earthquake victim location through building rubble, ground penetrating radar or other through-lossy-dielectric slab applications. The data resulting from this system was shown to be in agreement with the model for both free-space and through-lossy-dielectric slab imaging. This system was shown to be capable of imaging various small targets behind a slab. Possible future work for the near real-time through-slab imaging system includes:

1. Increasing the rate at which data can be read from the digitizer. This can be done by upgrading to a National Instruments PXI bus digitizer or by developing a proprietary high speed data acquisition system. By doing this the image refresh rate should be increased from one image every 1.9 seconds to at lest 1 or 2 per second or better. A rate of 5 or 6 images per second is desirable.

2. Increase digitizer sampling speed to greater than 200 KSPS which would increase the maximum alias-free down range of the radar system.

3. Developing a better antenna design for the array such as a Vivaldi.

4. Increased transmit power to at least 1 or 2 watts which would allow the system to be capable of imaging through a number of dielectric slabs.

5. Increasing the chirp bandwidth to cover 1-4 GHz.

6. Using multiple BFO carriers and IF filters to allow for multiple simultaneous range gates.

The research area of through-dielectric slab imaging is diverse. It was decided to focus on S-band through-dielectric slab radar imaging in this dissertation. An

entire proof of concept program was developed to completion starting with modeling and ending with three operational prototypes. The model drove all design aspects and the results were in agreement with the model. The resulting near real-time imaging system was very effective at imaging objects as small as metal rods and 12 oz aluminum soda cans placed behind a lossy-dielectric slab. More work could be done in this area and the future shows great potential for the eventual fielding of reliable through-dielectric slab imaging systems.

APPENDICES

APPENDIX A

MATLAB CODE FOR SIMULATING MULTIPLE POINT SCATTERERS

The following MATLAB program was written to simulate SAR data of three different point scatterers at various locations in a target scene.

```
%Range Migration Algorithm from ch 10 of Spotlight Synthetic
%Aperture Radar
%Signal Processing Algorithms, Carrara, Goodman, and Majewski


clear all;
c = 3E8; %(m/s) speed of light


%**********************************************************************
%radar parameters
fc = 3E9; %(Hz) center radar frequency
B = 2E9; %(hz) bandwidth
Rs = 0; %(m) y coordinate to scene center (down range)
Xa = 0; %(m) beginning of new aperture length
L = 8*.3048; %(m) aperture length
Xa = linspace(-L/2, L/2, 48); %(m) cross range position of
%radar on aperture L
Za = 0;
Ya = Rs; %THIS IS VERY IMPORTANT, SEE GEOMETRY FIGURE 10.6
fsteps = 500;
```

```
%*************************************************************************
%create SAR if data according to eq 10.4 and 10.5 (mocomp
%to a line) ignoring RVP term

%target parameters, 3 targets
at1 = 1;
xt1 = 2*.3048;
yt1 = -10*.3048;
zt1 = 0;

at2 = 1;
xt2 = 0*.3048;
yt2 = -5*.3048;
zt2 = 0;

at3 = 1;
xt3 = -2*.3048;
yt3 = -10*.3048;
zt3 = 0;

%Rt and Rb for 3 targets according to equation 10.26
Rb1 = sqrt((Ya - yt1)^2 + (Za - zt1)^2);
Rt1 = sqrt((Xa - xt1).^2 + Rb1^2);
%Rt1 = sqrt(yt1^2 + (Xac-xt1).^2);
Rb2 = sqrt((Ya - yt2)^2 + (Za - zt2)^2);
Rt2 = sqrt((Xa - xt2).^2 + Rb2^2);
%Rt2 = sqrt(yt2^2 + (Xac-xt2).^2);
```

```
Rb3 = sqrt((Ya - yt3)^2 + (Za - zt3)^2);
Rt3 = sqrt((Xa - xt3).^2 + Rb3^2);
%Rt3 = sqrt(yt3^2 + (Xac-xt3).^2);

Kr = linspace(((4*pi/c)*(fc - B/2)), ((4*pi/c)*(fc + B/2)), fsteps);
%according to range defined on bottom of page 410
for ii = 1:fsteps %step thru each time step to find phi_if
    for jj = 1:size(Xa,2) %step thru each azimuth step
        phi_if1(jj,ii) = Kr(ii)*(Rt1(jj) - Rs);
        phi_if2(jj,ii) = Kr(ii)*(Rt2(jj) - Rs);
        phi_if3(jj,ii) = Kr(ii)*(Rt3(jj) - Rs);
    end
end
sif1 = at1*exp(-j*phi_if1);
sif2 = at2*exp(-j*phi_if2);
sif3 = at3*exp(-j*phi_if3);
sif = sif1+sif2+sif3; %superimpose all three targets

clear sif1;
clear sif2;
clear sif3;
clear phi_if1;
clear phi_if2;
clear phi_if3;

s = sif;
save thruwall s;
```

```
%view simulated range history after range compression (figure 10.7) OK
%for ii = 1:size(sif,1);
%    sview(ii,:) = fftshift(fft(sif(ii,:)));
%end

%************************************************************************
%a note on formatting, our convention is sif(Xa,t)

%*************************************************************
%plot the real value data for the dissertation
set(0,'defaultaxesfontsize',13);
imagesc(Kr*c/(4*pi*1E9), Xa/.3048, real(sif));
colormap(gray);
ylabel('x position (ft)');
xlabel('recieved chirp frequency (GHz)');
title('real values of the single point scatter SAR data matrix');
colorbar;
cbar = colorbar;
set(get(cbar, 'Title'), 'String', 'V/m','fontsize',13);
print(gcf, '-djpeg100', 'real_value_of_single_pt_scatterer_raw_data.jpg');
```

APPENDIX B

MATLAB CODE FOR OPENING SAR DATA TO BE PROCESSED BY THE RMA

The following MATLAB program was used throughout the dissertation to open simulated SAR data and condition that data to be processed by the RMA MATLAB program shown in appendix C.

```
%Range Migration Algorithm from ch 10 of Spotlight Synthetic
%Aperture Radar
%Signal Processing Algorithms, Carrara, Goodman, and Majewski
clear all;
c = 3E8; %(m/s) speed of light
%**************************************************************************
load thruwall s; %load variable sif %for image data
sif = s; %image without background subtraction
clear s;
%clear sif_sub;
%**************************************************************************
%radar parameters
fc = 3E9; %(Hz) center radar frequency
B = 4E9 - 2E9; %(hz) bandwidth
cr = 2E9/10E-3; %(Hz/sec) chirp rate
Tp = 10E-3; %(sec) pulse width
%VERY IMPORTANT, change Rs to distance to cal target
Xa = 0; %(m) beginning of new aperture length
delta_x = (2*1/12)*0.3048; %(m) 2 inch antenna spacing
```

```
L = delta_x*(size(sif,1)); %(m) aperture length
Xa = linspace(-L/2, L/2, (L/delta_x)); %(m) cross range
%position of radar on aperture L
Za = 0;
t = linspace(0, Tp, size(sif,2)); %(s) fast time, CHECK SAMPLE RATE
Kr = linspace(((4*pi/c)*(fc - B/2)), ((4*pi/c)*(fc + B/2)), (size(t,2)));
Rs = 0; %(m) y coordinate to scene center (down range),
%make this value equal to distance to cal target
Ya = Rs; %THIS IS VERY IMPORTANT, SEE GEOMETRY FIGURE 10.6
%*********************************************************e**********************
%Save background subtracted and callibrated data
save sif sif delta_x Rs Kr Xa;
%clear all;
%run IFP
SBAND_RMA_IFP;
```

APPENDIX C

RMA MATLAB CODE

This is the RMA SAR imaging algorithm coded in MATLAB. In order to image theoretical data you must first run the data conditioning program in Appendix B. In order to image measured data using calibration you must first run the data conditioning program in appendix J.

```
%Range Migration Algorithm from ch 10 of Spotlight
%Synthetic Aperture Radar
%Signal Processing Algorithms, Carrara, Goodman, and Majewski

%************************************************************************
%a note on formatting, our convention is sif(Xa,t)

% YOU MUST RUN THIS FIRST TO CAL AND BACKGROUND SUBTRACT DATA:
%RMA_FINAL_opendata

%load data
clear all;
load sif;

figcount = 1;
close_as_you_go = 0;
do_all_plots = 0;

set(0,'defaultaxesfontsize',13); %set font size on plots
```

```
%so we can see it in the dissertation

% NOTE: the function 'dbv.m' is just dataout = 20*log10(abs(datain));
%************************************************************************
if do_all_plots == 1,
    figure(figcount);
    S_image = angle(sif);
    imagesc(Kr, Xa, S_image);
    colormap(gray);
    title('Phase Before Along Track FFT');
    xlabel('K_r (rad/m)');
    ylabel('Synthetic Aperture Position, Xa (m)');
    cbar = colorbar;
    set(get(cbar, 'Title'), 'String', 'radians','fontsize',13);
    print(gcf, '-djpeg100', 'phase_before_along_track_fft.jpg');
    if close_as_you_go == 1,
        close(figcount);
    end
    figcount = figcount + 1;
end

%along track FFT (in the slow time domain)
%first, symetrically cross range zero pad so that the radar can squint
zpad = 256; %cross range symetrical zero pad
szeros = zeros(zpad, size(sif,2));
for ii = 1:size(sif,2)
    index = (zpad - size(sif,1))/2;
```

```
    szeros(index+1:(index + size(sif,1)),ii) = sif(:,ii); %symetrical
    %zero pad
end
sif = szeros;
clear ii index szeros;

S = fftshift(fft(sif, [], 1), 1);
%S = fftshift(fft(sif, [], 1));
clear sif;
Kx = linspace((-pi/delta_x), (pi/delta_x), (size(S,1)));

if do_all_plots == 1,
    figure(figcount);
    S_image = dbv(S);
    imagesc(Kr, Kx, S_image, [max(max(S_image))-40,
     max(max(S_image))]);
    colormap(gray);
    title('Magnitude After Along Track FFT');
    xlabel('K_r (rad/m)');
    ylabel('K_x (rad/m)');
    cbar = colorbar;
    set(get(cbar, 'Title'), 'String', 'dB','fontsize',13);
    print(gcf, '-djpeg100', 'mag_after_along_track_fft.jpg');
    if close_as_you_go == 1,
        close(figcount);
    end
    figcount = figcount + 1;
```

```
end

if do_all_plots == 1,
    figure(figcount);
    S_image = angle(S);
    imagesc(Kr, Kx, S_image);
    colormap(gray);
    title('Phase After Along Track FFT');
    xlabel('K_r (rad/m)');
    ylabel('K_x (rad/m)');
    cbar = colorbar;
    set(get(cbar, 'Title'), 'String', 'radians','fontsize',13);
    print(gcf, '-djpeg100', 'phase_after_along_track_fft.jpg');
    if close_as_you_go == 1,
        close(figcount);
    end
    figcount = figcount + 1;
end

if do_all_plots == 1,
    figure(figcount);
    S_image = dbv(fftshift(fft(S, [], 2), 2));
    imagesc(linspace(-0.5, 0.5, size(S, 2)), Kx, S_image,
     [max(max(S_image))-40, max(max(S_image))]);
    colormap(gray);
    title('Magnitude of 2-D FFT of Input Data');
    xlabel('R_{relative} (dimensionless)');
```

```
    ylabel('K_x (rad/m)');
    cbar = colorbar;
    set(get(cbar, 'Title'), 'String', 'dB','fontsize',13);
    print(gcf, '-djpeg100', 'mag_after_2D_fft.jpg');
    if close_as_you_go == 1,
        close(figcount);
    end
    figcount = figcount + 1;
end

%************************************************************************
%matched filter

%create the matched filter eq 10.8
for ii = 1:size(S,2) %step thru each time step row to find phi_if
    for jj = 1:size(S,1) %step through each cross range in the
    %current time step row
        %phi_mf(jj,ii) = -Rs*Kr(ii) + Rs*sqrt((Kr(ii))^2 - (Kx(jj))^2);
        phi_mf(jj,ii) = Rs*sqrt((Kr(ii))^2 - (Kx(jj))^2);
        Krr(jj,ii) = Kr(ii); %generate 2d Kr for plotting purposes
        Kxx(jj,ii) = Kx(jj); %generate 2d Kx for plotting purposes
    end
end
smf = exp(j*phi_mf); %%%%%%%%%%%
%smf = exp(-j*phi_mf); %%%%%%%%%% THIS IS THE KEY ISSUE !!!!!

%note, we are in the Kx and Kr domain, thus our convention is S_mf(Kx,Kr)
```

```
%appsly matched filter to S
S_mf = S.*smf;

%clear smf phi_mf;

if do_all_plots == 1,
    figure(figcount);
    S_image = angle(S);
    imagesc(Kr, Kx, S_image);
    colormap(gray);
    title('Phase After Matched Filter');
    xlabel('K_r (rad/m)');
    ylabel('K_x (rad/m)');
    cbar = colorbar;
    set(get(cbar, 'Title'), 'String', 'radians','fontsize',13);
    print(gcf, '-djpeg100', 'phase_after_matched_filter.jpg');
    if close_as_you_go == 1,
        close(figcount);
    end
    figcount = figcount + 1;
end

clear S;

if do_all_plots == 1,
    figure(figcount);
```

```
    S_image = dbv(fftshift(fft(S_mf, [], 2), 2));
    imagesc(linspace(-0.5, 0.5, size(S_mf, 2)), Kx, S_image,
     [max(max(S_image))-40, max(max(S_image))]);
    colormap(gray);
    title('Magnitude of 2-D FFT of Matched Filtered Data');
    xlabel('R_{relative} (dimensionless)');
    ylabel('K_x (rad/m)');
    cbar = colorbar;
    set(get(cbar, 'Title'), 'String', 'dB','fontsize',13);
    print(gcf, '-djpeg100',
     'mag_after_downrange_fft_of_matched_filtered_data.jpg');
    if close_as_you_go == 1,
        close(figcount);
    end
    figcount = figcount + 1;
end

%************************************************************************
%perform the Stolt interpolation

%NOTICE:  Must change these parameters!!!!
%Ky_even = linspace(6, 13, 1028); %create evenly spaced Ky for
%interp for book example
%Ky_even = linspace(334.5, 448, 512); %create evenly spaced Ky for
%interp for real data
%Ky_even = linspace(200, 515, 512); %create evenly spaced Ky for
%interp for real data
```

```
%FOR DATA ANALYSIS
%kstart = 42.5; %for 1 to 3 ghz
%kstop = 118.5; %for 1 to 3 ghz
kstart =85.4; %for 2 to 4 ghz
kstop = 153.8; %for 2 to 4 ghz


%FOR DISSERTATION TO SHOW STOLT WORKING
%kstart = 50;
%kstop = 200;

Ky_even = linspace(kstart, kstop, 512); %create evenly spaced Ky
%for interp for real data
Ky_eeven = linspace(kstart, kstop, zpad); %make this same size as
%kx so we can find downrange

clear Ky S_St;
for ii = 1:size(Kx,2)
    Ky(ii,:) = sqrt(Kr.^2 - Kx(ii)^2);
    %S_st(ii,:) = (interp1(Ky(ii,:), S_mf(ii,:), Ky_even)).*H;
    S_st(ii,:) = (interp1(Ky(ii,:), S_mf(ii,:), Ky_even));
end
S_st(find(isnan(S_st))) = 1E-30; %set all Nan values to 0
clear S_mf ii Ky;

if do_all_plots == 1,
```

```
    figure(figcount);
    S_image = angle(S_st);
    imagesc(Ky_even, Kx, S_image);
    colormap(gray);
    title('Phase After Stolt Interpolation');
    xlabel('K_y (rad/m)');
    ylabel('K_x (rad/m)');
    cbar = colorbar;
    set(get(cbar, 'Title'), 'String', 'radians','fontsize',13);
    print(gcf, '-djpeg100', 'phase_after_stolt_interpolation.jpg');
    if close_as_you_go == 1,
        close(figcount);
    end
    figcount = figcount + 1;
end
%*********************************************************************
%perform the inverse FFT's
%new notation:  v(x,y), where x is crossrange
%first in the range dimmension
clear v Kr Krr Kxx Ky_even;
%v = fftshift(ifft2(S_st,(size(S_st,1)*1),(size(S_st,2)*1)),1);
v = ifft2(S_st,(size(S_st,1)*4),(size(S_st,2)*4));
xx = sqrt(Kx.^2 + Ky_eeven.^2);
%bw = (3E8/(4*pi))*(max(xx)-min(xx));
bw = 3E8*(kstop-kstart)/(4*pi);
max_range = (3E8*size(S_st,2)/(2*bw) - Rs)/.3048;
    figure(figcount);
```

```
    S_image = dbv(v);
    imagesc(linspace(-1*(zpad*delta_x/2)/.3048, 1*(zpad*delta_x/2)
     /.3048, size(v, 1)), linspace(0,-1*max_range, size(v,2)),
 flipud(rot90(S_image)), [max(max(S_image))-15,
  max(max(S_image))-0]);
    colormap(gray); %MUST DO THIS FOR DISSERTATION FIGS
    %colormap('default');
    title('Final Image');
    ylabel('Downrange (ft)');
    xlabel('Crossrange (ft)');
    cbar = colorbar;
    set(get(cbar, 'Title'), 'String', 'dB','fontsize',13);
    print(gcf, '-djpeg100', 'final_image.jpg');
    if close_as_you_go == 1,
        close(figcount);
    end
    figcount = figcount + 1;
clear cbar close_as_you_go figcount jj do_all_plots;
v = ifft2(S_st); %creat an un-zero padded version of the image
%clear S_st;
save lastimage v max_range zpad delta_x;
%save the set of un-zero padded image data
```

APPENDIX D

MATLAB CODE FOR CALCULATING PEC CYLINDER ECHO WIDTH AND RANGE PROFILES

The following MATLAB program was written to calculate and plot the echo width (σ_{2D}/λ) and the range profile of a 2D PEC cylinder for an TM^z plane wave incidence.

```
%Scattering of a PEC cyldiner from sec 11.5.1 in Balanis
%this program measures echo width and a range profile


clear all;
close all;
set(0,'defaultaxesfontsize',18);


%constants
mu0 = 4*pi*10^-7; %(H/m) free space permeability
eps0 = 8.85418E-12; %(F/m) free space permittivity
E0 = 1; %(V/m) incident field magnitude
c = 3E8; %(m/sec) speed of light


%frequency chirp
fstart = 2E9; %(Hz) start freq
fstop = 4E9; %(Hz) stop freq
f = linspace(fstart, fstop, 256); %(Hz) frequency chirp
w = 2*pi*f;
k00 = w*sqrt(mu0*eps0); %free space wave number
```

```
%cylinder distance from radar
r3n = 20*.3048; %(m)

%cylinder parameters
a = 0.6; %(m) radius of the cylinder
N = 200; %must be high enough for convergance on larger cylinders

%***********************************************
%calculate the range profile here
%***********************************************
phi_rp = -pi; %observation angle mono-static
for ii = 1:size(k00,2) %collect the chirp data
    k0 = k00(ii);
    %calculated the scattered field
    sum = 0;
    for jj = 1:N
        n = jj - 1;
        if n == 0
            epsn = 1;
        else
            epsn = 2;
        end
        sum = sum + (-j)^n*epsn*besselj(n,k0*a)*
         besselh(n,2,k0*r3n)/besselh(n,2,k0*a)*cos(n*phi_rp);
    end
    Es(ii) = E0*-1*sum;
end
```

```
%accont for the plane wave delay incident on the cylinder
Es = Es.*exp(-j*k00*r3n);
%plot the range profile
figure
bw = fstop-fstart;
max_time = size(Es,2)/(bw);
plot(linspace(0, max_time/1E-9, size(Es,2)),real(ifft(Es)),'k');
grid on;
title(['radius of cylinder ',num2str(a),'m and distance ',
num2str(r3n/.3048),'ft']);
xlabel('time (ns)');
ylabel('scattered electric field E^s (V/m)');
print(gcf, '-djpeg100', 'cylinder_realrp_pt6m.jpg');

figure
bw = fstop-fstart;
max_time = size(Es,2)/(bw);
plot(linspace(0, max_time/1E-9, size(Es,2)),dbv(ifft(Es)),'k');
grid on;
title(['radius of cylinder ',num2str(a),'m and distance ',
num2str(r3n/.3048),'ft']);
xlabel('time (ns)');
ylabel('scattered electric field E^s (dB)');
print(gcf, '-djpeg100', 'cylinder_dbrp_pt6m.jpg');

%*********************************************
%calculate the echo width here
```

```
%*********************************************
clear Ei Es w f;
N = 400; %need more N terms to converge the incident field
phii = linspace(0, pi, 100); %(rad) rip through a bunch of obsv. angles
lambda = 3E8/2E9; %(m) wavelength at 2 GHz (low freq of radar)
a = 0.6*lambda; %(m) diameter of cylinder
r3n = 20*.3048; %(m) distance to cylinder
w = 2*pi*c/lambda; %(rad/sec) radial frequency in terms of wavelength
k0 = w*sqrt(mu0*eps0); %free space wave number in terms of wavelength
for ii = 1:size(phii,2)
    phi = phii(ii);
    %calculate the scattered field
    sum = 0;
    for jj = 1:N
        n = jj - 1;
        if n == 0
            epsn = 1;
        else
            epsn = 2;
        end
        sum = sum + (-j)^n*epsn*besselj(n,k0*a)*
         besselh(n,2,k0*r3n)/besselh(n,2,k0*a)*cos(n*phi);
    end
    Es(ii) = E0*-1*sum;
    %calculate the incident field
    sum = 0;
    for jj = 1:N
```

```
        n = jj - 1;
        if n == 0
            epsn = 1;
        else
            epsn = 2;
        end
        sum = sum + (-j)^n*epsn*besselj(n,k0*r3n)*cos(n*phi);
    end
    Ei(ii) = E0*sum;
end
sigma = 2*pi*r3n*(abs(Es).^2)./(abs(Ei).^2);

figure
semilogy(phii*180/pi,sigma/lambda,'k')
axis([0 180 1 25]);
title('echo width (units in \sigma_{2D}/\lambda) of a
0.6\lambda radius cylinder');
xlabel('observation angle (degrees)');
ylabel('echo width');
grid on;
print(gcf, '-djpeg100', 'cylinder_echowidth.jpg');
```

APPENDIX E

MATLAB CODE FOR SIMULATING SAR DATA OF THE 2D PEC CYLINDER MODEL

The following MATLAB code was written to simulate SAR data for the 2D PEC cylinder model developed in Chapter 3. The resulting data from this program can be fed into the data conditioning program in Appendix B and the RMA SAR imaging algorithm written in Appendix C resulting in a simulated SAR image of a 2D PEC cylinder.

```
%theoretical RAIL SAR data for imaging the
%Balanis cylinder model


clear all;
close all;


%constants
mu0 = 4*pi*10^-7; %(H/m) free space permeability
eps0 = 8.85418E-12; %(F/m) free space permittivity
sigma = 0.13; %(S/m) conductivity
E0 = 1; %(V/m) incident field magnitude


%frequency chirp
fstart = 2E9; %(Hz) start of chirp
fstop = 4E9; %(Hz) stop of chirp
f = linspace(fstart, fstop, 256); %(Hz) frequency chirp
w = 2*pi*f;
```

```
k00 = w*sqrt(mu0*eps0); %free space wave number

%geometry constants
d3 = 20*.3048; %(m) distance from rail to target center
L = 8*.3048; %(m) length of the rail
inc = linspace(-L/2, L/2, 48); %(m) location of radar
%on the rail, accross all rail positions

%first, build the phi_n matrix, the incident angle
phi_n = acos(d3./(sqrt(inc.^2 + d3^2)));

%next, build the r matricies
r3n = d3./(cos(phi_n));

%cylinder parameters
a = (3/12)*.3048; %(m) radius of the cylinder
N = 400; %must be high enough for proper
%convergance on larger cylinders
phi_rp = -pi; %observation angle mono-static

for ii = 1:size(k00,2)
    k0 = k00(ii);
    %calculated the scattered field of the cylinder
    sum = 0;
    for jj = 1:N
        n = jj - 1;
        if n == 0
```

```
            epsn = 1;
        else
            epsn = 2;
        end
        sum = sum + (-j)^n*epsn*besselj(n,k0*a)*
         besselh(n,2,k0*r3n)/besselh(n,2,k0*a)*cos(n*phi_rp);
    end
    %Es plus some plane wave range between that and the boundar
    s(:,ii) = -1*sum.*exp(-j*k0*r3n);
end

figure
bw = fstop-fstart;
max_time = size(s,2)/(bw);
plot(linspace(0, max_time/1E-9, size(s,2)),dbv(ifft(s(16,:))));
%index of 16 was choosen to make nearly normal incidence
grid on;
title(['radius of cylinder ',num2str(a),'m and distance '
,num2str(r3n(16)/.3048),'ft']);
xlabel('time (ns)');
ylabel('scattered electric field E^s (dB)');

save thruwall s;
```

APPENDIX F

MATLAB CODE FOR CALCULATED A SIMULATED RANGE PROFILE OF A LOSSY-DIELECTRIC SLAB

The following MATLAB program was written simulate a range profile of the lossy-dielectric slab model developed in Chapter 4.

```
%Wave Matrix method for a lossless dielectric sheet at some
%oblique angle of incidence (from Collin)


clear all;
close all;
set(0,'defaultaxesfontsize',13);


%*****************************
%constants
%*****************************
mu0 = 4*pi*10^-7; %(H/m) free space permeability
eps0 = 8.85418E-12; %(F/m) free space permittivity
E0 = 1; %(V/m) incident field magnitude


%dielectric properties
%epsr = 1.00005;%relative dielectric constant of layer 1
epsr = 5;
d = 0.1; %(m) thickness of the dielectric region 2
phi_i = 0*pi/180; %(rad) incidence angle
```

```
%frequency chirp and wave number calculations
fstart = 2E9; %(Hz) start freq
fstop = 4E9; %(Hz) stop freq
f = linspace(fstart, fstop, 256); %(HZ) chirp frequency
w = 2*pi*f; %(rad/m) radial freq

%conductivity approximation (from a model)
%sigma = 0.219 + (f - 1E9)*.036/1E9; %porosity factor of 0.15
sigma = 0.1194 + (f - 1E9)*.0222/1E9; %porosity factor of 0.10
%sigma = 0;

%wave number calculations
k0 = w*sqrt(mu0*eps0); %(rad/m) wave number in free space
k = w.*sqrt(mu0*(epsr*eps0+sigma./(j*w)));

%*****************************
%calculations
%*****************************

%calculate the normalized dielectric impedance wrt incidence angle
%perpendicular polarization (TMz)
Z = cos(phi_i)./sqrt((epsr + sigma./(j*w*eps0)) - (sin(phi_i))^2);

%calculate the relection coefficients wrt incidence angle
R1 = (Z-1)./(Z+1);
R2 = (1-Z)./(1+Z);
```

```
%calculate the transmission coefficients wrt incidence angle
T1 = 1 + R1;
T2 = 1 + R2;

%calculate the elecrical length of layer 1, phase length of layer 1
theta = d*sqrt(epsr + sigma./(w.*j*eps0) - (sin(phi_i)).^2).*k0;%;

%calcualte c1, the incident fileld at the first boundary face
r = 10*.3048; %(m) distance from interface
c1 = E0*exp(-j*k0*r);

%calculate the radar target function
r_target = 10*.3048; %(m) range to target away from the wall
rcs = 0; %0 for the case of dielectric only imaging and range profiles
rcs = rcs.*exp(-j*2*k0*r_target);

%calculate c3 the tranmitted into region 3 coeficient wrt phase legnth of
%layer 1
c3 = T1.*T2.*c1./(exp(j*theta)+R1.*R2.*exp(-j*theta)+
rcs.*(R2.*exp(j*theta)+R1.*exp(-j*theta)));

%calculate b1 the reflected coefficient, wrt phase length of layer 1
b1 = (c3./(T1.*T2)).*(R1.*exp(j*theta)+R2.*exp(-j*theta)
+rcs.*(R1.*R2.*exp(j*theta)+exp(-j*theta)));

%plane wave takes some distance to get back to receiver,
%thus the received field is
```

```
Es = b1.*exp(-j*k0*r);


%plot the conductivity
figure
plot(f/1E9, sigma,'k');
grid on;
title(['conductivity \sigma  over freqeuncy range,
with \epsilon_r = ',num2str(epsr)]);
xlabel('frequency (GHz)');
ylabel('conductivity');
print(gcf, '-djpeg100', 'dielectric_conductivity.jpg');


%plot the time domain figure
figure
bw = fstop-fstart;
max_time = size(Es,2)/(bw);
plot(linspace(0, max_time/1E-9, size(Es,2)),dbv(ifft(Es)),'k');
grid on;
title(['incident angle \phi_{ i} = ',num2str(phi_i*180/pi),' (deg)']);
xlabel('time (ns)');
ylabel('scattered electric field E^s (dB)');
print(gcf, '-djpeg100', 'dielectric_only_deg_incidence.jpg');
```

APPENDIX G

MATLAB CODE FOR SIMULATING RAIL SAR DATA OF THE DIELECTRIC SLAB MODEL

The following MATLAB program was written to simulate rail SAR data of the dielectric slab model developed in Chapter 4.

```
%rail SAR data is theoretically calculated using this program for a
%dielectric wall ONLY

%this is the final simulation program

clear all;
%close all;
set(0,'defaultaxesfontsize',18);

%*****************************
%constants
%*****************************
mu0 = 4*pi*10^-7; %(H/m) free space permeability
eps0 = 8.85418E-12; %(F/m) free space permittivity
E0 = 1; %(V/m) incident field magnitude

%dielectric properties
epsr = 5;%relative dielectric constant of layer 1

%frequency chirp and wave number calculations
```

```
fstart = 2E9; %(Hz) start freq
fstop = 4E9; %(Hz) stop freq
f = linspace(fstart, fstop, 256); %(HZ) chirp frequency
w = 2*pi*f; %(rad/m) radial freq

%conductivity approximation (from a model)
%sigma = 0.219 + (f - 1E9)*.036/1E9; %porosity factor of 0.15
sigma = 0.1194 + (f - 1E9)*.0222/1E9; %porosity factor of 0.10
%sigma = 0;

%wave number calculations
k0 = w*sqrt(mu0*eps0); %(rad/m) wave number in free space
k = w.*sqrt(mu0*(epsr*eps0+sigma./(j*w)));

%****************************************
%unique geometry and incidence angles
%****************************************
%geometry constants
d1 = 10*.3048; %(m) distance from rail to wall
d = 4/12*.3048; %(m) thickness of wall
d3 = 20*.3048; %(m) distance from rail to target center
L = 8*.3048; %(m) length of the rail
inc = linspace(-L/2, L/2, 48); %(m) location of radar on the rail, accross
%all rail positions
%inc = 4*.3048

%first, build the phi_n matrix, the incident angle
```

```
phi_n = acos(d3./(sqrt(inc.^2 + d3^2)));

%next, build the r matricies
r1n = d1./(cos(phi_n));
r3n = (d3-d1-d)./(cos(phi_n));



%cylinder parameters
a = (3/12)*.3048; %(m) radius of the cylinder
N = 200; %must be high enough for proper convergance on larger cylinders

%************************************************
%calculatons
%************************************************
for n = 1:size(inc,2)
phi_i = phi_n(n);

    n

    %calculate the normalized dielectric impedance wrt incidence angle
    %perpendicular polarization (TMz)
    Z = cos(phi_i)./sqrt((epsr + sigma./(j*w*eps0)) - (sin(phi_i))^2);

    %calculate the relection coefficients wrt incidence angle
    R1 = (Z-1)./(Z+1);
    R2 = (1-Z)./(1+Z);
```

```
%calculate the transmission coefficients wrt incidence angle
T1 = 1 + R1;
T2 = 1 + R2;

%calculate the elecrical length of layer 1, phase length of layer 1
theta = d*sqrt(epsr + sigma./(w.*j*eps0) - (sin(phi_i)).^2).*k0;%;

%calcualte c1, the incident fileld at the first boundary face
r = r1n(n); %(m) distance to wall
c1 = E0*exp(-j*k0*r);

rcs = 0; %0 for the case of dielectric only imaging and range profiles
%rcs = rcs.*exp(-j*2*k0*r3n(n));

%calculate c3 the tranmitted into region 3 coeficient wrt
% phase legnth of layer 1
c3 = T1.*T2.*c1./(exp(j*theta)+R1.*R2.*exp(-j*theta)+rcs.*
 (R2.*exp(j*theta)+R1.*exp(-j*theta)));

%calculate b1 the reflected coefficient, wrt phase length of layer 1
b1 = (c3./(T1.*T2)).*(R1.*exp(j*theta)+R2.*exp(-j*theta)+
 rcs.*(R1.*R2.*exp(j*theta)+exp(-j*theta)));

%plane wave takes some distance to get back to receiver,
%thus the received field is
Es(n,:) = b1.*exp(-j*k0*r);
```

```
end


s = Es;

save thruwall s;

SBAND_RMA_opendata
```

APPENDIX H

MATLAB CODE FOR ACQUIRING A SIMULATED RANGE PROFILE OF A PEC CYLINDER ON THE OPPOSITE SIDE OF A DIELECTRIC SLAB

The following MATLAB program was written to simulate a range profile of a PEC cylinder on the opposite side of a dielectric slab. This code was based on the model developed in Chapter 5.

```
%Range profile data is theoretically calculated using this program for a
%dielectric wall and cylinder

%this is the final simulation program

clear all;
%close all;
set(0,'defaultaxesfontsize',18);

%*****************************
%constants
%*****************************
mu0 = 4*pi*10^-7; %(H/m) free space permeability
eps0 = 8.85418E-12; %(F/m) free space permittivity
E0 = 1; %(V/m) incident field magnitude

%dielectric properties
epsr = 5;%relative dielectric constant of layer 1
```

```
%frequency chirp and wave number calculations
fstart = 2E9; %(Hz) start freq
fstop = 4E9; %(Hz) stop freq
f = linspace(fstart, fstop, 256); %(HZ) chirp frequency
w = 2*pi*f; %(rad/m) radial freq

%conductivity approximation (from a model)
%sigma = 0.219 + (f - 1E9)*.036/1E9; %porosity factor of 0.15
sigma = 0.1194 + (f - 1E9)*.0222/1E9; %porosity factor of 0.10
%sigma = 0;

%wave number calculations
k0 = w*sqrt(mu0*eps0); %(rad/m) wave number in free space
k = w.*sqrt(mu0*(epsr*eps0+sigma./(j*w)));

%****************************************
%unique geometry and incidence angles
%****************************************
%geometry constants
d1 = 20*.3048; %(m) distance from rail to wall
d = 4/12*.3048; %(m) thickness of wall
d3 = 30*.3048; %(m) distance from rail to target center
L = 8*.3048; %(m) length of the rail
%inc = linspace(-L/2, L/2, 48); %(m) location of radar on the rail, accross
%all rail positions
%inc = 4*.3048
```

```
inc = [0 -L/2] %take range profiles at only these locations

%first, build the phi_n matrix, the incident angle
phi_n = acos(d3./(sqrt(inc.^2 + d3^2)));

%next, build the r matricies
r1n = d1./(cos(phi_n));
r3n = (d3-d1-d)./(cos(phi_n));

%cylinder parameters
a = (3/12)*.3048; %(m) radius of the cylinder
N = 400; %must be high enough for proper convergance on larger cylinders
phi_rp = -pi; %IMPORTANT: this is the monostastic observation angle

%************************************************
%calculatons
%************************************************
for n = 1:size(inc,2)
    phi_i = phi_n(n);

    n

    %calculate the normalized dielectric impedance wrt incidence angle
    %perpendicular polarization (TMz)
    Z = cos(phi_i)./sqrt((epsr + sigma./(j*w*eps0)) - (sin(phi_i))^2);

    %calculate the relection coefficients wrt incidence angle
```

```
R1 = (Z-1)./(Z+1);
R2 = (1-Z)./(1+Z);

%calculate the transmission coefficients wrt incidence angle
T1 = 1 + R1;
T2 = 1 + R2;

%calculate the elecrical length of layer 1, phase length of layer 1
theta = d*sqrt(epsr + sigma./(w.*j*eps0) - (sin(phi_i)).^2).*k0;%;

%calcualte c1, the incident fileld at the first boundary face
r = r1n(n); %(m) distance to wall
c1 = E0*exp(-j*k0*r);

%calculate the radar target function
%calculated the scattered field of the cylinder
for ii = 1:size(k0,2)
sum = 0;
for jj = 1:N
     nn = jj - 1;
    if nn == 0
        epsn = 1;
    else
        epsn = 2;
    end
    sum = sum + (-j)^nn*epsn*besselj(nn,k0(ii)*a).*besselh(nn,2,k0(ii)*
     r3n(n))./besselh(nn,2,k0(ii)*a).*cos(nn*phi_rp);
```

```
    end
    rcs(ii) = sum;
    end
    rcs = -1*exp(-j*k0*r3n(n)).*rcs;

    %calculate c3 the tranmitted into region 3 coeficient wrt
    %phase legnth of layer 1
    c3 = T1.*T2.*c1./(exp(j*theta)+R1.*R2.*exp(-j*theta)
     +rcs.*(R2.*exp(j*theta)+R1.*exp(-j*theta)));

    %calculate b1 the reflected coefficient, wrt phase length of layer 1
    b1 = (c3./(T1.*T2)).*(R1.*exp(j*theta)+R2.*exp(-j*theta)
     +rcs.*(R1.*R2.*exp(j*theta)+exp(-j*theta)));

    %plane wave takes some distance to get back to receiver,
    %thus the received field is
    Es(n,:) = b1.*exp(-j*k0*r);

end

phi_i = phi_n(1);
%plot the time domain figure for normal incidence
figure
bw = fstop-fstart;
max_time = size(Es,2)/(bw);
plot(linspace(0, max_time/1E-9, size(Es,2)),dbv(ifft(Es(n,:))),'k');
grid on;
```

```
title(['incident angle \phi_{ i} = ',num2str(phi_i*180/pi),' (deg)']);
xlabel('time (ns)');
ylabel('scattered electric field E^s (dB)');
print(gcf, '-djpeg100', 'rp_cylinder_wall_normal_inc.jpg');

phi_i = phi_n(2);
%plot the time domain figure for oblique incidence
figure
bw = fstop-fstart;
max_time = size(Es,2)/(bw);
plot(linspace(0, max_time/1E-9, size(Es,2)),dbv(ifft(Es(n,:))),'k');
grid on;
title(['incident angle \phi_{ i} = ',num2str(phi_i*180/pi),' (deg)']);
xlabel('time (ns)');
ylabel('scattered electric field E^s (dB)');
print(gcf, '-djpeg100', 'rp_cylinder_wall_oblique_inc.jpg');
```

APPENDIX I

MATLAB CODE FOR SIMULATING SAR DATA OF A PEC CYLINDER ON THE OPPOSITE SIDE OF A DIELECTRIC SLAB

The following MATLAB program was written to simulate rail SAR data of a PEC cylinder on the opposite side of a dielectric slab. This code was based on the model developed in Chapter 5.

```
%rail SAR data is theoretically calculated using this program for a
%dielectric wall and cylinder


%this is the final simulation program


clear all;
%close all;
set(0,'defaultaxesfontsize',18);


%*****************************
%constants
%*****************************
mu0 = 4*pi*10^-7; %(H/m) free space permeability
eps0 = 8.85418E-12; %(F/m) free space permittivity
E0 = 1; %(V/m) incident field magnitude


%dielectric properties
epsr = 5;%relative dielectric constant of layer 1
```

```
%frequency chirp and wave number calculations
fstart = 2E9; %(Hz) start freq
fstop = 4E9; %(Hz) stop freq
f = linspace(fstart, fstop, 256); %(HZ) chirp frequency
w = 2*pi*f; %(rad/m) radial freq

%conductivity approximation (from a model)
%sigma = 0.219 + (f - 1E9)*.036/1E9; %porosity factor of 0.15
sigma = 0.1194 + (f - 1E9)*.0222/1E9; %porosity factor of 0.10
%sigma = 0;

%wave number calculations
k0 = w*sqrt(mu0*eps0); %(rad/m) wave number in free space
k = w.*sqrt(mu0*(epsr*eps0+sigma./(j*w)));

%****************************************
%unique geometry and incidence angles
%****************************************
%geometry constants
d1 = 20*.3048; %(m) distance from rail to wall
d = 4/12*.3048; %(m) thickness of wall
d3 = 30*.3048; %(m) distance from rail to target center
L = 8*.3048; %(m) length of the rail
inc = linspace(-L/2, L/2, 48); %(m) location of radar on the rail, accross
%all rail positions
%inc = 4*.3048
```

```
%first, build the phi_n matrix, the incident angle
phi_n = acos(d3./(sqrt(inc.^2 + d3^2)));

%next, build the r matricies
r1n = d1./(cos(phi_n));
r3n = (d3-d1-d)./(cos(phi_n));

%cylinder parameters
a = (3/12)*.3048; %(m) radius of the cylinder
N = 400; %must be high enough for proper convergance on larger cylinders
phi_rp = -pi; %IMPORTANT: this is the monostastic observation angle

%************************************************
%calculatons
%************************************************
for n = 1:size(inc,2)
phi_i = phi_n(n);

    n

    %calculate the normalized dielectric impedance wrt incidence angle
    %perpendicular polarization (TMz)
    Z = cos(phi_i)./sqrt((epsr + sigma./(j*w*eps0)) - (sin(phi_i))^2);

    %calculate the relection coefficients wrt incidence angle
    R1 = (Z-1)./(Z+1);
    R2 = (1-Z)./(1+Z);
```

```
    %calculate the transmission coefficients wrt incidence angle
    T1 = 1 + R1;
    T2 = 1 + R2;

    %calculate the elecrical length of layer 1, phase length of layer 1
    theta = d*sqrt(epsr + sigma./(w.*j*eps0) - (sin(phi_i)).^2).*k0;%;

    %calcualte c1, the incident fileld at the first boundary face
    r = r1n(n); %(m) distance to wall
    c1 = E0*exp(-j*k0*r);

    %calculate the radar target function
    %calculated the scattered field of the cylinder
    for ii = 1:size(k0,2)
    sum = 0;
    for jj = 1:N
         nn = jj - 1;
        if nn == 0
            epsn = 1;
        else
            epsn = 2;
        end
        sum = sum + (-j)^nn*epsn*besselj(nn,k0(ii)*a).
         *besselh(nn,2,k0(ii)*r3n(n))
./besselh(nn,2,k0(ii)*a).*cos(nn*phi_rp);
    end
```

```
    rcs(ii) = sum;
    end
    rcs = -1*exp(-j*k0*r3n(n)).*rcs;

    %rcs = 0; %0 for the case of dielectric only imaging
    %and range profiles
    %rcs = rcs.*exp(-j*2*k0*r3n(n));

    %calculate c3 the tranmitted into region 3 coeficient wrt phase
    %legnth of layer 1
    c3 = T1.*T2.*c1./(exp(j*theta)+R1.*R2.*exp(-j*theta)
     +rcs.*(R2.*exp(j*theta)+R1.*exp(-j*theta)));

    %calculate b1 the reflected coefficient, wrt phase length of layer 1
    b1 = (c3./(T1.*T2)).*(R1.*exp(j*theta)+R2.*exp(-j*theta)
     +rcs.*(R1.*R2.*exp(j*theta)+exp(-j*theta)));

    %plane wave takes some distance to get back to receiver,
    %thus the received field is
    Es(n,:) = b1.*exp(-j*k0*r);

end

s = Es;
save thruwall s;
SBAND_RMA_opendata
```

APPENDIX J

MATLAB CODE FOR OPENING MEASURED CALIBRATION AND SAR DATA

The following MATLAB program was written to open measured SAR data and calibration data. This program calibrates the SAR data and conditions the data to be fed into the MATLAB RMA program in appendix C.

```
%Range Migration Algorithm from ch 10 of Spotlight Synthetic Aperture Radar
%Signal Processing Algorithms, Carrara, Goodman, and Majewski


clear all;
c = 3E8; %(m/s) speed of light


%*********************************************************************
%load IQ converted data here
load rback2 s; %load variable sif %for background subtraction cal data


%*********************************************************************
%perform background subtraction
sif_sub = s;
load rsphere s; %load variable sif %for image data
sif = s-sif_sub; %perform coherent background subtraction
%sif = sif_sub; %image just the background
%sif = s; %image without background subtraction
clear s;
clear sif_sub;
```

```
%*************************************************************************
%radar parameters
fc = (4.069E9 - 1.926E9)/2 + 1.926E9; %(Hz) center radar frequency
B = (4.069E9 - 1.926E9); %(hz) bandwidth
cr = 2E9/10E-3; %(Hz/sec) chirp rate
Tp = 10E-3; %(sec) pulse width
%VERY IMPORTANT, change Rs to distance to cal target
Rs = (37.1)*.3048; %(m) y coordinate to scene center (down range),
%make this value equal to distance to cal target
Xa = 0; %(m) beginning of new aperture length
delta_x = 2*(1/12)*0.3048; %(m) 2 inch antenna spacing
L = delta_x*(size(sif,1)); %(m) aperture length
Xa = linspace(-L/2, L/2, (L/delta_x)); %(m) cross range
%position of radar on aperture L
Za = 0;
Ya = Rs; %THIS IS VERY IMPORTANT, SEE GEOMETRY FIGURE 10.6
t = linspace(0, Tp, size(sif,2)); %(s) fast time, CHECK SAMPLE RATE
Kr = linspace(((4*pi/c)*(fc - B/2)), ((4*pi/c)*(fc + B/2)), (size(t,2)));

%*************************************************************************
%callibration
load rcal37pt1_2 s; %load callibration file to standard target
s_cal = s;
load rcalback_2 s; %load background data for cal to standard target
s_cal = s_cal - s; %perform background subtraction
cal = s_cal;
```

```
%calculate ideal cal target parameters
%target parameters, 3 targets
at1 = 1; %amplitude of cal target
xt1 = 0;
yt1 = (37.1)*.3048; %(m) distance to cal target
zt1 = 0;

%Rt and Rb for 1 cal target according to equation 10.26
Rb1 = sqrt((Ya - yt1)^2 + (Za - zt1)^2);
xa = 0;
Rt1 = sqrt((xa - xt1).^2 + Rb1^2);
Kr = linspace(((4*pi/c)*(fc - B/2)), ((4*pi/c)*(fc + B/2)), (size(t,2)));
%according to range defined on bottom of page 410
for ii = 1:size(t,2) %step thru each time step to find phi_if
    phi_if1(ii) = Kr(ii)*(Rt1 - Rs);
end
cal_theory = at1*exp(-j*phi_if1);
clear phi_if1;

%calculate the calibration factor
cf = cal_theory./(cal);

%apply the cal data
for ii = 1:size(sif,1)
     sif(ii,:) = sif(ii,:).*cf; %turn off cal
end
```

```
%Save background subtracted and callibrated data
save sif sif delta_x Rs Kr Xa;
%clear all;

%run IFP
SBAND_RMA_IFP;
```

BIBLIOGRAPHY

BIBLIOGRAPHY

[1] N. C. Currie, F. J. Demma, D. D. Ferris Jr., R. B. McMillan, V. C. Vannicola, M. C. Wicks, "Survey of state of-the-art technology in remote concealed weapon detection," Investigative and Trial Image Processing, Proceedings of SPIE Volume 2567, 1 September 1995.

[2] D. D. Ferris, Jr., N. C. Currie, "Microwave and millimeter-wave systems for wall penetration," SPIE Conference on Targets and Backgrounds: Characterization and Representation IV SPIE Volume 3375, April 1998.

[3] N. C. Currie, D. D. Ferris, Jr., R. W. McMillan, M. C. Wicks, "New law enforcement applications of milimeter wave radar," Radar Sensor Technology II, Proceedings of SPIE Volume 3066, 10 June 1997, pp. 2-10.

[4] M. Mahfouz, A. Fathy, Y. Yang, E. E. Ali, A. Badawi, "See-Through-Wall Imaging using Ultra Wideband Pulse Systems," IEEE Proceedings of the 34th Applied imagery and Pattern Recognition Workshop, 2005.

[5] Y. Yang, A. Fathy, "Design and Implementation of a Low-Cost Real-Time Ultra-Wide Band See-Through-Wall Imaging Radar System," IEEE/MTT-S International Microwave Symposium, 3-8 June, 2007, pp.1476-1470.

[6] Y. Yang, C. Zhang, S. Lin, A. E. Fathy "Developement of an Ultra Wideband Vivaldi Antenna Array," IEEE Antennas and Propagation Society International Symposium, Vol. 1A, 2-8 July 2005, pp. 606-609.

[7] C. P. Lai, R. M Narayanan, "Through-wall imaging and characterization of human activity using ultrawideband (UWB) random noise radar," Sensors, and Command, Control, Communications, and Intelligence (C3I) Technologies for Homeland Security and Homeland Defense IV, Proceedings of SPIE Volume 5778, 20 May 2005.

[8] R. Dilsavor, W. Ailes, P. Rush, F. Ahmad, W. Keichel, G. Titi, M. Amin, "Experiments of Wideband Through the Wall Imaging," Algorithms for Synthetic Aperture Radar imagery XII, Proceedings of SPIE Volume 5808, 19 May 2005, pp. 196-209.

[9] A. R. Hunt, "Image formation through walls using a distributed radar sensor array," Proceedings of the 32nd IEEE Applied Imagery Pattern Recognition Workshop, 15-17 Oct. 2003, pp. 232-237.

[10] A. R. Hunt, "Image formation through walls using a distributed radar sensor network," Sensors, and Command, Control, Communications, and Intelligence (C3I) Technologies for Homeland Security and Homeland Defense IV, Proceedings of SPIE Volume 5778, 20 May 2005, pp. 169-174.

[11] L. M. Frazier, "Surveillance through walls and other opaque materials," Public Safety/Law Enforcement Technology, Proceedings of SPIE Volume 2497, 30 May 1995.

[12] D. G. Folconer, R. W. Ficklin, K. G. Konolige, "Detection, location, and identification of building occupants using a robot-mounted through-wall radar," Digitization of the Battlespace V and Battlefield Biomedical Technologies II, Proceedings of SPIE Volume 4037, 4 August, 2000, pp. 72-81.

[13] D. G. Falconer, R. W. Ficklin, K. G. Konolige, "Robot-Mounted Through-Wall Radar for Detecting, Locating, and Identifying Building Occupants," Proceedings of the IEEE International Conference on Robotics and Automation, 24-28 April 2000, Vol. 2, pp. 1869-1875.

[14] A. Lin, H. Ling, "Through-Wall Measurements of a Doppler and Direction-of-Arrival (DDOA) Radar for Tracking Indoor Movers," IEEE Antennas and Propagation Society International Symposium, 3-8 July 2005, vol. 3B, pp. 322-325.

[15] M. Schacht, E. J. Rothwell, C. M. Colememan, "Time-domain imaging of objects within enclosures," IEEE Transactions on Antennas Propagation, Vol. 50, pp. 895-898, June 2002.

[16] S. Nag, M. A. Barnes, T. Payment, G. W. Holladay, "An Ultra-Wideband Through-Wall RAdar for Detecting the Motion of People in Real Time," Radar Sensor Technology and Data Visualization, Proceedings of SPIE Volume 4744, 2002.

[17] M. A. Barnes, S. Nag, T. Payment, "Covert Situational Awareness With Handheld Ultra-Wideband Short Pulse Radar," Radar Sensor Technology VI, Proceedings of SPIE Volume 4374, 2001.

[18] A. Berri, R. Daisy, "High-Resolution Through-Wall Imaging," Sensors, and Command, Control, Communications, and Intelligence (C3I) Technologies for Homeland Security and Homeland Defense V, Proceedings of SPIE Volume 6201, 6201J, 2006.

[19] R. Benjamin, I. J. Craddock, E. McCutcheon, and R. Nilavalan, "Through-Wall Imaging using Real-Aperture Radar," Sensors, and Command, Control, Communications, and Intelligence (C3I) Technologies for Homeland Security and Homeland Defense IV, Proceedings of SPIE Volume 5778, 20 May 2005, pp. 169-174.

[20] W. Zhiguo, L. Xi, F. Yuanchun, "Moving Target Position with Through-Wall Radar," Proceedings of the CIE '06 International Conference on Radar, Oct. 2006.

[21] H. Burchett, "Advances in Through Wall Radar for Search, Rescue and Security Applications," The Institution of Engineering and Technology Conference on Crime and Security, 13-14 June 2006, pp. 511-525.

[22] A. Berri, R. Daisy, "Non-uniform integration for Through-Wall imaging Radar," Unmanned/Unattended Sensors and Sensor Networks III, Proceedings of SPIE Volume 63940P, 5 October 2006.

[23] F. Ahmad, M. G. Amin, S. A. Kassam, "Synthetic Aperture Beamformer for Imaging Through a Dielectric Wall," IEEE Transactions on Aerospace and Electronic Systems, Vol. 41, No. 1, January 2005, pp. 271-283.

[24] F. Ahmad, M. G. Amin, S. A. Kassam, G. J. Frazer, "A Wideband, Synthetic Aperture Beamformer for Through-The-Wall Imaging," IEEE International Symposium on Phased Array Systems and Technology 2003, pp 187-192.

[25] F. Ahmad, M. G. Amin, S. A. Kassam, "Through-the-wall Wideband Synthetic Aperture Beamformer," IEEE Antennas and Propagation Society International Symposium, 20-25 June 2004, vol. 3, pp. 3059-3062.

[26] F. Ahmad, M. G. Amin, S. A. Kassam, G. J. Frazer, "A Wideband, Synthetic Aperture Beamformer for Through-the-Wall Imaging," IEEE International Symposium on Phased Array Systems and Technology, 14-17 Oct. 2003, pp. 187-192.

[27] M. Lin, Z. Zhongzhao, T. Xuezhi, "A Novel Through-Wall Imaging Method Using Ultra Wideband Pulse System," IIH-MSP '06 International Conference on Intelligent Information Hiding and Multimedia Signal Processing, Dec. 2006, pp. 147-150.

[28] F. Aryanfar, K. Sarabandi, "Through Wall Imaging at Microwave Frequencies using Space-Time Focusing," IEEE Antennas and Propagation Society International Symposium, 20-25 June 2004, Vol. 3, pp. 3063-3066.

[29] A. A. Vertiy, S. P. Gavrilov, V. N. Stepanyuk, I. V. Voynovskyy, "Through-Wall and Wall Microwave Tomography Imaging," IEEE Antennas and Propagation Society International Symposium, 20-25 June 2004, Vol. 3, pp. 3087-3090.

[30] L. P. Song, C. Yu, Q. H. Liu, "Through-Wall Imaging (TWI) by Radar: 2-D Tomographic Results and Analyses," IEEE Transactions on Geoscience and Remote Sensing, December 2005, Vol. 42, Issue 12, pp. 2793-2798.

[31] S. Hantscher, B. Praher, A. Reisenzahn, C. G. Diskus, "2D Imaging Algorithm for the Evaluation of UWB B-Scans," The Third International Conference on Ultrawideband and Ultrashort Impulse Signals, Sept. 2006, pp. 139-141.

[32] F. Soldovieri, R. Solimene, "Through-Wall Imaging via a Linear Inverse Scattering Algorithm," IEEE Geoscience and Remote Sensing Letters: Accepted for future publication as of August 2007.

[33] F. Soldovieri, R. Solimene, A. Brancaccio, R. Pierri, "Localization of the Interfaces of a Slab Hidden Behind a Wall" IEEE Transactions on Geoscience and Remote Sensing, Aug. 2007, Vol. 45, Issue 8, pp. 2471-2482.

[34] R. J. Sullivan, *Radar Foundations for Imaging and Advanced Concepts*, Scitech Publishing Inc., Raleigh, NC, 2004.

[35] M. Soumekh, *Synthetic Aperture Radar Signal Processing with MATLAB Algorithms*, John Wiley & Sons Inc., New York, NY, 1999.

[36] D. L. Mensa, *High Resolution Radar Cross-Section Imaging*, Artech House, Boston, MA, 1991.

[37] W.G. Carrara, R.S. Goodman, and R.M. Majewski, *Spotlight Synthetic Aperture Radar Signal Processing Algorithms*, Artech House, Boston, MA, 1995.

[38] S. Gauthier, W. Chamma, "Surveillance Through Concrete Walls," Sensors, and Command, Control, Communications, and Intelligence (C3I) Technologies for Homeland Security and Homeland Defense III, Proceedings of SPIE Volume 5403, 2004.

[39] X. Huang, B. Chen, H. L. Cui, K. Wang, R. Pastore, M. Farwell, W. Chin, J. Ross, M. Mingle, "Theoretical study of sensing targets through the wall using ultra-wideband technology," Radar Sensor Technology IX, Proceedings of SPIE Vol. 5788, 2005.

[40] X. Huang, B. Chen, H. L. Cui, K. Wang, R. Pastore, M. Farwell, W. Chin, J. Ross, M. Mingle, "Sensing targets behind the opaque structures based on the combined method of ray tracing and diffraction," Infrared to Terahertz Technologies for Health and the Environment, Proceedings of SPIE Volume 6010, 17 November 2005.

[41] A. T. S. Ho, W. H. Tham, K S. Low, "Through-Wall Radar Image Reconstruction Based on Time-Domain Transient Signals in the Presence of Noise," 2005 IEEE International Geoscience and Remote Sensing Symposium, Proceedings, 25-29 July 2005, pp 4271-4274.

[42] J. H. Richmond, "Scattering by a Dielectric Cylinder of Arbitrary Cross Section Shape," IEEE Transactions on Antennas and Propagation, May 1965, pp. 334-341.

[43] J. H. Richmond, "TE-Wave Scattering by a Dielectric Cylinder of Arbitrary Cross-Section Shape," IEEE Transactions on Antennas and Propagation, July 1966, Vol. AP-14, No. 4, pp. 460-464.

[44] R. F. Harrington, *Field Computation by Moment Methods,* IEEE Press, Piscataway, NJ, 1992.

[45] W. C. Chew, *Waves and Fields in Inhomogeneous Media,* IEEE Press, Piscataway, NJ, 1995.

[46] E. L. Mokole, S. N. Samaddar, "Pulsed Reflection and Transmission for a Dispersive Half Space," Naval Research Laboratory, Washington DC, June 29, 1998, NRL/FR/5340-98-9847.

[47] E. L. Mokole, S. N. Samaddar, "Transmission and reflection of normally incident, pulsed electromagnetic plane waves upon a Lorentz half-space," J. Opt. Soc. Am. B/Vol. 16, No. 5, May 1999.

[48] G. L. Charvat, E. Rothwell, "A Theoretical Model of a Lossy Dielectric Slab for the Characterization of Radar System Performance Specifications," Antennas Measurement Techniques Association Conference, Austin Texas, October 2006.

[49] W. D. Burnside, K. W. Burgener, "High Frequency Scattering by a Thin Lossless Dielectric Slab," IEEE Transactions on Antennas and Propagation, Vol. AP-31, No. 1, January 1983, pp. 104-110.

[50] M. P. G. Capelli, "Radio Altimeter," IRE Transactions on Aeronautical and Navigational Electronics, Vol. 1, June 1954, pp. 3-7.

[51] F. T. Wimberly, J. F. Lane, "The AN/APN-22 Radio Altimeter," IRE Transactions on Aeronautical and Navigational Engineering, Vol. 1, June 1954, pp. 8-14.

[52] A. Black, K. E. Buecks, A. H. Heaton, "Improved Radio Altimeter," Wireless World, Vol. 60, March 1954, pp. 138-140.

[53] A. G. Stove, "Linear FMCW radar techniques," IEE Proceedings of Radar and Signal Processing, Vol. 139, October 1992, pp. 343-350.

[54] E. L. Mokole, "Behavior of Ultrawideband-Radar Array Antennas," IEEE International Symposium on Phased Array Systems and Technology, 15-18 October 1996, pp. 113-118.

[55] P. J. F. Swart, J. Schier, A. J. van Gemund, W. F. van der Zwan, J. P. Karelse, G. L. Reijns, P. van Genderen, L. P. Ligthart, H. T. Steenstra, "The Colarado Multistatic FMCW Radar System," IEEE European Microwave Conference, October 1998, Vol. 2, pp. 449-454.

[56] V. Katkovnik, M. S. Lee, Y. H. Kim, "High-Resolution Signal Processing for a Switch Antenna Array FMCW Radar with a Single Channel Receiver," IEEE Proceedings of Sensor Array and Multichannel Signal Processing, 4-6 August 2002, pp. 543-547.

[57] M. S. Lee, V. Katkovnik, Y. H. Kim, "System Modeling and Signal Processing for a Switch Antenna Array," IEEE Transactions on Signal Processing, Vol. 52, Issue 6, June 2004, pp. 1513-1523.

[58] G.W. Stimson, *Introduction to Airborne Radar,* Hughes Aircraft Company, El Segundo, California, 1983.

[59] G.L. Charvat, and L.C. Kempel, "Synthetic Aperture Radar Imaging Using a Unique Approach to Frequency Modulated Continuous-Wave Radar Design," IEEE Antennas Propagat. Magazine, Febuary 2006.

[60] G.L. Charvat, "Low-Cost, High Resolution X-Band Laboratory Radar System for Synthetic Aperture Radar Applications," Antenna Measurement Techniques Association Conference, Austin, Texas, October 2006.

[61] C.A. Balanis, *Advanced Engineering Electromagnetics,* John Wiley & Sons, New York, NY, 1989.

[62] C.A. Balanis, *Antenna Theory Analysis and Design, Second Edition,* John Wiley & Sons, New York, NY, 1997.

[63] R.E. Collin, *Field Theory of Guided Waves,* Second Edition, IEEE Press, Piscataway, NJ, 1991.

[64] U.B. Halabe, K. Maser, and E. Kausel, "Propagation Characteristics of Electromagnetic Waves in Concrete, Technical Report," AD-A207387, March 1989.

[65] C.J. Savant Jr., R.C. Howard, C.B. Solloway, and C.A. Savant, *Principles of Inertial Navigation,* McGraw-Hill Book Company, Inc, New York, NY, 1961.

[66] E.J. Rothwell and M.J. Cloud, *Electromagnetics,* CRC Press, Boca Raton, Florida, 2001.

[67] U. L. Rhode, J. Whitaker, T. T. N. Bucher, *Communications Receivers, 2nd Ed.,* McGraw-Hill, New York, NY, 1996.

[68] P. Vizmuller, *RF Design Guide Systems, Circuits, and Equations,* Artech House, Norwood, MA, 1995.

[69] R. E. Ziemer, W. H. Tranter, *Principles of Communications, Systems, Modulation, and Noise* John Wiley & Sons, Inc., New York, NY, 1995.

[70] *The ARRL Handbook, 71st Edition,* The American Radio Relay League, Inc., Newington, CT, 1994.

[71] R. Janaswamy, D. H. Schaubert, and D. M. Pozar, "Analysis of the transverse electromagnetic mode linearly tapered slot antenna," Radio Science, Volume 21, No. 5, pp. 797-804, September-October 1986.

[72] R. Janaswamy, D. H. Schaubert, "Analysis of the Tapered Slot Antenna," IEEE Transactions on Antennas and Propagation, Vol. AP-35, No. 9, September 1987, pp. 1058-1065.

[73] R. Janaswamy, "An Accurate Moment Method Model for the Tapered Slot Antenna," IEEE Transactions on Antennas and Propagation, Vol. 37, No. 12, December 1989.

[74] Y. S. Kim, S. Yngvesson, "Characterization of Tapered Slot Antenna Feeds and Arrays," IEEE Transactions on Antennas and Propagation, Vol. 38, No. 10, October 1990.

[75] P. S. Kooi, T. S. Yeo, M. S. Leong, "Parametric Studies of the Linearly Tapered Slot Antenna (LTSA)," IEEE Microwave and Optical Technology Letters, Vol. 4, No. 5, April 1991.

[76] E. Thiele, A. Taflove, "FD-TD Analysis of Vivaldi Flared Horn Antennas and Arrays," IEEE Transactions on Antennas and Propagation, Vol. 42, No. 5, May 1994.

[77] X. D. Wu, and K. Chang, "Compact Wideband Integrated Active Slot Antenna Amplifier," IEEE Electronics Letters, Vol. 29, No. 5, 4 March 1993.

[78] P. Horowitz, W. Hill, *The Art of Electronics,* Cambridge University Press, London, 1980.

[79] D. Lancaster, *Active Filter Cookbook,* 17^{th} *Edition,* Synergetics Press, Thatcher, AZ, 1995.